23 August 2019 | $10

Science



AAAS

EDITORIAL

820 Maintaining Science Eminence
Alan I. Leshner

NEWS OF THE WEEK

826 A roundup of the week's top stories

NEWS & ANALYSIS

828 Diplomatic Flap Threatens E.U.-Israeli Research Ties

829 How NASA Tried to Save Its Prime Planet-Spotter

830 Half of All Papers Now Free in Some Form, Study Claims

831 Can China Age Gracefully? A Massive Survey Aims to Find Out

NEWS FOCUS

833 The CRISPR Craze

837 The Save-the-World Foundation
>> Science *Podcast*

LETTERS

840 Archaeobotanical Archiving
S. E. J. Golzari

Response
M. Zeidi et al.

Alleviating Poverty in India: Biodiversity's Role
R. M. Lasley Jr. et al.

Protecting the Right to Benefit from Science
J. H. Matsuura

Response
A. R. Chapman and J. M. Wyndham

842 CORRECTIONS AND CLARIFICATIONS

BOOKS *ET AL.*

843 After the Grizzly
P. S. Alagona, reviewed by S. Redpath

844 Game-Theoretical Models in Biology
M. Broom and J. Rychtář, reviewed by B. Allen and M. A. Nowak

EDUCATION FORUM

845 Can Rating Pre-K Programs Predict Children's Learning?
T. J. Sabol et al.

POLICY FORUM

847 A Critical Crossroad for BLM's Wild Horse Program
R. A. Garrott and M. K. Oli

PERSPECTIVES

849 Mysterious Ribosomopathies
K. L. McCann and S. J. Baserga
>> *Science* Podcast

850 Megacity Megaquakes—Two Near Misses
R. S. Stein and S. Toda

852 An Arsenic Forecast for China
H. A. Michael
>> *Report p. 866*

853 Gene Therapy That Works
I. M. Verma
>> *Research Articles pp. 864 and 865*

855 Nucleation from Solution
A. S. Myerson and B. L. Trout
>> *Report p. 885*

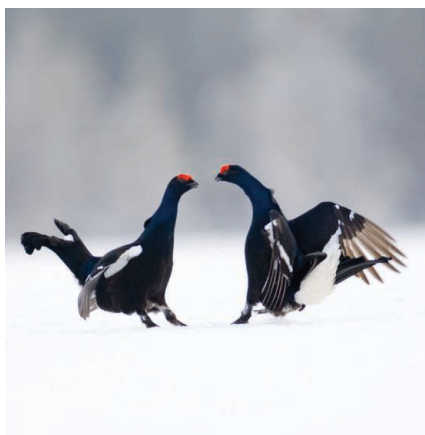
856 The Health Risk of Obesity—Better Metrics Imperative
R. S. Ahima and M. A. Lazar

858 Functional Ion Defects in Transition Metal Oxides
S. V. Kalinin and N. A. Spaldin

CONTENTS continued >>



page 831

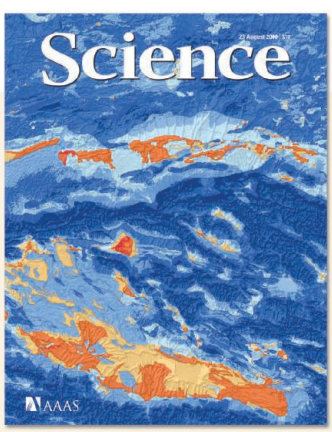


page 844

ON THE WEB THIS WEEK

>> Ongoing Series: Neurodevelopment
Check out the latest installment in this ongoing series, a Review on neural crest cell development and disease, on page 860 and at www.sciencemag.org/extra/neurodev.

>> Find More Online
Check out *Science* Express, our podcast, videos, daily news, our research journals, and *Science* Careers at **www.sciencemag.org**.



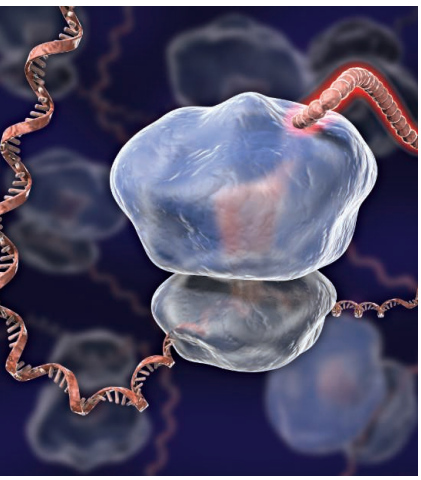
COVER

Partial view of the predictive map of high levels of arsenic in groundwater resources in China (blue, low probability; red, high probability; width, 600 kilometers; resolution, 1 square kilometer). Chronic arsenic poisoning from contaminated groundwater is a major health problem in many parts of China. An estimated 19.6 million people are potentially exposed to elevated arsenic concentrations in their drinking water. See pages 852 and 866.

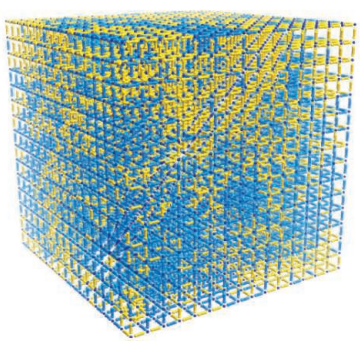
Image: Luis Rodríguez-Lado and Michael Berg, Eawag

DEPARTMENTS

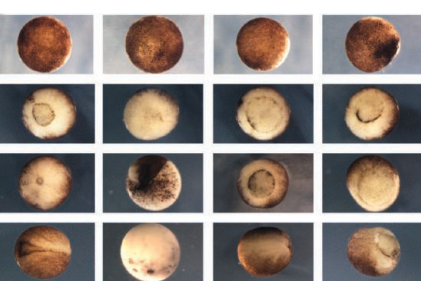
819 This Week in *Science*
821 Editors' Choice
824 *Science* Staff
907 New Products
908 *Science* Careers



page 849



page 882



page 893

REVIEW

860 Tissue Interactions in Neural Crest Cell Development and Disease
Y. Takahashi et al.

RESEARCH ARTICLES

864 Lentiviral Hematopoietic Stem Cell Gene Therapy Benefits Metachromatic Leukodystrophy
A. Biffi et al.
Lentivirus-mediated gene therapy produces encouraging results in three children with a rare lysosomal storage disease.
Research Article Summary; for full text: http://dx.doi.org/10.1126/science.1233158

865 Lentiviral Hematopoietic Stem Cell Gene Therapy in Patients with Wiskott-Aldrich Syndrome
A. Aiuti et al.
Lentivirus-mediated gene therapy produces encouraging results in three children with a rare immunodeficiency disorder.
Research Article Summary; for full text: http://dx.doi.org/10.1126/science.1233151
>> Perspective p. 853

REPORTS

866 Groundwater Arsenic Contamination Throughout China
L. Rodríguez-Lado et al.
A predictive map of arsenic in Chinese groundwater aquifers reveals a potential health risk to 19.6 million people.
>> Perspective p. 852

868 Hillslopes Record the Growth and Decay of Landscapes
M. D. Hurst et al.
Changes in tectonic rates can be quantitatively derived from hillslope morphology.

871 Mapping Tectonic Deformation in the Crust and Upper Mantle Beneath Europe and the North Atlantic Ocean
H. Zhu and J. Tromp
Anisotropy of the crust and mantle under Europe is a relict of the continent's formation.

875 Abundant Porewater Mn(III) Is a Major Component of the Sedimentary Redox System
A. S. Madison et al.
Soluble manganese(III) accounts for up to 90% of the total manganese in the near-surface porewaters of hemipelagic sediments.

878 14-Step Synthesis of (+)-Ingenol from (+)-3-Carene
L. Jørgensen et al.
A chemical route to a diterpenoid could enhance production efficiency of a drug that treats a precancerous skin condition.

882 Mapping of Functional Groups in Metal-Organic Frameworks
X. Kong et al.
Solid-state nuclear magnetic resonance and simulations map the distribution of linking groups in metal-organic frameworks.

885 Microscopic Evidence for Liquid-Liquid Separation in Supersaturated $CaCO_3$ Solutions
A. F. Wallace et al.
The preordering seen during calcium carbonate crystallization may be due to a liquid-liquid separation process.
>> Perspective p. 855

889 Molecular Mechanism for Plant Steroid Receptor Activation by Somatic Embryogenesis Co-Receptor Kinases
J. Santiago et al.
Crystal structures reveal why the brassinosteroid receptor kinase requires another kinase helper protein for activation.

893 Titration of Four Replication Factors Is Essential for the *Xenopus laevis* Midblastula Transition
C. Collart et al.
Increasing numbers of nuclei compared with the cytoplasmic volume promotes a key developmental step in frog embryos.

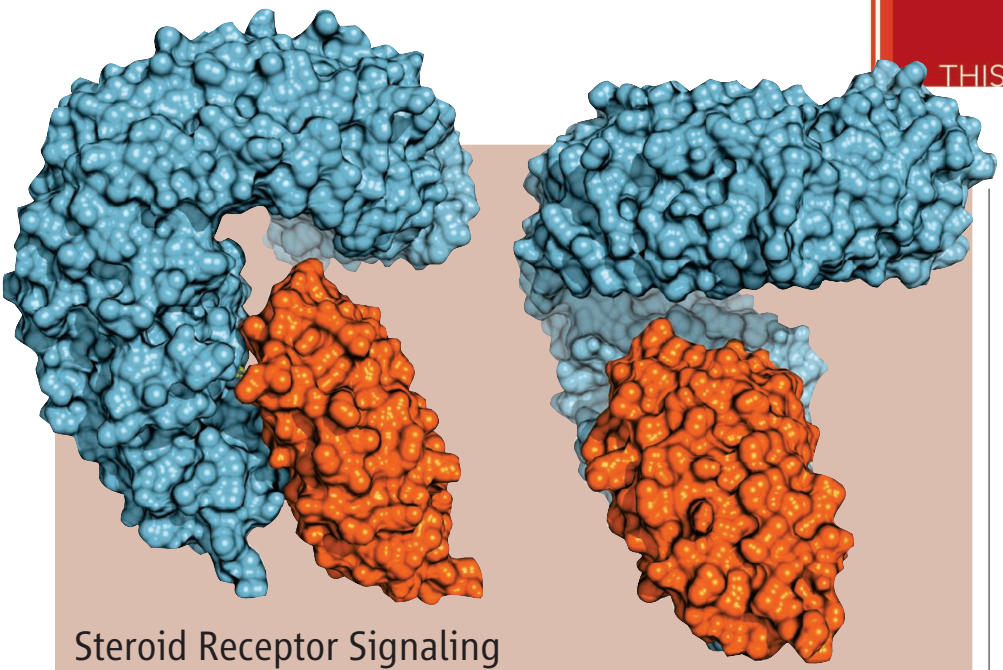
896 SGK196 Is a Glycosylation-Specific *O*-Mannose Kinase Required for Dystroglycan Function
T. Yoshida-Moriguchi et al.
An atypical kinase genetically associated with muscular dystrophies recognizes a unique trisaccharide structure.

899 Conformational Motions Regulate Phosphoryl Transfer in Related Protein Tyrosine Phosphatases
S. K. Whittier et al.
Differences in the rate of an internal protein loop closure are coupled to differences in enzyme reaction rates.

903 Cyclic GMP-AMP Synthase Is an Innate Immune Sensor of HIV and Other Retroviruses
D. Gao et al.
Cell culture experiments suggest that detection of retroviral DNA activates cellular defense systems.

SCIENCE (ISSN 0036-8075) is published weekly on Friday, except the last week in December, by the American Association for the Advancement of Science, 1200 New York Avenue, NW, Washington, DC 20005. Periodicals Mail postage (publication No. 484460) paid at Washington, DC, and additional mailing offices. Copyright © 2013 by the American Association for the Advancement of Science. The title SCIENCE is a registered trademark of the AAAS. Domestic individual membership and subscription (51 issues): $149 ($74 allocated to subscription). Domestic institutional subscription (51 issues): $990; Foreign postage extra: Mexico, Caribbean (surface mail) $55; other countries (air assist delivery) $85. First class, airmail, student, and emeritus rates on request. Canadian rates with GST available upon request, GST #1254 88122. Publications Mail Agreement Number 1069624. **Printed in the U.S.A.**

Change of address: Allow 4 weeks, giving old and new addresses and 8-digit account number. **Postmaster:** Send change of address to AAAS, P.O. Box 96178, Washington, DC 20090–6178. **Single-copy sales:** $10.00 current issue, $15.00 back issue prepaid includes surface postage; bulk rates on request. **Authorization to photocopy** material for internal or personal use under circumstances not falling within the fair use provisions of the Copyright Act is granted by AAAS to libraries and other users registered with the Copyright Clearance Center (CCC) Transactional Reporting Service, provided that $30.00 per article is paid directly to CCC, 222 Rosewood Drive, Danvers, MA 01923. The identification code for *Science* is 0036-8075. *Science* is indexed in the *Reader's Guide to Periodical Literature* and in several specialized indexes.



Steroid Receptor Signaling

Plant brassinosteroids signal to diverse pathways in plant physiology. These steroid hormones are perceived at the cell surface, where they bind to the receptor BRASSINOSTEROID INSENSITIVE 1 (BRI1). **Santiago *et al.*** (p. 889, published online 8 August) now show that somatic embryogenesis receptor kinase 1 (SERK1) complexes with BRI1. Together, these receptor kinases form the steroid binding site, with the hormone acting as a "molecular glue" that stabilizes the interaction. Hormone-induced heteromerization of BRI1 with SERK1 leads to the activation of the cytoplasmic signaling cascade, triggering plant growth and differentiation.

Arsenic and Populace

The solubility of arsenic in groundwater aquifers is controlled by a number of hydrologic and geochemical factors. In rural communities that rely on groundwater for drinking water, the risk from exposure may pose a public health threat, especially when groundwater pumping can increase arsenic solubility. In an effort to provide a focused assessment of risk to arsenic exposure from groundwater, **Rodríguez-Lado *et al.*** (p. 866; see the Perspective by **Michael**) constructed a geostatistical model that incorporates a number of factors that control arsenic solubility across China. Most of the risk centers in a few provinces—Xinjiang, Inner Mongolia, Henan, Shandong, and Jiangsu—but the total population exposed to arsenic levels above 10 micrograms per liter could be upwards of 19 million people.

Closing the Loop

Many studies have shown that protein dynamics are important to enzyme function. For example, enzyme protein movements have been shown to optimize the active site, enable binding of substrate and cofactor, and facilitate product release. **Whittier *et al.*** (p. 899) now show that in two tyrosine phosphatases, the rate of cleavage is coupled to motion of a loop. The two phosphatases have different catalytic rates; however, in both, a loop containing a catalytic residue switches between an inactive open and a catalytically competent closed state. The rates of closure are equivalent to the cleavage rates, suggesting that the leaving group tyrosine is protonated simultaneously with loop closure. Thus, tuning of the loop motion plays a regulatory role in the catalytic cycle.

Gotta Get Up to Get Down

By examining high-resolution satellite topography data of a ridge along the San Andreas Fault in California, **Hurst *et al.*** (p. 868) demonstrate how hill slope curvature may be used to infer long-term rates of tectonic uplift and erosion. Numerical modeling shows a lag phase between uplift events and changes in morphology, which, combined with the observational data, shows that topography can reveal whether landscapes are active or decaying. These fundamental relationships may help to improve seismic hazard forecasts or to interpret topographic data collected on other terrestrial planets.

Mn at Work

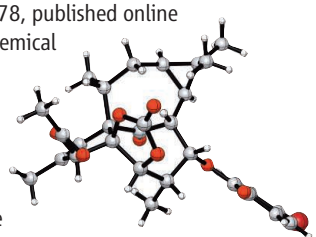
Biogeochemical cycling involves oxidation-reduction reactions with common metals like iron and manganese. Depending on the oxygen concentration and pH of the surrounding water, these metals—which exist in multiple oxidation states—can either accept or donate electrons; however, detecting which chemical species is dominant in these reactions often proves difficult. Using a spectrophotometric method sensitive to Mn oxidation state, **Madison *et al.*** (p. 875) show that up to 90% of the total Mn in porewater collected from sediment cores in the St. Lawrence Estuary is soluble Mn(III)—a phase traditionally assumed to be unimportant in aqueous redox reactions except in a few niche environments.

Regulating the MBT

It has been known for more than 30 years that a defined number of cell divisions in the frog embryo precede a crucial developmental event called the midblastula transition (MBT). **Collart *et al.*** (p. 893, published online 1 August) now elucidate a mechanism involved in the control of the MBT. DNA replication initiation factors are titrated out during early cell divisions, which controls the elongation of the cell cycle and the onset of zygotic transcription during the MBT.

Ingenol Ingenuity

The diterpenoid ingenol is the core structure of a topical drug recently commercialized to treat actinic keratosis, a precancerous skin condition. Sourcing the compound from the *Euphorbia* plants that produce it is relatively inefficient, so **Jørgensen *et al.*** (p. 878, published online 1 August) devised a chemical synthesis starting from the comparatively simple and inexpensive monoterpene chiral (+)-3-carene. The synthetic sequence involves 14 steps—less than half as long as prior chemical routes to the target—and relies on a two-stage approach, inspired by the posited biosynthetic pathway, in which preliminary assembly of the fused ring framework precedes hydroxylation of the periphery.



HIV Detection Is a (c)GAS

Despite it being one of the most highly studied viruses, there are still many unknowns when it comes to HIV—including how it triggers the innate immune response. **Gao *et al.*** (p. 903, published 8 August) now demonstrate that the DNA sensor cyclic GMP-AMP synthase (cGAS) detects HIV infection. Reverse-transcribed HIV DNA triggers cGAS and downstream activation of antiviral immunity. Detection of HIV, as well as the retroviruses simian immunodeficiency virus and murine leukemia virus, was abrogated in mouse and human cells deficient in cGAS—suggesting that cGAS may be a critical activator of innate immunity in response to retroviral infection.

CREDITS (TOP TO BOTTOM): SANTIAGO *ET AL.*; JØRGENSEN *ET AL.*

Additional summaries

Neural Crest Development

The vertebrate neural crest is characterized by a migratory population of multipotent cells that spread out from the dorsal side of the neural tube. Many different cell types and tissues originate here, including cells of the peripheral nervous system, the adrenal medulla, melanocytes, and some skeletal cells. Dysregulation of neural crest cells can lead to defects in cell differentiation and the cell cycle, as well as to the formation of ectopic tissue, which can result in various human diseases. **Takahashi *et al.*** (p. 860) review the normal development of neural crest cells, highlighting important associations of this cell population with local environments to influence tissue interactions and function, and describe pathogenesis that results when developmental events go awry.

Next-Generation Gene Therapy

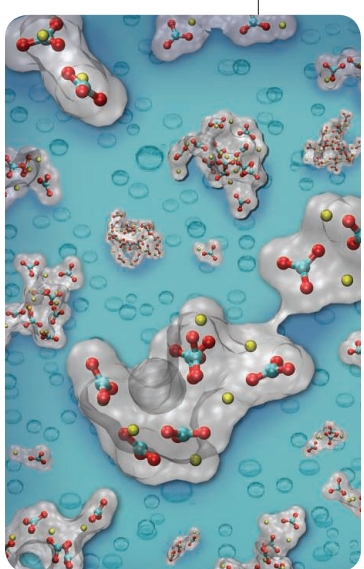
Few disciplines in contemporary clinical research have experienced the high expectations directed at the gene therapy field. However, gene therapy has been challenging to translate to the clinic, often because the therapeutic gene is expressed at insufficient levels in the patient or because the gene delivery vector integrates near proto-oncogenes, which can cause leukemia (see the Perspective by **Verma**). **Biffi *et al.*** (p. 864, published online 11 July) and **Aiuti *et al.*** (p. 865; published online 11 July) report progress on both fronts in gene therapy trials of three patients with metachromatic leukodystrophy (MLD), a neurodegenerative disorder, and three patients with Wiskott-Aldrich syndrome (WAS), an immunodeficiency disorder. Optimized lentiviral vectors were used to introduce functional *MLD* or *WAS* genes into the patients' hematopoietic stem cells (HSCs) ex vivo, and the transduced cells were then infused back into the patients, who were then monitored for up to 2 years. In both trials, the patients showed stable engraftment of the transduced HSC and high expression levels of functional *MLD* or *WAS* genes. Encouragingly, there was no evidence of lentiviral vector integration near proto-oncogenes, and the gene therapy treatment halted disease progression in most patients. A longer follow-up period will be needed to further validate efficacy and safety.

Mapping Molecular Linkers

In metal-organic framework compounds, inorganic centers (metal atoms or clusters) are linked by bidentate organic groups. Normally, the same group is used throughout the structure, but recently, synthesis with linkers bearing different functional groups has produced well-defined materials. **Kong *et al.*** (p. 882, published online 25 July) combined solid-state nuclear magnetic resonance and molecular simulations to map the distributions of linkers in these materials as random, well-mixed, or clustered.

Making Crystals

The initial transition from a disordered solution to the formation of nuclei that grow into crystals continues to be a puzzle. Recent experiments suggested the formation of stable ordered clusters that appear prior to the formation of the first nuclei. **Wallace *et al.*** (p. 885; see the Perspective by **Myerson and Trout**) used molecular dynamics to look at the potential structure and dynamics of these clusters and lattice gas simulations to explore the population dynamics of the cluster populations prior to nucleation. A liquid-liquid phase separation process was observed whereby one phase becomes more concentrated in ions and becomes the precursor for nuclei to form.



CREDIT: ADAM F. WALLACE/UNIVERSITY OF DELAWARE

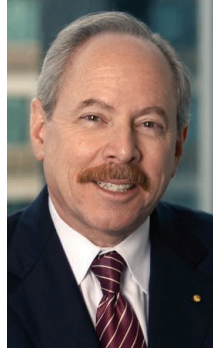
Dissecting Dystrophies

Defects in α-dystroglycan lead to various congenital muscular dystrophies, and its ability to bind to extracellular matrix (ECM) is dependent on formation of a specific O-linked sugar structure. Previous efforts to understand the molecular mechanisms underlying α-dystroglycan's ability to bind to the ECM led to the identification of a phosphorylated *O*-mannosyl trisaccharide on α-dystroglycan and to the demonstration that addition of this residue is a prerequisite for formation of the ligand-binding motif. However, the biosynthetic pathway that leads to production of the phosphorylated *O*-mannosyl glycan has not been delineated. **Yoshida-Moriguchi *et al.*** (p. 896, published online 8 August) elucidate the functions of three genes recently found to cause dystroglycan-related disorders and explain the defects in the production of the phosphorylated *O*-mannosyl glycan that underlie the pathologies of patients with the relevant mutations.

European History at Depth

The preferential alignment of mineral grains as a result of flow direction can polarize seismic waves traveling through Earth's interior, based on velocity and direction. **Zhu and Tromp** (p. 871, published online 8 August) mapped this anisotropy beneath the European continent and the North Atlantic Ocean—which are products of several tectonic events across varying temporal and spatial scales—using seismic tomography. The model generated correlates well with plate motion in the region, and, compared to geodetic measurements, much of the anisotropic features are consistent with modern strain rates. Some features below Eastern Europe, however, appear to be remnants of tectonic events that occurred over 350 million years ago.

Published by AAAS



Alan I. Leshner is the chief executive officer of AAAS and executive publisher of *Science*.

Maintaining Science Eminence

THE U.S. SCIENTIFIC ENTERPRISE IS HEAVILY BELEAGUERED. THE ECONOMY IS ONLY NOW RECOVERING from bad times, and there is great pressure to get the federal budget deficit under control. The "sequester," an across-the-board cut in the entire federal budget, is making matters even worse for science, whose budget has failed to keep pace with inflation for at least the past 4 years. These realities are coming at the same time as other countries are increasing their R&D investments, in spite of similar economic conditions, responding to the clear relationship between a nation's research capacity, its economic strength, and the well-being of its people. The inequality in science funding trends is threatening America's standing in the global scientific community. Losing its eminence in science would probably result in fewer foreign scientists coming to study and work in the United States (and even perhaps some "brain drain" of U.S. scientists), fewer U.S.-based science and technology breakthroughs, and fewer U.S. startup companies and jobs.



Agricultural R&D provides a dramatic example of how neglect can undermine a scientific domain. Recent recommendations to restore America's standing in agricultural science illustrate how the policies surrounding R&D and their use must include, but also go beyond, increased funding. U.S. Department of Agriculture (USDA) spending on R&D has declined by 26% (in constant dollars) over the past decade, while investments by China, India, and Brazil have increased dramatically.* When adjusted for purchasing power parity, the government of China now invests substantially more than the United States in that area. In parallel (and even though a correlation cannot be taken to prove causality), agricultural productivity has grown markedly in those countries while remaining static in the United States.† A 2012 study by the President's Council of Advisors on Science and Technology (PCAST) concluded that America's agricultural research enterprise is no longer prepared to meet the challenges it will face in this century and that the country's "innovation ecosystem for agriculture" requires a fundamental restructuring.‡

The PCAST report offers a refreshed approach that not only rebalances funding strategies but also supports new collaborations and calls for more efficient technology transfer. More intramural and extramural funds would be awarded through competitions based on excellence rather than allocated as formula-based block grants. Challenges not likely to be adequately taken up by the private sector, such as dealing with new pests and pathogens and adapting to a changing climate, would also receive increased attention. Funding strategies would foster the collaboration of scientists from traditional agricultural fields with those from other biological domains and the physical sciences, particularly from the basic sciences. In addition to research support, the PCAST report urges increased investments in scientific workforce development and in research infrastructure. To facilitate technology transfer to industry, the report recommends the creation of multidisciplinary innovation institutes supported by public/private partnerships and a comprehensive review of federal regulatory policies for agriculture.

If the core elements of this approach—combining increased funding, focused new programs, and the strategic rebalancing of existing funding, programs, and policies—are put in place, the United States will stand a much better chance of maintaining a leadership position in agricultural research, development, and innovation. Similar analyses and the same kinds of strategies might be very beneficial to maintaining the nation's overall scientific stature.

– Alan I. Leshner

10.1126/science.1244269

*USDA Economic Research Service and International Food Policy Research Institute, based on N. Beintema, G.-J. Stads, K. Fuglie, P. Heisey, *ASTI Global Assessment of Agricultural R&D Spending: Developing Countries Accelerate Investment* (International Food Policy Research Institute and Global Forum on Agricultural Research, Washington and Rome, 2012). †USDA Economic Research Service, based on K. O. Fuglie, S. L. Wang, V. E. Ball, Eds., *Productivity Growth in Agriculture: An International Perspective* (CAB International, Wallingford, UK, 2012). ‡PCAST, Executive Office of the President, *Report to the President on Agricultural Preparedness and the Agriculture Research Enterprise* (Washington, DC, 2012).

CREDITS: (RIGHT) COLELLA PHOTOGRAPHY; (LEFT) ANDREASREH/ISTOCKPHOTO

Published by AAAS

EDITED BY GILBERT CHIN AND MARIA CRUZ



ECOLOGY

Pay Attention

Males of many species display elaborate sexually selected traits, with the peacock's train as a classic case. We might presume that peahens would perceive a trait as we would, but the intricacy of the train suggests that its appeal could be considerably more complicated than it might seem at a glance. Yorzinski *et al*. take advantage of the development of gaze-tracking technology to look at the peacock train from the vantage point of the hen. Specifically, they trained females to wear a gaze-tracking device and then let them interact with males. They found that during the majority of the time the females were with the males, they weren't even looking at them, although males could attract their attention by shaking their wings. Further, when they did pay attention to the males, they looked not at the showy top of the fan, but at the feathers at the bottom and at the male's feet and legs. Though these results might at first suggest that the fan is perhaps a byproduct of selection for the lower feathers, subsequent experiments showed that the tops of the fans were in fact useful for attracting females at long distances. Overall, these results show that multicomponent male displays are the cumulative result of an attraction dance, and they suggest that to understand the evolution of such traits, we should study them through the eyes of the intended target. — SNV

J. Exp. Biol. **216**, 3035 (2013).

TECHNOLOGY

Social Transfers

Under pressure to demonstrate economic returns on public investments in research, universities often point to evidence that the knowledge they generate can spill over and stimulate regional economies that are based, at least in part, on innovation. Yet, despite studies of technology transfer practices, university funding, and other factors, there is much to be learned about why places that aspire to become the next Silicon Valley might not attain their dreams. Casper examines regional social networks in which universities are embedded as potential modulators of the economic impact of research. He compared biotechnology communities in the San Francisco and Los Angeles regions, both of which include multiple universities that share similar characteristics. Whereas San Francisco attracted only 30% more research funding than Los Angeles over a 25-year period, Bay Area universities obtained more than twice as many biotech patents and spun out three times as many biotech firms. By tracking which people were linked as co-inventors on patent applications, Casper found that social networks were larger and more cohesive in San Francisco than in Los Angeles, spanning universities and firms, with upticks in network size and connectivity over time correlating with growth in patenting. This work suggests that community social networks can modulate the ability of universities to transmit and receive knowledge benefits. — BW

Res. Policy **42**, 10.1016/j.respol.2013.04.005 (2013).



CREDITS (TOP TO BOTTOM): © KRISTINE DEPPE; © PROEHL STUDIOS/CORBIS

PHYSIOLOGY

Next Generation

Many signaling factors and tissues interact to enable successful fertilization, gestation, and delivery. Failure of any one of a number of these elements can result in a failed pregnancy. The *Lrh-1* gene encodes an orphan nuclear receptor, liver receptor homolog-1. When Zhang *et al.* knocked out this gene in the ovarian follicle of mice, females displayed regular mating and successful ovulation but were infertile. Analysis of the corpora lutea of these mice showed that transcripts from genes involved in steroidogenesis decreased after ovarian stimulation, and hence progesterone levels were reduced, with resultant implantation failure. The defect in implantation could be rescued by the administration of progesterone, but other problems remained, including an improper spacing of embryos and differences in fetoplacental size. In addition to being expressed in the corpus luteum, *Lrh-1* is also expressed in the endometrium of mice and humans. Without it, abnormal expression of endometrial genes results in uterine dysfunction and aberrant gestation. This work shows the critical roles that *Lrh-1* plays in successful pregnancy via activities in both luteal function for decidualization and the formation of the placenta. — BAP

Nat. Med. **19**, 1061 (2013).

HUMAN GENETICS

Slide Show

Countless freezers and cabinet drawers are filled with fixed specimens on slides, whole organisms in some cases, tissue slices in others. In order to probe the specifics of gene expression within fixed cells and tissues, Ke *et al.* have developed a method to apply single-cell RNA sequencing in situ and show that they can see mRNA molecules

Continued on page 823

Published by AAAS

Continued from page 821

that differ by a single nucleotide between cells. Although the sequencing is limited to stretches of four nucleotides, the authors are able to detect cell-specific mutations within KRAS genes, and they demonstrate multiplex expression profiling with different genes within breast tissue. Further development and application of this technique may yield dividends in developmental biology, epigenetics, and tumor and stem cell research. — LMZ

Nat. Methods **10**, 10.1038/nmeth.2563 (2013).

MATERIALS SCIENCE

Mesoporous Oxides via Carbonates

Mesoporous oxide materials have potential applications in light harvesting and catalysis and as electrode materials. Thin films of these materials are most often formed through a soft-templating process in which a precursor gel is patterned by nanoscale micelles that form from diblock copolymers during solvent evaporates. This route has proven difficult with some oxides, notably zinc oxide (ZnO) and cobalt oxide (Co_3O_4), because of problems with the three main types of precursors (alkoxides, nanoparticles, and thermally decomposed precursors). Eckhardt *et al*. show that both mesoporous zinc and cobalt oxides can be formed from soft templates by first forming mesoporous metal carbonates. These materials were formed with triblock poly(ethylene) oxide (PEO)–poly(butadiene) (PB) copolymer (PEO-PB-PEO) micelles and used metal nitrates and citric acid in mixed ethanolwater solvent as the precursor. This solution was dip-coated on substrates at room temperature and then heated for 1 hour at 250°C for zinc and 200°C for cobalt to form the carbonates. Additional heating (25 min at 400°C for zinc and 20 min at 300°C for cobalt) formed the oxides. For zinc, the amorphous wall of the mesoporous carbonate transformed into the crystalline oxide and increased the surface area. For cobalt, the carbonate appeared to retain the micelle template, and mesoporosity developed only in the final thermal processing step as spinel oxide phase walls formed. — PDS

Chem. Mater. **25**, 2749 (2013).

EDUCATION

Active Investment

Traditional classrooms, where rows of students face an instructor, may be an obstacle as science education moves toward inquiry-based learning. However, is reconfiguring these classrooms to encourage active and team-based learning worth the cost? Looking at introductory biology courses where the same syllabus, exams, and instructors were used, Cotner *et al.* compared student performance in a traditional (TC) versus active learning classroom (ALC). Observational data was collected on 50% of randomly selected students in both classrooms, with the amount of time appearing to be "on task" and actions of both the instructor and the students being recorded. Additionally, students responded to a survey detailing their experiences and perceptions once the course had finished. Results showed that the same instructor spent more time encouraging and consulting in group activities in the ALC environment than in the TC setting. ALC students reported a higher level of engagement and more room flexibility in regard to in-class activities and perceived a higher alignment between the room and the course itself than did their counterparts in the TC. Taken together, the results show that students in an ALC are able to outperform their peers in a TC, suggesting that ALC environments positively enhance student learning and are worth the investment. — MM

J. Coll. Sci. Teach. **42**, 82 (2013).

GEOLOGY

Megafloods from Tibet

In between the Tibetan plateau and the Himalaya runs the Yarlung-Tsangpo River. In general, the balance of tectonic uplift and erosion—usually caused by rivers that carry abraded bedrock downstream—controls the elevation of such mountainous regions. Lang *et al.* used U-Pb dating to record the source of zircon grains in sediments deposited downstream of the Tsangpo Gorge, a steep, narrow canyon cut by the Yarlung-Tsangpo River as it enters the Eastern Himalaya. The ages and composition of these grains suggest they were deposited by large flood events from rapid drainage of glacial lakes in Tibet in the past few million years. Although these historical events may be infrequent, they probably contribute substantially to the overall evolution of the landscape. One megaflood alone could erode more material than the baseline erosion rate typically removes in 1000 to 4000 years. — NW

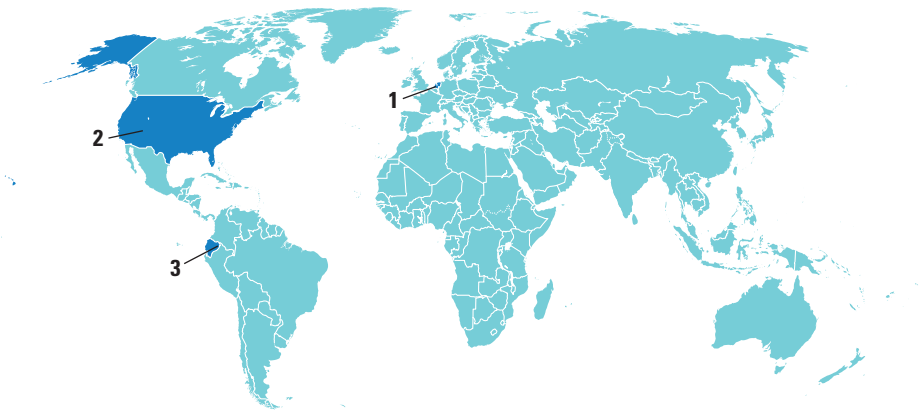


Geology **41**, 1003 (2013).

CREDIT: BGABEL AT WIKIVOYAGE SHARED/WIKIMEDIA COMMONS

Published by AAAS

AROUND THE WORLD



Emmeloord, the Netherlands **1**

Tiger Mosquito Moves North in Europe



A series of outbreaks in the Netherlands of the Asian tiger mosquito (*Aedes albopictus*), which can transmit viral diseases such as dengue and chikungunya, has raised the possibility that the mosquito could be establishing its northernmost beachhead in Europe.

The mosquito often hitches a ride in secondhand tires (*Science*, 16 May 2008, p. 864), and this summer it has turned up near seven tire-importing companies in the Netherlands. In each case, the Food and Consumer Product Safety Authority has moved in quickly with insecticides. Tire companies have also agreed to store tires from tropical countries in dry places, depriving mosquito eggs of the water they need to hatch. Yet without more aggressive measures, the tropical insect will soon become a fixture in the Netherlands, predicts Bart Knols of In2Care, a company focusing on mosquito control. One study by the European Centre for Disease Prevention and Control has suggested that the mosquito could survive as far north as Scandinavia.

Page, Arizona **2**

Drought Forces Cutbacks On the Colorado River

In an ominous precedent, operators of the Glen Canyon Dam on the Colorado River will reduce the water released over next year from the Lake Powell reservoir by 9%, the U.S. Bureau of Reclamation announced last week. Millions of farms and homes depend on the river for their water supply. "I view this as another serious warning to users of the Colorado River that we're headed for big trouble," says Peter Gleick of the Pacific Institute in Oakland, California.

Thanks to a 14-year drought, less water has been flowing into the upper Colorado River. Flows in July were just 13% of normal. According to a 2007 agreement between seven Western states, the bureau must keep a certain amount of water in the reservoirs. For now, a gigantic downstream reservoir, Lake Mead, will remain full enough for the same amount of water to be released from the Hoover Dam as this year. So the supply to homeowners and farmers will not be reduced, but the decision highlights the likelihood of future shortages as early as 2015. **http://scim.ag/Colowater**



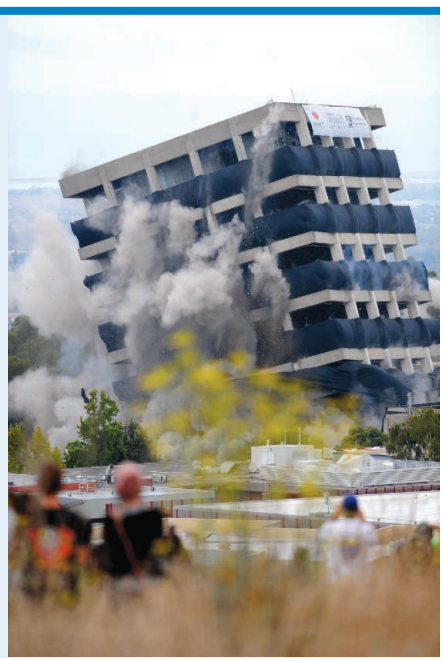
Low water. Lake Powell at the Glen Canyon Dam.

The Science of a Falling Building

What do an imploding tower and an earthquake have in common? Seismic energy. Before Warren Hall, a 13-story building overlooking California's San Francisco Bay, toppled to the ground on 17 August, U.S. Geological Survey (USGS) scientists planted nearly 600 seismometers in a 2.5-kilometer-radius ring around the building to record the resulting seismic signals. By studying these signals, the scientists hope to better map the complicated fault lines of the Hayward fault zone, which runs east of the bay, through Oakland, San Jose, and Berkeley.

The last major earthquake (magnitude 6.8) on the Hayward fault was in 1868. But in 2009, USGS declared that a major earthquake on the fault is "increasingly likely"—and that there's a 27% chance that the Hayward fault will rupture before 2032. Such a temblor could devastate the Bay Area, but forewarned is forearmed: By mapping out the fault zone's traces and the ground's response to shaking, scientists hope to better understand the potential hazard.





CREDITS: (TOP LEFT TO RIGHT) JAMES GATHANY/CDC; T. ROSS REEVE; (BOTTOM LEFT TO RIGHT) JENNIFER WILLIAMS/FIRE HORSE LEO/WIKIMEDIA COMMONS; DAN HONDA/BAY AREA NEWS GROUP/AP PHOTO

Published by AAAS



Flash point. Cobalt-winged parakeets in Yasuni National Park, site of a controversial drilling plan.

Yasuni National Park, Ecuador **3**

Opponents Vow to Block Amazon Drilling

Ecuador will move ahead with controversial plans to drill for oil in a renowned Amazon park, President Rafael Correa announced on 15 August. But opponents are hoping to block the move in a national vote.

Yasuni National Park is a biological hot spot and home to the Waorani people, including two clans who live in voluntary isolation. The park also holds lots of oil. In 2010, Correa promised to forgo drilling if the international community donated $3.6 billion—one-half of the oil's value—to a special fund. But lackluster fundraising forced the government to act, Correa said. "The world has failed us."

Polls suggest that a majority of Ecuadorians oppose drilling, and opponents are pushing for a referendum. Meanwhile, they are encouraged by antidrilling demonstrations in Guayaquil, a bellwether city. "This is now not just about a handful of environmentalists," says Kevin Koenig of Amazon Watch in Quito. "It has become a point of pride." **http://scim.ag/Yasunidrill**

THEY SAID IT

"1996-2012. The world has become safer."

—A plaque at "Plutonium Mountain," a Soviet-era nuclear test site in eastern Kazakhstan, commemorating a secret 17-year collaboration between Russian and U.S. scientists to remove nuclear materials to keep them out of terrorist hands. The Harvard Kennedy School published a report on the collaboration on 15 August.

FINDINGS

A Blood Test for Suicide?

What if a psychiatrist could tell whether someone was about to commit suicide by sampling their blood? That's the potential promise of a study of blood samples from nine men with bipolar disorder, taken while they were reporting suicidal thoughts. After comparing these blood samples to others taken when the men did not report feeling suicidal, researchers identified five proteins that they say indicate higher risk of imminent suicide.

Previous studies showed several of those proteins in higher-than-normal amounts in the blood of people who died from suicide. When combined with psychological measures of anxiety and mood, the presence of these proteins was 80% predictive of future hospitalization for suicide in bipolar patients, the authors report this week in *Molecular Psychiatry*.

The small study needs to be replicated in larger and more diverse populations, and "it's unlikely these markers are specific" to the complex behavior of suicide, says lead author Alexander Niculescu III, a psychiatrist at the Indiana University School of Medicine in Indianapolis. Instead, they are likely to indicate contributing factors, such as abnormal cellular function and stress. **http://scim.ag/suicideblood**

Random Sample

Out of Oil? Just Add Fungi



The long-held view of the origin of shale oil—a buried leaf cooking for 70 million years under pressure from mud and sand—might leave out a vital component of the process: fungi. A new experiment suggests that endophytic fungi—fungi living symbiotically inside plants—can generate hydrocarbons as they eat away at their decaying hosts. Gary Strobel, a plant microbiologist at Montana State University in Bozeman, says that fungi could have speeded up oil production by tens of millions of years.

Strobel calls his experiment the Paleobiosphere (pictured), a kitchen-sink–sized contraption designed to simulate a Cretaceous-era rainforest floor. Strobel mixed leaves from maple, sycamore, and aspen trees with a fungus that grows inside semitropical Key lime trees, then sandwiched the concoction between two layers of bentonite shale and flooded the whole thing with water a few times. A mere 3 weeks later, the growing fungi had digested the leaf matter's sugars, starches, and cellulose, converting them into a variety of hydrocarbons that seeped into the shale layers—closely resembling the oil-rich Montana shale around Strobel's lab. "Not all of the hundreds of compounds found in diesel are present in this simple experiment, but representative molecules in each of the major classes of hydrocarbons are there," he explains.

Entrepreneur Bryan Blatt hopes to use Strobel's hydrocarbon-producing fungi to churn out new biofuels. His company, Endophytics LLC, will announce its first patent on a promising organism this month. "We just don't have to sit here and assume that at some point there's an end to the oil," he says.

CREDITS (TOP TO BOTTOM): PRISMA BILDAGENTUR AG/ALAMY; GARY STROBEL

Published by AAAS



Sea change? Research at the West Bank lab of AHAVA Dead Sea Laboratories would no longer be funded under Horizon 2020.

RESEARCH FUNDING

Diplomatic Flap Threatens E.U.-Israeli Research Ties

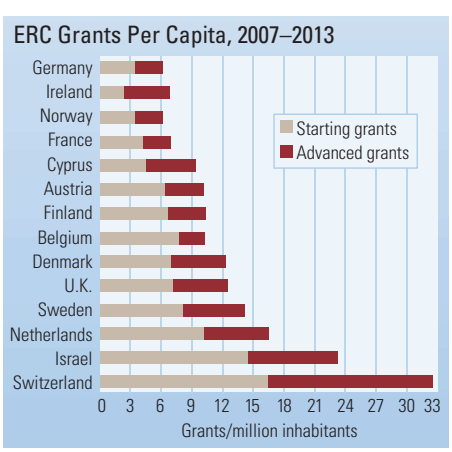
A diplomatic row between the European Union and the Israeli government could spell a sharp loss in funding for Israeli science as well as the end for countless collaborations with European scientists. At issue are 3 pages of guidelines issued by the European Commission on 19 July, which stipulate that starting in 2014, E.U. grants, prizes, and financial instruments may not support organizations or activities in areas not under Israel's control before 1967—which include the occupied West Bank, East Jerusalem, the Gaza strip, and the Golan Heights.

In an angry response, the Israeli government said last week that it may forgo participation in Horizon 2020, the European Union's new €70 billion, 7-year research program. The two sides had a first round of talks about Horizon 2020 at the E.U. Delegation's Tel Aviv office on 14 August and will continue discussions in Brussels in September. An Israeli withdrawal would put an end to 17 years of successful participation in E.U. science funding schemes.

The European Union stresses that the new document is a clarification of existing policies whose effects will be minimal, as little research is going on in the territories. But to the Israeli government, the issue is bigger than that. "We will not accept any outside diktat about our borders," Prime Minister Benjamin Netanyahu said last month.

At stake isn't just grant money, but also "the contacts, the networks, the recognition," says Nobel laureate Ada Yonath, a crystallographer at the Weizmann Institute of Science in Rehovot who last year bagged a €2.5 million grant from the European Research Council (ERC), funded by Horizon 2020's predecessor, Framework Programme 7 (FP7). "Israel will be in a ghetto," she says. Israel's withdrawal would be "catastrophic for Israeli scientists and a big loss for Europe," adds ERC President Helga Nowotny.

Since 1996, Israel has taken part in E.U. research programs as an "associated country"—a status that allows a non-E.U. country to benefit from the European Union's funding bonanzas in return for a fixed contribution based on gross domestic product. Israel paid €534 million into FP7, which spanned 2007 to 2013; in return, almost 1600 Israeli scientists will have received a total of €634 million in funding. They fared particularly well in the battle for ERC grants (see graphic); on a per capita basis, Israel was bested only by Switzerland, also an associated country.



European Commission spokesperson Michael Jennings says that the European Union banned funding for organizations established in the occupied territories all along, although it did not explicitly rule out supporting any research there. The only currently funded research that would no longer be eligible for E.U. grants is being done by a company called AHAVA Dead Sea Laboratories, which produces skin care products from Dead Sea mud and salt at a West Bank facility.

Still, at the Tel Aviv meeting last week, Israeli representatives told a delegation from the European Commission that without "positive understandings on the guidelines' implementation … Israel will be unable to join the European R&D program," according to an Israeli government statement. "If Israel is going to lose a few dollars, or euros, rather than accepting [the European Union] damaging national security interests, then we don't have a choice," says Paul Hirschson, a spokesperson for the Israeli Ministry of Foreign Affairs.

Other international funding schemes also exclude projects in the occupied territories, including the United States-Israel Binational Science Foundation, which has funded dozens of Nobel laureates, and a similar foundation aimed at fostering scientific friendships between Israel and Germany. Hirschson could not say whether those foundations are problematic as well. He says Israel also takes issue with the timing of the E.U. guidelines, just as U.S. Secretary of State John Kerry had launched a new round of peace talks between Israel and Palestine. "They give the Palestinians the false sense that they can achieve anything without making any compromises," he says.

Not everyone is so gloomy about the damage a withdrawal from Horizon 2020 would cause. If Israel invests its contribution

CREDITS (TOP TO BOTTOM): CODEPINK WOMEN FOR PEACE; (SOURCE) ERC

Published by AAAS

in domestic research instead, "it doesn't have to be such a tragedy," says Alex Lubotzky, a mathematician at Hebrew University of Jerusalem who co-founded a West Bank settlement called Efrat. Lubotzky, himself an ERC grant winner, adds that the European Union has every right to determine what is done with its money.

It's hard to predict whether either side will budge, says Jonathan Rosenhead, a professor emeritus at the London School of Economics and Political Science. He urges the European Commission to stick to its position. "They have drawn a line in the sand. They would look stupid if they back down now," says Rosenhead, who chairs the British Committee for the Universities of Palestine, an academic group that opposes the Israeli occupation of Palestinian lands.

Israel, too, is likely to take a hard line, says Oded Beja, an environmental genomicist at the Technion-Israel Institute of Technology in Haifa who says that his €2 million ERC grant helped him "enter the big league" of his field. "It's not that they want to move E.U. money into the occupied territories," Beja says. "But by agreeing, they admit that something is wrong with the territories."

–MARTIN ENSERINK

NEWSMAKER INTERVIEW: CHARLES SOBECK

How NASA Tried to Save Its Prime Planet-Spotter

Since its launch in 2009, NASA's Kepler spacecraft has discovered 130 new extrasolar planets and identified hundreds of candidates. On 15 August, however, NASA announced that the hardworking planet-hunter could no longer continue doing science as before. Two of the four reaction wheels that keep the craft precisely pointed at target stars had seized up



and could not be revived. Charles Sobeck, deputy project manager for Kepler at NASA's Ames Research Center in Moffett Field, California, describes what happened and what lies in store for the probe. The interview has been edited for clarity and brevity.

–YUDHIJIT BHATTACHARJEE

Q: When did you first realize there was a problem?

C.S.: The first time was a year ago when wheel 2 failed. The spacecraft wasn't holding fine point on its science target [staying precisely pointed] because that wheel had stopped spinning.

Q: What was the status of Kepler after wheel 2 broke?

C.S.: It was still pointing well, but not precisely. Within a few days, we were able to take the failed wheel offline, reset some parameters that essentially told the spacecraft that you only have three wheels; use those wheels. It snapped right back into fine point, but now our concern was, we couldn't afford to lose another one.

We went back and looked at all our data and were able to find advance indications that a wheel is having problems. And indeed, what we found is that wheel 4 was showing intermittent signs of stress.

In early January, we saw the wheel exhibit some elevated friction that didn't come down. We knew we only had a few months left, so we began quickly developing a thruster control mode so that we could use the thrusters on the spacecraft to stabilize it and point it. In May, wheel 4 seized up and stopped turning.

Online
sciencemag.org
Longer version of interview (http://scim.ag/PlanetSpot).

Q: Was there anything left to do?

C.S.: Functionally, the wheels were still working, and we wanted to find out how well they could point the spacecraft. We did that test last week [beginning Thursday, 8 August].

Normally, we would like to see the wheels hold the spacecraft to within 1 or 2 arcseconds of the target; it was holding at within 10 arcseconds.

Q: Did that allow you to do something useful?

C.S.: We pointed Kepler's high-gain antennae at Earth and downlinked the data that has been on its solid state recorder for the past 3 months.

As we were pointing the antennae, wheel number 2 started experiencing very high friction. A good wheel should have something like 2 or 3 millinewton-meters. Now, the friction jumped up to over 100. During the 4 hours, we saw the friction stay in that very high regime, it was getting closer and closer to the 200 millinewton-meter limit that our motors have on them.

Q: That's like watching an emergency room patient's pulse rate going up.

C.S.: Yes, and there's nothing you can do about it, other than hoping that it comes to some sort of stable state. We had several of us in one office at Ames looking at the data in real time. At first, we thought, it's going to die almost immediately. But then it didn't. It started to rise slowly. We thought, well, it's going to die in an hour or two. Then it peaked out and started coming down again, and it just sort of teased us. Then the friction exceeded the limit, we could no longer spin the wheels with our motor, and the spacecraft autonomously put itself in safe mode.

Q: Are you still hoping that the Kepler spacecraft will be able to do some science?

C.S.: We will now try to define what kind of pointing can we get with two good wheels and thrusters. And we're going to see what kind of science can we do with it. We've issued a call for white papers inviting the scientific community to submit ideas. We're not limiting it to extrasolar planets. Some ideas would be to do microlensing [studying images magnified by the gravity of matter in space] and to look for near-Earth asteroids. We're not throwing in the towel.

CREDIT: NASA

Published by AAAS

SCIENTIFIC PUBLISHING

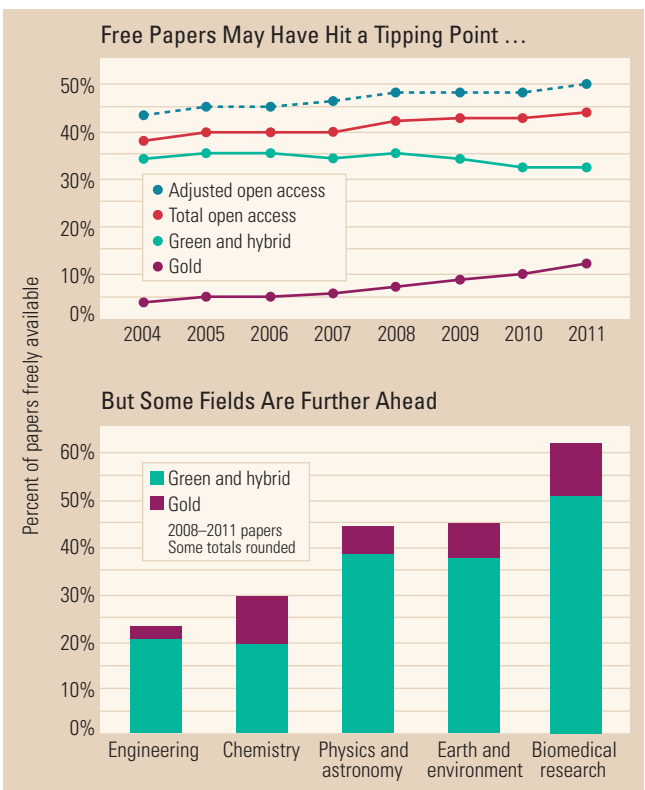
Half of All Papers Now Free in Some Form, Study Claims

Efforts to give the public free access to peer-reviewed papers have reached a milestone: One-half of all papers are now freely available within a year or two of publication, concludes a new study sponsored by the European Commission. That means so-called open-access publishing has reached a "tipping point" and will now accelerate, suggests Éric Archambault, the lead author of the study and president of Science-Metrix Inc. in Montreal, Canada. "Things are likely to move much faster now." But some open-access observers have been quick to criticize the study, which yielded a number twice as high as other analyses.

The findings come as open access is set to expand: This week, U.S. science agencies were due to send the White House draft plans describing how they will make government-funded research papers freely available, generally within 12 months of publication. And the European Commission will soon require that most articles it funds be free within 6 months. The new "findings underline that open access is here to stay," said Máire Geoghegan-Quinn, European commissioner for research, innovation, and science, in a statement.

The open-access movement took off more than a decade ago when some scientists began pushing to make full-text papers free. Today, some papers are published in journals that make papers immediately free upon publication and cover costs by charging authors a fee. Some other papers, published in traditional subscription-based journals, are made freely available on an author's website or through an institutional or government archive, often after a 6- or 12-month "embargo" imposed by the publisher to protect subscription revenue. (Papers in *Science* are free with registration after 12 months, and authors can post copies sooner.) Like other analysts, Archambault defines papers published in immediately free journals as the "gold" version of open access, and those posted in archives, sometimes after a delay, as "green"; other forms his team dubbed "hybrid."

To find out how many gold, green, and hybrid papers are now available, Archambault and his colleagues randomly sampled 320,000 papers published between 2004 and 2011 drawn from Scopus, a database. They then built a software robot that scoured the Internet and online archives in April 2013 for the full text. Unlike some other analysts, they included papers that are only temporarily free (such as a journal's sample issue). As a check, they also manually searched for 500 papers, revealing that the robot had missed a few. After correcting for this error, the Science-Metrix group concluded that open access reached a 50% "tipping point" in 2011, meaning that one-half of the papers published that year are now freely available.



Gaining ground. More papers are available in free-to-read journals (gold open access) or in "green" online archives and "hybrid" journals.

The team also found that the proportion of gold papers grew from about 4% of all papers in 2004 to 12% in 2011 (see graph). Over the same period, the share of green and hybrid papers hovered around 34% then fell to about 32%. That decline probably reflects the fact that more recently published papers hadn't yet come out from under embargo, Archambault says. Overall, he notes, the number of open-access papers has been growing by about 2% a year, and the absolute total jumps each year as journals and authors make batches of old papers free.

Archambault's group also broke the results down by field and country. Biomedical research leads with 61% of papers freely available. Open access is well over 50% in a few countries (defined by author's country), including Macedonia (67%), the Netherlands (58%), and the United States (56%).

Such numbers haven't persuaded other analysts that open access is making a historic transition. "Eric has given us good news about access, not open access," says Stevan Harnad of the University of Quebec in Montreal, who thinks that delayed access shouldn't count. Bo-Christer Björk of the Hanken School of Economics in Helsinki, who's calculated a smaller number, says that for methodological reasons he's "not fully convinced" that the 50% figure is valid. However, he says the study is "important" and will be influential—but not necessarily in the way the authors hope: It may prompt subscription publishers to lengthen embargoes and tighten enforcement.

One publisher says that even if the 50% number is real, publishing hasn't necessarily reached a tipping point. Fred Dylla, executive director of the American Institute of Physics in College Park, Maryland, argues that open access is expanding because it's being driven by public policy mandates, not favorable economics. For that reason, "I don't see us reaching the top of a hill and now rushing to the bottom. It's more like the slope is getting smaller," he says.

However imperfect, the Archambault analysis is welcome, says open-access advocate Peter Suber, director of Harvard University's Office for Scholarly Communication. It shows that open access "has entered the mainstream," he says. "When we're on a long journey, we have a right to celebrate when the odometer rolls over at some round number of miles, even if we're perfectly aware that the round number is somewhat arbitrary."

–JOCELYN KAISER

CREDIT: (SOURCE) E. ARCHAMBAULT *ET AL.*, PROPORTION OF OPEN ACCESS PEER-REVIEWED PAPERS AT THE EUROPEAN AND WORLD LEVELS—2004-2011 (JUNE 2013), SCIENCE-METRIX, PRODUCED FOR THE EUROPEAN COMMISSION

Published by AAAS



CREDIT: TPG/GETTY IMAGES

Graying nation. Nearly a quarter of China's elderly live in poverty.

DEMOGRAPHY

Can China Age Gracefully? A Massive Survey Aims to Find Out

SHANGHAI, CHINA—When Nie Huasheng and Yin Yifei show up for their appointment at the convenience store on a hot summer afternoon, its owner is sleeping in the back room. That's the first clue that interviewing the 50-year-old woman is not going to be easy. As Yin pulls out a laptop and starts asking survey questions, their travails continue: When Yin asks the woman's age, she says "teenager." Customers wander in to buy cigarettes and groceries. She evades questions about finances. "Sometimes people lie to us," Nie says later. "It's very difficult."

Nie and Yin, college students at Peking University, are interviewers for the China Health and Retirement Longitudinal Study (CHARLS), a mammoth effort to understand one of the world's most momentous demographic shifts: China's ongoing transition from a nation of young workers to one of elderly pensioners. Designed by Chinese and American researchers, the survey is monitoring more than 10,000 households and nearly 18,000 individuals—a representative sample of all Chinese over 45.

China is getting old before it gets rich—a massive shift that could strain the economy, health care system, and labor market. The introduction of the one-child policy in 1980 coincided with rapid economic development that extended lifespans, creating a generation of only children who are burdened with caring for their aging parents. The number of people aged 60 and over is on course to increase from 12% of China's population in 2010 to 34% in 2050, according to U.N. Population Division projections. "What took 80 years in Europe is taking 20 to 30 years in China," says James P. Smith, director of the Center for Chinese Aging Studies at the RAND Corporation in Santa Monica, California, and a member of the survey's advisory board.

Overseen by Peking University's China Center for Economic Research (CCER), with $5.25 million in funding from the U.S. National Institute on Aging (NIA) and additional support from sources including the Natural Science Foundation of China, CHARLS is designed to gauge the health, wealth, and emotional well-being of older Chinese as they transition into retirement. The survey, which launched nationally in 2011, "will be the definitive source of information about the aging population of China for many years to come," says Donald Treiman, a sociologist at the University of California, Los Angeles, who is not affiliated with the undertaking.

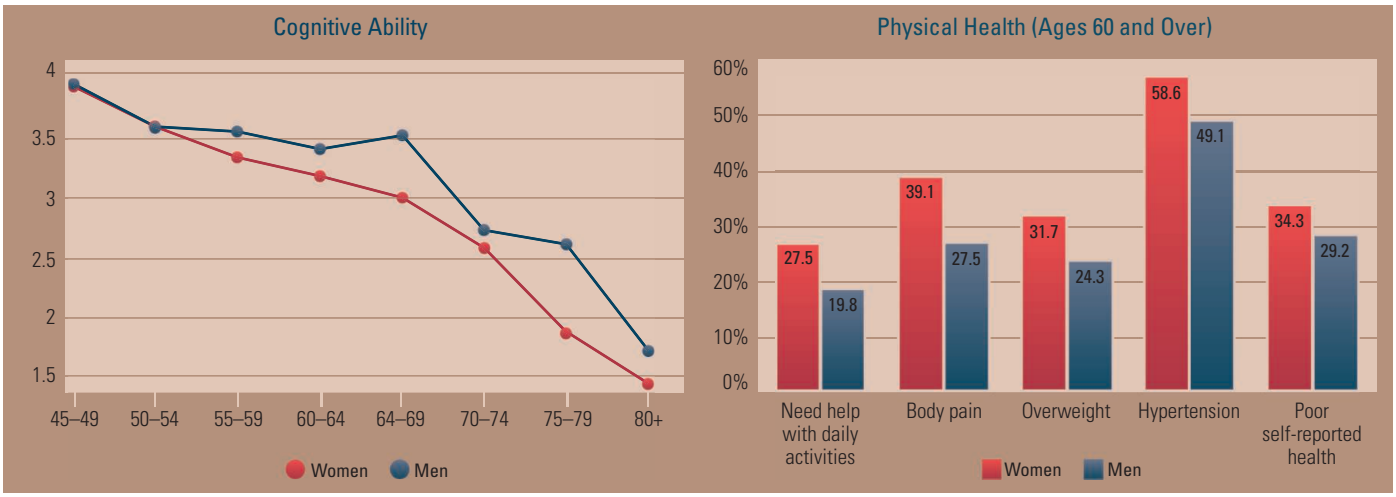
With results made available online within a year of the completion of a survey round, the study will also be a boon to social science research in a country where both the government and researchers closely guard data (*Science*, 31 May, p. 1037), says Zhao Yaohui, an economist at CCER and a co–principal investigator on the survey. That openness "sets an example for other studies in China," says Yu Xie, a demographer at the University of Michigan, Ann Arbor, and the chair of the academic committee that oversees surveys at Peking University.

Data from a pilot survey in two provinces were released in 2009, and results from the study's national baseline, which concluded in 2012, were released in February. Now, a 500-strong team of interviewers is in the field again, canvassing a sample that includes urban sophisticates, Tibetan herders, and Mongolian nomads. In the first round, besides asking about finances and life satisfaction, interviewers measured blood pressure, height, weight, waistlines, lung function, and frailty, among other biomarkers. The team also collected blood samples that were used to screen for anemia, diabetes, and risk factors for cardiovascular disease.

So far, CHARLS has painted a largely bleak picture for China's 185 million residents ages 60 and over, nearly a quarter of them living in poverty. Fully 40% show obvious symptoms of depression, and more than half have hypertension, a worrisome finding for China as it vastly expands its health care coverage (*Science*, 1 February, p. 505).

On many health measures, from body pain to depression, women fare worse than men. The convenience store owner is typical: When Yin asks the woman whether she felt unhappy at some point the day before, she responds, "I feel that way every day."

Published by AAAS



Gender gap. Elderly Chinese women scored worse in both cognition and physical health.

The women surveyed so far also do worse on tests of cognitive skills and memory. The cognitive gap is more pronounced in older age groups, where women typically received less education than men. But nutritional and other factors may play a role as well, Smith notes: For older generations, discrimination "permeates the entire society."

The survey has a U.S. model: the Health and Retirement Study (HRS), an NIA-funded survey of 22,000 Americans over 50 that addresses health, social issues, and finances. Richard Suzman, a demographer who oversaw the launch of the HRS in 1992 and now directs NIA's Division of Behavioral and Social Research, has helped develop similar studies of aging in more than 30 other countries—including South Korea, Japan, and India—and encouraged the development of an international network to ensure that countries measure and share data in common formats. Expanding to China was a no-brainer to Suzman: Among other reasons, he says, "how China handles the challenge of aging will indirectly affect trade and relations with the United States."

> *"What took 80 years in Europe is taking 20 to 30 years in China."*
>
> —JAMES P. SMITH, CENTER FOR CHINESE AGING STUDIES, RAND CORPORATION

In 2006, Suzman approached CCER about overseeing a Chinese survey. The requirement that surveys in the network make data available struck a chord with Zhao, who remembers returning to China while a student at the University of Chicago and vainly trying to obtain data—any data—for her dissertation research. "I knew how scarce data was, and I was a little tired of having to beg for it."

Executing such a survey in China is challenging. The problems began with crafting a sample. Many areas of China do not keep lists of mailing addresses, and widespread rural-to-urban migration renders listings maintained by the government inadequate. So the survey relied on a geographic information system. The researchers marked out every building on Google Earth images, listed every dwelling within each building, and then selected a random sample of homes.

Culture introduces other challenges. When asking about age and dates, interviewers need to check whether a response is based on the lunar or solar calendar; many Chinese elderly remember birthdates and other milestones as lunar calendar events. Similarly, questions about health must account for both the use of Chinese medicine and the fact that many elderly Chinese have pieced together information on their health from a mishmash of sources. "A lot of people have never seen a doctor in their life," Zhao says.

The survey also has to contend with China's diversity of languages and dialects, says Kong Tao, an economist at Peking University and the survey's manager. Organizers assigned student interviewers to regions based on the dialects they speak, but in some areas the project has had to use translators. "That can introduce error," Kong notes. Another issue is an increasingly wary urban population, Kong adds: "The social trust has eroded to such an extent to the point that people are very suspicious" of strangers knocking on doors. Still, the response rate for the first survey round was 81%, which outside observers say is very high.

With follow-up rounds every 2 years, the most critical research findings are yet to come. Longitudinal data will offer "the real payoff" for researchers, Treiman says, and it could help flesh out some of the early findings. The gender difference in cognition, for example, could be exaggerated by the fact that women live longer than men. CHARLS's investigators also hope to analyze subjects' DNA, using blood samples collected in the baseline survey. By pooling that data with results from other aging surveys, researchers can search for genetic markers linked to cognition, personality, and behavior.

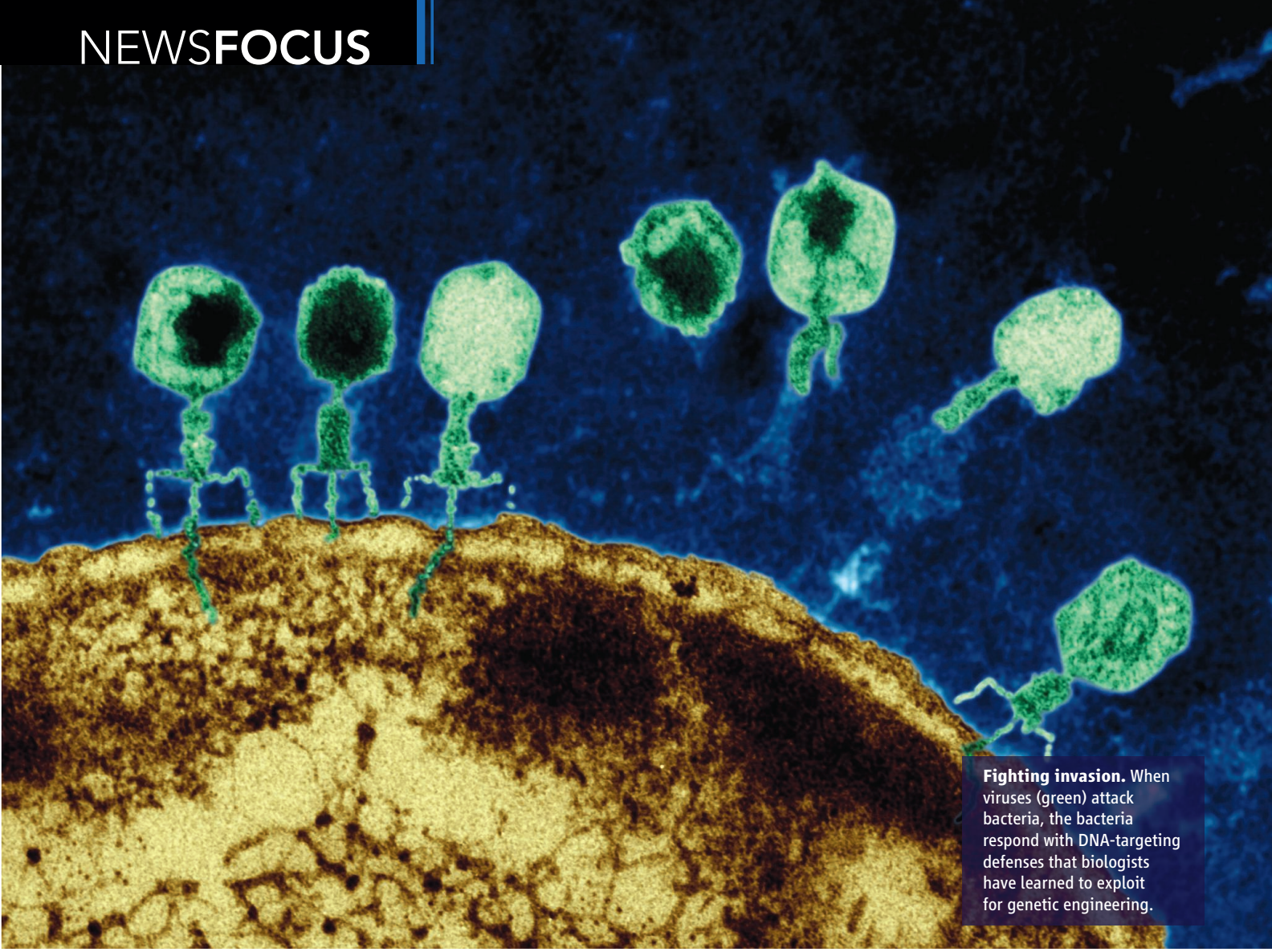
In the meantime, the survey could help inform policy discussions. Proposals for raising the retirement age—the age for collecting pensions ranges from 50 for low-level women workers to 60 for men—have so far proven unpopular in China, with upcoming retirees alleging that they're being treated unfairly. CHARLS showed that urban Chinese retire early, supported in part by millions of rural migrants, while "in the countryside they work until they drop," Zhao says. Postponing retirement would reduce inequity, not create it, she says. And knowing underdiagnosis rates for diseases such as hypertension, Smith says, could help the government plan for health care spending, an urgent task. "China cannot be spending the kind of money that they are in the United States," he says.

As China grapples with its demographic shift, the survey should give researchers a chance to watch policy changes and their effects in real time, Smith notes. "This next 20 years is going to be monitored."

–MARA HVISTENDAHL

CREDIT: (SOURCE) CHARLS

Published by AAAS



Fighting invasion. When viruses (green) attack bacteria, the bacteria respond with DNA-targeting defenses that biologists have learned to exploit for genetic engineering.

CREDIT: EYE OF SCIENCE/SCIENCE SOURCE

The CRISPR Craze

A bacterial immune system yields a potentially revolutionary genome-editing technique

BACTERIA MAY NOT ELICIT MUCH SYMPAthy from us eukaryotes, but they, too, can get sick. That's potentially a big problem for the dairy industry, which often depends on bacteria such as *Streptococcus thermophilus* to make yogurts and cheeses. *S. thermophilus* breaks down the milk sugar lactose into tangy lactic acid. But certain viruses—bacteriophages, or simply phages—can debilitate the bacterium, wreaking havoc on the quality or quantity of the food it helps produce.

In 2007, scientists from Danisco, a Copenhagen-based food ingredient company now owned by DuPont, found a way to boost the phage defenses of this workhouse microbe. They exposed the bacterium to a phage and showed that this essentially vaccinated it against that virus (*Science*, 23 March 2007, p. 1650). The trick has enabled DuPont to create heartier bacterial strains for food production. It also revealed something fundamental: Bacteria have a kind of adaptive immune system, which enables them to fight off repeated attacks by specific phages.

That immune system has suddenly become important for more than food scientists and microbiologists, because of a valuable feature: It takes aim at specific DNA sequences. In January, four research teams reported harnessing the system, called CRISPR for peculiar features in the DNA of bacteria that deploy it, to target the destruction of specific genes in human cells. And in the following 8 months, various groups have used it to delete, add, activate, or suppress targeted genes in human cells, mice, rats, zebrafish, bacteria, fruit flies, yeast, nematodes, and crops, demonstrating broad utility for the

Published by AAAS

technique. Biologists had recently developed several new ways to precisely manipulate genes, but CRISPR's "efficiency and ease of use trumps just about anything," says George Church of Harvard University, whose lab was among the first to show that the technique worked in human cells.

With CRISPR, scientists can create mouse models of human diseases much more quickly than before, study individual genes much faster, and easily change multiple genes in cells at once to study their interactions. This year's CRISPR craze may yet slow down as limitations of the method emerge, but Church and other CRISPR pioneers are already forming companies to harness the technology for treating genetic diseases. "I don't think there's any example of any field moving this fast," says Blake Wiedenheft, a biochemist at Montana State University in Bozeman.

Humble beginnings

The first inkling of this hot new genetic engineering tool came in 1987, when a research team observed an oddly repetitive sequence at one end of a bacterial gene. Few others took much notice. A decade later, though, biologists deciphering microbial genomes often found similar puzzling patterns, in which a sequence of DNA would be followed by nearly the same sequence in reverse, then 30 or so seemingly random bases of "spacer DNA," and then a repeat of the same palindromic sequence, followed by a different spacer DNA. A single microbe could have several such stretches, each with different repeat and intervening sequences. This pattern appears in more than 40% of bacteria and fully 90% of microbes in a different domain, the archaea, and gives CRISPR its name. (It stands for clustered regularly interspaced short palindromic repeats.)

Many researchers assumed that these odd sequences were junk, but in 2005, three bioinformatics groups reported that spacer DNA often matched the sequences of phages, indicating a possible role for CRISPR in microbial immunity. "That was a very key clue," says biochemist Jennifer Doudna of the University of California (UC), Berkeley. It led Eugene Koonin from the National Center for Biotechnology Information in Bethesda, Maryland, and his colleagues to propose that bacteria and archaea take up phage DNA, then preserve it as a template for molecules of RNA that can stop matching foreign DNA in its tracks, much the way eukaryotic cells use a system called RNA interference (RNAi) to destroy RNA.

Enter the Danisco team. In 2007, Rodolphe Barrangou, Philippe Horvath, and others with the company showed that they could alter the resistance of *S. thermophilus* to phage attack by adding or deleting spacer DNA that matched the phage's. At the time, Barrangou, who is now at North Carolina State University in Raleigh, didn't see CRISPR's full potential. "We had no idea that those elements could be readily exploitable for something as attractive as genome editing," he says.



Precise cuts. In just 8 months, CRISPR modifications of DNA resulted in dumpier nematodes (*top*, bottom), zebrafish embryos with an excess of ventral tissue (*middle*, bottom), and fruit flies with dark eyes (*bottom*, right), demonstrating its broad utility for editing genes in animals.

Doudna and Emmanuelle Charpentier, currently of the Helmholtz Centre for Infection Research and Hannover Medical School in Germany, took the next step. They had independently been teasing out the roles of various CRISPR-associated proteins to learn how bacteria deploy the DNA spacers in their immune defenses. But the duo soon joined forces to focus on a CRISPR system that relies on a protein called Cas9, as it was simpler than other CRISPR systems.

When CRISPR goes into action in response to an invading phage, bacteria transcribe the spacers and the palindromic DNA into a long RNA molecule that the cell then cuts into short spacer-derived RNAs called crRNAs. An additional stretch of RNA, called tracrRNA, works with Cas9 to produce the crRNA, Charpentier's group reported in *Nature* in 2011. The group proposed that together, Cas9, tracrRNA, and crRNA somehow attack foreign DNA that matches the crRNA.

The two teams found that the Cas9 protein is a nuclease, an enzyme specialized for cutting DNA, with two active cutting sites, one site for each strand of the DNA's double helix. And in a discovery that foreshadowed CRISPR's broad potential for genome engineering, the team demonstrated that they could disable one or both cutting sites without interfering with the ability of the complex to home in on its target DNA. "The possibility of using a single enzyme by just changing the RNA seemed very simple," Doudna recalls.

Before CRISPR could be put to use, however, Doudna's and Charpentier's teams had to show that they could control where Cas9 went to do its cutting. First, Doudna's postdoc, Martin Jinek, figured out how to combine tracrRNA and spacer RNA into a "single-guide RNA" molecule; then, as a proof of principle, the team last year made several guide RNAs, mixed them with Cas9, and showed in a test tube that the synthetic complexes could find and cut their DNA targets (*Science,* 17 August 2012, p. 816). "That was a milestone paper," Barrangou says.

This precision targeting drives the growing interest in CRISPR. Genetic engineers have long been able to add and delete genes in a number of organisms. But they couldn't dictate where those genes would insert into the genome or control where gene deletions occurred. Then, a decade ago, researchers developed zinc finger nucleases, synthetic proteins that have DNA-binding domains that enable them to home in and break DNA at specific spots. A welcome addition to the genetic engineering toolbox, zinc fingers even spawned a company that is testing a zinc finger to treat people infected with HIV (*Science,* 23 December 2005,

CREDITS (TOP TO BOTTOM): FRIEDLAND *ET AL.*, *NATURE METHODS* **10** (JUNE 2013); ANDREW GONZALES/JOANNA YEH; SCOTT GRATZ/UNIVERSITY OF WISCONSIN, MADISON

Published by AAAS

p. 1894). More recently, synthetic nucleases called TALENs have proved an easier way to target specific DNA and were predicted to surpass zinc fingers (*Science,* 14 December 2012, p. 1408).

Now, CRISPR systems have stormed onto the scene, promising to even outcompete TALENs. Unlike the CRISPR system, which uses RNA as its DNA-homing mechanism, zinc finger and TALEN technologies both depend on custom-making new proteins for each DNA target. The CRISPR system's "guide RNAs" are much easier to make than proteins, Barrangou says. "Within a couple weeks you can generate very tangible results that using alternative methods would take months."

Harnessing CRISPR

Speed is not its only advantage. Church's group had been pushing the use of TALENs in human cells, but when he learned of Doudna and Charpentier's results, he and his colleagues made guide RNA against genes they had already targeted with TALENs. In three human cell types, the CRISPR system was more efficient than TALENs at cutting the DNA target, and it worked on more genes than TALENs did (*Science,* 15 February, p. 823). To demonstrate the ease of the CRISPR system, Church's team synthesized a library of tens of thousands of guide RNA sequences, capable of targeting 90% of human genes. "You can pepper the genome with every imaginable CRISPR," he says.

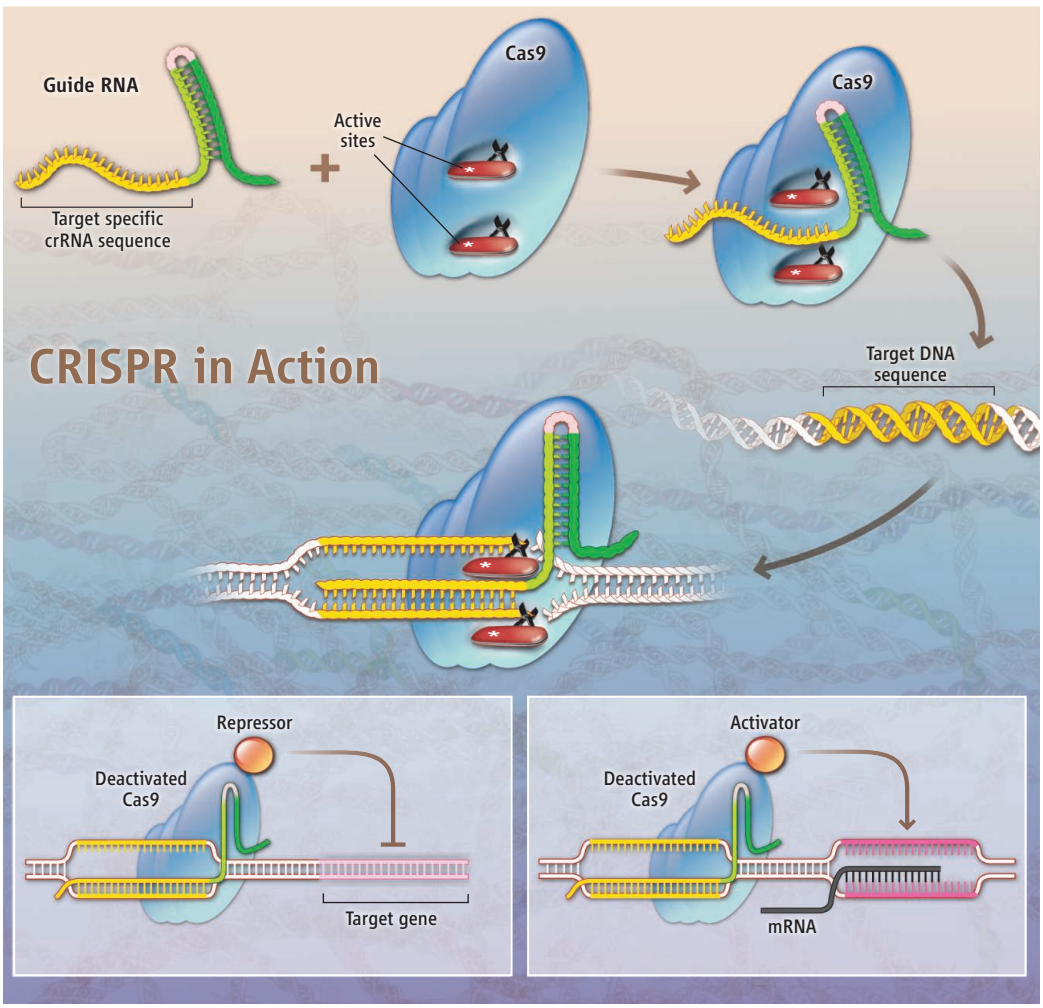
That makes it possible to alter virtually any gene with Cas9, exploiting its DNA-cutting ability to either disable the gene or cut it apart, allowing substitute DNA to be inserted. In an independent paper that appeared at the same time as Church's, Feng Zhang, a synthetic biologist at the Broad Institute in Cambridge, Massachusetts, and his colleagues showed that CRISPR can target and cut two genes at once in human cells (*Science,* 15 February, p. 819). And working with developmental biologist Rudolf Jaenisch at the Whitehead Institute for Biomedical Research in Cambridge, Zhang has since disrupted five genes at once in mouse embryonic stem (ES) cells.

Such work lays the foundation for generating mutant mice, a key tool for biomedical research. One approach would be to add the altered mouse ES cells to a developing embryo and breed the resulting animals. But Zhang has demonstrated a faster option. His team found it could simply inject fertilized mouse eggs, or zygotes, with Cas9 messenger RNA and two guide RNAs and, with 80% efficiency, knock out two genes. They could also perform more delicate genomic surgery on the embryos by shackling Cas9, so that it nicks target DNA instead of cutting it. In this way, they could introduce a new part of a gene through a process called homology-directed repair, they reported in the 2 May issue of *Cell*.

Developing a new mouse model for a disease now entails careful breeding of multiple generations and can take a year; with Zhang's CRISPR technique, a new mouse model could be ready for testing in a matter of weeks. And Zhang thinks the approach is not limited to mice. "As long as you can manipulate the embryo and then reimplant it, then you will be able to do it" in larger animals, perhaps even primates.

Doudna's group and a Korean team reported using CRISPR to cut DNA in human cells 3 weeks after Zhang's and Church's papers went online, and, at the same time, another group revealed they had used CRISPR to make mutant zebrafish. This cascade of papers has had a synergistic effect, commanding the attention of a broad swath of the biology community. "If a single paper comes out, it gets some attention, but when six papers come out all together, that's when people say, 'I have to do this,' " says Charles Gersbach, a biomedical engineer at Duke University in Durham, North Carolina.

Once she saw Doudna and Charpentier's paper a year ago, Gao Caixia became one of the early converts. Her group at the Chinese

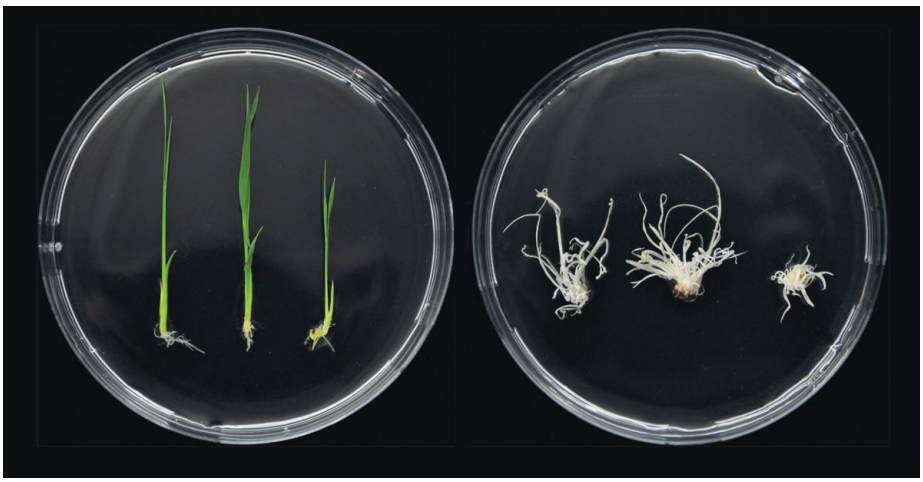


DNA surgeon. With just a guide RNA and a protein called Cas9, researchers first showed that the CRISPR system can home in on and cut specific DNA, knocking out a gene or enabling part of it to be replaced by substitute DNA. More recently, Cas9 modifications have made possible the repression (*lower left*) or activation (*lower right*) of specific genes.

CREDIT: K. SUTLIFF/*SCIENCE*

Published by AAAS

Academy of Sciences' Institute of Genetics and Developmental Biology in Beijing had been using zinc finger and TALENs technology on rice and wheat. Using CRISPR, they have now disabled four rice genes, suggesting that the technique could be used to engineer this crucial food crop. In wheat, they knocked out a gene that, when disabled, may lead to plants resistant to powdery mildew. In a measure of the excitement that CRISPR has generated, the team's report in the August issue of *Nature Biotechnology* was accompanied by four other papers describing CRISPR successes in plants and in rats.



CRISPRed rice. Earlier this month, researchers showed CRISPR works in plants, such as rice, where the knocked-out gene resulted in dwarf albino individuals (*right*).

The cost of admission is low: Free software exists to design guide RNA to target any desired gene, and a repository called Addgene, based in Cambridge, offers academics the DNA to make their own CRISPR system for $65. Since the beginning of the year, Addgene—to which 11 teams have contributed CRISPR-enabling DNA sequences—has distributed 5000 CRISPR constructs, and in a single July week the repository received 100 orders for a new construct. "They are kind of crazy hot," says Joanne Kamens, Addgene's executive director.

Fine-tuning gene activity

The initial CRISPR genome-editing papers all relied on DNA cutting, but other applications quickly appeared. Working with Doudna, Lei S. Qi from UC San Francisco and his colleagues introduced "CRISPRi," which, like RNAi, turns off genes in a reversible fashion and should be useful for studies of gene function. They modified Cas9 so it and the associated guide RNA would still home in on a target but would not cut DNA once there. In bacteria, the presence of Cas9 alone is enough to block transcription, but for mammalian applications, Qi and colleagues add to it a section of protein that represses gene activity. Its guide RNA is designed to home in on regulatory DNA, called promoters, which immediately precede the gene target.

Last month, that team and three other groups used a Cas9 to ferry a synthetic transcription factor—a protein fragment that turns on genes—enabling them to activate specific human genes. Just using one CRISPR construct had a weak effect, but all four teams found a way to amplify it. By targeting multiple CRISPR constructs to slightly different spots on the gene's promoter, says Gersbach, one of the team leaders, "we saw a huge synergistic effect."

> "I don't think there's any example of any field moving this fast."
>
> —Blake Wiedenheft, Montana State University

In the 25 July issue of *Nature Methods*, he reported activating genes tied to human diseases, including those involved in muscle differentiation, controlling cancer and inflammation, and producing fetal hemoglobin. Two other teams also targeted biomedically important genes. CRISPR control of such genes could treat diseases ranging from sickle cell anemia to arthritis, Gersbach suggests.

CRISPR technology may yet have limitations. It's unclear, for example, how specific the guide RNAs are for just the genes they are supposed to target. "Our initial data suggest that there can be significant off-target effects," says J. Keith Joung from the Massachusetts General Hospital in Boston, who back in January demonstrated that CRISPR would alter genes in zebrafish embryos and has used CRISPR to turn on genes. His work shows that nontarget DNA resembling the guide RNA can become cut, activated, or deactivated.

Joung's group showed that a guide RNA can target DNA that differs from the intended target sequence in up to five of its bases. Zhang has gotten more reassuring results but says that "the specificity is still something we have to work on," especially as more people begin to think about delivering CRISPR systems as treatments for human diseases. "To really make the technology safe, we really have to make sure it goes where we want it to go to and nowhere else."

Researchers must also get the CRISPR components to the right place. "Delivery is an enormous challenge and will be cell type and organism specific," Joung notes. With zebrafish, his team injects guide RNA and messenger RNA for Cas9 directly into embryos; with mammalian cells, they use DNA constructs. How CRISPR might be delivered into adult animals, or to treat disease in people, is just now being considered.

Ultimately, CRISPR may take a place beside zinc fingers and TALENs, with the choice of editing tool depending on the particular application. But for now, researchers are dazzled by the ease by which they can make and test different CRISPR variants and by the technology's unexplored potential. Charpentier and others are looking at the versions of Cas9 in other bacteria that might work better than the one now being used. Microbiologists have harnessed the CRISPR system to vaccinate bacteria against the spread of antibiotic resistance genes. Church, Doudna, Charpentier, and others are forming CRISPR-related companies to begin exploring human therapeutic applications, including gene therapy.

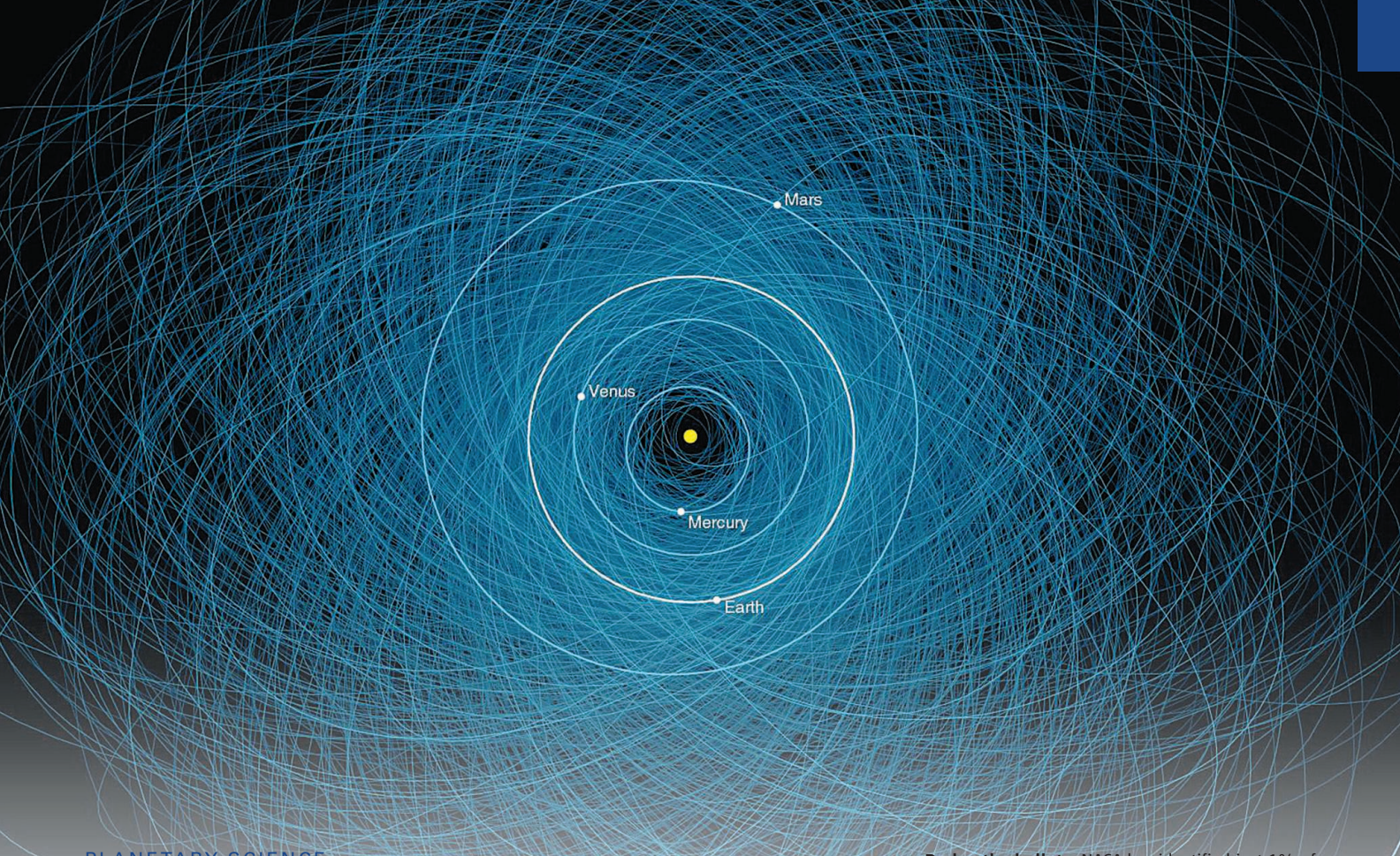
And there's more that can be done, Barrangou says. "The only limitation today is people's ability to think of creative ways to harness [CRISPR]."

Not bad for a system that started with sickly bacteria.

–ELIZABETH PENNISI

CREDIT: GAO CAIXIA LABORATORY

Published by AAAS



Dodge the bullets. NASA has identified just 1% of the 1 million sizable asteroids thought to swirl close to Earth's realm. This plot shows the orbits of the known Near-Earth Objects more than 140 meters across—those most dangerous should they collide with our planet.

CREDIT: NASA/JPL-CALTECH

PLANETARY SCIENCE

The Save-the-World Foundation

Convinced that NASA will not finish the job, a private foundation intends to raise $450 million for a space mission to find asteroids that may threaten Earth

MENLO PARK, CALIFORNIA—In Antoine de Saint-Exupéry's beloved novella, *The Little Prince*, a pilot stranded in the Sahara Desert encounters a being from an asteroid called B-612. "There are also hundreds of others," Saint-Exupéry wrote, "some of which are so small that one has a hard time seeing them through the telescope."

That figure was far too conservative. There may be a million asteroids with masses far greater than ocean liners in Earth-approaching orbits, nearly all of which telescopes have yet to see. Far from being benign abodes like the Little Prince's domain, some of those Near-Earth Objects (NEOs) are potential killers.

Those at least 40 meters across could wipe out a metropolis; a kilometer-wide asteroid could devastate part of a continent and shroud the planet in soot. NASA-sponsored searches, mostly from the ground, have found most of the kilometer-size, civilization-threatening asteroids, but only a fraction—perhaps 1%—of the smaller, but still menacing, objects. Two former astronauts with a soft spot for Saint-Exupéry and a drive to safeguard fellow citizens have set out to find the rest.

Planetary scientists agree that a full inventory of NEOs will require a dedicated space observatory—at least a half-billion-dollar proposition. That's a stretch for NASA, in a thin budgetary era when new planetary missions without "Mars" in the title are rare. Even the agency's current assignment, a 2005 mandate from Congress to identify 90% of NEOs at least 140 meters wide, is behind schedule. More than halfway toward the target date of 2020, NASA has found just 10% of them.

"I believe the agency has ducked its responsibility a little bit," says Lindley Johnson, NASA's program executive for NEO Observations. "I never dreamed it would take as long as it has to develop a robust capacity." Although it now seems feasible to deflect an incoming asteroid, scientists would need many years of advance warning to do so—an unlikely cushion at current rates of discovery.

Into this breach have stepped the astronauts and their B612 Foundation. The foundation has set its sights on launching a $450 million mission by July 2018. The infrared telescope, called Sentinel, would spy a half-million NEOs from a vantage point near Venus. B612 has a star-studded team of planetary science veterans and a fixed-price contract with Ball Aerospace & Technologies to build and operate the satellite.

In the new economy of commercial ventures into Earth's orbit, the B612 Foundation is aiming for much farther—into deep space—propelled by nothing but philanthropic dollars. Although the team's mission design has sparked some dissent and the fundraising goal is steep, all agree that Sentinel's dynamic cartography of the swarm of objects in Earth's milieu would transform planetary science. Says physicist Mark Boslough, an impact specialist at Sandia National Laboratories in Albuquerque, New Mexico: "If we're going to take the impact threat seriously, we have to do something like this."

Online

sciencemag.org

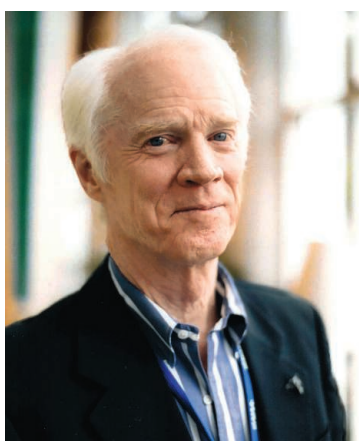
Podcast interview with Robert Irion (http://scim.ag/pod_6148).

Published by AAAS

The Mercury 7 mystique

The public faces of B612 are astronauts from two generations: CEO Edward ("Ed") Lu, 50, and Russell ("Rusty") Schweickart, 77, chair emeritus of the board of directors. Their passions and cultural cachet have lifted B612's profile. "The Mercury 7 mystique of 'the best of the best' still exists," says Sentinel program architect Scott Hubbard of Stanford University in Palo Alto, California, and former Mars program director for NASA. "They have a special place in society."





Protectors. Former NASA astronauts Ed Lu (*top*) and Rusty Schweickart spearhead the B612 Foundation.

Lu, an astrophysicist and solar scientist, flew on two space shuttle missions before spending 6 months on the International Space Station in 2003, in the wake of the Columbia shuttle disaster. He and Russian cosmonaut Yuri Malenchenko maintained the station and ran experiments, but Lu also had time for photography, playing a compact electric piano (his renditions of Beethoven's *Moonlight Sonata* and *Linus and Lucy* by Vince Guaraldi are both on YouTube), and Earth-gazing. "You see shooting stars below you," he says. "You know where the impact craters are. It's a constant reminder." After leaving NASA in 2007, Lu worked as program manager for advanced projects at Google—but protecting Earth had become an irresistible pull.

That transition took longer for Schweickart, a U.S. Air Force fighter pilot chosen for NASA's third class of astronauts in 1963. He flew on Apollo 9 in March 1969, the first test of the lunar module in orbit—a critical step in the sequence leading to the moon landing. During a spacewalk, Schweickart had the rare luxury of simply watching Earth pass under him for 5 minutes as one of his crewmates fixed a jammed camera. Not until 1974, during a remarkable unscripted speech to the Lindisfarne Association—a group dedicated to issues of spirituality and consciousness—did he express how that serendipity had changed him. "You know very well at that moment … that you're the sensing element for man," he said. "You're a piece of this total life. You have to bring that back somehow. And that becomes a special responsibility."

Schweickart took a step toward fulfilling those words in 1995 by founding the Association of Space Explorers, a cadre of former astronauts devoted to public education and planetary stewardship. Then in 1998, he saw Stanford University geophysicist Norman Sleep speak about Earth's impact history. "The incredible energies blew my mind," he says.

Lu and Schweickart soon began discussing how to prevent such blasts from happening again. They founded the B612 Foundation in 2002 with astrophysicist Piet Hut of the Institute for Advanced Study in Princeton and planetary scientist Clark Chapman of the Southwest Research Institute in Boulder. For a decade, they and colleagues examined ways to nudge an NEO off a collision course given at least 10 years of warning. Lu and fellow astronaut Stanley Love devised the "gravity tractor," a spacecraft hovering near an NEO to alter its orbit a touch. Another leading concept, ramming a projectile into an asteroid, would also do the trick if done far enough in advance, studies showed.

"We were four guys and a website and tens of dollars," says Lu, who talks about planetary cataclysms with next-door-neighbor informality. "We came to the conclusion that deflection was doable. Finding the other 99% [of NEOs] is the entire problem."

All along, the team pushed NASA to ramp up the search for hazardous asteroids—often in harsh terms from the characteristically blunt Schweickart. But when Lu spoke at Google and lamented that the government seemed incapable of putting money down, an engineer approached him and said, "Why don't you just do it?" Lu called Schweickart, and B612's new purpose was clear to both of them.

"We put together a list of the 10 best people in the world, and we hired them all," Lu says. "That took about 2 weeks." In addition to Hubbard, they recruited veteran mission director Harold Reitsema, retired from Ball Aerospace; program manager John Troeltzsch, also of Ball Aerospace, who also manages the Kepler planet-hunting telescope; and mission scientist Marc Buie of the Southwest Research Institute, an asteroid authority. B612 also convened a review team that Troeltzsch calls "a *Who's Who* of every deep-space mission flown in the last 45 years."

To Venus, and beyond

Troeltzsch describes Sentinel as a "pinnacle mission" for its heritage of proven systems from other space probes—notably Kepler, the infrared Spitzer Space Telescope, and the comet-colliding Deep Impact. Ball Aerospace played a central role in each one.

The contract between Ball and B612 lays out a cost of about $250 million for Sentinel; launch, operations, and staffing will take about $200 million more. In his talks, Lu specifies a launch date of 20 July 2018, the anniversary of Neil Armstrong's famous step. Plans call for a 6.5-year mission, the time needed to find 90% of the NEOs larger than 140 meters in diameter and perhaps half of the ones down to 40 meters across. Extending the mission to 10 years would sweep up many others.

Sentinel's half-meter-wide telescope will spot NEOs with new infrared detectors sensitive to 10 microns—a long wavelength at which asteroids warmed by the sun pop out against the cold backdrop of space. But the most notable aspect of Sentinel's design is its planned orbit in a path similar to that of Venus. This perch, Buie says, will allow Sentinel a view of fully illuminated asteroids as it looks out toward Earth's orbit, away from the sun. Ball engineers first made a pitch for a Venus-like orbit in 2002, Buie recalls: "I said, 'You guys have got the answer.' I could see it in an instant."

But the choice forces compromises. For instance, Sentinel's remote position means that it will not detect as many smaller NEOs in the 40-meter range as it might from a closer vantage, says Tim Spahr, director of the Minor Planet Center at the Smithsonian Astrophysical Observatory in Cambridge, Massachusetts. That's the suspected size of the object that blew up in 1908 over Tunguska, Siberia, flattening 2000 square kilometers of forest. B612's website leads off with the bold slogan "Sentinel: Prevent the Next Tunguska." But as Spahr points out, "If you want that as your goal, you must stay near the Earth."

In another tradeoff, Sentinel's distance from Earth—between roughly 40 million kilometers to 250 million kilometers—limits the amount of data it can beam back. B612

CREDITS (TOP TO BOTTOM): NASA; COURTESY OF THE B612 FOUNDATION

Published by AAAS

signed an agreement with NASA to use its Deep Space Network of radio antennae to download data, but to limit the burden an onboard computer will allow Sentinel to transmit only image frames in which an object appears to have moved within 1 hour. "The vast majority of the sky will not have changed," Reitsema says. That step, he projects, will trim data rates by a factor of 1000.

Spahr frets about that purge, as does astronomer Amy Mainzer of NASA's Jet Propulsion Laboratory (JPL) in Pasadena, California, who has proposed that NASA fund an alternative NEO-hunting satellite, called NEOCam, to be stationed closer to Earth. "Most of what you'll find that's new is at the faintest limit of detection," she says. "You have to have all of the data [to find them]. If you don't, you might as well cut the telescope aperture in half." As a case in point, Mainzer notes that a deeper analysis of the full data set from a recent extension of NASA's Wide-field Infrared Survey Explorer (WISE) mission, called NEOWISE, should yield NEOs beyond the 134 new ones her team announced in 2011.

Reitsema says that the B612 team parsed its orbital options thoroughly and knows Sentinel won't catch everything. But he says the goal driving the design—notwithstanding the Tunguska banner on the website—is finding 90% of the 140-meter-size asteroids and above, as Congress dictated. For that, Reitsema states, "We're quite confident Venus is the preferred orbit."

If the satellite spies an NEO that could make a very close pass by Earth, large radar antennae on the ground will bounce signals off the asteroid to zero in on its trajectory. A precise orbit usually rules out an impact, but Lu pegs the odds that Sentinel will find an NEO requiring deflection sometime in the next century at 3-in-10. If one looms, nations will confront the tangled geopolitics of deflection. Altering an orbit, Schweickart points out, may shift the likeliest impact spot from one country to another until the projected path misses Earth. Years of debate about asteroids in U.N. committees, he says, haven't led to a set of "mission rules" about what to do. "In some ways this will be the first global decision on survival," he says. "Will we recognize our commonality well enough to overcome our differences?"



Space surprise. A 17-meter-wide asteroid that no one saw coming exploded in February near Chelyabinsk, Russia, but even space surveys will strain to find objects that small.



Sentinel (artist's concept)

CREDITS (TOP TO BOTTOM): © JIANG KEHONG/XINHUA PRESS/CORBIS; B612 FOUNDATION/BALL AEROSPACE

Museum wings and observatories

The overall reaction to B612's plans has been positive. "I think they're doing everything right," says Donald Yeomans, manager of NASA's NEO program office at JPL. But he worries that the philanthropic goals are too ambitious.

The foundation's immediate goal is $20 million in donations by the new year, followed by at least $40 million each year for a decade. To oversee the effort, Lu hired Karen Putnam, a veteran of East Coast museum fundraising and former CEO of the Central Park Conservancy in New York. Lu compares Sentinel's costs to the wing of a major art museum—a "midsize project," he says, "with the added benefit that you can help save the world." Putnam declined to state the amount raised to date, noting only that "we have the $20 million in various stages in the pipeline."

A recent study by economist Alexander MacDonald, program executive for NASA's emerging space office, suggests that B612's financial goals are no more ambitious than those of classic astronomy ventures. MacDonald examined the costs of major observatories built before World War II, almost entirely with private money. When he scaled those expenses to 2008 dollars as comparable fractions of the U.S. gross domestic product, he found that Mount Wilson Observatory in California and Yerkes Observatory in Wisconsin would have cost $408 million and $441 million, respectively. Others were even more lavish.

If B612 falls short, might NASA carry the project? "We'd be happy to talk about a deeper public-private partnership, sure," Lu says. "Our goal isn't us building the telescope; our goal is completing the telescope." Johnson at NASA headquarters says the climate in Washington, D.C., for asteroid detection is "the best that it has been." At a House of Representatives science committee hearing in March, 1 month after the surprising airburst of a 17-meter-wide asteroid near Chelyabinsk, Russia, receptive legislators heard the B612 Foundation called out seven times by NASA Administrator Charles Bolden and Office of Science and Technology Policy Director John Holdren. Lu has testified twice on Capitol Hill as well.

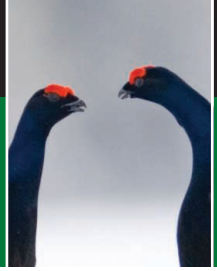
Some in the field regret that it took Chelyabinsk to trigger this rush of concern. "It's unlikely any space survey would find such [small] objects, and they should not be sold that way," says planetary scientist Edward Beshore of the University of Arizona in Tucson, former director of the Catalina Sky Survey—the world leader in numbers of NEOs found to date.

Distinctions among asteroid sizes may elude the public, but B612 team members report they've never encountered such rapt reactions in classrooms, public forums, and elevators when they describe their goals. And if Sentinel flies, the new NEO catalog will yield rich insights into our solar system's flotsam and jetsam—and how best to stay out of its way. "I've always thought that asteroids were solvable," Spahr says.

That's just how two problem-solving astronauts see it. **–ROBERT IRION**

Robert Irion directs the Science Communication Program at the University of California, Santa Cruz.

Published by AAAS



Guide to games of life
844



Ribosome diseases
849

LETTERS | BOOKS | POLICY FORUM | EDUCATION FORUM | PERSPECTIVES

LETTERS

edited by Jennifer Sills

Archaeobotanical Archiving

IN THEIR REPORT "EMERGENCE OF AGRICULTURE IN THE FOOTHILLS of the Zagros Mountains of Iran" (5 July, p. 65), S. Riehl *et al.* describe the advent of agriculture and domestication of wild plants in the Zagros Mountains, Iran. The authors write that the samples are currently archived at the University of Tübingen, but we believe that the site of conservation and archiving should be in Iran.

According to the First Code of Ethics, adopted by World Archaeological Congress Codes of Ethics, archaeologists and anthropologists agree to fulfill their commitments to the ethical principles governing the study of the human past (*1*). Among these principles is the importance of indigenous ancestral human remains to native peoples. Archaeologists are required to acknowledge that the indigenous cultural heritage rightfully belongs to the indigenous descendants of that heritage. Human remains, artifacts, or objects of special cultural significance of indigenous peoples should not be removed from their indigenous discovery site or country.

The archaeobotanical samples used in the Riehl *et al.* study reflect the thousands-year-old heritage of civilizations and should be conserved and archived where they were found in order to respect the rights of the indigenous descendants.

SAMAD E. J. GOLZARI

Cardiovascular Research Center, Tabriz University of Medical Sciences, Tabriz, Iran. E-mail: dr.golzari@hotmail.com



Sorting carbonized plant remains.

Response

WE SHARE GOLZARI'S CONCERN FOR THE conservation of Iran's cultural heritage. Two of us (M.Z. and N.J.C.) are the Iranian and German directors of the Chogha Golan excavations. Furthermore M.Z. is a graduate of Tehran University who has spent most of his professional career employed by the Iranian Department of Antiquities. The project served as an important training excavation for numerous Iranian students, who learned how to use state-of-the-art methods to carefully excavate this pre-ceramic tell. Our team has a formal partnership with the Iranian Department of Antiquities to conduct archaeobotanical research. We were granted a permit to export the botanical materials from Chogha Golan.

Given that there is no established facility for conducting archaeobotanical research, nor a facility for long-term storage of archaeobotanical materials in Iran, the University of Tübingen, with its excellent infrastructure and long record of research in the fields of botany and archaeobotany, is an appropriate place to study the botanical remains from Chogha Golan. Our team, which is composed of Iranian and other international scholars, works closely with the Department of Antiquities in Iran, with whom we have a long relationship based on shared scientific goals, trust, and mutual respect. When our research has been completed, we will work closely with our colleagues at the Department of Antiquities to decide where and how to best archive the botanical material from Chogha Golan.

MOHSEN ZEIDI,[1] NICHOLAS J. CONARD,[1] SIMONE RIEHL[2]*

[1]Department of Early Prehistory and Quaternary Ecology, Senckenberg Center for Human Evolution and Paleoenvironment, University of Tübingen 72070, Tübingen, Germany. [2]Institute of Prehistory and Quaternary Ecology, Department of Archaeological Sciences, Tübingen University, 72070 Tübingen, Germany.

*Corresponding author. E-mail: simone.riehl@uni-tuebingen.de

Reference

1. The World Archaeological Congress, *First Code of Ethics* (Adopted by WAC Council in 1990 at WAC-2, Barquisimeto, Venezuela); www.worldarchaeologicalcongress.org/about-wac/codes-of-ethics/167-codes-of-ethics.

Alleviating Poverty in India: Biodiversity's Role

IN THEIR NEWS FOCUS STORY "SCIENCE FOR all" (31 May, p. 1032), P. Bagla and R. Stone describe advances in technology, medicine, and information technology geared toward alleviating poverty in India. However, they did not highlight the link between biodiversity conservation, judicious natural resource management, and the quality of life and upward economic mobility of poor people in (sub)tropical countries such as India.

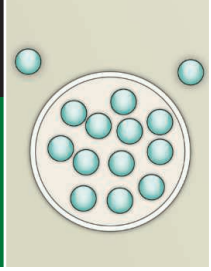
Biodiversity loss is one of the greatest economic problems affecting the world (*1*) and is inextricably linked with development. In India, deforestation in the Himalaya is not only driving endemic extinctions (*2*), it is also affecting villages by causing periodic droughts (p. 1033) and extreme flooding events (*3*), which could be exacerbated by the effects of climate change on glaciers (*4*). Thirty-one percent of the world's coastal fishermen rely on the Bay of Bengal, an area enduring longstanding overfishing and

CREDIT: UNIVERSITY OF TÜBINGEN

Published by AAAS



Promising gene therapy
853



How crystals nucleate
855

pollution that will likely worsen with increasing trade (*5*). Healthy ecosystems aid in climate change adaptation as well as disaster risk reduction (*6*); for example, mangroves protected coasts during the 2004 tsunami. Infectious disease and biodiversity loss in India are strongly linked (*7*, *8*).

Given the synergy between biodiversity and sustainable development, the current scientific race against time can only take India so far in the fight against poverty if research on biodiversity conservation and relevant fields of social sciences do not experience comparable growth. Technological innovation and interdisciplinary collaboration on biodiversity research should be encouraged. For example, harnessing India's advancements in space research could improve satellite mapping of ecosystems and natural resources in difficult parts of the country (*9*). Changes are also needed in biodiversity and conservation policies (*10*). A country that boasts four biodiversity hotspots (*11*) and tremendous recent economic development (despite continuing income inequality and poverty) should be able to provide focus on biodiversity conservation. Intensive research in biodiversity conservation and related social sciences will inform India's national policy on long-term economic development while improving the quality of life of the underprivileged majority.

ROBERT MURRAY LASLEY JR.,[1]* ANUJ JAIN,[1] KRUSHNAMEGH KUNTE[2]

[1]Department of Biological Sciences, National University of Singapore, 117543. Singapore. [2]National Center for Biological Sciences, Bengaluru, India.

*Corresponding author. E-mail: rlasleyjr@gmail.com

References

1. D. Helm, C. Hepburn, *Oxford Rev. Econ. Pol.* **28**, 1 (2012).
2. M. K. Pandit, N. S. Sodhi, L. P. Koh, A. Bhaskar, B. W. Brook, *Biodiversity Conserv.* **16**, 153 (2007).
3. R. Deshpande, "Earth sciences secretary blames Uttarakhand rains on climate change," *The Times of India* (22 June 2013).
4. T. Bolch *et al.*, *Science* **336**, 310 (2012).
5. Anonymous, "The Bay of Bengal: New bay dawning," *The Economist* (27 April 2013).
6. R. Munang, I. Thiaw, K. Alverson, J. Liu, Z. Han, *Curr. Opin. Environ. Stability* **5**, 47 (2013).
7. D. Taylor, Q. Rahman, *Environ. Health Perspect.* **104**, 266 (1996).
8. F. Keesing *et al.*, *Nature* **468**, 647 (2010).
9. N. J. Singh, S. Bagchi, *J. Appl. Ecol.* **50**, 4 (2013).
10. G. Shahabuddin, "The endangered wildlife biologist," *Nature, Wildlife, People: A Symposium on Wildlife Protection and People's Livelihoods* #577 (2007); www.india-seminar.com/2007/577/577_ghazala_shahabuddin.htm.
11. Conservation International, "The Biodiversity Hotspots" (20 July 2013); www.conservation.org/where/priority_areas/hotspots/asia-pacific/Pages/asia-pacific.aspx.

Protecting the Right To Benefit from Science

IN THEIR POLICY FORUM "A HUMAN RIGHT TO science" (14 June, p. 1291), A. Chapman and J. Wyndham describe action the science and engineering community can take to implement Article 15 of the International Covenant on Economic, Social, and Cultural Rights (ICESCR) (*1*), which details the right to benefit from science. However, they do not address one salient detail: To date, the United States (along with Cuba, Belize, Comoros, Palau, San Marino, and South Africa) has signed but not yet ratified the ICESCR (*2*).

Until the United States fully accepts the terms of the ICESCR, including Article 15, activism of the sort recommended by Chapman and Wyndham is likely to have limited impact. Their call for action by the science and engineering community is entirely appropriate and timely; however, it appears that the first target of that activism should be the U.S. Senate.

JEFFREY H. MATSUURA

Falls Church, VA 22043, USA. E-mail: jmatsuura@eblg.com

References

1. International Covenant on Economic, Social, and Cultural Rights (www.ohchr.org/EN/ProfessionalInterest/Pages/CESCR.aspx).
2. United Nations Treaty Collection (http://treaties.un.org/Pages/ViewDetails.aspx?src=Treaty&mtdsg_no=IV-3&chapter=4&lang=en).

Letters to the Editor

Letters (~300 words) discuss material published in *Science* in the past 3 months or matters of general interest. Letters are not acknowledged upon receipt. Whether published in full or in part, Letters are subject to editing for clarity and space. Letters submitted, published, or posted elsewhere, in print or online, will be disqualified. To submit a Letter, go to www.submit2science.org.

Response

AS MATSUURA POINTS OUT, THE UNITED STATES is not a party to the ICESCR (*1*) and, therefore, is not legally bound to implement the treaty, including its Article 15 recognizing the right to enjoy the benefits of scientific progress. Nonetheless, opportunities do exist for the U.S. science and engineering community to contribute to the implementation of this right. Although it has not ratified the ICESCR, the United States did sign this human rights treaty in 1977. The legal implication is that the United States must not violate the "object and purpose" of the ICESCR. In this vein, former U.S. Assistant Secretary of State Michael Posner (*2*) and Science Adviser to the Secretary of State William Colglazier have stated publicly that the United States "as a policy matter" upholds the "values and principles" of the right to benefit from science (*3*).

There are three ways the U.S. science and engineering community can contribute to the implementation of Article 15:

(i) The UN body that monitors implementation of the ICESCR regularly reviews reports of states outlining how they implement their obligations. Any group may submit a "shadow report" to supplement this information. U.S. scientists and engineers could provide information about the persecution of scientists, budgetary restrictions, or positive strides in strengthening science education.

(ii) Every 4.5 years, the UN Human Rights Council reviews the human rights record of all members of the United Nations. This universal periodic review is not limited to a review of treaties ratified by a country. As part of this process, the U.S. science and engineering community could submit information about U.S. policies and programs relating to science and their impact on and implications for human rights.

(iii) The framework provided by Article 15 need not be legally binding to inform U.S. policies and programs. Taking specific elements of Article 15, the science and engineering community could work with relevant agencies to assess or develop programs that reflect the principles of Article 15 and inform policy development.

AUDREY R. CHAPMAN[1]* AND JESSICA M. WYNDHAM[2]

[1]Community Medicine, University of Connecticut Health Center, Farmington, CT 06030, USA. [2]Scientific Responsibility, Human Rights, and Law, AAAS, Washington, DC 20005, USA.

*Corresponding author. E-mail: achapman@uchc.edu

References

1. International Covenant on Economic, Social, and Cultural Rights (www.ohchr.org/EN/ProfessionalInterest/Pages/CESCR.aspx).

Published by AAAS

2. Assistant Secretary Michael Posner Remarks: Scientific and Academic Freedom in the Digital Age, American Association for the Advancement of Science, Washington, DC (10 October 2012); http://srhrl.aaas.org/coalition/Meetings/2012/Posner/Transcript.pdf.
3. G. Pinholster, AAAS, "Scientific Freedom and Cross-Border Cooperation Underlie Core Human Right" (30 July 2013); www.aaas.org/news/releases/2013/0730_article-15.shtml?utm_source=tw&utm_medium=sm&utm_content=article-15&utm_campaign=release.

CORRECTIONS AND CLARIFICATIONS

News of the Week: "World food prize" (28 June, p. 1507). The story should have noted that in 1983, Marc Van Montagu, Jeff Schell, and colleagues at Ghent University (Belgium) also reported developing genetically modified plants.

News & Analysis: "Supreme Court rules out patents on 'natural' genes" by E. Marshall (21 June, p. 1387). The story reported incorrectly that Myriad Genetics Inc. "sued a number of private outfits" for infringement of Myriad's gene patents. Before the recent Supreme Court case, Myriad points out, the company engaged in litigation in one other dispute over BRCA patents, involving Oncormed Inc., and only after Oncormed sued Myriad.

Perspectives: "A theory of city size" by M. Batty (21 June, p. 1418). The plot in the figure on p. 1419 is logarithmic in scale. The *y*-axis label should have been "log (Accessibility)"; the *x*-axis label should have been "log (Population)." The labels have been corrected in the HTML and PDF versions online.

Table 1. Original and corrected correlations for analyses associated with Fig. 2, A to D.

Correlation between integrated prevalence and	Associated with	Original correlation	Corrected correlation
Maximum prevalence	Text result	$r = 0.89, P = 0.008$	$r = 0.90, P = 0.006$
Evolutionary change	Fig. 2A	$r = 0.86, P = 0.030$	$r = 0.83, P = 0.041$
Predation index (body size)	Fig. 2B	$r = 0.86, P = 0.029$	$r = 0.87, P = 0.024$
Total nitrogen (TN)	Fig. 2C	$r = 0.83, P = 0.040$	$r = 0.83, P = 0.043$
Total phosphorus (TP)	Fig. 2D	$r = 0.5, P = 0.3$	$r = 0.6, P = 0.2$

Table 2. Corrected analyses associated with Fig. 2, E and F, analyzing differences between the two evolutionary groups (populations evolving increased resistance versus increased susceptibility).

Difference between two evolutionary groups in	Original *t* test	Corrected *t* test	Repeated measures analysis on corrected data
Predation index (body size)	$t = 3.19, P = 0.033$	$t = 2.21, P = 0.092$	$F = 10.67, P = 0.011$
Total nitrogen (TN)	$t = 3.18, P = 0.034$	$t = 2.16, P = 0.097$	$F = 13.42, P = 0.005$
Total phosphorus (TP)	$t = 0.88, P = 0.43$	$t = 0.88, P = 0.43$	$F = 1.23, P = 0.33$

Reports: "Ecological context influences epidemic size and parasite-driven evolution," by M. A. Duffy *et al*. (30 March 2012, p. 1636). Correction of a data error has resulted in minor quantitative but no qualitative changes to results presented in this study. New correlation statistics in Fig. 2, A to D, appear in Table 1. All correlations remain significant at the $\alpha = 0.05$ level. For Fig. 2, E and F, the updated data prompted use of a more powerful analysis (Table 2). The authors had used three *t* tests to compare values of key variables between lakes in which hosts evolved increased resistance or increased susceptibility. Using the revised data, *t* tests for predation index (body size) and total nitrogen became insignificant (Table 2). However, these *t* tests have very low power ($N = 6$ total). With a more powerful repeated measures analysis [Proc Mixed in SAS, using an AR(1) covariance structure to account for autocorrelated error structure], the new results mirror conclusions from the original *t* tests (Table 2). Thus, after correcting the data, the conclusions remain unchanged: (i) Hosts can evolve enhanced susceptibility to their virulent parasites during epidemics, and (ii) ecological context influences epidemic size, which, in turn, determines evolutionary responses of hosts to epidemics.

CONSERVATION BIOLOGY

We Need More Than Preservation

Stephen Redpath

I read *After the Grizzly* during a field trip to northern India. Together with colleagues from the Snow Leopard Trust, I was staying in the small village of Kibber in Spiti Valley, high up in the Himalayas, surrounded by snow-capped peaks and deep, dramatic gorges. As it turns out, for reasons that I will later explain, this was an entirely appropriate place to read Peter Alagona's captivating work.

The book focuses on the history of endangered species conservation in California. Alagona (a historian at the University of California, Santa Barbara) offers absorbing accounts of the changing fortunes of five species in the Golden State: grizzly bear (*Ursus arctos horribilis*), California condor (*Gymnogyps californianus*), Mojave desert tortoise (*Gopherus agassizii*), San Joaquin kit fox (*Vulpes macrotis mutica*), and Delta smelt (*Hypomesus transpacificus*). He presents each of these stories in its rich historical and political context, amid evocative descriptions of the landscapes and habitats where the species live. These case studies highlight the evolving challenges involved in conserving threatened species in a state that is now home to one in eight Americans. Over the past hundred years, attitudes toward wildlife, wildlife management, and wilderness have been transformed, and this has altered the arguments and focus of conservation.

Alagona, a gifted writer, skillfully brings to life the people involved in each of these case studies, from the grizzly hunters of the 19th century to those at the sharp end of conservation today. In particular, he writes in depth about Joseph Grinnell (founder of the University of California's Museum of Vertebrate Zoology) and his influential Berkeley circle, who decided they needed to save California's wildlife from the ravages of modern man. Through these stories, Alagona deftly draws together his central argument: that the conservation of endangered species requires more than simply protecting patches of specific habitat. For example, condors can travel up to 240 km in a day and therefore often hunt in places such as the low-elevation working rangelands of western California. Similarly, kit foxes do not behave as a "true" endangered species should; they now live in suburban Bakersfield.

Having presented these studies in delightful detail, Alagona then calls for us to start thinking about how we can move away from our reliance on protected areas and start delivering a broader vision for conservation. He ends the book by suggesting that "figuring out how to achieve [more sustainable landscapes] is one of the greatest environmental challenges of the twenty-first century."

Although I thoroughly enjoyed reading the book, I have to question the assertion that we have not moved on from solely focusing on protected areas as the way to conserve biological diversity. Of course we have. As Alagona himself points out, Aldo Leopold recognized the need to also develop conservation strategies in working landscapes over 80 years ago. So it has long been obvious that we can't just rely on pockets of protected areas if we want to help threatened species expand in range and numbers. We also have to work with the communities that are affected by conservation objectives and negotiate solutions to the shared problems that arise when trying to balance conservation with livelihoods. Indeed, across the world there have been numerous attempts to develop such a bottom-up approach of working with the people and communities involved, through agri-environment schemes (*1*) and a variety of community-based conservation approaches [e.g., see "The Evolution of Policy" in (*2*)].

So this brings me back to the Himalayas and thinking about how we might conserve the globally threatened snow leopard (*Uncia uncia*), which suffers from retaliatory killing by pastoralist communities. One might take the top-down approach that Alagona describes—identifying core habitat, establishing large protected areas, and then using legislation and enforcement to penalize communities for illegally killing leopards that attack their livestock. This seems unlikely to work in remote areas, where leopards occur at very low density and many people living on the edge of poverty are scattered through the landscape. Alternatively, one could work with these communities, recognizing shared problems that need to be resolved and negotiating solutions that both villagers and conservation organizations can live with. So far, in the few places this has been tried, this tack seems to be paying huge dividends, in terms of both social and ecological outcomes. The communities trust the conservationists, and retaliatory killing has stopped. Through various schemes, such approaches are being tested around the world, with mixed success.



More symptom than cause. The Delta smelt became embroiled in California's water wars.

The book would have benefited from at least a nod to these other approaches and a glimpse into their documented successes and failures. It seems to me that the big question Alagona raises in the "Epilogue" needs to be recast to focus instead on the relative merits of various approaches to conservation in different contexts. We need to understand when and where particular approaches will deliver sustainable outcomes for the species and the people involved.

Despite this oversight, I highly recommend *After the Grizzly* to anyone interested in gaining insight into the wonderful richness of conservation. Alagona adroitly documents the roles that historical contingency and a few influential, passionate people can play in shaping the mixed fortunes of endangered species.

After the Grizzly
Endangered Species and the Politics of Place in California

by Peter S. Alagona
University of California Press, Berkeley, 2013. 331 pp. $34.95, £24.95. ISBN 9780520275065.

The reviewer is at the Institute of Biological and Environmental Science, Aberdeen University, Tillydrone Avenue, Aberdeen AB24 2TZ, UK. E-mail: s.redpath@abdn.ac.uk

References
1. D. Kleijn, W. J. Sutherland, *J. Appl. Ecol.* **40**, 947 (2003).
2. M. Borgerhoff Mulder, P. Coppolillo, *Conservation: Linking Ecology, Economics, and Culture* (Princeton Univ. Press, Princeton, NJ, 2005).

10.1126/science.1241300

CREDIT: B. MOOSE PETERSON/U.S. FISH AND WILDLIFE SERVICE

Published by AAAS

EVOLUTION

O Brave New World with Such Games

Benjamin Allen[1] and Martin A. Nowak[2]

A stag might fight to death over a territory or concede it uncontested to another. Neighboring trees invest varying amounts of energy into growth, with the tallest blocking sunlight to others. Viruses infecting a common cell can either make all proteins required for their reproduction or free ride on those made by others. How does evolution shape the strategic phenotype of organisms in life-and-death contests?

Such questions fall within the domain of evolutionary game theory, a field that combines strategic concerns with the fundamental principles of evolution. A game is a simple way to represent interactions. Players choose from a set of possible strategies; for example, fight or retreat, cooperate or defect. The results are recorded as payoffs received by each player. The basic idea of evolutionary game theory is to link payoff to reproductive success (*1*). Thus, a successful strategy will increase in abundance over generations as it is successively transmitted from parent to offspring. Evolutionary game theory applies whenever fitness depends on the phenotypes or actions of others; the fitness landscape changes as the population explores it (*2*). The resulting evolutionary dynamics can lead to dominance of a single strategy, coexistence of multiple strategies, periodic cycling, or even chaos (*3*).

In its first decades, evolutionary game theory focused primarily on notions of evolutionary stability and deterministic dynamics. Previous textbooks (*3*–*6*) concentrated on these early themes. However, the scope of evolutionary game theory is rapidly expanding—both in terms of the range of situations considered and the variety of underlying models of evolution. Mark Broom and Jan Rychtář's *Game-Theoretical Models in Biology* provides a comprehensive, up-to-date introduction that uniquely blends mathematical clarity and biological intuition.

Game-Theoretical Models in Biology

by Mark Broom and Jan Rychtář
Chapman and Hall/CRC Press, Boca Raton, FL, 2013. 520 pp. $79.95, £39.99. ISBN 9781439853214.



Crucial contest. Black grouse (*Tetrao tetrix*) clashing at Finnish lek.

The first half explores the many ways that the concepts "game" and "evolution" can be realized. Moving beyond the traditional focus on matrix games, Broom and Rychtář (mathematicians at City University, London, and the University of North Carolina at Greensboro, respectively) explore nonlinear and asymmetric games, games among many players, games with sequential moves, and games that change with players' ages and other variables. They discuss not only evolution in terms of competition among existing strategies but also long-term evolution through successive trait substitutions. The authors also examine the effects of population size and structure, providing an entry point into one of the most active and exciting new directions in the field.

The second half brings to life the mathematical frameworks introduced earlier, focusing on specific investigations of important biological phenomena. Through detailed exposition and modeling of conflicts that arise in the contexts of group living, mating, foraging, and predation, the authors illuminate not only the behaviors that emerge in these particular contexts but also the process of matching mathematical framework to biological reality, a critical skill for aspiring evolutionary theorists. One especially interesting analysis considers a sperm-allocation dilemma: males must produce the amount that maximizes their reproductive chances, given that each female may mate with multiple males.

One chapter concerns the evolution of cooperation, a topic of great interest in biology, psychology, economics, and philosophy. A controversy in this field exists over kin selection, by which cooperation can spread if the benefits go primarily to genetic relatives. In some simplified models, this idea can be formulated as Hamilton's rule. In dispute is whether kin selection is a universal explanation for cooperation or merely one mechanism among several (*7*). This seemingly straightforward question has become clouded for two reasons. First, some researchers apply the term "kin selection" to any situation in which there is association (genetic or not) among like phenotypes, thus vastly stretching its meaning. Second, some use linear regression to rewrite frequency changes so that Hamilton's rule appears to be satisfied, regardless of the underlying biological reasons for change. In contrast, Broom and Rychtář offer a refreshingly clear exposition of kin selection, using a simple model with direct biological interpretation. They present this alongside other, distinct, mechanisms for cooperation such as direct and indirect reciprocity, avoiding the confusion that muddles much of the literature on this topic.

Legend has it that John Maynard Smith invented the concept of evolutionary stability after quitting a technical account on game theory a few pages before he would have encountered the Nash equilibrium. Students of evolutionary game theory, however, would do well to read *Game-Theoretical Models in Biology* all the way to the finish line. This engaging primer demonstrates that there is no tension between mathematical elegance and biological fidelity: both are needed to further our understanding of evolution.

[1]Department of Mathematics, Emmanuel College, Boston, MA 02115, USA. [2]Program for Evolutionary Dynamics, Harvard University, Cambridge, MA 02138, USA. E-mail: martin_nowak@harvard.edu

References

1. J. Maynard Smith, G. R. Price, *Nature* **246**, 15 (1973).
2. M. A. Nowak, K. Sigmund, *Science* **303**, 793 (2004).
3. J. Hofbauer, K. Sigmund, *Evolutionary Games and Population Dynamics* (Cambridge Univ. Press, Cambridge, 1998).
4. J. Maynard Smith, *Evolution and the Theory of Games* (Cambridge Univ. Press, Cambridge, 1982).
5. J. W. Weibull, *Evolutionary Game Theory* (MIT Press, Cambridge, MA, 1995).
6. K. Sigmund, *The Calculus of Selfishness* (Princeton Univ. Press, Princeton, NJ, 2010).
7. M. A. Nowak, *Science* **314**, 1560 (2006).

10.1126/science.1241750

CREDIT: DAVID TIPLING/ALAMY

Published by AAAS

EDUCATION

Can Rating Pre-K Programs Predict Children's Learning?

Systems intended to rate the quality of early education programs may not actually reflect impacts on learning.

T. J. Sabol,[1]* S. L. Soliday Hong,[2] R. C. Pianta,[3] M. R. Burchinal[2]

Early childhood education programs [e.g., prekindergarten (pre-K)]—characterized by stimulating and supportive teacher-child interactions in enriched classroom settings—promote children's learning and school readiness (*1*–*3*). But in the United States, most children, particularly those from low-income backgrounds, attend programs that may not be of sufficient quality to improve readiness for school success (*4*). States are adopting Quality Rating and Improvement Systems (QRISs) as a market-based approach for improving early education, but few states have evaluated the extent to which their QRIS relates to child outcomes. We studied the ability of several QRISs to distinguish among meaningful differences in quality that support learning.

QRISs are designed to rate individual programs and to disseminate ratings to inform parents' decisions about enrollment and policy-makers' decisions about investment, so as to create a local market for quality improvement intended to lead to better school readiness (*5*). Because of increased federal and state support, over half of all U.S. states now have a QRIS (*5*). The U.S. Department of Education invested $500 million in selected states in the Race to the Top—Early Learning Challenge program to expand QRISs.

Development of each state's QRIS is typically based on local professionals' judgment and involves (i) selecting measures of "quality" that form the individual indicators; (ii) categorizing each indicator into different levels of quality, and (iii) creating rules for how to combine indicators into composite ratings. Differing from many accountability policies, QRISs typically do not measure child outcomes to assess school quality. Instead, they assess process-oriented and structural indicators (e.g., teachers' qualifications). Some indicators, such as quality of the learning environment, are modestly related to children's skills (*2*). There is less evidence that other indicators, such as family partnership, have a robust relation to child outcomes (*6*). Small-scale QRIS evaluations have shown mixed evidence as to whether ratings discriminate among programs that are better or worse in fostering learning (*7*). Neither the selection of quality indicators, their categorization into levels, nor the composite ratings have been systematically studied as they relate to children's learning.

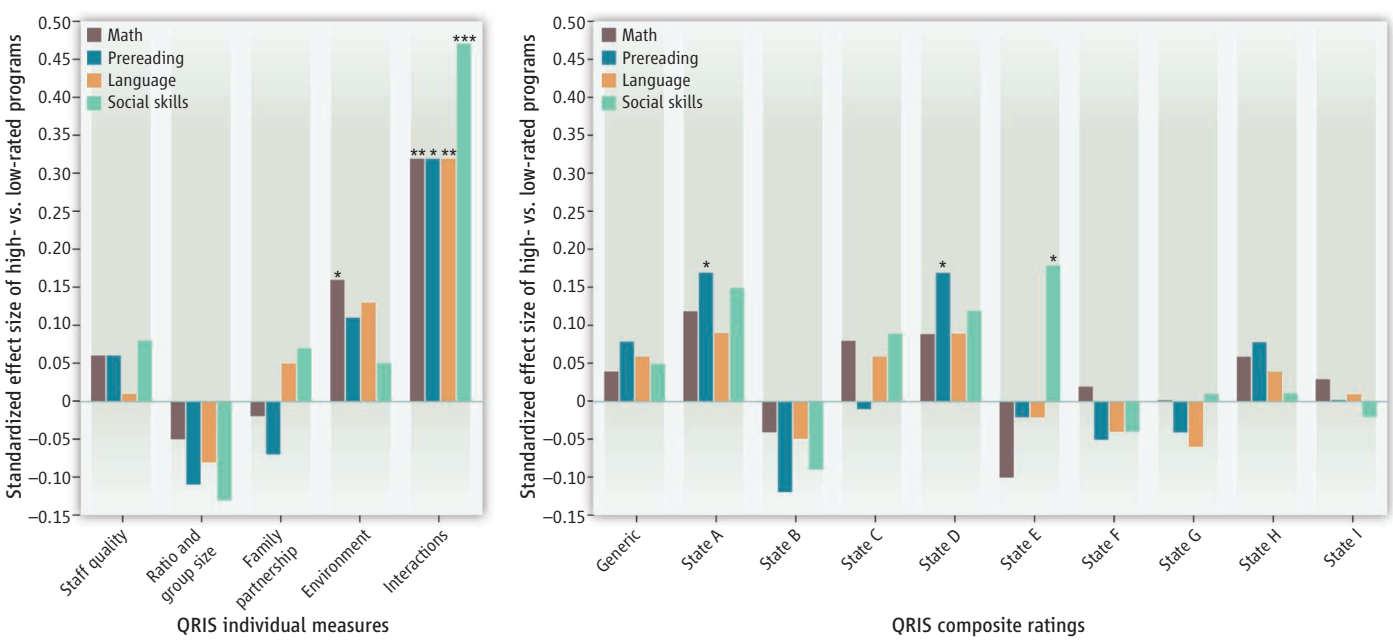
[1]Institute for Policy Research, Northwestern University, Evanston, IL 60208, USA. [2]Frank Porter Graham Child Development Institute, University of North Carolina, Chapel Hill, NC 27599, USA. [3]Center for the Advanced Study of Teaching and Learning, University of Virginia, Charlottesville, VA 22904, USA.

*Corresponding author: terri.sabol@northwestern.edu

Replicating Systems, Relating Outcomes

We estimated associations between QRIS ratings and measures of children's learning using a data set that included 2419 children in 673 public pre-K programs across the United States [see supplementary materials (SM) for details]. Data are from two studies that represented the variety of pre-K models in the United States at the time (2001–04): the National Center for Early Development and Learning (NCEDL) multistate study of prekindergarten and the State-Wide Early Education Programs (SWEEP) Study. The studies used a stratified random sample

On most measures of children's learning, programs rated high by QRIs produce outcomes that are not significantly better than those of low-rated programs. Stars indicate a statistically significant difference in math, prereading, expressive language, and social skills (*$P < 0.05$, **$P < 0.01$, ***$P < 0.001$), see SM. (**Left**) QRIS individual measures. (**Right**) Composite ratings, see (*10*).



Published by AAAS

design to select programs within each state system (*8*).

We used the NCEDL-SWEEP data set to replicate as closely as possible a number of individual state's QRIS scoring algorithms (see SM). These QRISs used the same four popular quality indicators to determine program ratings: (i) staff qualifications, including teacher and director level of education and years of experience; (ii) staff-child ratio and group size; (iii) family partnerships; and (iv) learning environment, measured by the Early Childhood Education Rating System–Revised (ECERS–R) (*9*, *10*).

We also selected an additional indicator, (v) interactions, measured using the Classroom Assessment Scoring System (CLASS) (*11*) to assess the quality of interactions in the classroom. None of the selected existing QRISs used the CLASS in program ratings. We created and tested a generic system that included all five quality indicators [(i) to (v) above], representing the most simplified and best predictor scoring system we could design based on available data (see SM).

All analyses examined the relation among QRIS measures and end-of-year child outcomes, accounting for nesting in classrooms; beginning-of-year scores; state location of the pre-K program; and child, family, and program characteristics. All programs in the sample were subject to states' minimum requirements in terms of structural features and teacher qualifications. Our findings can be interpreted as an estimate of the association among quality measures and child outcomes beyond these minimum requirements.

Few Associations of QRISs with Outcomes

Of the five individual quality indicators, the CLASS measure of teacher-child interaction quality consistently was the strongest predictor of children's learning, followed by the learning environment (ECERS-R; see SM). The structural quality measures of staff qualifications, staff-child ratio, and family partnership provided weaker and less consistent prediction of children's learning.

The relation of child outcomes when children attended a program rated in the highest level versus the lowest level for each quality indicator is shown in the chart (left) and is based on cut-points from our generic QRIS. Results were similar when we used cut-points for the nine states regardless of small variations in scoring methods (see SM). The high-low contrast on the measure of teacher-child interactions had the strongest association with children's skills. Children had stronger math skills, but not prereading, expressive language, or social skills, when they attended programs with the highest environmental rating scale compared with the lowest rating scale.

We then aggregated individual quality indicators according to generic and state QRIS scoring rubrics, converted to overall composite ratings, and compared the relation among high- and low-rated programs on child outcomes (see the chart, right). Generic system composite ratings were not significant predictors of child outcomes. There were few associations of composite ratings to children's learning in the nine replicated state QRISs. The association among composite ratings and child outcomes were about half the size of that for the single indicator of teacher-child interactions.

There are important limitations of our approach. Most state QRISs are designed to be used for child care and early-learning programs serving children from birth through preschool ages and typically incorporate both public and private programs. The NCEDL-SWEEP studies only include public pre-K programs serving preschool-age children. We model the association between QRIS ratings and child outcomes by controlling for beginning-of-year scores that may reflect preexisting differences between children. This value-added approach has limitations that may lead to biased estimates (*12*, *13*). We do not show evidence of causal impacts of QRIS indicators and composites on children's learning.

Implications for QRISs

For QRISs to increase the likelihood of pre-K programs improving children's school readiness, programs that receive the highest composite ratings should improve children's skills more than programs that receive the lowest ratings. As presently designed and implemented, QRIS evaluation may not realize these aims. Although individual observational measures of quality, particularly teacher-child interactions, were related to children's learning, once multiple indicators were aggregated and converted to ratings, they failed to yield consistent relations to learning.

States should capitalize on the rich information they are collecting and consider new methods for analyzing and disseminating it. Given costs associated with collecting multiple indicators of quality, states may conserve resources and enhance the validity of QRIS ratings by focusing on indicators with demonstrable links to children's learning. To provide easily interpretable levels of quality to parents and communities, states often transform levels of measurements from continuous to ordinal scales. Some states already present information for each individual quality indicator, without aggregating multiple indicators to form one composite rating.

These findings may have implications for other education accountability efforts that attempt to translate ratings to the public but, in so doing, convert multiple assessments of performance that are only obliquely related to learning, which obscures possibly important effects of key indicators.

Observational measures of teacher-child interactions demonstrate promise for discerning meaningful levels of pre-K quality. Yet QRISs are not capitalizing on this empirical evidence. As QRISs become more commonplace and pre-K programs plan to expand enrollments, it is increasingly important that ratings link to children's learning to ensure that states incentivize and improve the aspects of quality that matter most.

References and Notes

1. W. S. Barnett, *Science* **333**, 975–978 (2011).
2. R. C. Pianta, W. S. Barnett, M. R. Burchinal, K. R. Thornburg, *Psychol. Sci.* **10**, 49–88 (2009).
3. W. T. Gormley Jr., D. Phillips, T. Gayer, *Science* **320**, 1723–1724 (2008).
4. J. Jacobson-Chernoff, K. Flanagan, C. McPhee, J. Park, *Preschool: First Findings From the Preschool Follow-up of the Early Childhood Longitudinal Study, Birth Cohort (ECLS-B)* (National Center for Education Statistics, U.S. Department of Education, Washington, DC, 2007).
5. K. Tout *et al.*, *The Child Care Quality Rating System Assessment: Compendium of Quality Rating Systems and Evaluations* (Office of Planning, Research & Evaluation, Administration for Children & Families, U.S. Department of Health and Human Services, Washington, DC, 2010).
6. G. Camilli *et al.*, *Teach. Coll. Rec.* **112**, 579–620 (2010).
7. G. Zellman, M. Perlman, M., V. Le, C. M. Setodji, *Assessing the Validity of the Qualistar Early Learning QRIS as a Tool for Improving Child-Care Quality* (RAND Corporation, Santa Monica, CA, 2008).
8. D. Early *et al.*, "Pre-kindergarten in eleven states: NCEDL's Multi-State Study of Prekindergarten and State-Wide Early Education Program Study" (Tech. Rep. Frank Porter Graham Child Development Institute, Chapel Hill, NC, 2005).
9. T. Harms, R. M. Clifford, D. Cryer, *The Early Childhood Environment Rating Scale: Revised Edition* (Teachers College Press, New York, 1998).
10. Because we were using a common data set to replicate individual QRISs, we were not able to include all quality indicators used by a state, and in the case of family partnership or staff qualifications, our measures often did not align exactly with states' measures (see SM). For this reason, we removed identifying names of each state in the right side of the figure.
11. R. C. Pianta, K. La Paro, B. K. Hamre, *Classroom Assessment Scoring System Manual: Pre-Kindergarten* (Brookes, Baltimore, MD, 2004).
12. S. W. Raudenbush, *J. Educ. Behav. Stat.* **29**, 121–129 (2004).
13. J. Rothstein, *Educ. Finance Policy* **4**, 537–571 (2009).

Acknowledgments: The authors are supported by Institute of Education Sciences, U.S. Department of Education, Grant R305A060021. R.C.P. is coauthor of tCLASS and cofounder and shareholder of Teachstone Training, LLC, a company focused on measuring and improving teacher-student interactions. The University of Virginia owns an equity share in Teachstone.

Supplementary Materials

www.sciencemag.org/cgi/content/full/341/6148/845/DC1

10.1126/science.1233517

Published by AAAS

CONSERVATION

A Critical Crossroad for BLM's Wild Horse Program

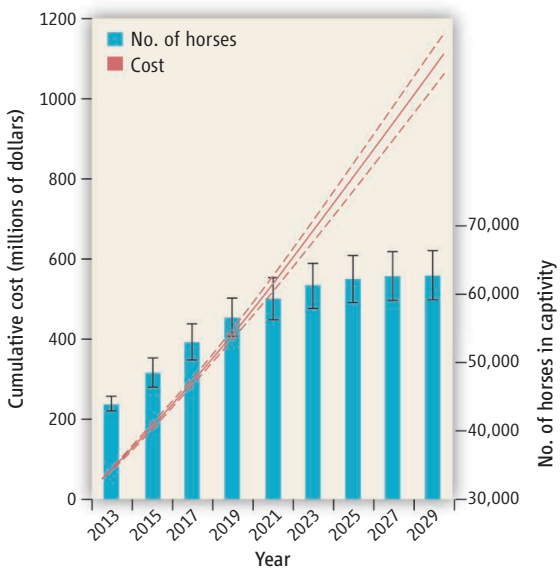
Captive wild horses will cost the United States over $1 billion by 2030 unless management approaches change

Robert A. Garrott, [1]* and Madan K. Oli[2]

Although horses evolved in North America, they went extinct 10 to 12 thousand years ago. Spanish conquistadors returned domestic horses to the continent in the mid-1500s, and since then, domestic horses have escaped captivity and also were purposefully released onto western rangelands where they thrive today. Most free-roaming horse populations are managed primarily by the Bureau of Land Management (BLM) of the U.S. Department of the Interior (*1*).

In 1971, the Wild Free-Roaming Horses and Burros Act (*2*) was passed, which establishes public ownership of free-roaming horses and instructs federal agencies to "protect and manage" horses as "an integral part of the natural system of the public lands." The act mandates that BLM and other federal agencies monitor horse numbers, determine appropriate population levels, and remove excess horses from public lands "to preserve and maintain a thriving natural ecological balance." However, at present, tens of thousands of horses are not living the life of "wild mustangs" as Congress intended in passing the Wild and Free-Roaming Horses and Burros Act; instead, they have reverted back to the status of captive, domestic livestock, and the cost of the captive horse program is increasingly unsustainable.

The BLM currently reports ~33,000 free-roaming horses in the western United States. The National Wild Horses and Burros (WHB) Program has 179 designated Herd Management Areas, with population objectives for each, and an aggregate maximum goal of 23,622 horses (*3*). Since its inception, the WHB Program has been embroiled in controversy over appropriate population goals, management activities, and the accuracy of its estimates of population size and growth rates (*4*–*7*). The BLM monitors numbers using aerial surveys and captures and removes horses from rangelands when horse numbers exceed target population size. As of 2012, BLM has removed >195,000 horses from public lands under this program (*3*). The act requires BLM to place removed horses into "private maintenance and care for which … an adoption demand exists," with unadoptable, old, and excess animals, beyond the adoption demand, either sold or "destroyed in the most humane manner possible" (*2*). The number of horses BLM removes from public lands routinely exceeds adoption demand (*8*). However, because of pressure from horse advocates, administrative directives and congressional appropriation bills prohibit killing healthy horses (*9*); therefore, BLM is left with large numbers of captive horses that must be maintained indefinitely.



Projections of U.S. captive wild horses and costs (with 95% confidence intervals). (see SM for more details).

These policies have led to a complex and costly system for maintaining captive horses. Horses removed from public lands are processed in short-term holding facilities similar to cattle feed lots and held for several months or more. Many mature females are pregnant when captured and foal in the facilities, which adds to the captive population. Most adult males are castrated. Horses can be adopted from the short-term holding facilities, and some are removed through deaths, sales, or release back onto public lands. Excess animals are eventually transferred to private pastures, primarily in the Midwest, that are contracted as long-term holding facilities. Although small numbers are sold, horses typically remain in these facilities until they die of natural causes. Currently, the ~45,000 horses in captivity exceeds the estimated 33,000 free-ranging horses on public rangelands (*3*).

In a recently released National Research Council (NRC) report (*7*), a committee of 14 scientists concluded that, left unmanaged, horse numbers on public lands would triple every 6 to 8 years until food and water became limited. Under these conditions, horses would be in poor health, reproduction would be suppressed, and deaths from starvation and dehydration would become common, with mass mortality events possible during periods of drought. High horse populations and limited resources would also degrade rangelands, which would affect all native species and public uses of these lands. Thus, although the NRC committee concluded that BLM must actively manage wild horse populations, it asserts that continuing "business as usual" will impede effective management of wild horses on public lands and recommends management changes to put the WHB Program on a more sustainable course (*7*).

Although the NRC report focused on scientific issues, a major impetus for changing the WHB Program is the escalating costs of maintaining increasing numbers of horses in captivity. The WHB Program budget grew from $19.8 million in 2000 (*10*) to $74.9 million in 2012 (*3*). More than 60% of the 2012 budget was used to maintain captive horses, 11% expended to capture and remove animals from public lands, and 10% for adoption programs (*3*). To inform the policy debate, we extend the implications of the NRC report to provide a projection of the captive horse population and associated costs if current policies and management approaches continue.

[1]Ecology Department, Fish and Wildlife Ecology and Management Program, Montana State University, Bozeman, MT 59717, USA. [2]Department of Wildlife Ecology and Conservation, University of Florida, Gainesville, FL 32611, USA.

*Corresponding author. rgarrott@montana.edu

Published by AAAS

The Consequences of Business as Usual

We used records of the sex and age of 165,459 horses removed from public lands and placed in captive facilities between 1990 and 2011 to develop demographic projections and associated costs (see the chart) [see supplementary materials (SM) for details]. We made two basic assumptions. First, we projected the life span of 33,946 unadoptable horses currently in long-term holding facilities. Under this scenario, BLM will accrue 366,846 horse-years of maintenance costs over a 30-year period before all animals currently in captivity die. Given that $45.9 million was budgeted to maintain 42,835 horses in captivity during 2011 (*10*), annual per-horse maintenance costs would be ~$1074. Thus, the 30-year cost of maintaining horses currently in long-term holding facilities would be ~$394 million ($449 million with 2% annual inflation).

Second, we assumed the current management program would continue, with a mean of 9412 horses in short-term holding facilities and 3803 horses transferred annually to long-term holding facilities. Expenses would be ~$1.1 billion between 2013 and 2030, and annual costs thereafter would be $67 million. Although some citizens may support such expenditures, these projections reinforce assertions (*7*, *8*) that BLM's current approach to managing horse numbers is not sustainable.

A Way Forward

More than 30 years of research on contraceptive agents for feral horses have resulted in the development of effective vaccines that prevent pregnancy in both captive and free-ranging mares for 1 to 3 years (*7*). Experimental application of these vaccines has contributed to the control of a small horse population on an Atlantic Coast barrier island, and limited experiments on western horse herds have also produced encouraging results. The Environmental Protection Agency recently sanctioned two contraceptive vaccines, which enables their routine use for horse population management on western rangelands (*7*). The average life-expectancy of horses entering long-term holding facilities is about 15 years (see SM). Therefore, every horse that does not enter long-term holding facilities would save, because of contraceptive application, $16,110 in maintenance cost (or savings of $1 million for every 62 horses), not considering the modest costs of contraceptive application.

Uncertainties exist when attempting to deliver vaccines to large numbers of horses. Although concerns have been raised regarding behavioral, physiological, and demographic consequences of contraceptive vaccines, none of these concerns preclude their use for managing rapidly increasing populations (*7*). The level of reduction in population growth that can be realistically attained for western horse herds through application of contraceptive vaccines remains unclear. Large-scale management experiments, perhaps within an adaptive management framework, would help address some of this uncertainty (*11*).

We estimate that the typical 15 to 20% annual population increase of western horse herds (*7*) could be halved by means of contraceptive vaccines. If a gather-and-removal effort reduced the western horse population to the BLM's goal of 23,622 horses and aggressive contraception treatment was initiated, then BLM need only remove 2000 to 3000 horses annually to maintain its goal. The number of horses annually removed would then more closely match adoption demand and that would minimize or eliminate the need for long-term maintenance of unadopted animals.

Although broad-scale use of contraceptives can help reduce the number of horses that BLM must remove to control populations, it is not a panacea. Current contraceptive vaccines are most effective when hand-injected, and remote delivery of vaccines via dart is impractical for most free-ranging horse populations (*7*). Accordingly, vaccine delivery will require continuing, and perhaps increasing, the frequency of horse captures. It may also take a decade of experiment and refinement of treatment regimens and contraceptive methods to scale-up management to include the entire population of horses on western rangelands. Furthermore, most populations already exceed management objectives, and population modeling efforts indicate that current contraceptives can only reduce, not stabilize or reverse, population growth. Thus, even with the changes suggested by the NRC report, BLM must continue removing horses from public lands for the foreseeable future.

It is up to society to decide how they want their government to manage wild horses, how many wild horses should be accommodated on public lands, what should be done with excess horses, and how much they are willing to spend. The debate has gone on for many decades; however, we are at a critical juncture. BLM recently announced that because of funding constraints and lack of additional capacity for maintaining captive animals, it will substantially reduce scheduled removals of horses from public lands this year. This decision has been made despite worsening drought conditions that are causing severe shortages of forage and water for horses, wildlife, and livestock (*12*). Terminating or reducing active management will lead to a rapid increase in the number of horses, further exacerbating resource limitations.

The current situation in Australia provides a sobering view of what might be in store for western rangelands in the United States if the current management dilemma is not resolved. The wild horse population in Australia is estimated to exceed 400,000 animals (*13*), and severe drought conditions in central Australia have reportedly forced government agencies to propose shooting 10,000 horses from helicopters to reduce animal suffering and environmental degradation (*14*). One can only hope that there is the political will to change current policy and place BLM's WHB Program on a more sustainable trajectory.

References and Notes

1. BLM, www.blm.gov/wo/st/en/prog/whbprogram/herd_management/HMA_and_HA_Maps.html.
2. Pub. L. No. 92-195, 85 Stat. 649 (1971) (codified as amended at 16 U.S.C. §§ 1331–1340).
3. BLM, www.blm.gov/wo/st/en/prog/whbprogram/history_and_facts/quick_facts.html.
4. NRC, *Wild and Free-Roaming Horses and Burros: Current Knowledge and Recommended Research* (National Academies Press, Washington, DC, 1980).
5. NRC, *Wild and Free-Roaming Horses and Burros: Final Report* (National Academies Press, Washington, DC, 1982).
6. NRC, *Wild Horse Populations: Field Studies in Genetics and Fertility* (National Academies Press, Washington, DC, 1991).
7. NRC, *Using Science to Improve the BLM Wild Horse and Burro Program: A Way Forward* (National Academies Press, Washington, DC, 2013).
8. U.S. General Accounting Office, *Effective Long-Term Options Needed to Manage Unadoptable Wild Horses* (GAO-09-77, GAO, Washington, DC, 2008).
9. GAO, *Rangeland Management: Improvements Needed in Federal Wild Horse Program* (RECD-90-110, GAO, Washington, DC, 1990).
10. BLM, *Caring for America's Wild Horses and Burros: Fundamental Reforms—An Overview* (BLM, Washington, DC, 2011); www.blm.gov/pgdata/etc/medialib/blm/wo/Communications_Directorate/public_affairs/news_release_attachments.Par.4000.File.dat/WHB_Fundamental_022411.pdf.
11. C. Walters, *Adaptive Management of Renewable Resources* (MacMillan, New York, 1986).
12. BLM, announcement; www.blm.gov/wo/st/en/info/newsroom/2013/july/nr_07_19_2013.html.
13. S. Csurhes, G. Paroz, A. Markula, *Pest Animal Risk Assessment: Feral Horse* Equus caballus (Queensland Primary Industries and Fisheries, Queensland, Australia, 2009); www.daff.qld.gov.au/__data/assets/pdf_file/0004/51961/IPA-Feral-Horses-Risk-Assessment.pdf.
14. Australian Associated Press, *The Australian*, 22 May 2013; www.theaustralian.com.au/news/breaking-news/wild-horses-to-be-culled-in-nt/story-fn3dxiwe-1226648548218.

Supplementary Materials

www.sciencemag.org/cgi/content/full/341/6148/847/DC1

10.1126/science.1240280

Published by AAAS

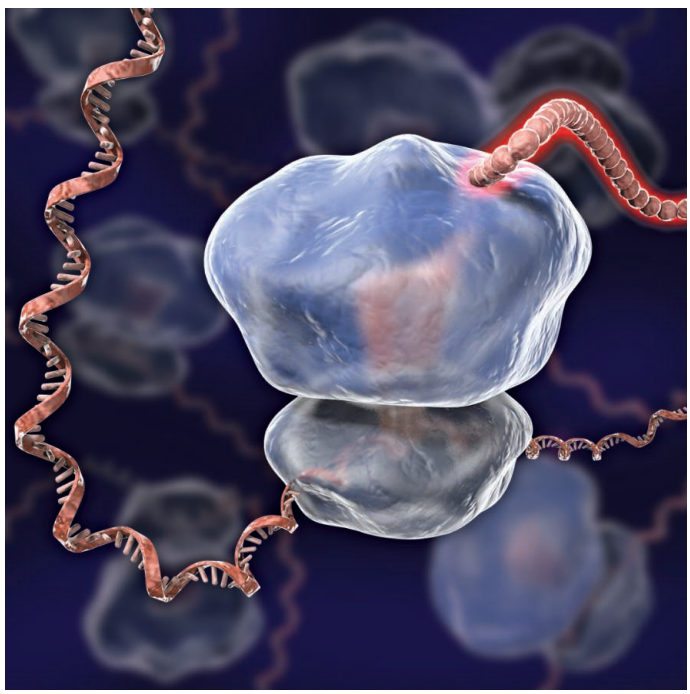
GENETICS

Mysterious Ribosomopathies

Ribosomes are essential in all cell types, yet mutations to ribosomal proteins or assembly factors cause tissue-specific disease.

Kathleen L. McCann[1] and Susan J. Baserga[1,2,3]

Ribosomes are absolutely essential for life, generating all cellular proteins required for growth. The prevailing thought for many years was that mutations in ribosomal proteins or ribosome assembly factors would be lethal to developing embryos. Complete loss of any single ribosomal protein often leads to embryonic lethality in mice (*1*). Yet, mutations in ribosomal proteins or ribosome assembly factors result in a puzzling phenomenon—a specific mutation can affect a specific cell type and cause a tissue-specific human disease. What accounts for this tissue proclivity has been a mystery. Why do defects in a macromolecule as ubiquitous and essential as the ribosome cause diseases—ribosomopathies—only in select tissues?



Monolith no longer. Mutations in ribosomal proteins or ribosome biogenesis factors have been found in patients with varying tissue-specific diseases.

Eukaryotic ribosomes are large, intricate cellular machines that translate messenger RNA (mRNA) into protein. They comprise four different ribosomal RNAs (rRNAs; 18*S* in the small subunit and 28*S*, 5.8*S*, and 5*S* in the large subunit), as well as ~80 ribosomal proteins (see the figure). More than 200 assembly factors and small RNAs are needed to synthesize ribosomes in the nucleolus. Some of the structural components also control the processing of precursor ribosomal RNA (pre-rRNA), assembly of the ribosomal subunits, and the translation process itself. Over the past 15 years, mutations in ribosomal proteins or ribosome biogenesis factors have been found in patients with varying diseases. At least 50% of patients with Diamond-Blackfan anemia carry mutations in ribosomal proteins (*2*). Other ribosomopathies identified include Treacher-Collins syndrome, North American Indian childhood cirrhosis, chromosome 5q- syndrome (*3*, *4*), and isolated congenital asplenia (*5*).

With the exception of 5q- syndrome, ribosomopathies are congenital, indicating that they impair development, but this impairment is not universal among all tissues or organs. For example, in isolated congenital asplenia, the most recently discovered ribosomopathy, haploinsufficiency (having only one functional copy of a gene, with the other copy inactivated by mutation) of the ribosomal protein RPSA prevents splenic development. These patients are prone to severe bacterial infections because they lack a spleen, but they are otherwise healthy and have no other observable developmental anomalies (*5*). This is surprising because RPSA is a component of the small subunit of the ribosome and is thus ubiquitously expressed. The mutation in RPSA is present in all tissues, not just the spleen, so one might expect haploinsufficiency of RPSA to affect development of all tissues, not just the spleen.

In the case of Diamond-Blackfan anemia, mutations in any of 11 different ribosomal proteins lead to bone marrow failure. The haploinsufficiencies can affect pre-rRNA processing and ribosome assembly, but not the same steps. In North American Indian childhood cirrhosis, a mutation in the ribosome biogenesis factor hUTP4/Cirhin causes biliary cirrhosis, for which the only treatment is liver transplantation required by early adolescence. Little is known about the molecular mechanisms that lead to this disease. Shwachman-Bodian-Diamond syndrome arises from mutations in the SBDS protein, which is involved in large ribosomal subunit maturation. Patients with this disorder suffer not only from dysfunction of the pancreas, but also from bone marrow failure, skeletal abnormalities, and an enlarged liver. Although there are some shared defects among many of the different ribosomopathies (e.g., bone marrow failure, skeletal abnormalities, growth retardation, and increased risk of cancer), these diseases are clinically distinct and require different therapeutic interventions.

One possible explanation for the conundrum of ribosomopathies is that the affected tissues are rapidly dividing and therefore are highly sensitive to mutations that might reduce the number of ribosomes. It is true that bone marrow cells need large numbers of ribosomes to make proteins, grow in size, and divide. However, this cannot be the full explanation, as all organ systems in a developing embryo are rapidly dividing and therefore require a large number of ribosomes.

An alternative explanation is that the composition of ribosomes may be different in different cell types, which could account for the various effects of ribosomal protein haploinsufficiency. This idea may contradict the notion that ribosomes are monolithic machines, but it is not completely unfounded. Surprisingly, the reduction of a specific ribosomal protein can lead to changes in the spectrum of translated mRNAs without affecting overall protein synthesis. For example, when the ribosomal protein L38

Online
sciencemag.org
Podcast interview with author Susan J. Baserga (http://scim.ag/ed_6148).

[1]Department of Genetics, Yale University School of Medicine, New Haven, CT 06520, USA. [2]Department of Molecular Biophysics and Biochemistry, Yale University School of Medicine, New Haven, CT 06520, USA. [3]Department of Therapeutic Radiology, Yale University School of Medicine, New Haven, CT 06520, USA. E-mail: susan.baserga@yale.edu

CREDIT: C. BICKEL/*SCIENCE*

Published by AAAS

(Rpl38) is depleted, a subset of mRNAs that encode homeobox genes are not translated during mouse embryogenesis (*6*). Likewise, reduction of Rpl40 impairs translation of vesicular stomatitis virus mRNAs in cultured human cells (*7*). Indeed, the amounts of mRNA that encode ribosomal proteins also vary among tissues in the developing mouse embryo (*6*). It is not clear whether these differences are reflected in the constituents of the functioning ribosome. If so, this raises the question of "specialized" ribosomes, and one must look closely for whether ribosome composition influences the pathogenesis of ribosomopathies.

Another possible explanation for tissue proclivity is that mutations in ribosomal proteins or assembly factors result in reduced numbers of fully functional cytoplasmic ribosomes. Although ribosome amounts would be adequate for survival, a smaller number of ribosomes could alter the mRNAs that are translated. This may, in turn, inhibit normal cellular growth and differentiation in specific cell types. In Diamond-Blackfan anemia, a mutation in Rpsl9 results in defects in the processing of the pre-18*S* rRNA, thereby reducing the amount of the small subunit that is assembled (*1*, *2*). Indeed, in mouse erythroblasts with reduced amounts of Rpsl9, translation of a subset of mRNAs is decreased (*8*). Other ribosomopathies with proposed nucleolar dysfunction, such as North American Indian childhood cirrhosis, may similarly result in reduced amounts of ribosomal subunits (*9*).

Additionally, in some cases, mutations that disrupt ribosome assembly can cause the nucleolar stress response in some cell types. This response involves increased synthesis of the protein p53. This tumor suppressor protein arrests cell division in response to such stress, which leads to programmed cell death (apoptosis) (*10*). In a mouse model for Treacher-Collins syndrome, craniofacial dysmorphology was rescued when p53 expression was reduced (*11*). Treacher-Collins syndrome often results from haploinsufficiency in *TCOF1*, the gene that encodes Treacle, a nucleolar protein involved in pre-rRNA synthesis. Similarly, in mouse (haploinsufficiency in Rpsl9) and zebrafish (haploinsufficiency in Rps29) models for Diamond-Blackfan anemia, p53 inactivation rescued some of the red cell lineage abnormalities (*12*). However, in a zebrafish model for Shwachman-Bodian-Diamond syndrome, loss of p53 did not rescue the associated exocrine pancreas developmental defects (*13*). Do some cell types more readily succumb to nucleolar stress? Activation of p53 may contribute to the tissue proclivity of some ribosomopathies, but perhaps not all.

Mutations in ribosomal proteins and assembly factors confer a broad clinical spectrum. Although the mechanisms underlying the tissue proclivity in ribosomopathies are yet to be defined, these disorders do make it increasingly clear that the days of thinking of ribosomes as unchanging monoliths are coming to an end.

References and Notes

1. K. A. McGowan *et al.*, *Nat. Genet.* **40**, 963 (2008).
2. D. M. Raiser, A. Narla, B. L. Ebert, *Leuk. Lymphoma* 1 (2013).
3. E. F. Freed, F. Bleichert, L. M. Dutca, S. J. Baserga, *Mol. Biosyst.* **6**, 481 (2010).
4. N. Burwick, A. Shimamura, J. M. Liu, *Semin. Hematol.* **48**, 136 (2011).
5. A. Bolze *et al.*, *Science* **340**, 976 (2013).
6. N. Kondrashov *et al.*, *Cell* **145**, 383 (2011).
7. A. S. Lee, R. Burdeinick-Kerr, S. P. J. Whelan, *Proc. Natl. Acad. Sci. U.S.A.* **110**, 324 (2013).
8. R. Horos *et al.*, *Blood* **119**, 262 (2012).
9. E. F. Freed, J. L. Prieto, K. L. McCann, B. McStay, S. J. Baserga, *PLoS Genet.* **8**, e1002892 (2012).
10. C. P. Rubbi, J. Milner, *EMBO J.* **22**, 6068 (2003).
11. N. C. Jones *et al.*, *Nat. Med.* **14**, 125 (2008).
12. J. Boultwood *et al.*, *Adv. Enzyme Regul.* **52**, 196 (2012).
13. E. Provost *et al.*, *Development* **139**, 3232 (2012).

Acknowledgments: Supported by NIH GM 52581.

10.1126/science.1244156

GEOPHYSICS

Megacity Megaquakes—Two Near Misses

Seismicity patterns after large earthquakes suggest that the earthquake hazard can rise sharply in areas well beyond the mainshock rupture zone.

Ross S. Stein[1] and Shinji Toda[2]

Two recent earthquakes left their mark on Santiago de Chile and Tokyo, well beyond the rupture zones, raising questions about the future vulnerability of these and other cities that lie in seismically active regions. Though spared strong shaking, the megacities nevertheless lit up in small quakes, perhaps signaling an abrupt change in the condition for failure on the faults beneath the cities. To detect such changes in earthquake rate requires good seismic monitoring networks; to respond to such hazard increases with civic preparations requires good government.

When the moment magnitude M_w = 8.8 Maule earthquake struck the Chilean coast before dawn on 27 February 2010, its strong shaking and modest tsunami killed 550 people and led to the collapse of some large buildings. Chile's capital city Santiago lies 400 km from the high-slip portion of the rupture and 100 km beyond its edge. On the afternoon of 11 March 2011, the M_w = 9.0 Tohoku earthquake struck the coast of Japan, causing a massive tsunami that claimed most of the earthquake's 18,564 victims and wreaked great damage. Reminiscent of Santiago, Japan's capital city Tokyo lies 400 km from the high-slip portion of the rupture and 100 km beyond its edge. Because of this distance, both cities largely escaped the consequences of the quakes.

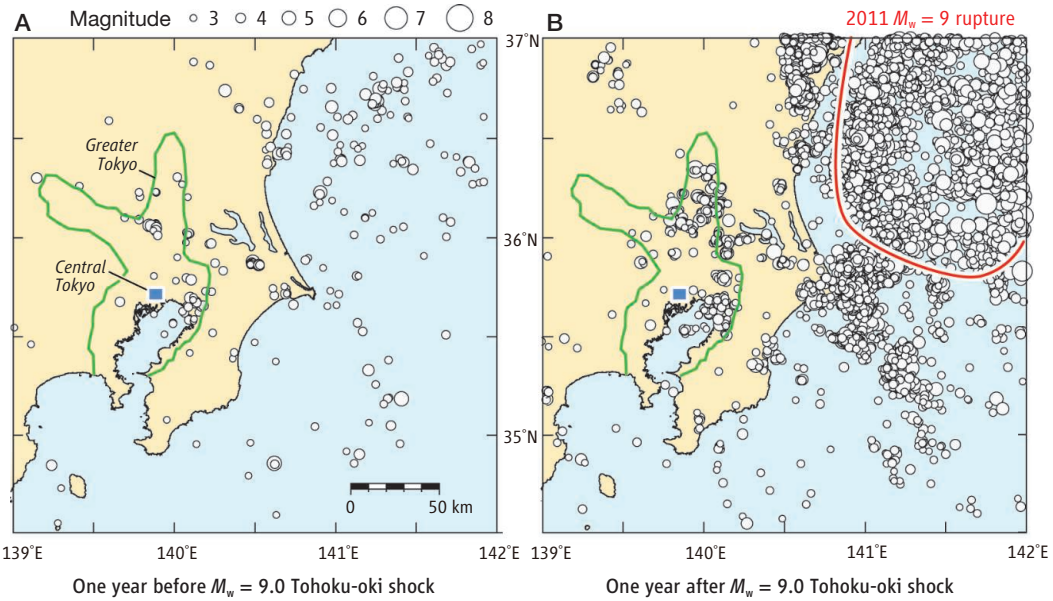
But it may not have been a clean getaway. Immediately after both megaquakes, the rate of small shocks beneath each city jumped by a factor of about 10. In Santiago, the quake rate remains twice as high today as it was before the Maule shock; at Tokyo it is three times as high (see the figure). What this higher rate of moderate ($M_w < 6$) quakes portends for the likelihood of large ones is difficult—but imperative—to answer, because Tokyo and Santiago are probably just the most striking recent cases of a common phenomenon: seismicity increases well beyond the rupture zone.

Tokyo and Santiago, both founded in about 1600, were all but destroyed twice by earthquakes, Santiago in 1647 and 1730, Tokyo in 1855 and 1923. Santiago's 6 million inhabitants constitute 38% of the Chil-

[1]U.S. Geological Survey, Menlo Park, CA 94025, USA. [2]IRIDeS, Tohoku University, Sendai, Japan. E-mail: rstein@usgs.gov; toda@irides.tohoku.ac.jp

Published by AAAS

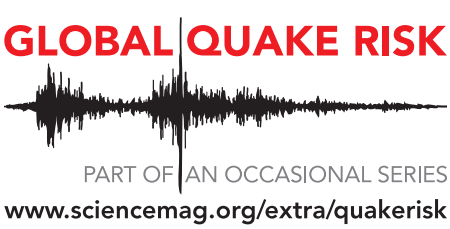
ean population; greater Tokyo's staggering 35.6 million inhabitants represent 28% of Japan's population. Fortunately, they are among the world's most earthquake-resilient cities, because they have regularly updated and strictly enforced construction codes. Nevertheless, the concentration of people, older buildings, wealth, and governmental functions renders the fate of these cities important not only for their nations, but for the world. Furthermore, other great cities within reach of megaquakes (M_w > 8), such as Vancouver, Taipei, Manila, Lima, and Jakarta, could suffer a similar fate; many are in developing nations that are far less well prepared for earthquakes (*1*).



Before and after. Seismicity 1 year before (**A**) and 1 year after (**B**) the 11 March 2011 M_w = 9.0 Tohoku-Oki, Japan, earthquake beyond the southwest edge of the rupture (*7*); shallower shocks are plotted atop deeper ones. The sharp jump in the rate of shocks beneath greater Tokyo was unexpected and continues today. In the figure, magnitude is the JMA magnitude (*12*).

Following a crustal mainshock of any size, the rate of quakes smaller than the mainshock jumps and then rapidly decays over years to decades; these are termed aftershocks. The rate increase commonly occurs up to a distance equal to the rupture dimension (so, aftershocks could lie 100 km from the end of a 100-km-long rupture). But the aftershocks can sometimes extend much farther. Aftershocks just one magnitude unit smaller than their mainshock are common, and there is a small probability that an aftershock will be larger than its mainshock (*2*). They can thus not be dismissed as harmless, particularly in light of the damaging M = 7.1 Düzce shock that struck 3 months after the M_w = 7.6 Izmit, Turkey, mainshock (17 August 1999), and the M_w = 6.3 Christchurch quake that struck 5 months after the M_w = 7.1 Darfield, New Zealand, earthquake (4 September 2010), each 20 km beyond the initial rupture. Several countries issue short-term aftershock forecasts in the months after large earthquakes. But despite promising experiments and proposals (*3*–*5*), aftershock hazard has yet to be incorporated into national seismic hazard assessments. A hazard assessment that includes aftershocks will make its debut in the new U.S. Geological Survey–California Geological Survey–Southern California Earthquake Center model for California later this year (*6*). This will be based on seismicity observations and stress transfer calculations.

So, are the Tokyo and Santiago earthquakes, 100 km from the fault rupture, aftershocks? The seismicity beneath Santiago is occurring on the adjacent unruptured section of the Chile-Peru trench megathrust; most earthquake scientists would thus deem them off-fault aftershocks. The shocks beneath Tokyo, however, illuminate a deeper, separate fault system. Calculations suggest that the stress imparted by the nearby megaquakes brought the faults beneath Santiago and Tokyo closer to failure, as well as those to the south of the Tohoku rupture, where seismicity also increased (*7*, *8*). Thus, they are aftershocks in the sense that they are contingent on the mainshock and undergo decay.



Aftershocks do not necessarily signal a heightened likelihood of large shocks. They could simply accompany postseismic creep, with the creep shedding the stress imposed by the megaquakes. The aftershocks beneath Santiago and Tokyo are too deep for Global Positioning System observations to reveal unequivocally whether the faults are locked or creeping. But one clue is that the ratio of small to large shocks was not changed by the megaquakes. Given that we are not seeing a heightened rate of small shocks alone, large shocks may now indeed be more probable than before the megaquakes by a factor of at least 2, calling for seismic monitoring and civic preparedness. It is encouraging that Tokyo is already the best-monitored site in the world, and that Chile has just installed a new seismic network.

This view of seismic hazard, predicated on the behavior of the abundant small shocks and guided by stress calculations, contrasts with national and insurance industry hazard assessments. Hazard assessments and models tend to assume that after a great quake, the probability of large shocks first plummets as earthquakes relieve accumulated tectonic stress on the ruptured fault and then gradually rises as tectonic loading restresses the fault over centuries to millennia. This time-dependent hazard has proven difficult to validate and remains the subject of debate (*9*, *10*). The difficulty perhaps arises because the postmainshock hazard drop is not uniform over the rupture surface; pockets of high stress remain that could nucleate the next large earthquake, and stress increases near the edge of rupture can trigger overlapping events.

A further limitation of global seismic hazard modeling is that countries often employ independent approaches based on their seismic history, data quality, and scientific strategies. Differences are found not just in regions far apart, but even between Canada and the United States. The Global Earthquake Model (GEM) (*11*) was founded in 2009 as a public-private partnership to overcome this problem. In 2014, it will launch an open, public model

CREDIT: ADAPTED FROM (7)

Published by AAAS

of global earthquake risk that includes not just the hazard, but its consequences in terms of lives and money saved and damage diminished when protective measures are taken. GEM is also producing OpenQuake, a hub for earthquake risk assessment that aims to give scientists in all countries access to a common modeling resource.

In the years ahead, we hope that GEM also tackles the time and space dependencies seen in Tokyo and Santiago and after many other earthquakes. More broadly, we need to understand whether such seismicity rate increases indeed signal a greater chance that a large earthquake will strike, because without this knowledge, governments will be reluctant to act.

References and Notes

1. T. L. Holzer, J. C. Savage, *Earthq. Spectra* **29**, 155 (2013).
2. P. M. Shearer, *J. Geophys. Res.* **117**, B06310 (2012).
3. D. A. Rhoades, M. C. Gerstenberger, *Bull. Seismol. Soc. Am.* **99**, 636 (2009).
4. T. H. Jordan *et al.*, *Ann. Geophys.* **54**, 320 (2011).
5. O. S. Boyd, *Bull. Seismol. Soc. Am.* **102**, 909 (2012).
6. E. H. Field, Aftershock statistics constitute the strongest evidence for elastic rebound in large earthquakes? Abstract S22B-08 presented at 2011 Fall Meeting, AGU, San Francisco, CA, 5 to 9 December; http://adsabs.harvard.edu/abs/2011AGUFM.S22B..08F.
7. S. Toda, R. S. Stein, *Geophys. Res. Lett.* **40**, 2562 (2013).
8. S. Lorito *et al.*, *Nat. Geosci.* **4**, 173 (2011).
9. Y. Y. Kagan, D. D. Jackson, *Geophys. J. Int.* **143**, 438 (2000).
10. K. R. Berryman *et al.*, *Science* **336**, 1690 (2012).
11. See www.globalquakemodel.org.
12. For local earthquakes, Japan uses the JMA magnitude (Mjma), which differs only slightly from M_w. JMA, Japan Meteorological Agency.

Acknowledgments: R.S.S. is chair of the Scientific Board of the GEM Foundation (a voluntary and uncompensated role).

10.1126/science.1238944

GEOCHEMISTRY

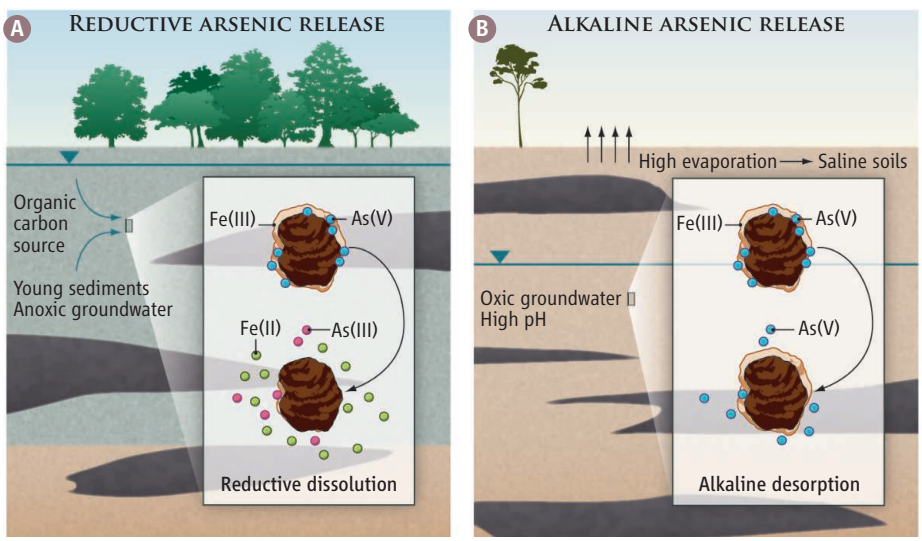
An Arsenic Forecast for China

A map of possible arsenic contamination in China's aquifers may guide mitigation efforts.

Holly A. Michael

About 140 million people worldwide drink groundwater containing unsafe levels of arsenic (*1*). Chronic exposure to this tasteless, odorless poison leads to health effects such as skin lesions and cancer. In China, pollution is pervasive and anthropogenic groundwater contamination has attracted attention (*2*). Naturally-occurring arsenic is perhaps less widespread, yet equally dangerous to those exposed. Though the problem has been known for decades (*3*) and mitigation is ongoing (*4*), estimates of the exposed population differ widely (*5*, *6*). On page 866 of this issue, Rodríguez-Lado *et al.* (*7*) assess the probability of the occurrence of unsafe arsenic levels in China's groundwater and identify at-risk areas where data are sparse. They suggest that more than 19 million Chinese may be drinking water above the World Health Organization guideline of 10 μg/liter. Such predictive models could guide action toward minimizing the impact of this widespread threat to human health.

More than two decades of research on groundwater arsenic that occurs naturally in aquifers has laid the foundation for predicting conditions in which arsenic concentrations are likely to be high. Two hydrogeologic settings that promote release of arsenic from sediments to the dissolved forms that contaminate and move with groundwater are shown in the figure. In reducing environments (panel A) under anoxic conditions, organic carbon drives chemical reactions that dissolve iron minerals on which arsenic is bound. This reductive dissolution often occurs in wet, flat regions and is the main mechanism producing high arsenic concentrations in the large river basins of South and Southeast Asia (*8*, *9*). Arsenic release also happens in oxic, high-pH waters that promote desorption of arsenic from mineral oxides (see the figure, panel B). This generally occurs in arid regions; for example, in Argentina, Spain, and the southwest United States (*1*). High arsenic concentrations resulting from both conditions occur in localized areas of China (*10*, *11*).



How arsenic is mobilized. Rodríguez-Lado *et al.* use land surface attributes such as geology, soil texture, salinity, river density, and slope to predict areas where reductive (**A**) or alkaline (**B**) arsenic release into groundwater may occur, producing a map of probability of arsenic concentration above 10 μg/liter over all of China.

Can arsenic-releasing environments be identified in areas where no testing has been done? Easily measurable characteristics of land surface that indicate conditions favoring release and build-up of high arsenic concentrations would be ideal predictors. However, identification of such proxies is challenging, because arsenic release is affected by complex, three-dimensional processes in the subsurface. Rodríguez-Lado *et al.* meet this challenge by first identifying land surface characteristics that can indicate arsenic release and then using statistical analysis to determine which proxies have predictive power for aquifers in China. A combination of eight factors explains much of the variability in known arsenic concentrations and could therefore be used as a reliable set of indicators to predict the probability of arsenic occurrence in areas without data.

CREDIT: P. HUEY/*SCIENCE*

Departments of Geological Sciences and of Civil and Environmental Engineering, University of Delaware, Newark, DE 19716, USA. E-mail: hmichael@udel.edu,

Published by AAAS

To estimate health risk, the authors combine the probability maps with population data. Although the estimated population affected may be high owing to mitigation efforts or model false positives, such estimates can be valuable tools for prioritizing action. In Bangladesh, where arsenic poisoning is perhaps most acute, a random survey to establish nationwide trends in arsenic concentration, completed in 2000 (*8*), provided a foundation for impact estimates and more targeted studies. China is 67 times the size of Bangladesh, with 9 times the population, but arsenic occurrence is likely much less pervasive. Nationwide monitoring activities are under way (*2*, *6*), but risk maps could guide more targeted screening. Risk maps may also prompt private well-testing initiatives (*12*) or public pressure for mitigation in affected areas.

Historically, arsenic in groundwater has tended to be detected only after diagnosis of health effects (*1*, *5*). In areas where such effects have not yet been identified, predictive models will enable action before the appearance of symptoms, which can require decades of chronic exposure to manifest. The ability to predict contamination of water with arsenic and potentially other poisons is also important where groundwater is not currently used for drinking and agriculture but may be used in the future. In Bangladesh (*13*), widespread installation of wells began in the 1970s to mitigate the problem of microbial contamination of surface water. Arsenic was not widely recognized as a natural groundwater contaminant, and its concentrations were not measured when wells were installed. Understanding of the conditions that threaten the quality of water sources can help to better predict, identify, and prevent threats in areas where little is known about groundwater quality.

Recognition of the extent of the problem is, however, only the first step toward relief of health impacts. Arsenic concentrations can vary widely on the scale of tens of meters. These small-scale patterns cannot be predicted from surface features that vary on the scale of kilometers. This variability is the result of a complex set of hydrological, geological, and biogeochemical factors that affect release of arsenic from sediments and the movement of dissolved arsenic through aquifers. Understanding this complexity, along with social and economic factors, is critical for identifying appropriate mitigation options. In Bangladesh, despite decades of hydrogeochemical investigations and screening of about half of the existing wells (*14*), tens of millions of people continue to be exposed (*15*), illustrating the challenges in moving from identification to mitigation.

Many arsenic-affected basins, deltas, and floodplains are among the most populated in the world; humans have fundamentally changed these landscapes and altered their hydrology. Understanding the anthropogenic factors that affect natural hydrological and biogeochemical processes will be critical in predicting where arsenic and other problems exist, determining how they will evolve in the future, and implementing effective mitigation strategies to improve the health and livelihood of millions of people worldwide.

References and Notes

1. P. Ravenscroft, H. Brammer, K. Richards, *Arsenic Pollution: A Global Synthesis* (Wiley, United Kingdom, 2009).
2. J. L. Li, *Nature* **499**, 14 (2013).
3. L. Wang, J. Huang, in *Arsenic in the Environment, Part II: Human Health and Ecosystems Effects*, J. O. Nriagu, Ed. (Wiley, New York, 1994), pp. 159–172.
4. G. Sun, Y. Xu, Q. Zheng, S. Xi, *Kaohsiung J. Med. Sci.* **27**, 377 (2011).
5. G. Yu, D. Sun, Y. Zheng, *Environ. Health Perspect.* **115**, 636 (2007).
6. Z. Lan, C. Changjie, *J. Hyg. Res* **26**, 310 (1997).
7. L. Rodriguez-Lado *et al.*, *Science* **341**, 866 (2013).
8. D. G. Kinniburgh, P. L. Smedley, Eds., *Arsenic Contamination of Ground Water in Bangladesh* (BGS Technical Report WC/00/19, British Geological Survey, Keyworth, UK, 2001), vol. 2.
9. S. Fendorf, H. A. Michael, A. van Geen, *Science* **328**, 1123 (2010).
10. J. He, L. Charlet, *J. Hydrol.* **492**, 79 (2013).
11. M. Currell, I. Cartwright, M. Raveggi, D. Han, *Appl. Geochem.* **26**, 540 (2011).
12. C. M. George, J. Inauen, S. M. Rahman, Y. Zheng, *Am. J. Trop. Med. Hyg.* **89**, 138 (2013).
13. B. K. Caldwell, J. C. Caldwell, S. N. Mitra, W. Smith, *Int. J. Popul. Geogr.* **9**, 23 (2003).
14. R. B. Johnston, M. H. Sarker, *J. Environ. Sci. Health A* **42**, 1889 (2007).
15. S. V. Flanagan, R. B. Johnston, Y. Zheng, *Bull. World Health Organ.* **90**, 839 (2012).

Acknowledgments: Helpful input from Y. Zheng, C. Harvey, and C. Voss greatly improved this Perspective.

10.1126/science.1242212

MEDICINE

Gene Therapy That Works

Gene therapy trials show a beneficial effect in children suffering from a neurodegenerative disorder or an immunodeficiency disease.

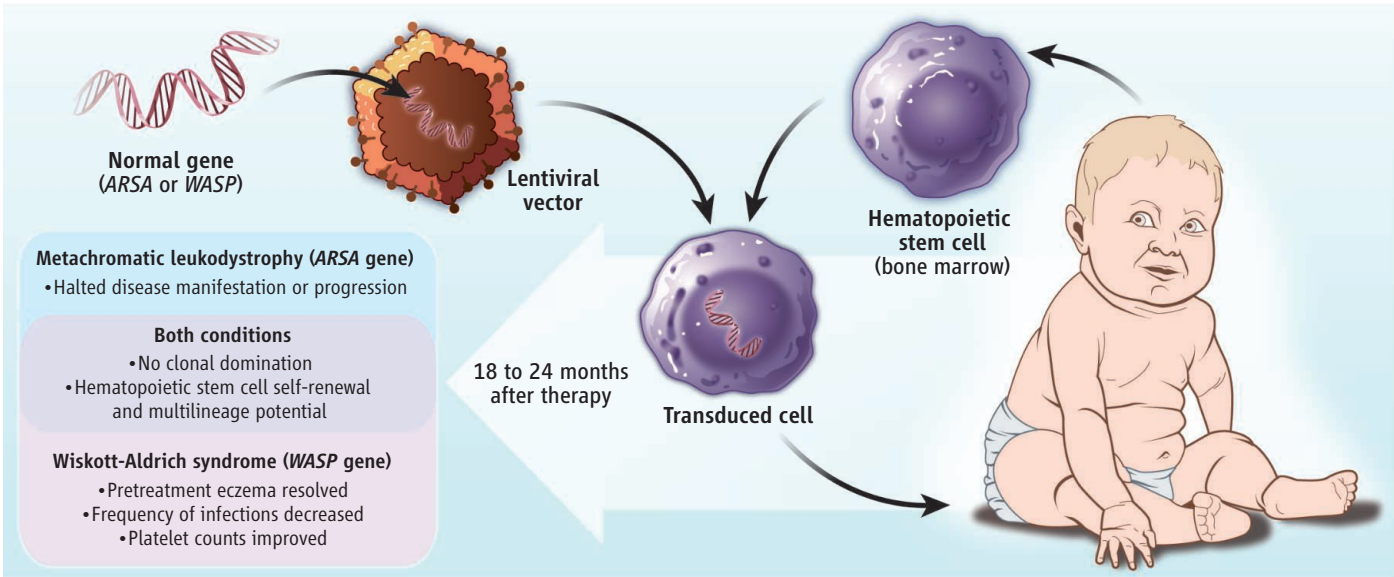
Inder M. Verma

The concept of gene therapy is disarmingly simple: Introduce a healthy gene in a patient and its product should alleviate the defect caused by a faulty gene or slow the progression of disease (*1*). Why then, over the past three decades, have there been so few clinical successes in treating patients with this approach? A major obstacle has been the delivery of genes to the appropriate cell, tissue, and organ. How does one introduce a gene into the brain with trillions of cells, or the liver with billions of cells, or the rare hematopoietic adult stem cell that has the potential to populate all lineages of lymphoid and myeloid cells? Much effort has been devoted to finding ways to efficiently deliver a therapeutic gene to the desired cell type, resulting in sustained production of the gene product, ideally through the entire life of the recipient, without unwanted side effects like genotoxicity or unsettling the immune balance (*2*). On pages 864 and 865 in this issue, Biffi *et al*. (*3*) and Aiuti *et al*. (*4*) report encouraging results using lentivirus-mediated gene therapy to treat children with rare genetic defects.

For scientists in the field of gene therapy, good news, tinged with occasional setbacks, has been trickling in over the past decade, starting with the successful clinical trials of children with X-linked severe combined immunodeficiency disease (SCID) (*5*). Currently, more than 1700 clinical trials are under way worldwide, drawing on a wide array of gene therapy approaches for both acquired and inherited diseases (*6*). The approach involves genetically engineering a virus so that it infects a target cell to deliver a gene, but does not cause disease. Retroviruses (such as lentiviruses) integrate their genetic material, including the new gene, in to the host cell genome. Such transduced host cells are transplanted back into the patient and proliferate with the correct gene, producing healthy cells (see the figure). Biffi *et al*. and Aiuti *et al*. provide new hope to children with metachromatic leu-

Laboratory of Genetics, The Salk Institute, La Jolla, CA 92037, USA. E-mail: verma@salk.edu

Published by AAAS



Clinical benefit. Children with the rare genetic diseases shown were treated with gene therapy. The approach delivered a normal gene, whose product halted or slowed gene progression up to 2 years after treatment.

kodystrophy (MLD) and Wiskott-Aldrich syndrome (WAS), respectively, both genetic defects that result in a deficiency of proteins essential for the early years of life and lack any effective treatments. MLD is an autosomal recessive lysosomal storage disease caused by mutations in the *ARSA* gene, leading to a deficiency of the enzyme arylsulfatase A, and hence the buildup of toxic sulfatide, causing widespread demyelination and neurodegeneration. Children with this disease appear healthy at birth, but gradually lose their cognitive and motor skills, with no possibility of arresting the neurodegenerative process. Children born with WAS, an X-linked primary immunodeficiency, lack WASP, a protein that regulates the cytoskeleton. Its loss leads to a faulty immune system that makes them vulnerable to the development of infections, autoimmune diseases, and cancer, as well as causing a defect in platelets that results in frequent bleeding. Bone marrow transplantations, when feasible, have proved to be a successful therapeutic approach for these two diseases (*7*). So, in 2010, clinical trials were initiated using lentiviral vectors to transfer functional *ARSA* and *WASP* genes in bone marrow–derived hematopoietic stem cells (expressing the marker $CD34^+$) from 16 patients, 6 of whom suffered from WAS and 10 from MLD. The studies of Biffi *et al*. and Aiuti *et al*. report results from three patients from each group, for whom sufficient time has passed since administration of the therapy to allow conclusions to be drawn regarding its safety and efficacy.

Biffi *et al*. found that in three presymptomatic children with late infantile MLD, treatment halted disease manifestation or progression for follow-up times ranging from 18 to 24 months, as compared to predicted disease onset in 7 to 21 months. Similarly, in three children with symptoms of WAS, Aiuti *et al*. showed that pretreatment eczema (chronic inflammation of the skin) resolved between 6 and 12 months; decreased, progressively, the frequency of infections; and improved platelet counts after gene therapy. In both clinical trials, no clonal domination was observed. Analysis of the vector insertion site in hematopoietic cells showed no preferential integrations in a particular gene locus, thus decreasing the likelihood of generating an abundance of abnormally proliferating cells. Increasing presence over time of $CD34^+$ progenitors and mature cells of myeloid and lymphoid lineages marked by identical integration sites of the delivered gene is strong evidence of self-renewal and multilineage potential of vector-transduced hematopoietic stem cells after engraftment. In this regard, the studies of Biffi *et al*. and Aiuti *et al*. are similar to those reported for two boys with X-linked adrenoleukodystrophy, a severe demyelinating disease caused by deficiency of an adenosine 5′-triphosphate transporter, where no clonal dominance was observed in lentiviral vector–transduced hematopoietic stem cells (*8*). In all three trials, partial bone marrow ablation of the patients was required to achieve maximum transplantation efficiency.

In the last 12 to 13 years, more than 50 patients affected by primary immunodeficiencies have been treated with genetically transduced autologous hematopoietic stem cells, mostly with gamma retroviral vectors (*9*). Most patients received clinical benefits, but occurrence of leukemia and myelodysplasia in some patients with SCID-X1, chronic granulomatous disease, and WAS have raised questions about their long-term safety. These adverse events have generally been ascribed to vector integration in the vicinity of specific proto-oncogenes, leading to their aberrant expression and resulting in neoplasias (*10*–*12*). The integration sites can be identified by deep sequencing of genomes, but because it is not possible to efficiently propagate clonal populations of hematopoietic stem cells, analysis can be performed only after transplantation. Although data from lentiviral-transduced hematopoietic stem cells in patients is limited, it appears not to favor any specific integration sites, though the appearance of a self-limiting dominant clone in the myeloid compartment of an individual with β(E)/β(0)-thalassemia whose hematopoietic stem cells were transduced with lentiviral vectors caused concern. In this clone, activation of the gene *HMGA2* (which encodes a transcriptional regulator) was caused by vector-mediated generation of a truncated transcript whose overexpression in mice is associated with the development of proliferative hematopoiesis and clonal expansion (*13*). Nevertheless, there was no clinical evidence supporting the existence of a preleukemic state or a substantial hematopoietic imbalance.

CREDIT: V. ALTOUNIAN/*SCIENCE*

Published by AAAS

Why are gamma retroviral vectors prone to increased genotoxicity? Perhaps the simplest explanation is that their genome contains long-terminal repeats, harboring intact promoter and enhancer sequences which, upon integration in the vicinity of a growth-promoting gene of the host cell, can enhance its transcription, leading to abnormal cell growth. Self-inactivating (SIN) gamma retroviral vectors are being tested in clinical trials for comparison with SIN-lentivectors in terms of their genotoxicity, efficiency of transduction, and sustained expression of the transgene. Another unknown is the conditioning regime and the precise state of the hematopoietic stem cells being transduced, which may differ from patient to patient.

With continued progress in gene therapy, scientists will likely take somatic cells from a patient, convert them into induced pluripotent stem cells, replace the defective gene "surgically" with the normal gene by homologous recombination, and differentiate them into hematopoietic stem cells, followed by conventional transplantation back into the patient. Alternatively, ways will be found to grow and proliferate hematopoietic stem cells, and bypass the need for generation of induced pluripotent stem cells. This is all good news for patients suffering from incurable genetic diseases.

References and Notes

1. I. M. Verma, N. Somia, *Nature* **389**, 239 (1997).
2. M. A. Kay, *Nat. Rev. Genet.* **12**, 316 (2011).
3. A. Biffi *et al*., *Science* **341**, 1233158 (2013); 10.1126/science.1233158.
4. A. Aiuti *et al*, *Science* **341**, 1233151 (2013); 10.1126/science.1233151.
5. M. Cavazzana-Calvo *et al*., *Science* **288**, 669 (2000).
6. T. Wirth, N. Parker, S. Ylä-Herttuala, *Gene* **525**, 162 (2013).
7. J. J. Boelens, *J. Inherit. Metab. Dis.* **29**, 413 (2006).
8. N. Cartier *et al*., *Science* **326**, 818 (2009).
9. A. Aiuti *et al*., *Science* **296**, 2410 (2002).
10. L. Biasco, C. Baricordi, A. Aiuti, *Mol. Ther.* **20**, 709 (2012).
11. S. Hacein-Bey-Abina *et al*., *J. Clin. Invest.* **118**, 3132 (2008).
12. S. Stein *et al*., *Nat. Med.* **16**, 198 (2010).
13. M. Cavazzana-Calvo *et al*., *Nature* **467**, 318 (2010).

Acknowledgments: I.M.V is an inventor of lentiviral vector technology that is owned by the Salk Institute and is entitled to receive royalties (U.S. Patent No. 6,013,516 with the Salk Institute).

10.1126/science.1242551

CHEMISTRY

Nucleation from Solution

Computer simulations of crystal nucleation provide evidence for two-step nucleation.

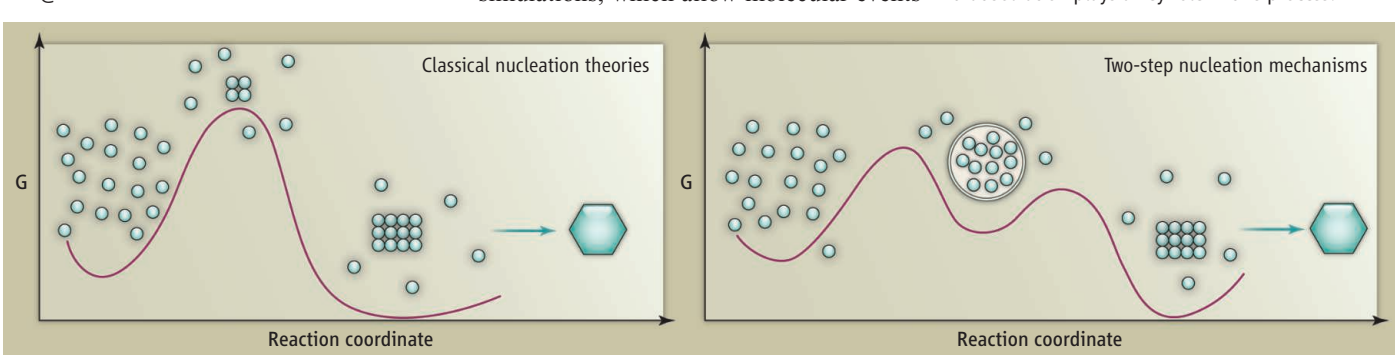
Allan S. Myerson and Bernhardt L. Trout

The formation of crystalline solids from solution is fundamental to many natural and industrial processes. Crystallization may even be the key to the formation of life itself (*1*). The crystallization process begins with nucleation, which plays a central role in determining the structure and size distribution of the crystals. In the past decade, experimental and molecular modeling studies of ionic materials such as calcium carbonate, proteins, and organic molecular crystals has suggested that nucleation of solids from solution does not proceed via the classical pathway but follows much more complex routes. These routes are generally referred to as two-step nucleation, but actually encompass a number of potential mechanisms (*2*–*4*). On page 885 of this issue, Wallace *et al*. (*5*) use molecular simulations to probe $CaCO_3$ nucleation. The results provide evidence for a dense liquid-liquid phase in which solvated $CaCO_3$ clusters come together during nucleation.

Calcium carbonate nucleation and crystallization have been studied intensively because of their importance in many biomineralization processes. Recent experimental studies (*6*) have provided evidence for stable $CaCO_3$ clusters with diameters as large as 2 nm. The authors suggest that these large clusters coalesce and then rearrange to form nuclei. Other experimental studies with cryotransmission electron microscopy and scanning electron microscopy have reported both stable amorphous $CaCO_3$ clusters and $CaCO_3$ as a dense liquid phase. In all cases, some type of amorphous or liquid like precursor is observed. It is difficult, however, to separate nucleation from the growth process in these experimental studies.

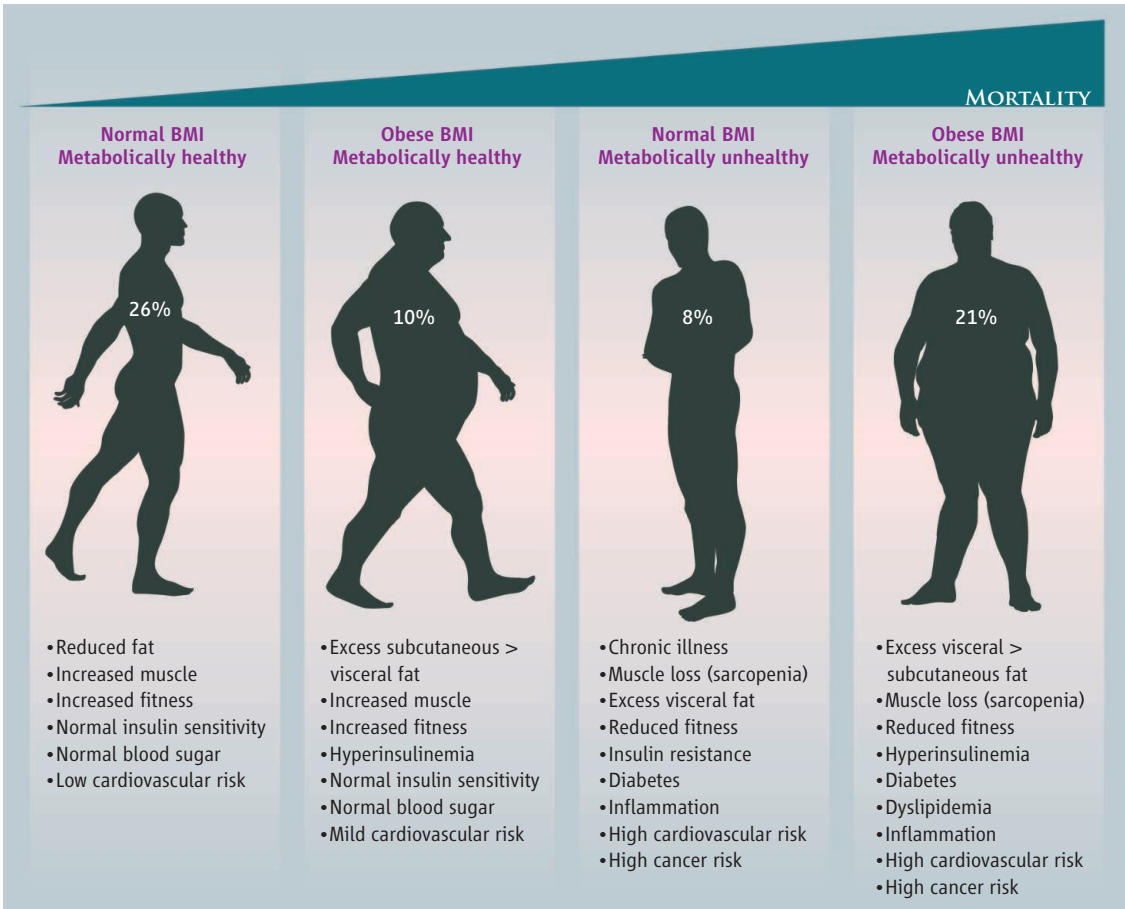
This difficulty is avoided in computer simulations, which allow molecular events to be analyzed in detail in a way that is currently unfeasible experimentally. In their molecular simulations of $CaCO_3$ nucleation, Wallace *et al*. provide evidence for a dense liquid-liquid phase in which solvated $CaCO_3$ clusters come together during the nucleation process (see the figure). There are two important points to note about this result. First, solvent effects may govern nucleation, yet are often ignored (*7*). Second, this and other simulation studies over the past decade indicate that liquid-like or amorphous precursors and even crystal-like configurations that differ from the final crystal are essential steps in the nucleation process (*8*–*10*).

Department of Chemical Engineering, Massachusetts Institute of Technology, 77 Massachusetts Avenue, E19-502, Cambridge MA 02130, USA. E-mail: myerson@mit.edu trout@mit.edu



How crystals nucleate. According to classical nucleation theory, nucleation proceeds as a one–step process (**left**). Recent experimental and computational studies have pointed to more complex mechanisms, referred to as two-step nucleation (**right**). Using computer simulations, Wallace *et al*. provide support for two-step nucleation and show that solvation plays a key role in this process.

Published by AAAS



Two faces of obesity and mortality? Obesity, defined by a high BMI, substantially increases the risk of developing diabetes, cardiovascular diseases, cancer, and other chronic diseases, leading to higher mortality. However, it has been estimated that about 10% of adults in the United States have obese BMI and are metabolically healthy, compared with 8% who have a normal BMI and are metabolically unhealthy. In contrast, 26% of adults have normal BMI and are healthy, whereas 21% have obese BMI and are unhealthy (*13*).

CREDIT: P. HUEY/*SCIENCE*

mal weight (defined as BMI 18.5 to <25), the combined grades 1, 2, 3 obesity, and grades 2 and 3 obesity, were associated with significantly higher all-cause mortality (*3*). In contrast, grade 1 obesity alone was not associated with higher mortality, and overweight was associated with significantly reduced mortality (*3*). These findings suggesting a protective influence of overweight and mild obesity have garnered a lot of publicity and controversy (*10*). There are concerns that the sampling methods used by Flegal *et al*. did not adequately adjust for weight loss and higher mortality from chronic illness, smoking, and aging (*10*). Furthermore, the classification of "normal weight" within a broad BMI range of 18.5 to 25 may have masked differences between people with BMI 18.5 to 22 and highest mortality, and those with BMI 22 to 25 and lowest mortality (*1*–*3*).

Nevertheless, recent studies have also challenged assumptions about the relationship between obesity and mortality in diabetes (*6*–*8*). Carnethon *et al*. analyzed the association of BMI and mortality in newly diagnosed diabetic patients in the United States (*6*). Deaths from all causes, cardiovascular, and other diseases were higher for normal BMI than for overweight or obese BMI. This inverse relationship between mortality and BMI was maintained even after adjusting the results for ethnicity, cardiovascular risk factors, waist circumference, and smoking (*6*). In another study involving 12 years follow-up of Taiwanese with type 2 diabetes, higher mortality was associated with older age, male gender, longer duration of diabetes, insulin therapy, hypertension, and smoking (*7*). Yet, a high BMI at the time of enrollment into the study was associated with fewer deaths compared with normal BMI (*7*). Furthermore, in a 15-year study of African-American and Caucasian male veterans with diabetes, BMI was inversely associated with mortality in both groups (*8*). Importantly, the mortality rate was lowered by increased physical activity independently of BMI and race (*8*).

Given the vast evidence of adverse effects of obesity on morbidity and mortality, how could overweight or obesity promote survival? Ultimately, this counterintuitive notion of health benefits of obesity requires careful examination of epidemiological data supported by mechanisms establishing causality. Although it is widely used, the BMI does not accurately measure fat content, reflect the proportions of muscle and fat, or account for sex and racial differences in fat content and distribution of intra-abdominal (visceral) and subcutaneous fat (*11*). Indeed, the body shape index (ABSI), a new index that quantifies abdominal adiposity relative to BMI and height is thought to be a better predictor of mortality than BMI (*11*). Excessive visceral fat in obesity predisposes to the "metabolic syndrome," associated with insulin resistance, diabetes, hyperlipidemia, and cardiovascular diseases (*12*) (see the figure). In contrast, massive fat storage in peripheral adipose tissue has been shown to be metabolically inert in certain mouse models (*12*). Likewise, it is possible that subcutaneous depots provide a safe harbor for potentially toxic lipids in obese individuals, thereby improving metabolic and cardiovascular health (*12*). The latter scenario may occur in some obese individuals with a healthy metabolic status, associated with a preponderance of subcutaneous fat, normal insulin sensitivity, absence of diabetes, and reduced risk of cardiovascular diseases (*13*). It is also possible that adipose tissue provides crucial energy reserves to meet metabolic demands during chronic illness, potentially decreasing mortality in obese patients. It must also be considered whether health care providers have increasingly adopted aggressive diagnostic and treatment strategies such as diet and exercise for obese diabetic patients, leading to better health outcomes and reduction in mortality.

How can a normal BMI be deleterious to health? Humans with genetic or acquired

Published by AAAS

defects that prevent fat storage in adipose tissue are thin and yet develop severe fatty liver, insulin resistance, and diabetes (*12*). Furthermore, it is estimated that about 24% of adults in the United States with normal BMI have unhealthy metabolic profiles, even in the absence of major intercurrent illness (*13*). This "metabolically unhealthy/normal BMI" phenotype manifested by hyperinsulinemia, insulin resistance, hyperlipidemia, and increased risk of cardiovascular diseases is of greater concern for Asians, who have increased body fat at normal BMI values and are highly susceptible to developing diabetes (*14*). A low BMI may mask poor nutritional status and fail to detect crucial differences in fat and skeletal muscle content. Because skeletal muscle accounts for the majority of glucose disposal, loss of skeletal muscle mass (sarcopenia) owing to aging or physical inactivity, despite a normal BMI, can impair insulin sensitivity and negatively affect cardiovascular health and mortality (*15*). Relative insulin deficiency or poor control of blood sugar in diabetes also lead to sarcopenia, visceral adiposity, oxidative stress, and inflammation. These, as well as other factors, may plausibly predispose to morbidity and mortality in individuals with apparently normal BMI.

Another limitation of the epidemiology leading to the obesity-diabetes-mortality paradox is that these studies are generally cross-sectional or longitudinal, without intervention. Since obesity is linked to diabetes, cardiovascular diseases, and other illnesses, weight loss remains a logical strategy for prevention and treatment. Recently, however, the Look AHEAD (Action For Health in Diabetes) study found that weight loss from an intensive diet and exercise program improved metabolic outcomes yet failed to reduce heart attack and stroke in participants with type 2 diabetes, possibly because the study was underpowered for cardiovascular outcomes (*16*). Furthermore, in the prospective pioglitazone clinical trial in macrovascular events (PROactive) study population, obese BMI patients treated with the antidiabetic drug pioglitazone, which induces weight gain, had a lower mortality compared to normal weight patients, and weight loss was associated with increased mortality and morbidity (*17*). Additional studies are needed to clarify the specific roles of weight intervention in normal versus obese BMI individuals who are metabolically normal or abnormal, and the optimal weight associated with reduced mortality in obese patients with diabetes and cardiovascular disease.

The optimal weight that is predictive of health status and mortality is likely to be dependent on age, sex, genetics, cardiometabolic fitness, pre-existing diseases, and other factors. To quote Galileo, "Measure what can be measured, and make measurable what cannot be measured." Clearly, there is an urgent need for accurate, practical, and affordable tools for assessing body composition, adipose hormones, myokines, cytokines, and other biomarkers to serve as predictive tools for phenotyping obesity and related metabolic disorders and assessing the risk of mortality. Advances in these areas will allow the examination of biological mechanisms and provide insights into the causal role of obesity in health and disease.

References and Notes

1. G. Whitlock *et al.* Prospective Studies Collaboration, *Lancet* **373**, 1083 (2009).
2. A. Berrington de Gonzalez *et al.*, *N. Engl. J. Med.* **363**, 2211 (2010).
3. K. M. Flegal, B. K. Kit, H. Orpana, B. I. Graubard, *JAMA* **309**, 71 (2013).
4. A. Oreopoulos *et al.*, *Am. Heart J.* **156**, 13 (2008).
5. A. Romero-Corral *et al.*, *Lancet* **368**, 666 (2006).
6. M. R. Carnethon *et al.*, *JAMA* **308**, 581 (2012) Erratum in: *J. Am. Med. Assoc.* 2012 308(20):2085.
7. C. H. Tseng, *Atherosclerosis* **226**, 186 (2013).
8. P. Kokkinos *et al.*, *Diabetes Care* **35**, 1021 (2012).
9. P. Boffetta *et al.*, *PLoS ONE* **6**, e19930 (2011).
10. V. Hughes, *Nature* **497**, 428 (2013).
11. N. Y. Krakauer, J. C. Krakauer, *PLoS ONE* **7**, e39504 (2012).
12. R. H. Unger, P. E. Scherer,. *Trends Endocrinol. Metab.* **21**, 345 (2010).
13. R. P. Wildman *et al.*, *Arch. Intern. Med.* **168**, 1617 (2008).
14. S. H. Lee *et al.*, *Clin. Endocrinol. (Oxf.)* **75**, 475 (2011).
15. M. Fogelholm, *Obes. Rev.* **11**, 202 (2010).
16. Look AHEAD Research Group, *N. Engl. J. Med.* **369**, 145 (2013).
17. W. Doehner *et al.*, *Int. J. Cardiol.* **162**, 20 (2012).

Acknowledgments: We thank A. H. Rubenstein for his helpful suggestions. R.S.A and M.A.L. are supported by National Institutes of Health grant P01-DK-049210.

10.1126/science.1241244

MATERIALS SCIENCE

Functional Ion Defects in Transition Metal Oxides

Dynamically tuning the concentration and profile of ions and vacancies in transition metal oxides provides a route to control of new functionalities.

Sergei V. Kalinin[1] and Nicola A. Spaldin[2]

Transition metal oxides exhibit an astonishing array of functionalities that result from a combination of the strongly polarizable metal-oxygen bond and the so-called strong correlations between the localized transition metal valence electrons. The polarizability of transition metal oxides causes a heightened sensitivity to external electric fields, which can be exploited in applications such as highly insulating dielectrics in microcapacitors. Strong electron correlations, which cause each valence electron to explicitly affect the response of all other valence electrons in the system, are believed to underlie exotic phenomena such as high-temperature superconductivity. The coexistence and cross-couplings between these functionalities (see the figure, panel A) enables materials properties that have led to the widespread use of oxides—for example, as piezoelectric transducers that convert mechanical energy to electrical energy—and may form the basis of new device paradigms, such as the control of magnetism with electric fields.

In addition to these intrinsic physical functionalities, ionic defects can play a crucial role in enabling or enhancing functionality in transition metal oxides. The importance of defects is familiar from semiconductor physics, where defects (usually in the form of atoms of different chemistry) transform chemically inert, covalently bonded semiconductors such as silicon and gallium arsenide into the efficient carriers of electronic charge on which the entire information age is based. In transition metal oxides, defects play perhaps an even more important role in that they can lead to entirely new properties. For example, the parent compounds of the high-temperature cuprate supercon-

[1]Center for Nanophase Materials Sciences, Oak Ridge National Laboratory, Oak Ridge, TN 37831, USA. [2]Materials Theory, ETH Zürich, 8093 Zürich, Switzerland. E-mail: sergei2@ornl.gov; nicola.spaldin@mat.ethz.ch

Published by AAAS

ductors are insulators, but the introduction of atomic point defects—either the removal of some ions (usually oxygen), or the substitution of some cations by others of different valence—is essential for the normal-state conductivity from which superconductivity emerges.

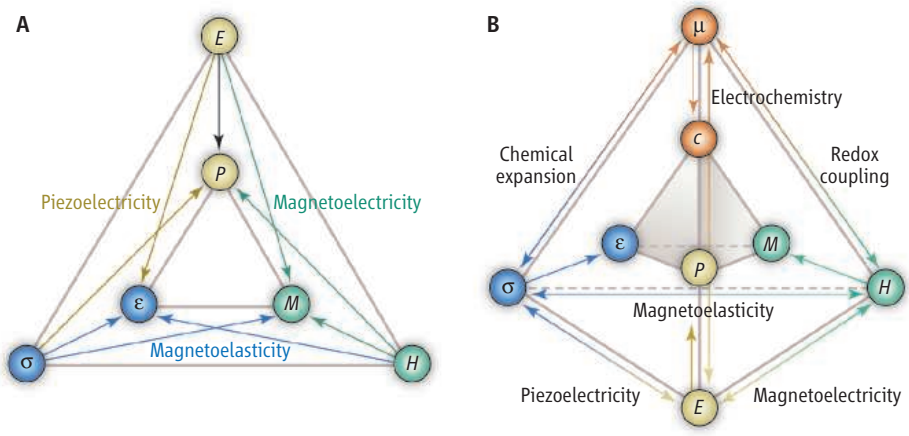
Often, very small changes in defect chemistry cause profound changes in function, for example, inducing magnetization from a nonmagnetic state or creating a transition between metallic and insulating states. Of particular interest, the defects—primarily the oxygen vacancies but also the cations—can move, both into and out of the sample as well as within it, causing, for example, metal-insulator transitions as a function of external oxygen pressure during electrochemical experiments (*1*). This sensitivity can be of tremendous physical interest, but also leads to difficulties in characterizing, reproducing, and understanding functional oxide behaviors, similar to those encountered in early studies of semiconductors (*2*).

Defect profiles in semiconductor devices are "static" states set during growth or synthesis by their concentration and chemical properties. In transition metal oxides, particularly in nanoscale systems, ion and vacancy diffusion lengths are comparable with system sizes at routinely accessible temperatures and electric fields (*3*). Ion migration is already exploited in the electrochemistry and electroceramics communities in applications such as solid-oxide fuel cells (*4*), lithium-ion batteries (*5*), and memristors (*6*). The concept we introduce here is the exploitation of the defect profile, captured in the chemical potential μ as a dynamical variable comparable to applied stress or magnetic or electric fields (see the figure, panel B).

Effects driven by such ionically active functionality, particularly those mediated by the dynamic oxygen vacancy behavior (*7*, *8*), are remarkably strong. For example, the introduction of oxygen vacancies by annealing in an oxygen-poor environment can induce strains between 1 and 10% (*9*); in contrast, conventional electric field–induced piezoelectric lattice strains are usually tenths of a percent. In turn, increases in volume greater than 1% can have drastic effects, such as inducing ferroelectricity in incipient ferroelectrics such as $SrTiO_3$, or changing magnetic orderings and susceptibilities by modifying the metal-oxygen-metal bond angles. Changes in cationic valence state associated with changes in oxygen vacancy concentration profoundly affect magnetic, electronic, and transport properties. Because oxygen vacancies are charged, ionic phenomena are strongly affected and can be controlled by electric fields. The role of the vacancy dynamics will likely prove particularly important at interfaces and surfaces, where mobilities are high and the redistribution of charged vacancies offers a route for screening electrostatic fields resulting from work function differences between materials or in response to applied electric fields.

There is also mounting evidence that oxygen vacancies, which have large atomic volumes relative to lattice oxygen, provide a channel for relieving tensile strain in oxides deposited on substrates with larger lattice constants (*10*, *11*). These findings suggest the possibility of forming heterostructures between materials with larger lattice mismatch than was previously considered feasible, although attempts to change bond lengths through coherent heteroepitaxy could be thwarted by this mechanism.

What are the prospects for ionically active functionality in transition metal oxides? Ongoing developments in electron microscopy and first-principles calculations will allow for increasingly accurate characterization and undoubtedly will reveal new phenomena. For example, recent work synergistically using both techniques points to oxygen vacancy ordering in strained thin films, suggesting in turn a route to engineering new kinds of periodicity in solids (*10*, *12*). Developments in synthesis, particularly thin-film growth, will allow greater control of dynamic ionic defect profiles. It may be possible to exploit the different mobilities of cations and anions to engineer gradients in static and dynamic chemistry and carrier concentrations (*13*). Mesoscopic scanning probe microscopy is opening a pathway for probing and manipulating vacancy dynamics locally (*14*), atomic-resolution scanning probe microscopes allow manipulation of vacancies with atomic precision (*15*), and x-ray techniques enable nanoscale patterning of device architectures (*16*). These capabilities for exploring and controlling ionically active functionality at an atomic level should help lay the basis for "ionotronic" technologies.



An extra functionality dimension from ionic activity. The usual control parameters for tuning the functionality of complex oxides—electric field *E*, which controls polarization *P*; magnetic field *H*, which controls magnetization *M*; and stress σ, which controls strain ε (**A**)—should be augmented (**B**) by the chemical potential μ to capture the functionalities driven by mobile ions and defects in these materials (as described by the concentration of mobile species, *c*).

PANEL A ADAPTED FROM (*17*); PANEL B ADAPTED FROM (*18*)

References and Notes

1. M. V. Patrakeev *et al.*, *J. Solid State Chem.* **172**, 219 (2003).
2. J. Gertner, *The Idea Factory: Bell Labs and the Great Age of American Innovation* (Penguin, New York, 2013).
3. T. Grande, J. R. Tolchard, S. M. Selbach, *Chem. Mater.* **24**, 338 (2012).
4. V. S. Bagotsky, *Fuel Cells: Problems and Solutions* (Wiley, Hoboken, NJ, 2009).
5. J. M. Tarascon, M. Armand, *Nature* **414**, 359 (2001).
6. R. Waser, R. Dittmann, G. Staikov, K. Szot, *Adv. Mater.* **21**, 2632 (2009).
7. H. T. Yi, T. Choi, S. G. Choi, Y. S. Oh, S. W. Cheong, *Adv. Mater.* **23**, 3403 (2011).
8. W. Jiang *et al.*, *J. Appl. Phys.* **110**, 034509 (2011).
9. X. Y. Chen, J. S. Yu, S. B. Adler, *Chem. Mater.* **17**, 4537 (2005).
10. U. Aschauer, R. Pfenninger, S. M. Selbach, T. Grande, N. A. Spaldin, http://arxiv.org/abs/1303.4749 (2013).
11. Y. M. Kim *et al.*, *Nat. Mater.* **11**, 888 (2012).
12. E. A. Eliseev *et al.*, *Phys. Rev. B* **86**, 085416 (2012).
13. M. Palcut, K. Wiik, T. Grande, *J. Phys. Chem. C* **111**, 813 (2007).
14. A. Kumar, F. Ciucci, A. N. Morozovska, S. V. Kalinin, S. Jesse, *Nat. Chem.* **3**, 707 (2011).
15. K. Fuchigami *et al.*, *Phys. Rev. Lett.* **102**, 066104 (2009).
16. N. Poccia *et al.*, *Nat. Mater.* **10**, 733 (2011).
17. N. A. Spaldin, M. Fiebig, *Science* **309**, 391 (2005).
18. S. Jesse *et al.*, *MRS Bull.* **37**, 651 (2012).

Acknowledgments: Supported by the Scientific User Facilities Division, U.S. Department of Energy (S.V.K.) and by ETH Zürich (N.A.S.). We thank A. Borisevich, S. Selbach, and T. Grande for valuable discussions.

10.1126/science.1243098

Tissue Interactions in Neural Crest Cell Development and Disease

Yoshiko Takahashi,[1,2]* Douglas Sipp,[3] Hideki Enomoto[3,4]*

The neural crest is a transient population of migratory cells in the embryo that gives rise to a wide variety of different cell types, including those of the peripheral nervous system. Dysfunction of neural crest cells (NCCs) is associated with multiple diseases, such as neuroblastoma and Hirschsprung disease. Recent studies have identified NCC behaviors during their migration and differentiation, with implications for their contributions to development and disease. Here, we describe how interactions between cells of the neural crest and lineages such as the vascular system, as well as those involving environmental signals and microbial pathogens, are critically important in determining the roles played by these cells.

The neural crest is a transient, migratory population of multipotent cells that emerges from the dorsal aspect of the neural tube during early vertebrate development and gives rise to a remarkable variety of differentiated cell types, including sensory, autonomic, and enteric ganglia in the peripheral nervous system; the adrenal medulla; melanocytes; and a range of skeletal, connective, adipose, and endocrine cells (*1*).

The capacity for long-range migration through the embryo is a second defining feature of neural crest cells (NCCs). The journey these cells take across the dynamic landscape of the developing embryo exposes them to myriad signals from surrounding tissue microenvironments, which vary by developmental site and stage. The paths of migrating NCCs are directed by molecular guidance cues mediated by the binding of external ligands with receptors on the NCC surface. The differentiation, morphology, and patterning of neural crest derivatives and the tissues with which they interact are also influenced by local tissue interactions.

Genetically determined cell-autonomous factors or exposure to environmental cues can result in inappropriate NCC differentiation, leading to ectopic tissue formation or an uncontrolled cell cycle. Defects in NCC function are associated with a number of serious diseases, many of which primarily affect pediatric patients. Thus, the great versatility and mobility of NCCs and their derivatives is a double-edged sword, capable of contributing to both normal embryogenesis and severe developmental pathologies (*2*).

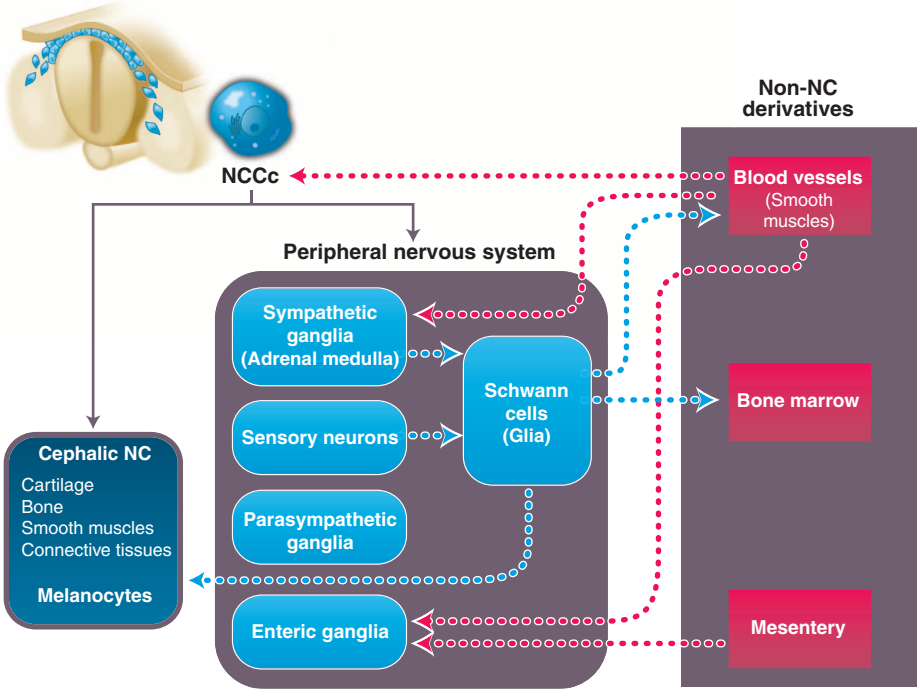


Fig. 1. Schematics showing interactions between neural crest– and non–neural crest derivatives. Neural crest–derived cells are presented in blue and light blue boxes. Cell-cell interactions are shown by dotted arrows (light blue and red).

Advanced genetics and imaging technologies have begun to lift the veil on the in vivo differentiation and migration of NCCs, revealing a number of unexpected behaviors of these cells and their derivatives in the development of the adrenal medulla, sympathetic and enteric ganglia, and glial Schwann cells throughout the peripheral nervous system, as well as in vascular remodeling and hematopoiesis (Fig. 1). In fulfilling their many roles, the cells of the neural crest work in close cooperation with other cells and tissues, and such interactions are now beginning to attract interest as potential targets in numerous diseases.

Tissue Interactions in the Sympathetic Lineage

Neuroblastoma is a solid tumor of the neuroendocrine system that frequently develops in the adrenal glands and sympathetic ganglia (*3*). Although a number of candidate mutations have been identified, the etiology of this cancer remains poorly understood. Its pathophysiology, however, is a caricature of the differentiation, growth, and migration of the emerging sympathetic lineage. Deciphering the development of the sympathetic nervous system and the closely associated adrenal medulla, and the regulatory roles of tissue interactions in this process, may thus contribute to our understanding of this neoplasm.

Neural crest–derived elements in the sympathetic lineage emerge early in development and travel considerable distances throughout the embryo. In addition to sympathetic ganglia, which are distributed along the anteroposterior axis, a defined region (corresponding to somites 18 to 24 in the chick embryo) gives rise to precursor cells capable of differentiation into the endocrine (chromaffin) cells of both the adrenal medulla and the sympathetic ganglia (*1*). Cell migration and differentiation in the sympathetic lineage have been extensively studied, but the great majority of reports have focused on in vitro differentiation or the restriction of migration pathways in vivo by repulsive signaling interactions, such as those established by Eph/ephrin, semaphorin/neuropilin, and Robo/Slit (*4*).

More recently, Saito *et al.* (*5*) examined how the migration and differentiation of cells in these lineages are regulated in vivo, showing how the

[1]Department of Zoology, Graduate School of Science, Kyoto University, Kitashirakawa, Sakyo-ku, Kyoto 606-8502, Japan. [2]Japan Science and Technology Agency (JST), Core Research for Evolutional Science and Technology (CREST), Japan. [3]Center for Developmental Biology, RIKEN, 2-2-3 Minatojima Minamimachi, Chuo-ku, Kobe 650-0047, Japan. [4]Department of Physiology and Cell Biology, Graduate School of Medicine, Kobe University, 7-5-1 Kusunoki-cho, Chuo-ku, Kobe 650-0017, Japan.

*Corresponding author. E-mail: yotayota@develop.zool.kyoto-u.ac.jp (Y.T.); enomotoh@med.kobe-u.ac.jp (H.E.); enomoto@cdb.riken.jp (H.E.)

Neurodevelopment
Part of an occasional series
www.sciencemag.org/extra/neurodev

dorsal aorta, which is the first blood vessel to form during embryogenesis, functions as a morphogenetic signaling center that coordinates NCC migration and lineage segregation (Fig. 2). In response to aortic bone morphogenetic protein (BMP) signals, precursor cells differentiate into separate sympathetic and adrenal medullary lineages, which subsequently occupy distinct regions of the embryo, with sympathetic ganglia remaining in the dorsal region and endocrine cells moving ventrally. These BMP factors not only induce chemotactic signals that attract the precursor cells to the aorta but also promote the segregation of their daughter-cell lineages and even lay down a chemical trail that leads the adrenal medullary cells to their destination. Each of these BMP functions plays out in a context-dependent manner, highlighting the importance of the in vivo environment to the fate determination and morphogenesis of NCCs.

The vascular system instructs sympathetic neural cell behavior later in development as well. The projection of certain sympathetic neurons follows patterns established by blood vessels and mediated by ligands, including artemin (*6*) and endothelin (*7*). Neurons from the superior cervical ganglia, for example, project along the external carotid artery. The smooth muscle cells (pericytes) that ensheathe this blood vessel express endothelin-converting enzyme, which converts inactive precursor molecules to the bioactive form of endothelin. Intriguingly, in the head region, these smooth muscle cells also derive from NCCs, illustrating how different neural crest lineages interact in complex ways to instruct the formation of complex multitissue systems.

Neural crest–derived cells can also influence the vasculature. Schwann cells are glial ensheathing cells that cover the entire length of every neuron in the peripheral nervous system (*8*). These neurons in turn project to every organ system, including the blood vessels, making Schwann cells the most widely distributed form of neural crest–derived cell in the body. In addition to their function in neural myelination, Schwann cells also play a role in vascular patterning. In the skin of embryonic mice at around day 15 of development, sensory neurons run parallel with arterial, but not venous, vessels during the period when the vascular network is forming. This nerve-artery association is mediated by the chemokine SDF1 (CXCL12) secreted by Schwann cells associated with sensory neurons (*9*).

In the adult body as well, Schwann cells can induce differentiation of cells outside the neural crest lineage. Yamazaki *et al*. (*10*) found that sympathetic nonmyelinating Schwann cells invade the bone marrow and serve as a component of the hematopoietic stem cell niche. An active form of transforming growth factor–β produced by these cells maintains these stem cells in a quiescent state. Future investigations should reveal how the balance between this Schwann cell–mediated dormancy and stem cell activation is regulated, particularly because it is known that the latter follows an oscillating circadian pattern, itself under the control of the sympathetic nervous system (*11*).

Interactive Migration in the Developing Enteric Nervous System

The enteric nervous system, which lines the entire gut and develops a wide range of independent functional capabilities, is also born from a migratory population of NCCs in the foregut. These enteric neural crest cells (ENCCs) colonize the full length of the intestine. Their migration has always been thought to closely track that of the gut wall, and when the process fails, resulting in Hirschsprung disease (aganglionosis of the gut), this absence of enteric neurons is usually observed in the distal intestine, as would be expected if ENCCs followed a purely linear course (*12*). In some rare and puzzling cases, however, patients exhibit "skip segments" in which partially innervated regions are found within otherwise aganglionic distal gut (*13*), seeming to defy the conventional model of Hirschsprung etiology in which NCCs simply fail to complete their journey down the intestinal trail (Fig. 3).

A recent time-lapse imaging study of ENCCs in mice may have found the answer to the riddle posed by these skip segments. Nishiyama *et al*. revealed that a subpopulation of these migrating cells traverses directly across the mesenteric boundary separating the mid- and hindgut at a 24-hour period during development when they are closely juxtaposed, rather than taking the long way around (*14*). This transmesenteric migration contributes considerably to the colonization of the distal intestine by ENCCs, and interference with this shortcut delays hindgut innervation. A mouse model of Hirschsprung disease displays decreased numbers of transmesenteric ENCCs, suggesting that impaired transmesenteric migration contributes to the etiology of this disease. Evidence suggests that migration across the mesentery relies on GDNF (the glial cell line–derived neurotropic factor) provided by hindgut mesenchyme and vascular-derived signals, showing the ability of ENCCs to sense environmental cues and adapt to changes in their migratory fields.

The hitherto enigmatic skip segments observed in certain forms of Hirschsprung disease may thus be explained as a consequence of a failure by the transmesenteric population of ENCCs to remerge with those that take the longer route along the gut wall, leaving gaps in the enteric innervation. Such interactions between NCCs (sympathetic ganglia, adrenal medullary cells, Schwann cells, and ENCCs) and those of other lineages (blood vessels, hematopoietic stem cells, and mesentery) play crucial roles in development and pathogenesis. Diseases of the peripheral nervous system may thus be caused not only by inherent defects in NCCs but also by aberrations in the interactions between these cells and their environments.

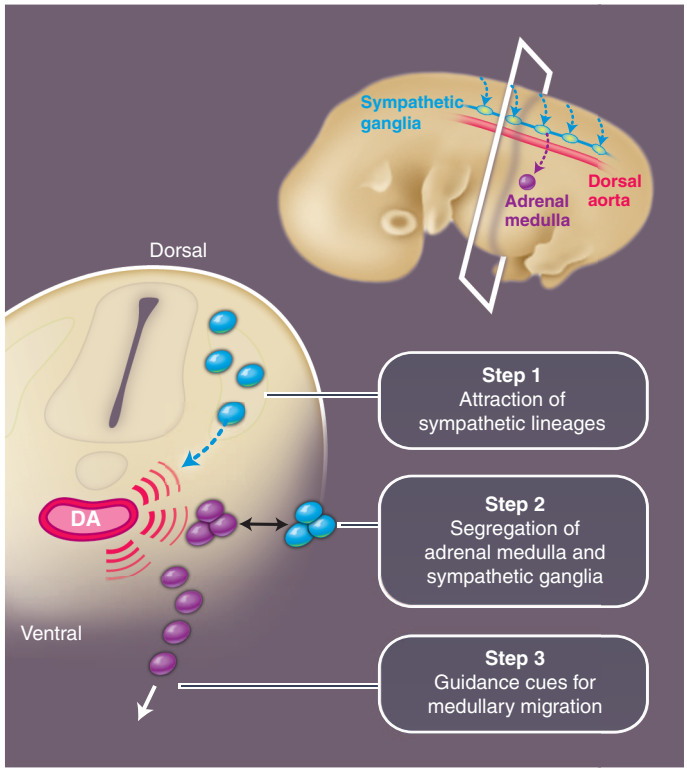


Fig. 2. The dorsal aorta acts as a morphogenetic center for sympathetic lineages. At the specific region (shown by the rectangle at the animal trunk) where common precursors of sympatho-adrenal lineages migrate, the dorsal aorta provides signals that attract early migrating cells (Step 1; transverse view in the scheme). Aortic signals also determine the segregation of adrenal medullary cells from sympathetic ganglia (Step 2). Finally, the dorsal aorta supports guidance molecule(s) for medullary cells to migrate ventrally.

Control and Dysregulation of Schwann Cell Plasticity

Neural crest–derived cells are remarkable not only for their migratory capabilities; recent evidence has shown that they are capable of considerable plasticity as well. During early neurodevelopment, Schwann cell precursors associate closely with projecting neurites, which they support through trophic interactions (*8*). Such interactions are also critical for subsequent Schwann cell differentiation and the maintenance of the mature cell state. In the adult, Schwann cells dedifferentiate in response to injury, reverting to the precursor state

to promote axon regeneration and remyelination (*8*) (Fig. 4).

It was recently shown that a subpopulation of Schwann cell precursors is also capable of giving rise to melanocytes in chick and mouse. If these cells lose contact with nerve cells during their migration, they autonomously acquire a melanocyte fate (*15*). The authors also showed that a similar conversion can happen in adult Schwann cells after injury. These new findings recall early work on the plasticity of neural crest–derived cells by Dupin and Le Douarin, who observed reciprocal conversion between glial cells and melanocytes (*16*, *17*) by dedifferentiation to an intermediate bipotential progenitor state. Clonal studies of multipotent neural crest–derived progenitors further revealed that the vast majority of bipotent progenitors in the neural crest lineage are able to differentiate into glia, irrespective of the identity of the other daughter cell (*18*, *19*), suggesting that the retention of glial identity may be linked to differentiative plasticity.

A number of in vivo studies have lent support to this notion. For example, many of the sensory neurons in the dorsal root ganglia derive from boundary cap cells (*20*), specialized glial cells found at border areas between the central and peripheral nervous systems. It has been found that hypoxia triggers reprogramming of glial cells in the carotid body to neurons (*21*), and chemical neurotoxicity in the enteric nervous system induces the transdifferentiation of enteric glia to neurons, a compensatory response to neuronal loss (*22*).

Glial plasticity has been shown to play a role in pathogenesis as well. In Hansen disease, more commonly known as leprosy, the pathogen *Mycobacterium leprae* initially infects Schwann cells and is secondarily incorporated into other cell types, such as macrophages and muscle, resulting in granuloma formation, sensory loss, and skin lesions. The mechanisms by which *M. leprae* disseminates after primary infection remained elusive until it was recently shown that Schwann cells dedifferentiate after infection, losing their glial identity and transforming into highly migratory "stem cell–like cells" that secrete soluble chemoattractants for macrophages and show the ability to differentiate into mesenchymal cells (*23*) (Fig. 4). Animal models of the disease have indicated that these reprogrammed stem cell–like cells and their mesenchymal progeny are responsible for the secondary distribution of the pathogen and for the formation of granulomas. The molecular mechanism behind this reprogramming remains unknown, but it appears that the bacterium

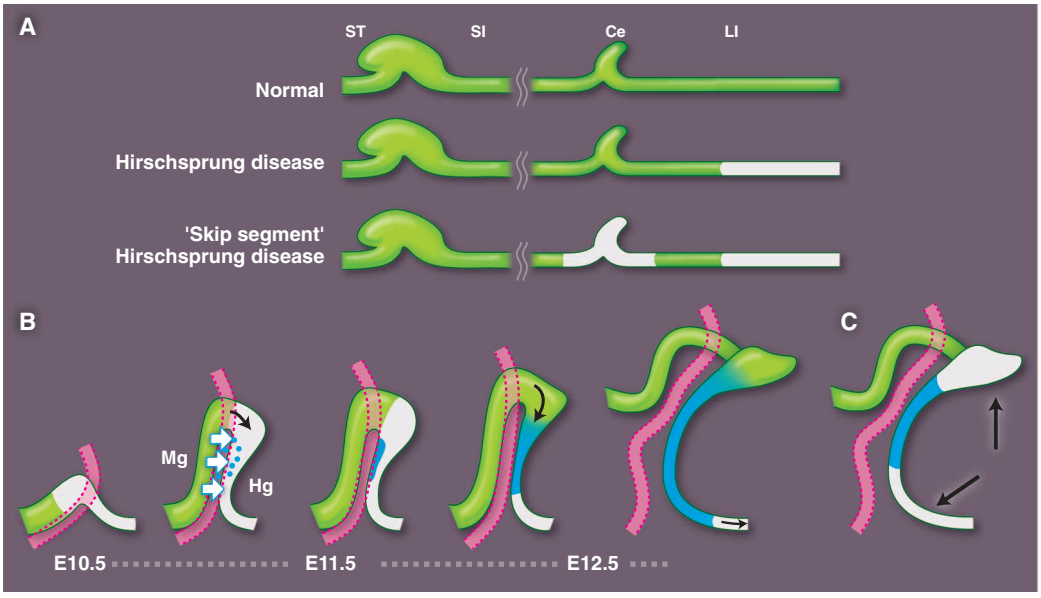


Fig. 3. Gut innervation and mode of ENCC migration. (**A**) Schematics of the gut showing ganglionized areas (green) in normal (top), Hirschsprung disease (middle), and its variant, skip segment (bottom). White regions (middle and bottom) indicate aganglionic segments. St, stomach; SI, small intestine; Ce, cecum; LI, large intestine. (**B**) Mode of hindgut colonization by ENCCs. During the period of midgut (Mg) and hindgut (Hg) looping, transmesenteric ENCCs (dark blue) shortcut (white arrow) by crossing the mesentery (magenta). Enteric nervous system progenitors migrating only within the gut wall are shown as green. (**C**) A hypothetical model for the skip segment. A defect in the merged area between transmesenteric (blue) and circumflex (green) ENCCs can cause two aganglionic segments (arrows).

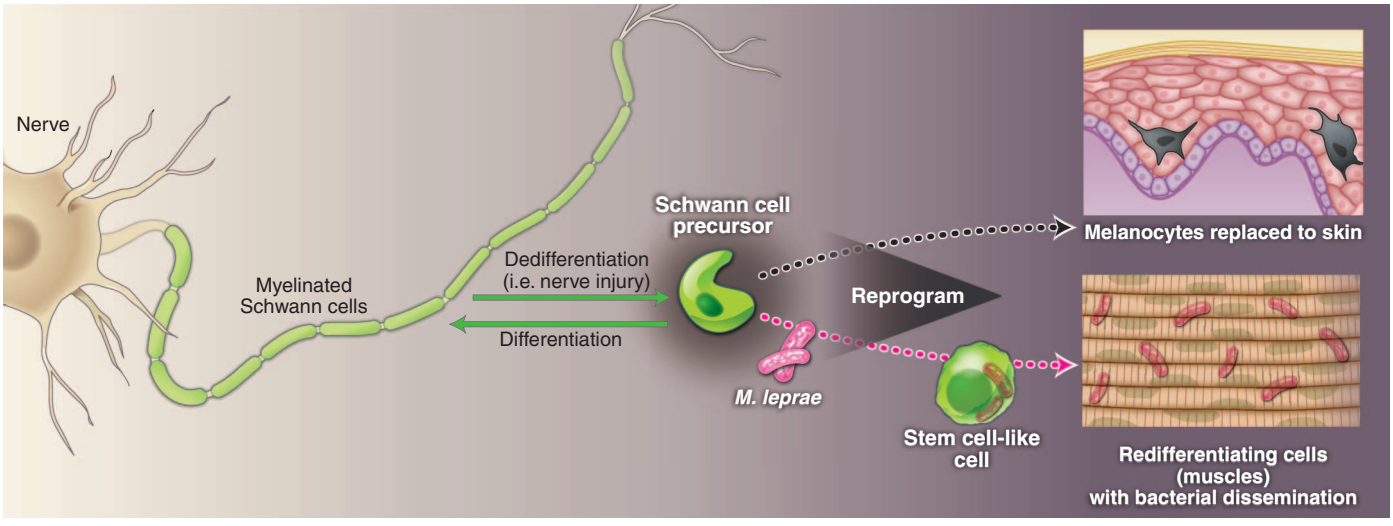


Fig. 4. Schwann cell plasticity during normal development and pathogenesis. Immature Schwann cells (Schwann cell precursors) either differentiating into or dedifferentiated from myelinated Schwann cells by nerve injury appear to be reprogrammed to take a melanocyte fate (black arrow). Upon *M. leprae* infection, Schwann cells are reprogrammed to stem cell–like cells (pink arrow), which is a critical step for disease dissemination.

exploits machinery specific to Schwann cells, which intrinsically show a high degree of cell fate plasticity.

As indicated from these studies, neural crest–derived glial cells possess a latent form of multipotency that is ordinarily suppressed by environmental cues, such as contact with neurons, but that can be activated in response to stimuli such as nerve injury and infection. Numerous forms of tissue stem cell–like cells have been identified in adult tissues, including skin, bone marrow, cornea, dental pulp, facial palate, and the nervous system (*24*–*26*), and several lines of evidence suggest that these cells, even those present in the same tissue, may have multiple distinct cellular origins (*27*, *28*). Given the widespread distribution and differentiative plasticity of Schwann cells, we may need to reexamine the possible contribution of reprogrammed Schwann cells to stem cell–like cell populations in various tissues.

Reprogrammed Schwann cells may serve as a cell source for neoplasms as well, although such cells may first lose their glial identity, as happens in the dissemination of *M. leprae*. Neuroblastoma may present a useful target for investigating this concept. At advanced stages, neuroblastoma may metastasize to the skin, something uncommon in other neoplasms, and in stage 4S neuroblastoma, small primary tumors and multiple metastases are found throughout the bone marrow, skin, and liver, despite which prognosis is generally favorable, because these tumors often spontaneously regress. Given what we now know about the biology of neural crest stem cells, these forms of neuroblastoma may be reconceptualized as a multifocal stem cell disease (*29*). Although the precise origin of tumor cells in these seemingly metastatic regions has yet to be identified, Schwann cells represent a highly plausible candidate. Indeed, one recent study showed that the forced expression of mutations associated with neuroblastoma susceptibility in mice causes differentiation of immature sympathetic ganglion progenitors to be biased toward the glial lineage (*30*).

Perspective

A number of diseases of the peripheral nervous system, particularly those prevalent in pediatric populations, appear to be caused by defects either in NCCs or in their complex interactions with non–neural crest tissue environments. A clearer picture of the properties and behaviors of neural crest–derived cells as they interact with their surroundings during physiological development may thus help inform our understanding of the etiology of such diseases and, perhaps, of pathologies in other lineages, such as those involving hematopoiesis or remodeling of the vasculature, as well. Fortunately, thanks to new techniques for genome-wide analysis and the direct visualization of cell migration in developing embryos, this picture is getting clearer all the time.

References and Notes

1. N. M. Le Douarin, C. Kalcheim, *The Neural Crest* (Cambridge Univ. Press, Cambridge, ed. 2, 1999).
2. H. C. Etchevers, J. Amiel, S. Lyonnet, *Adv. Exp. Med. Biol.* **589**, 213–234 (2006).
3. J. M. Maris, *N. Engl. J. Med.* **362**, 2202–2211 (2010).
4. E. Theveneau, R. Mayor, *Dev. Biol.* **366**, 34–54 (2012).
5. D. Saito, Y. Takase, H. Murai, Y. Takahashi, *Science* **336**, 1578–1581 (2012).
6. Y. Honma *et al.*, *Neuron* **35**, 267–282 (2002).
7. T. Makita, H. M. Sucov, C. E. Gariepy, M. Yanagisawa, D. D. Ginty, *Nature* **452**, 759–763 (2008).
8. K. R. Jessen, R. Mirsky, *Nat. Rev. Neurosci.* **6**, 671–682 (2005).
9. W. Li *et al.*, *Dev. Cell* **24**, 359–371 (2013).
10. S. Yamazaki *et al.*, *Cell* **147**, 1146–1158 (2011).
11. S. Méndez-Ferrer, A. Chow, M. Merad, P. S. Frenette, *Curr. Opin. Hematol.* **16**, 235–242 (2009).
12. T. A. Heanue, V. Pachnis, *Nat. Rev. Neurosci.* **8**, 466–479 (2007).
13. A. M. O'Donnell, P. Puri, *Pediatr. Surg. Int.* **26**, 1065–1069 (2010).
14. C. Nishiyama *et al.*, *Nat. Neurosci.* **15**, 1211–1218 (2012).
15. I. Adameyko *et al.*, *Cell* **139**, 366–379 (2009).
16. E. Dupin, C. Glavieux, P. Vaigot, N. M. Le Douarin, *Proc. Natl. Acad. Sci. U.S.A.* **97**, 7882–7887 (2000).
17. E. Dupin, C. Real, C. Glavieux-Pardanaud, P. Vaigot, N. M. Le Douarin, *Proc. Natl. Acad. Sci. U.S.A.* **100**, 5229–5233 (2003).
18. N. M. Le Douarin, E. Dupin, *Curr. Opin. Genet. Dev.* **13**, 529–536 (2003).
19. N. M. Le Douarin, E. Dupin, *Curr. Opin. Genet. Dev.* **22**, 381–389 (2012).
20. G. S. Maro *et al.*, *Nat. Neurosci.* **7**, 930–938 (2004).
21. R. Pardal, P. Ortega-Sáenz, R. Durán, J. López-Barneo, *Cell* **131**, 364–377 (2007).
22. C. Laranjeira *et al.*, *J. Clin. Invest.* **121**, 3412–3424 (2011).
23. T. Masaki *et al.*, *Cell* **152**, 51–67 (2013).
24. E. Dupin, L. Sommer, *Dev. Biol.* **366**, 83–95 (2012).
25. B. Kaltschmidt, C. Kaltschmidt, D. Widera, *Stem Cell Rev.* **8**, 658–671 (2012).
26. D. Widera *et al.*, *Stem Cells Dev.* **20**, 2053–2064 (2011).
27. K. J. Fernandes *et al.*, *Nat. Cell Biol.* **6**, 1082–1093 (2004).
28. C. E. Wong *et al.*, *J. Cell Biol.* **175**, 1005–1015 (2006).
29. M. M. van Noesel, *Lancet Oncol.* **13**, 229–230 (2012).
30. M. Nagashimada *et al.*, *J. Clin. Invest.* **122**, 3145–3158 (2012).

Acknowledgments: This work was supported by a Grant-in-Aid for Scientific Research on Innovative Areas from the Ministry of Education, Culture, Sports, Science and Technology of Japan.

10.1126/science.1230717

Lentiviral Hematopoietic Stem Cell Gene Therapy Benefits Metachromatic Leukodystrophy

Alessandra Biffi,* Eugenio Montini, Laura Lorioli, Martina Cesani, Francesca Fumagalli, Tiziana Plati, Cristina Baldoli, Sabata Martino, Andrea Calabria, Sabrina Canale, Fabrizio Benedicenti, Giuliana Vallanti, Luca Biasco, Simone Leo, Nabil Kabbara, Gianluigi Zanetti, William B. Rizzo, Nalini A. L. Mehta, Maria Pia Cicalese, Miriam Casiraghi, Jaap J. Boelens, Ubaldo Del Carro, David J. Dow, Manfred Schmidt, Andrea Assanelli, Victor Neduva, Clelia Di Serio, Elia Stupka, Jason Gardner, Christof von Kalle, Claudio Bordignon, Fabio Ciceri, Attilio Rovelli, Maria Grazia Roncarolo, Alessandro Aiuti, Maria Sessa, Luigi Naldini*

READ THE FULL ARTICLE ONLINE
http://dx.doi.org/10.1126/science.1233158

Cite this article as A. Biffi *et al.*, *Science* **341**, 1233158 (2013).
DOI: 10.1126/science.1233158

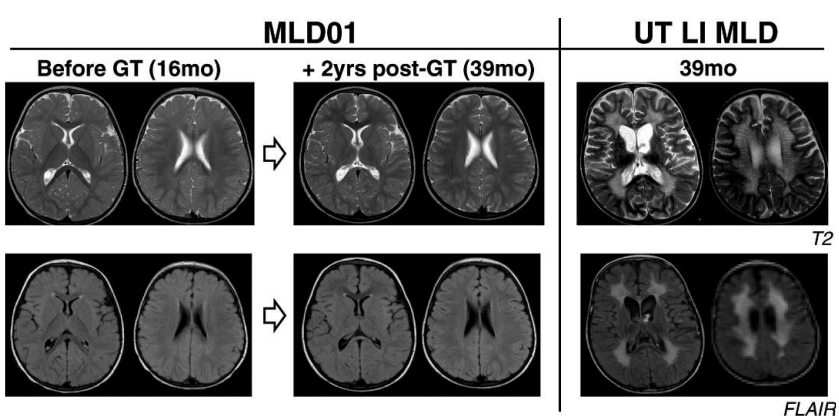
Introduction: Metachromatic leukodystrophy (MLD) is a neurodegenerative lysosomal storage disease caused by arylsulfatase A (ARSA) deficiency. The disease primarily affects children and invariably leads to premature death. In previous work with a mouse model of MLD, we used a lentiviral vector (LV) to introduce a functional *ARSA* gene into hematopoietic stem cells (HSCs) ex vivo and showed that reinfusion of the engineered HSCs prevented and corrected disease manifestations in the animals. To determine whether this gene therapy strategy is safe and can offer therapeutic benefit to patients with early-onset MLD, we designed a phase I/II trial.

Methods: We optimized LV manufacturing and HSC transduction in clinical grade conditions. Three children with ARSA deficiency and mutations associated with early-onset MLD were treated at the presymptomatic stage; all had at least one older sibling affected by the same disease variant. HSCs from the patients were transduced ex vivo with a LV carrying the *ARSA* gene.

Patients were treated with a myeloablative busulfan conditioning regimen before reinfusion of the engineered HSCs. Clinical and objective evaluations were collected up to 24 months after treatment. Molecular follow-up of vector integration site distribution was performed on hematopoietic cells derived from bone marrow and peripheral blood.

Results: There was high-level stable engraftment of the transduced HSCs in the bone marrow and peripheral blood of all patients at all times tested, with 45 to 80% of bone marrow–derived hematopoietic colonies harboring the vector. With these high gene marking levels, ARSA activity was reconstituted to above normal values in the hematopoietic lineages and in the cerebrospinal fluid. Analysis of >36,000 different LV integration sites showed that the high gene marking was sustained by highly polyclonal engraftment of transduced cells without evidence of aberrant clonal behavior. Several integration sites were shared among progenitors and mature myeloid, B- and T-cells sampled at long intervals after treatment, indicating efficient transduction and engraftment of HSCs. These findings were associated with a clear therapeutic benefit because the disease did not progress in any of the treated patients, even after the time of onset projected from sibling cases.

Discussion: Our gene therapy protocol allows stable engraftment of transduced HSCs at high levels and without evidence of vector-induced genotoxicity. The reconstitution of ARSA activity in the cerebrospinal fluid and the arrested progression of neurodegenerative disease in the three treated patients demonstrate that the transplanted cells, or their progeny, can seed the nervous system and deliver therapeutic levels of active enzyme. Although our data are promising, long-term follow-up of the patients is needed in order to establish the full therapeutic potential of this gene therapy strategy for MLD. In addition, our data position LV gene transfer as a feasible means to engineer human hematopoiesis to its near entirety—an approach that could be exploited for treatment of other diseases.



HSC gene therapy can prevent progression of metachromatic leukodystrophy. Magnetic resonance (MR) images of the brain of a patient (MLD01) before and after gene therapy. The brain of this patient appeared largely normal 2 years after treatment. In contrast, the brain of an untreated, age-matched late infantile MLD patient (UT LI MLD) showed severe demyelination associated with diffuse atrophy. (**Top**) Axial T2 weighted fast spin-echo MR images. (**Bottom**) Fluid-attenuated inversion recovery (FLAIR) MR images.

FIGURES IN THE FULL ARTICLE

Fig. 1. Gene marking in patients after HSC-GT.

Fig. 2. ARSA expression in patients after HSC-GT.

Fig. 3. Clinical follow up of MLD patients after HSC-GT.

Fig. 4. LV genomic integration profile.

Fig. 5. Common insertion site analysis.

Fig. 6. Stem cell marking and clonal dynamics.

SUPPLEMENTARY MATERIALS

www.sciencemag.org/cgi/content/full/science.1233158/DC1
Materials and Methods
Figs. S1 to S22
Tables S1 to S19
References

RELATED ITEMS IN *SCIENCE*

Aiuti *et al.*, Lentiviral hematopoietic stem cell gene therapy in patients with Wiskott-Aldrich syndrome. *Science* **341**, 1233151 (2013). doi:10.1126/science.1233151

I. Verma, Edging toward the promise of gene therapy. *Science* **341**, 853–855 (2013). doi:10.1126/science.1242551

The list of author affiliations is available in the full article online.
*Corresponding author. E-mail: biffi.alessandra@hsr.it (A.B.); naldini.luigi@hsr.it (L.N.)

Lentiviral Hematopoietic Stem Cell Gene Therapy Benefits Metachromatic Leukodystrophy

Alessandra Biffi,[1,2,3]*† Eugenio Montini,[1]* Laura Lorioli,[1,2,3,4] Martina Cesani,[1] Francesca Fumagalli,[2,4,5] Tiziana Plati,[1] Cristina Baldoli,[6] Sabata Martino,[7] Andrea Calabria,[1] Sabrina Canale,[2] Fabrizio Benedicenti,[1] Giuliana Vallanti,[8] Luca Biasco,[1] Simone Leo,[9] Nabil Kabbara,[10] Gianluigi Zanetti,[9] William B. Rizzo,[11] Nalini A. L. Mehta,[12] Maria Pia Cicalese,[2,3] Miriam Casiraghi,[2] Jaap J. Boelens,[13] Ubaldo Del Carro,[5] David J. Dow,[12] Manfred Schmidt,[14] Andrea Assanelli,[3,15] Victor Neduva,[12] Clelia Di Serio,[4] Elia Stupka,[16] Jason Gardner,[17] Christof von Kalle,[14] Claudio Bordignon,[4,8] Fabio Ciceri,[3,15] Attilio Rovelli,[18] Maria Grazia Roncarolo,[1,2,3,4] Alessandro Aiuti,[1,2,3,19] Maria Sessa,[2,5] Luigi Naldini[1,4]†

Metachromatic leukodystrophy (MLD) is an inherited lysosomal storage disease caused by arylsulfatase A (ARSA) deficiency. Patients with MLD exhibit progressive motor and cognitive impairment and die within a few years of symptom onset. We used a lentiviral vector to transfer a functional *ARSA* gene into hematopoietic stem cells (HSCs) from three presymptomatic patients who showed genetic, biochemical, and neurophysiological evidence of late infantile MLD. After reinfusion of the gene-corrected HSCs, the patients showed extensive and stable *ARSA* gene replacement, which led to high enzyme expression throughout hematopoietic lineages and in cerebrospinal fluid. Analyses of vector integrations revealed no evidence of aberrant clonal behavior. The disease did not manifest or progress in the three patients 7 to 21 months beyond the predicted age of symptom onset. These findings indicate that extensive genetic engineering of human hematopoiesis can be achieved with lentiviral vectors and that this approach may offer therapeutic benefit for MLD patients.

Metachromatic leukodystrophy (MLD) is an autosomal recessive lysosomal storage disease caused by mutations in the *ARSA* gene that result in a deficiency of the enzyme arylsulfatase A (*1*). ARSA deficiency causes accumulation of the enzyme substrate sulfatide in oligodendrocytes, microglia, and certain neurons of the central nervous system (CNS), and in Schwann cells and macrophages of the peripheral nervous system (PNS). This build-up of sulfatide leads to widespread demyelination and neurodegeneration, which is ultimately manifested in patients as severe progressive motor and cognitive impairment. MLD is classified into clinical variants according to the age of symptom onset. Patients with the late-infantile (LI) variant show symptoms within the second year of life, have the most severe manifestations of the disease, and die within a few years of symptom onset. Current treatments do not substantially delay the progression or fatal outcome of MLD (*2*, *3*).

Hematopoietic stem cell transplantation (HSCT) and HSC gene therapy (HSC-GT) have been investigated for the treatment of lysosomal storage diseases because enzyme-proficient hematopoietic progeny cells can migrate to the affected tissues, including the CNS, scavenge the stored material, such as sulfatide in MLD, and cross-correct the resident cells (*4*). The efficacy of these treatments varies among different types of lysosomal storage diseases (*3*, *5*–*7*) and with the extent of functional gene expression in the transplanted cells (*8*–*11*). Achieving a high level of functional gene replacement is particularly important in the setting of HSC-GT; to date, gene replacement in the hematopoietic cells of treated patients has been limited (*12*–*15*).

In a mouse model of MLD, we have demonstrated that disease manifestations can be prevented and corrected with lentiviral vector (LV)–based HSC-GT but not HSCT (*8*, *9*, *16*). This is consistent with the observation that HSCT fails to provide consistent benefits in MLD patients (*3*, *5*–*7*). LV-based HSC-GT induced extensive and supraphysiological expression of the functional *ARSA* gene throughout the HSC progeny, which in turn mediated widespread cross-correction of CNS and PNS resident cells (*8*, *9*).

Translating this strategy into a clinical protocol, however, posed several challenges, including gene transfer efficacy and safety. Although stable marking (10 to 15%) was reported in two patients with X-linked adrenoleukodystrophy (X-ALD) in the first trial of LV-mediated HSC-GT (*17*), it was not clear whether LVs could transduce human HSCs in clinically relevant settings with the efficiency required for application to MLD gene therapy. Vector safety is also a concern in light of the clinical experience with γ-retroviral vectors, which showed that genome-wide vector integration in hematopoietic stem/progenitor cells (HSPCs) has the potential to trigger leukemia through insertional mutagenesis (*14*, *18*). Although several studies have shown that LVs reduce the risk of genotoxic insertions because of their advanced design and the integration site selection typical of the parental HIV (*19*, *20*), it remained possible that increasing the total integration load in the infused HSPCs would offset the biosafety advantage.

In the present study, we optimized LV-mediated gene transfer into human HSCs for clinical translation and used this HSC-GT protocol to treat nine patients with early onset MLD in a phase I/II trial. Here, we report the outcome of the treatment in the first three treated patients at 24 months follow-up for patient MLD01 and 18 months follow-up for patients MLD02 and MLD03.

Results

Efficient ex Vivo Transfer of the ARSA *Gene into the HSPCs of MLD Patients*

Transduction of human bone marrow (BM)–derived $CD34^+$ cells was optimized to reach ≥2 vector copy number per genome (VCN) (fig. S1), based on the ARSA overexpression levels required for therapeutic efficacy in preclinical studies (*8*, *9*, *21*, *22*). $CD34^+$ cells were stimulated ex vivo with early acting cytokines in serum-free medium and transduced with purified third-generation LVs encoding the human ARSA cDNA under the control of the human phosphoglycerate kinase promoter (PGK) (fig. S2). VCN was measured in the progeny of the treated cells obtained by means of bulk liquid culture, colony-forming assays and repopulation of chimeric $Rag2^{-/-}$ $\gamma chain^{-/-}$ mice.

[1]San Raffaele Telethon Institute for Gene Therapy (TIGET), San Raffaele Scientific Institute, 20132 Milan, Italy. [2]TIGET Pediatric Clinical Research Unit, Division of Regenerative Medicine, Stem Cells and Gene Therapy, San Raffaele Scientific Institute, 20132 Milan, Italy. [3]Pediatric Immunohematology and Bone Marrow Transplant Unit, San Raffaele Scientific Institute, 20132 Milan, Italy. [4]Vita-Salute San Raffaele University, 20132 Milan, Italy. [5]Neurology Unit, Department of Neurology, San Raffaele Scientific Institute, 20132 Milan, Italy. [6]Neuroradiology Unit, Head and Neck Department, San Raffaele Scientific Institute, 20132 Milan, Italy. [7]Department of Experimental Medicine and Biochemical Sciences, University of Perugia, 06122 Perugia, Italy. [8]MolMed, 20132 Milan, Italy. [9]Distributed Computing Group, Center for Advanced Studies, Research and Development in Sardinia (CRS4), 09010 Pula, Italy. [10]Pediatric Hematology Oncology Division, Rafic Hariri University Hospital, Beirut, Lebanon. [11]Department of Pediatrics, University of Nebraska Medical Center, Omaha, NE 68198, USA. [12]Molecular and Cellular Technologies, GlaxoSmithKline, Stevenage 5G1 2NY, UK. [13]Pediatric Blood and Marrow Transplantation Program, University Medical Center 3584 CX Utrecht, Netherlands. [14]Department of Translational Oncology, National Center for Tumor Diseases and German Cancer Research Center, 69120 Heidelberg, Germany. [15]Hematology and Bone Marrow Transplant Unit, San Raffaele Scientific Institute, 20132 Milan, Italy. [16]Center for Translational Genomics and BioInformatics, San Raffaele Scientific Institute, 20132 Milan, Italy. [17]Regenerative Medicine Discovery Performance Unit, GlaxoSmithKline Research and Development, King of Prussia, PA 19406, USA. [18]Bone Marrow Transplant Unit, MBBM Foundation, Pediatric Department, Milano-Bicocca University at San Gerardo Hospital, 20052 Monza, Italy. [19]University of Rome Tor Vergata, 00133 Rome, Italy.

*These authors contributed equally to this work.
†Corresponding author. E-mail: biffi.alessandra@hsr.it (A.B.); naldini.luigi@hsr.it (L.N.)

A summary of the LV manufacturing process (flow chart, main steps, and yields) as well as the specifications set for testing the good manufacturing practice (GMP) lots released for this study are reported in fig. S3 and tables S1 and S2.

After optimizing the gene transfer procedures for human cells, we designed a clinical trial of HSC-GT in which autologous HSPCs from patients with MLD would be transduced ex vivo with ARSA-encoding LVs and then reinfused after the patients had been treated by a myeloablative regimen using the alkylating agent busulfan (fig. S4). Because MLD patients usually express residual, nonfunctional ARSA protein, they are unlikely to mount an immune response toward ARSA. Our trial design therefore did not include immunosuppressive agents.

Three presymptomatic MLD patients, biochemically characterized for ARSA deficiency and carrying mutations associated with LI MLD, were enrolled and treated; all patients had one or more older siblings with LI MLD onset within 2 years of age (table S3). At enrollment, patients were defined as presymptomatic based on the lack of obvious clinical signs of the disease, independent of the presence of abnormalities in instrumental tests [electroneurographic recordings (ENG) and/or brain magnetic resonance imaging (MRI)]. Treatment of the patients began 2 to 12 months before the reported age of onset of the disease in their affected matched siblings (*23*–*25*).

Twenty to 30 days after collection of an HSC back-up, a BM harvest was performed followed by isolation of $CD34^+$ cells by means of standard immunomagnetic procedures. Transduction of patients' $CD34^+$ cells was performed as described above. Cells were washed, resuspended, and kept at +4°C until successful completion of a first panel of fast quality control (QC) tests (table S4). The transduced $CD34^+$ cells were then released and infused fresh intravenously. Other relevant QC results (table S4) became available 2 to 5 weeks after infusion. VCN ranged from 2.5 to 4.4, transduction efficiency was 90 to 97%, and ARSA activity was reconstituted at ≥10-fold the level measured in healthy controls in the cultured progeny of the infused cells (fig. S1 and table S5).

A myeloablative, dose-adjusted busulfan regimen [target area under the curve (AUC) 4800 μg/L*hour] (table S5) was administered intravenously to the patients from day −4 up to day −1 before HSC-GT in a total of 14 doses, with the last busulfan dose administered ≥24 hours before transduced cell infusion. The conditioning regimen was well tolerated. The patients experienced severe neutropenia (absolute neutrophil count < 500/μl) from as early as day +9 up to day +45 after transplant at the latest (fig. S5 and table S5). No reduction or only a minor transient reduction of lymphocyte counts was observed in the absence of immunosuppressive/lymphotoxic drugs in the pretransplant conditioning (fig. S5). Patients required transfusional support up to day +45 after treatment for thrombocytopenia and anemia (fig. S5). Thereafter, the patients rapidly recovered hematological parameters matching the normal values for age. No abnormal expansion or clonal outgrowth was detected in the peripheral blood (PB) and BM by cell type composition, cytologic, karyotypic, or immunophenotypic studies (fig. S5). A mild (maximum National Cancer Institute/National Institutes of Health common toxicity criteria grade 2) transient increase in hepatocellular enzyme levels was detected within 2 to 3 weeks after treatment. Serious adverse events included two cases of central venous catheter–related infection, which promptly resolved upon antibiotic treatment. Replication competent LVs (RCLs), antibodies to HIV Gag p24, and antibodies to ARSA in patients' PB were negative at all times tested.

High-Level Engraftment of the Transduced HSPCs and Sustained ARSA Reconstitution

Beginning 1 month after transplant, we observed high-level stable engraftment of the transduced cells in the BM and PB of all patients at all times tested (Fig. 1A). Between 45 and 80% of the colonies outgrown from patients' BM in the colony-forming cell (CFC) assay harbored the LV genome (Fig. 1A). Quantitative polymerase chain reaction (PCR) on $CD34^+$ cells sorted from the patients' BM showed stable gene marking with VCN ranging from 0.9 to 1.9 up to the latest follow-up time (Fig. 1B). Considering the fraction of cells harboring the vector (estimated from the percentage of clonogenic progenitors outgrown from the patients' BM positive for LV DNA), these values imply a VCN of 2 to 4 in the engrafted transduced $CD34^+$ cells, which closely matches the data measured on the in vitro progeny of the infused cells. Correspondingly high and stable gene marking was observed in the circulating $CD15^+$ granulocytes and $CD14^+$ monocytes (Fig. 1C), and in myeloid cells and progenitors isolated from the BM (fig. S6), beginning with the first sampling and throughout the follow-up. A progressive increase in gene marking of lymphoid cells was observed—more rapid for B and NK cells and delayed for the longer-lived T cells—as expected from the choice of the conditioning regimen (Fig. 1C and fig. S6). The different repopulation kinetics of hematopoietic lineages by the transduced HSCs accounts for the progressive increase of the gene-marking level observed in total PB mononuclear cells (PBMCs) (Fig. 1D).

The high level of gene marking drove reconstitution of the defective ARSA activity up to above-normal values in the most therapeutically relevant myeloid populations (Fig. 2, A and B) as well as in other circulating cells (fig. S7, A and B). ARSA protein was isolated from patient hematopoietic cells as early as 1 month after treatment (fig. S7C) at above-normal expression levels in all tested samples (fig. S7D). The enzyme isolated from patient cells was found to hydrolyze the natural substrate sulfatide in vitro, confirming full functionality (0.003 mU of ARSA isolated from normal donor and treated patients' hematopoietic cells hydrolyzed 3.6 ± 1.2 nmol of substrate). In situ hybridization for LV mRNA and immunofluorescence for ARSA expression costained a high proportion of patients' blood cells consistently with the high VCN detected by means of quantitative PCR in these cells (fig. S8 and table S6). Func-

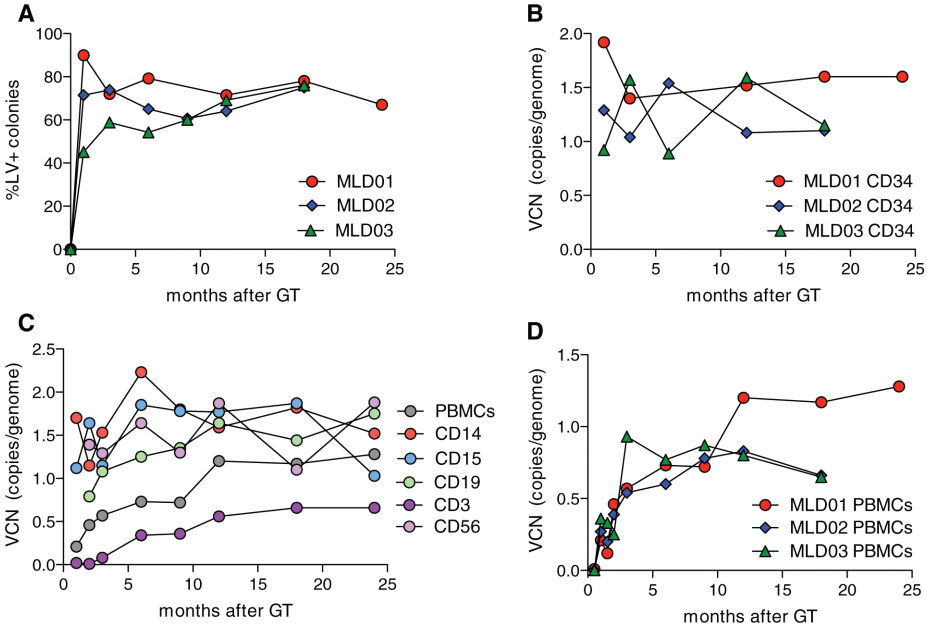


Fig. 1. Gene marking in patients after HSC-GT. (**A**) Engraftment of the transduced cells, evaluated with quantitative PCR on individual colonies from CFC assay performed on PB- and BM-derived cells and expressed as percentage (%) of LV^+ colonies on total tested colonies. (**B** to **D**) VCN expressed as copies of LV/human genome measured with quantitative PCR on BM-derived $CD34^+$ cells (B), individual subpopulations isolated from PB of patient MLD01 (C), and total PBMCs from patients MLD01, -02 and -03 (D).

tional ARSA was isolated from cerebrospinal fluid (CSF) collected from all three patients 1 year (and 2 years for MLD01) after HSC-GT at levels and activity comparable with those obtained from healthy donor samples, whereas no ARSA protein could be isolated from CSF before HSC-GT treatment (Fig. 2, C and D). These data demonstrate stable above-normal ARSA expression throughout the hematopoietic lineages and efficient delivery and bioavailability of the enzyme in the CNS after HSC-GT.

HSC-GT Provides Therapeutic Benefit to MLD Patients

Clinical observation and objective evaluations were collected up to 24 months after treatment for MLD01 and up to 18 months after treatment for MLD02 and MLD03. At the last follow-up, MLD01, MLD02, and MLD03 were 39, 30, and 25 months old, respectively (table S3). Because disease onset in the LI variant occurs invariably before 24 months of age and clinical manifestations are highly homogeneous, in particular among siblings (*23*, *24*), all three patients in our study were evaluated beyond their expected age of disease onset.

MLD01 is particularly informative because the follow-up time for this patient is longest and because the predicted time of symptom onset was earlier than that of the other two patients. This patient's two older siblings manifested regression of psychomotor performance and arrest of acquisition of new motor and cognitive skills at 18 months of age. Consistent with LI-MLD natural history (*26*), both siblings had rapid disease progression after onset and reached level 6 of the Gross Motor Function Scale for MLD (GMF-C MLD) (*27*) by 30 months of age, when they were wheelchair-bound and unable to support their head and trunk (table S7). In contrast, at 39 months of age MLD01 was able to stand independently and to walk and run with single aid (either the hand of another individual or an external walking device) (level 2 of the GMF-C MLD scale) (table S7). His Gross Motor Function Measure (GMFM) score progressively increased from enrollment (GMFM score of 164) up to a score of 193 at 39 months, which was substantially higher than all the scores recorded in our age-matched historical LI-MLD cohort [5.5 on average (*26*)], suggesting a continuous motor development (Fig. 3A and table S8). Cognitive evaluation by the Bayley Scale of Infant and Toddler Development revealed a normal composite IQ score for chronological age, with normal language and cognitive abilities (table S9) at all tested time points, including the last one at 39 months of age, an age at which the two affected siblings were incapable of any voluntary speech. The preexisting severe peripheral neuropathy of MLD01 [nerve conduction velocity (NCV) index (*26*) –11.5 at baseline] improved after treatment (NCV index –7.1 at last follow-up) (Fig. 3B). Brain MRI showed slight signal inhomogeneity, present since baseline evaluation and stable thereafter, and a small area of hyper-intensity in the corpus callosum that appeared at the 12-month follow-up and remained stable thereafter. All other brain MR findings were normal for age (Fig. 3C). In contrast, untreated LI-MLD patients invariably develop extensive and severe demyelination associated with diffuse atrophy by 24 to 36 months of age (Fig. 3C) (*26*, *28*). To our knowledge, no unequivocally diagnosed LI-MLD patient at the age of 39 months has been reported to display clinical features as positive as those we observed in MLD01.

Patients MLD02 and MLD03 remain fully asymptomatic, with normal motor and cognitive development for their ages (30 and 25 months, respectively); however, the clinical follow-up period for these patients after the predicted time of symptom onset was shorter than that for MLD01. At the latest clinical follow-up (18 months after treatment), MLD02 was 7 months beyond and MLD03 was 10 months beyond the predicted time of symptom onset. Both patients had a GMF-C MLD score of 0 at the last evaluation, which is in sharp contrast with the disease evolution documented in their affected siblings at the corresponding age (table S7). Their GMFM scores progressively increased after treatment, which is consistent with the acquisition of normal developmental motor milestones for age (Fig. 3A and table S8). Furthermore, in both patients the Bayley Scale of Infant and Toddler Development showed a normal composite IQ score for the age at all times tested (table S9). The ENG findings for both patients remained stable from baseline up to the latest follow-up; MLD02 showed near normal motor and sensory conduction velocities since baseline, whereas MLD03 showed a stable mild demyelinating neuropathy (Fig. 3B). Brain MRI revealed that both patients had a normal progression of white matter signal due to myelination up to the latest follow-up. MLD02 had small areas of T2 and fluid-attenuated inversion recovery (FLAIR) hyper-intensity signal in posterior and anterior periventricular white matter, present since baseline and stable up to the latest follow-up (fig. S9).

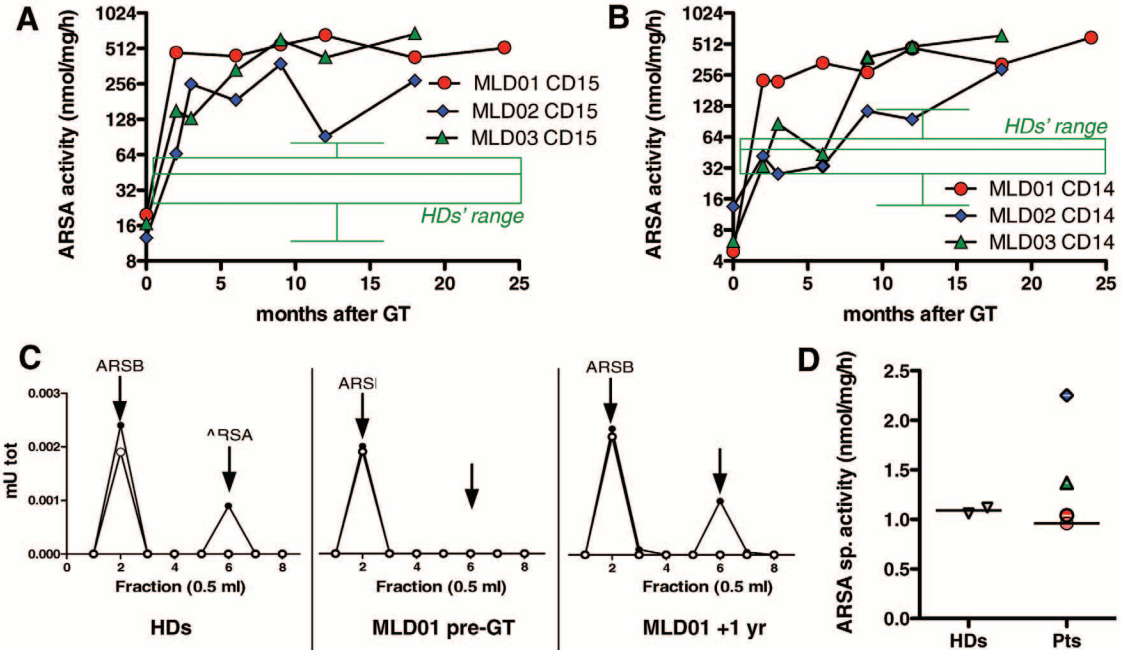


Fig. 2. ARSA expression in patients after HSC-GT. (**A** and **B**) ARSA activity measured with the *p*-nitrocatechol sulfate (PNC) assay on $CD15^+$ cells (A) and $CD14^+$ cells (B) isolated from the patients' PB. The activity range measured in a cohort of healthy donors (HDs) ($n \geq 10$ subjects) is shown. (**C**) Representative DEAE cellulose-chromatography analysis on 500 μl of cerebrospinal fluid (CSF) from a pool of four HDs, of a representative MLD patient before treatment (MLD01 pre-GT) and of the same patient 1 year after gene therapy. The peak of activity corresponds to the native form of the ARSA enzyme, as also demonstrated by its absence/very low residual activity in the patient's pretreatment sample. (**D**) Specific activity (toward MUS) of the ARSA enzyme isolated from the CSF of HDs (two cohorts of four donors each) and of the treated MLD patients (circles, MLD01; blue diamond, MLD 02; and green triangle, MLD03) sampled 12 months (red circle, MLD01; MLD02 and -03 were also sampled at 12 months) and 24 months (pink circle, MLD01) after treatment.

Polyclonal Reconstitution of Hematopoiesis Without Evidence of Vector Genotoxicity

To determine whether there was any cause for concern regarding the safety of the LV in these patients, we monitored the clonal dynamics of hematopoietic repopulation at the molecular level by analyzing the vector genomic integrations in the patients' reconstituted hematopoietic cells (figs. S10 and S11, table S10, and materials and methods). Because of the genome-wide quasi–random integration profile of LV, each insertion creates a different genetic marker that can be used to track the clonal behavior of individual transduced cells. Genomic DNA was obtained from whole BM, PB cells, and subsets (table S11) at 1, 3, 6, 9, and 12 months for all patients and, for MLD01 and MLD02, 18 months after HSC-GT (table S12). Vector-genome junctions were retrieved by means of linear amplification mediated–PCR (LAM-PCR) by using three different restriction enzymes (fig. S12). From the three patients, >800 independent LAM-PCRs were generated and sequenced by 454-Roche (Basel, Switzerland) and Illumina (San Diego, California) technologies to obtain >10×10^6 sequence reads. Using a bioinformatics analysis pipeline and collision/contamination filtering (fig. S10, fig. S13, and table S13, A to C), we mapped integration sites (IS) for patient MLD01 (1,120,414), MLD02 (1,518,802), and MLD03 (425,356) on the human genome (NCBI HG19). Because many identical ISs were retrieved from multiple lineages and/or time points, the number of distinct ISs was 14,482, 11,077, and 10,959 for patients MLD01, MLD02 and MLD03, respectively. The genomic distribution of IS, both in the in vitro–cultured $CD34^+$ cells and in vivo, matched the previously reported LV preference for integration within transcriptional units (on average, 80% of IS were within genes) (fig. S14). To identify the gene classes preferentially targeted by LV integrations, we analyzed IS data sets from either the in vitro progeny of the infused $CD34^+$ cells or a pool of all in vivo–harvested samples for each patient using the GREAT (Genomic Regions Enrichment of Annotations Tool) software (table S14, A to F). In all patients, the gene classes of chromatin modification/remodeling, major histocompatibility complex class II–related functions, steroid hormone receptors, and RNA processing were overrepresented (table S14, A to F). These gene classes were the same, or shared >75% genes, with gene classes overrepresented in the ALD HSC-GT (*17*, *29*) (Fig. 4A and fig. S15).

We measured the proportion of sequencing reads representing each IS within our data sets as a surrogate readout for the relative abundance of the cell clone harboring that integration at a given time. For each time point, we analyzed the IS data sets from the $CD34^+$, myeloid (pooled $CD13^+$, $CD14^+$, and $CD15^+$ data sets), B ($CD19^+$) and T cells ($CD3^+$). Almost every cell clone marked by a specific IS accounted for only a fraction of a percent of the total clones at any given time. A few IS-marked cell clones showed a higher percentage at one time point but then disappeared or were strongly reduced at later time points (Fig. 4, B and C, and fig. S16). From these results, we conclude that no clonal dominance events occurred in these patients.

To determine whether other hallmarks of insertional mutagenesis were present in the patients, we assessed the occurrence of common insertion sites (CISs), insertional hotspots that may result from integration bias at the time of transduction or in vivo selection of clones harboring integrations that confer growth advantage. CISs were identified with an algorithm based on Abel *et al.* (*30*) and by the Grubbs test for outliers (*29*). Both analyses showed that the MLD CISs were mostly distributed in clusters within gene-dense regions heavily targeted by LV integrations (Fig. 5A, figs. S17 to S19, and tables S15 and S16), many of which had already been described in the ALD HSC-GT trial (Fig. 5B) (*17*, *29*). Given the larger size of the MLD data set, it contained almost the entire ALD CIS data set. Moreover, the Grubbs test for outliers when applied to the genomic regions surrounding each CIS confirmed that the CIS from the MLD clinical trial were not significantly over-targeted with respect to the neighboring genes, with *OPTC* being the only exception (fig. S19F and table S16). Cell clones with IS targeting CIS genes did not represent the most

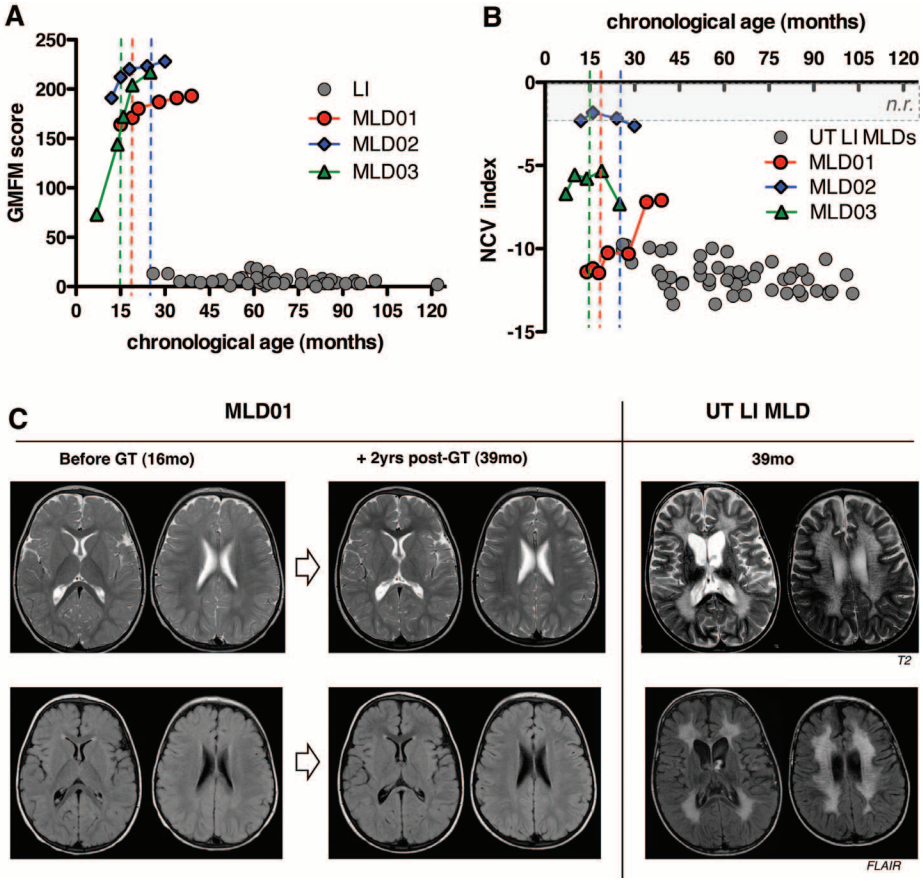


Fig. 3. Clinical follow up of MLD patients after HSC-GT. (**A** and **B**) GMFM score (A) and NCV index (B) of the three treated patients and of a historical cohort of LI-MLD patients (gray circles). The dotted lines indicate for each treated patient (inset, color code) the expected time of disease onset, according to the disease onset observed in their affected matched siblings; n.r., normal range of the NCV index. (**C**) Axial T2 weighted fast spin-echo MR images (top) and FLAIR MR images (bottom) obtained from patient MLD01 at baseline (before GT) and at +2 years after treatment, and corresponding (equivalent) images of an age-matched untreated patient with LI-MLD (in parenthesis, the chronological age at imaging acquisition in months). In MLD01 images, a small area of hyperintensity is present within the splenium of the corpus callosum, stable in extension and appearance as compared with that in the +12 months follow-up; subtle signal inhomogeneities are present within posterior periventricular and posterior centrum semiovale white matter, in the absence of focal lesions; these inhomogeneities, present since baseline as just barely T2 and FLAIR hyperintensity signal, are (now) more evident because of the normal signal of the surrounding myelin; subarachnoid and ventricular spaces are within normal limits, even if a little wider when compared with that of the baseline. Basal ganglia and thalami remain of normal appearance. In UT LI-MLD images, extensive, diffuse symmetric hyperintensities with typical "tigroid pattern" are seen within periventricular white matter, centrum semiovale, corpus callosum, external and internal capsules, and cerebellar deep white matter. A severe diffuse brain atrophy involving basal ganglia and thalamy, which show T2 hypointense signal, is also present.

abundant IS-marked cell clones at any given time point of the follow-up. IS targeting *OPTC* were not detected in samples from the longest follow-up time point.

Extensive HSC Gene Marking in Vivo

To assess HSC gene marking in vivo, we analyzed the subset of IS shared among three data sets representing progenitors and mature myeloid and mature lymphoid cells in each patient. After stringent filtering to reduce the false discovery rate due to the impurity of each cell fraction analyzed and the occurrence of collisions during IS processing (fig. S20 and table S17), a fraction of ISs were consistently shared among the three data sets of each patient (Fig. 6A). This fraction increased with follow-up time (Fig. 6B). We then plotted the occurrence of shared ISs in each subset of cells over time, considering the B and T cells separately, and ranked them for multiple hits (Fig. 6C and table S18). The increasing presence over time of $CD34^+$ progenitors and mature cells of myeloid and lymphoid lineages marked by identical integrations is evidence of self-renewal

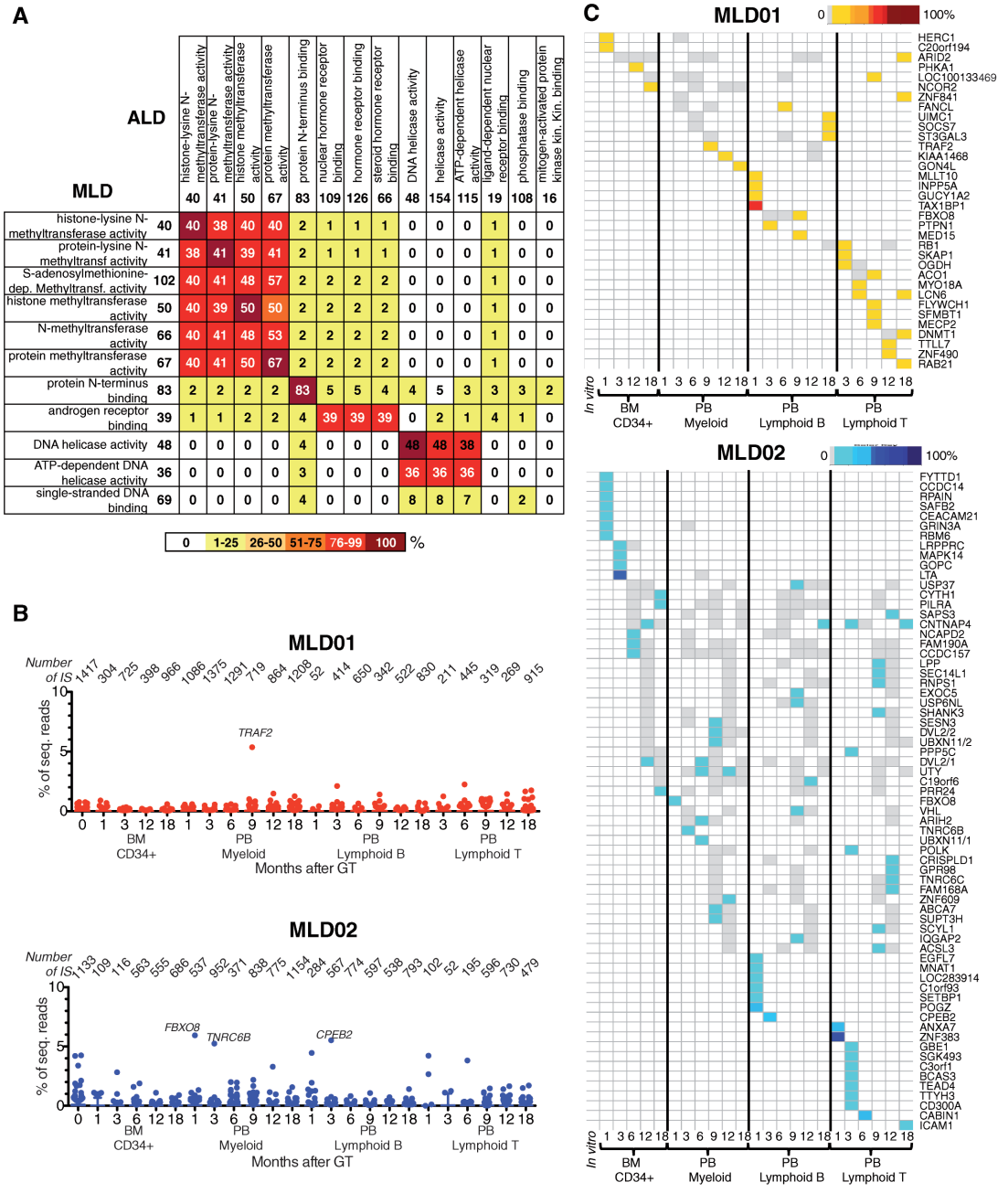


Fig. 4. LV genomic integration profile. (**A**) Gene ontology (GO) analysis on ISs from three patients with MLD and two patients with ALD who had been treated with HSC-GT (*17*). This analysis was performed using the GREAT software (http://bejerano.stanford.edu/great/). The genomic positions of ISs in each data set were weighted by the binomial test in order to evaluate the clustering at given genomic regions and by the hypergeometric test in order to evaluate the overrepresentation of gene functions. GO classes were considered significant when both tests provided a false discovery rate of <0.05. To compare the level of similarity between the gene classes preferentially targeted by LV integrations in ALD and MLD clinical trials, we counted the number of shared genes contained in the significantly overrepresented gene classes for GO molecular functions of each clinical trial (results for GO biological processes are shown in fig. S13). The extent of gene sharing between the overrepresented gene classes are indicated by a color scale. (**B**) Box plot of the percentage of sequence reads (*y* axis) for unequivocally mapped ISs from patients MLD01 and MLD02 in different cell types ($CD34^+$, myeloid, or lymphoid cells) from different sources (BM or PB) and time points (months after gene therapy, indicated below the *x* axis). The number of reads for each IS was normalized to the total number of sequence reads from the same time point and source. ISs over the 95 percentile of the data set are shown as dots distinct from the box and whiskers, which are mostly flattened to the bottom of the plot. The total number of ISs for each lineage and time point is shown on top. Most represented integrations (with the hit gene indicated next to the dot) are enriched in oligoclonal populations, such as in PB-derived B or T cells at early time points. (**C**) Follow-up of the most represented ISs during time in different cell types. Percentages of sequence reads for each IS are calculated on the total number of sequence reads from the same lineage so as to emphasize the maximum relative contribution, thus obtaining values that are greater or equal to percentages shown in (B). For each IS, colored cells indicate retrieval at ≥5%, with higher color intensity indicating higher percentage, whereas gray cells indicate retrieval at low percentage (from 0.006% to <5%). Lack of color indicates that the integration was not retrieved at the indicated time point and source. The targeted genes are indicated. Almost all integrations reached ≥5% at only one time point.

and multilineage potential of the transduced engrafted HSCs.

To estimate the number of HSCs contributing to hematopoietic reconstitution, we used the fraction of ISs shared between independent samplings of the same cell population (supplementary materials, materials and methods). For this analysis, we considered the output of short-lived mature myeloid cells in the PB long-term after HSC-GT as readout of total HSC activity at that time. We compared ISs shared between $CD14^+$ and $CD15^+$ PB cells at months 9, 12, and 18 after HSC-GT by the mark-recapture approach using the Petersen/Schnabel estimator method (*31*) and Chao Poisson regression model (table S19). The resulting lower bound population size estimates were 3.7×10^3 to 5.7×10^3 in patient MLD01 and 2.1×10^3 to 3.4×10^3 in MLD02, indicating an abundant pool of engrafted transduced self-renewing progenitors in both patients.

To quantify clonal diversity in each lineage over time, we calculated the Shannon Diversity Index (Fig. 6D and fig. S22). This index measures the entropy of an IS data set taking into account the total number of ISs and their relative contribution. The diversity of $CD34^+$ progenitors was lower early after HSC-GT as compared with that of the infused cell population and then increased and stabilized. PB myeloid cells showed high and stable diversity, which is consistent with that of the progenitor pool, whereas B and T cell diversity increased with time and stabilized 6 months after gene therapy. Patient MLD03 showed lower IS sharing between lineages and decreasing diversity of myeloid cells as compared with the other two patients, possibly because of the shorter follow-up and the higher VCN of the infused cells.

Overall, these data provide evidence that efficient ex vivo gene transfer was followed by substantial engraftment and sustained clonogenic activity of the transduced HSCs in the patients, resulting in extensive polyclonal reconstitution of hematopoiesis with gene-corrected cells.

Discussion

LI MLD is a devastating disease that invariably leads to death of affected children within a few years of symptom onset. We have shown that HSC-GT halted disease manifestation and/or progression in three presymptomatic children with LI-MLD for follow-up times ranging from 18 to 24 months after treatment (7 to 21 months after predicted disease onset).

The clinical benefit observed in the three patients was accompanied by measurable objective findings ascertained through brain imaging and electrophysiological and biochemical studies and is in contrast with the disease evolution observed in (i) the patients' older affected siblings with matched ARSA mutations and related genetic background and (ii) our historical cohort of untreated LI-MLD patients. MRI analysis detected a minor demyelinating lesion in the brain of MLD01 1 year after treatment. This minor lesion, which might have arisen before the infused cells reached a sufficient CNS engraftment to exert beneficial effects, remained stable at all subsequent follow-ups. This finding is clearly different from what is observed in untreated LI-MLD patients, who show rapidly progressive and widespread brain demyelination. The severe peripheral neuropathy already present in MLD01 at the time of HSC-GT improved after treatment, with amelioration of the amplitude of motor action potentials and of the nerve conduction velocities after treatment. These findings were associated with clinical evidence of normal cognitive evolution and continuous improvements in motor skills. Although the follow-up is shorter for MLD02 and MLD03, these patients remained asymptomatic at a chronological age when their disease was expected to have manifested.

In previous work with the MLD mouse model, we showed that the therapeutic benefit of

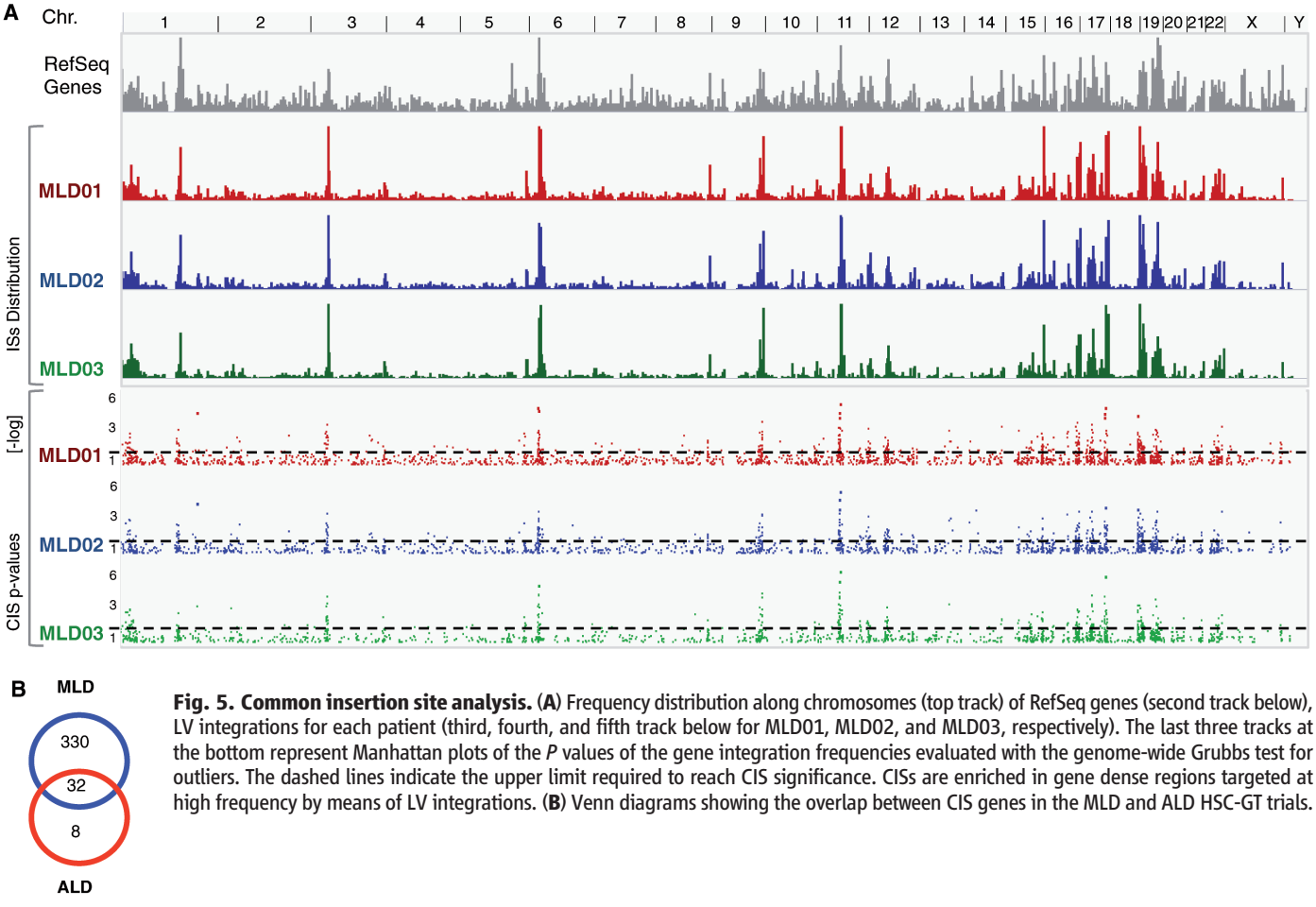


Fig. 5. Common insertion site analysis. (**A**) Frequency distribution along chromosomes (top track) of RefSeq genes (second track below), LV integrations for each patient (third, fourth, and fifth track below for MLD01, MLD02, and MLD03, respectively). The last three tracks at the bottom represent Manhattan plots of the *P* values of the gene integration frequencies evaluated with the genome-wide Grubbs test for outliers. The dashed lines indicate the upper limit required to reach CIS significance. CISs are enriched in gene dense regions targeted at high frequency by means of LV integrations. (**B**) Venn diagrams showing the overlap between CIS genes in the MLD and ALD HSC-GT trials.

HSC-GT arises from the homing of ARSA-overexpressing HSPCs and/or their myeloid progeny to the CNS and PNS, where they contribute to the replacement of a substantial fraction of microglia/resident macrophages, scavenge the stored sulfatide, and establish a local source of functional enzyme bioavailable throughout the neural tissues. Although we could not directly probe our patients for the migration of gene-modified cells into the CNS, we documented that CSF samples from the patients contained substantial levels of ARSA protein and activity long after HSC-GT. This objective finding, together with the halted progression of neural disease, suggests that the CNS and PNS were seeded by gene-corrected myeloid cells upon HSC-GT.

Recent studies in mice have shown that microglia mostly originates from an early seeding of neural tissues by embryonic lineage macrophages followed by in situ turnover under homeostatic conditions (*32*). However, substantial replacement of microglia with donor-derived cells was shown after myeloablation and intravenous infusion of HSPCs (*8*, *33*, *34*). The latter findings are consistent with clinical evidence that HSCT can provide therapeutic benefit in certain lysosomal storage diseases affecting the CNS, and with the few available studies investigating the donor origin of microglia cells within the brains of transplanted humans (*35*, *36*). We speculate that high-level engraftment of the myeloid compartment in PB and BM by the transduced HSPCs is likely needed to support their efficient migration to the neural tissues. It is possible, however, that myeloid progenitors, rather than mature monocytes, are primarily responsible for seeding the CNS in our patients (*34*).

At least three factors may have contributed to the high levels of gene replacement observed in patients' hematopoiesis. First, we optimized the LV-manufacturing process, aiming to produce vector with high titer, infectivity, and purity using stringent lot-release criteria so as to ensure efficient transduction while limiting detrimental effects on HSPCs. Second, we validated the transduction protocol for reproducible high-rate gene transfer into BM-derived mouse-repopulating human HSPCs and infused fresh cells after transduction to avoid incurring in any cell loss associated with freeze/thawing. Last, we administered a dose-adjusted myeloablative regimen before HSPC infusion to foster engraftment.

Another key goal of our study was to assess the long-term safety of HSC gene transfer. Using deep-sequencing and bioinformatics, we found no evidence that cell clones harboring ISs undergo in vivo expansion or selection. Rather, our data suggest that the genomic distribution of IS in patients' hematopoietic cells reflects the LV integration in the infused HSPCs. These findings are in sharp contrast with those reported at comparable times after HSC-GT in some other trials using γ-RV; in those trials, cell clones harboring

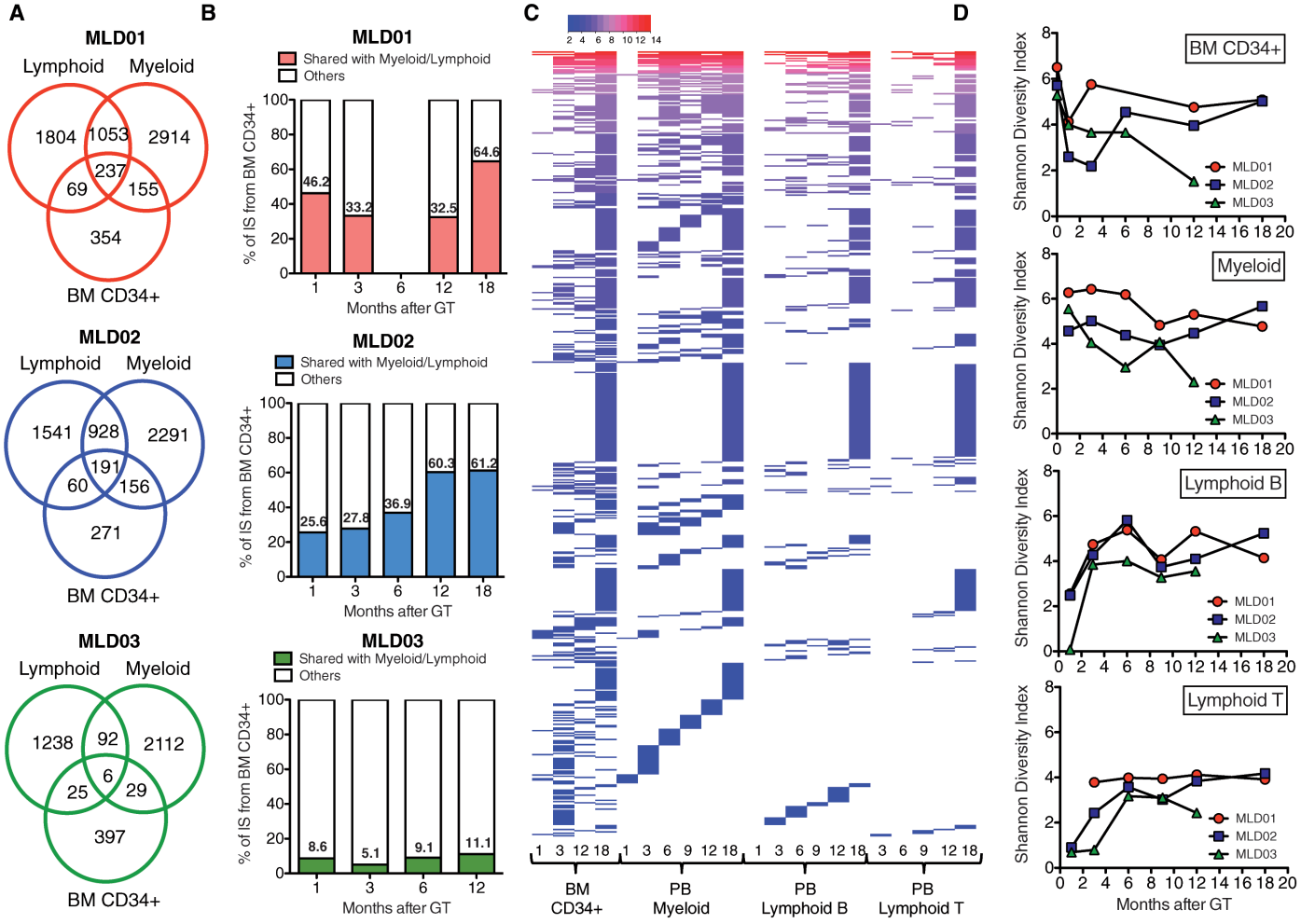


Fig. 6. Stem cell marking and clonal dynamics. Analysis of IS data was performed after filtering for collision and sample impurity. (**A**) Venn diagrams showing the sharing of ISs between CD34$^+$ cells and lymphoid and myeloid lineages. (**B**) Percentage of shared ISs (*y* axis) between BM-derived CD34$^+$ and myeloid or lymphoid lineages during time (months after GT, indicated below). (**C**) Tracking of ISs shared between multiple lineages with time in patient MLD01. Each row represents a specific IS, with colored bars indicating retrieval from the indicated cell lineage and time point after gene therapy (columns). The line color varies with the degree of sharing among lineages (red, high level of sharing; blue, low level of sharing; white, no integration retrieved). PB, peripheral blood; B, B cells; T, T cells; Myelo, myeloid cells. (**D**) Shannon Diversity Index (*y* axis) was calculated to measure the clonal diversity of hematopoietic reconstitution during time.

ISs that target oncogenes underwent expansion or selection in vivo and eventually progressed to leukemia (*14*, *18*, *37*–*40*). The LV IS distribution in MLD patients overlaps with that reported for ALD patients after LV-based HSC-GT, a reassuring finding considering that no adverse effect of gene transfer has been reported in that trial after more than 5 years of follow-up. A similar integration profile in the absence of clonal expansion was observed in three patients with Wiskott-Aldrich Syndrome treated by LV-based HSC-GT with a follow-up of up to 2.5 years (*47*). Overall, these data strongly support the improved safety of LV comprising self-inactivating long terminal repeat and moderately active internal promoters, which makes it unlikely that an insertion would activate a nearby oncogene (*19*, *20*, *41*). Nevertheless, we will continue longer-term evaluation of the treated and additional patients for full assessment of the risk-benefit ratio and therapeutic potential of HSC-GT.

The stability of gene marking together with the identification of several ISs shared among progenitors, mature myeloid cells, and both major lymphoid lineages long-term after HSC-GT provide evidence that bona fide HSCs were transduced. Furthermore, the estimated large number of active HSCs would imply that a good fraction of harvested HSCs were transduced and long-term engrafted the patients. These data position LV gene transfer as a feasible means to engineer human hematopoiesis to its near entirety, an approach that may be exploited to develop novel treatments for several inherited and acquired diseases.

Materials and Methods

Clinical Protocol and Patients

The Istituto Superiore di Sanità and the Ethical Committee of the San Raffaele Scientific Institute in Milan approved the study. The study promoter is TIGET, San Raffaele Hospital, Italy and the financial sponsor of the study is the Telethon Foundation. The medicinal product received Orphan Drug Designation (ODD) (EMEA/OD/102/06) by the European Medicines Agency (EMA) for the treatment of MLD.

We enrolled and treated three presymptomatic LI-MLD patients, who were classified as LI according to the disease in their affected older siblings using the historical classification based on age at symptom onset (table S3). The patients were from Lebanon, the United States, and Egypt. Upon obtaining informed consent, their diagnosis was molecularly and biochemically confirmed. In all patients, the definitive MLD diagnosis was based on pathologic low ARSA activity and the presence of disease-causing *ARSA* gene mutations on both alleles. Presymptomatic condition at enrollment was defined on the basis of a normal neurological and cognitive examination, independently from the presence of abnormalities at neurophysiological tests or brain imaging.

Details on clinical study enrollment criteria, endpoints, and study plan can be found at ClinicalTrials.gov #NCT01560182. The parents of all subjects provided written informed consent for experimental treatment. Biological samples were obtained from MLD patients—healthy children and adults as controls—with approval of the San Raffaele Scientific Institute's Ethics Committee and consent from parents or subjects.

Neurological and Motor Evaluation

A standard neurological evaluation was performed in all patients for assessing the presence of disease clinical signs. In addition, we applied GMFM (*26*, *42*) and the Gross Motor Function Classification for MLD (GMFC-MLD) (*27*) for proper quantification of patients' motor abilities. The same trained personnel applied the scales at each evaluation.

Neuropsychological Evaluation

Neuropsychological evaluation was performed by using the Bayley Scale for Infant and Toddler Development (BSID-II) (*43*), applied at baseline evaluation and then every 6 months.

Neurophysiological Evaluation

Sensory conduction of sural and median nerves, and motor conduction of deep peroneal and ulnar nerves were studied and a z score for NCV was calculated for each examined nerve (patient's NCV – normal donors' mean NCV/normal donors' NCV standard deviation); an NCV index was calculated as the average of z scores obtained from the four tested nerves for each patient per time, as described (*26*).

MR Examination

All children underwent anatomical MRI on a 1.5 Tesla scanner using a six-channel SENSE head coil (Gyroscan Intera, Philips, Netherlands). MRI scans were performed with Spin Echo T1 weighted images, repetition time (TR) 600 ms, echo time (TE) 15 ms, rec matrix 288, 22 slices, 5 and 3 mm thick, axial and sagittal planes; Turbo Spin Echo T2-weighted images, TE120 ms, TR 5500 ms 24 slices, axial, sagittal and coronal planes, 4.5 and 3 mm thick; fluid-attenuated inversion recovery Turbo Spin Echo, TE 140 ms, 24 slices, 4.5 mm thick; and volumetric T1 sequence (fast field echo, 110 slices, 1.4 mm thick, and 0 mm gap). MR examinations were performed under sedation by a senior experienced pediatric anesthesiologist (*44*); sedation was induced with intravenous 1 mg/kg propofol and maintained with 4 mg/kg/hour propofol continuous infusion. Throughout MRI examination, saturation of peripheral oxygen (SpO_2) was monitored with a MRI-compatible device (Magnitude, Invivo Corporation, Orlando, Florida). Desaturation ($SpO_2 <$ 95%) was recorded together with any adverse event requiring the intervention of the attending anesthesiologist.

Large-Scale Lentiviral Vector Production

The vector used in this study (pCCLsin.cPPT.hPGK.hARSA.WPREmut6 - PGK.ARSA.LV) is a self-inactivating lentiviral vector produced with a third-generation split packaging system and pseudotyped by the vesicular stomatitis virus G protein (VSV.G) (*6*). The vector lots were produced by MolMed (Milan, Italy) using a large-scale validated process. The vectors were produced following Good Manufacturing Practice (GMP) guidelines, except for initial studies of gene transfer protocol optimization, which used pre-GMP (GMP-like/large scale produced) vector. The protocol for vector production is detailed in fig. S3. Briefly, the ARSA LV was produced by means of transient four-plasmid transfection of 293T cells. 293T cells were derived from human embryonic kidney 293 cells with stable transfection of the temperature-sensitive SV40 T-antigen; a subclone of the 293T (from Stanford University) selected at the Salk Institute (La Jolla, California) for its high-yield performance in production of lentiviral vectors through transient transfection was used for MCB establishment; a 293T MCB was generated at Genethon (Paris, France) in GMP conditions. 293T cells from the master cell bank were expanded in T162 flasks and then in 10-tray cell factories and transiently transfected by means of calcium phosphate precipitation with four plasmids encoding for two core packaging constructs (pKLGag/pol and pKRev), the envelope construct (pK.G), and the transfer vector construct (pARSA). Twenty-four hours after removal of the transfection medium, the cell supernatant was harvested and stored at 4°C. The culture medium was replaced, and after a further 24 hours, a second harvest was performed. The medium collected from the two harvests was pooled and filtered through 5/0.45-μm filters so as to discard cell debris. The downstream purification process included a benzonase treatment overnight at 4°C, followed by a diethylamino anion exchange (DEAE) chromatography step, concentration, and gel filtration in CellGro medium. The benzonase treatment was aimed at degrading plasmid DNA and host cell–derived DNA present in the clarified cell supernatant, thus facilitating their removal through subsequent purification steps. Anion exchange chromatography involved the absorption of negatively charged lentiviral particles to positively charged chromatographic support; viral particles were eluted by increasing ionic strength. This step was aimed at the removal of contaminants such as host cell proteins and serum-derived proteins such as bovine serum albumin (BSA). Gel filtration, also defined as size exclusion chromatography, relies on the inability of the large lentiviral particles to be retained by matrix pores. This step was aimed at the removal of salts and small-sized contaminants such as DNA fragments as well as at medium exchange. The resulting LV preparation, in CellGro medium, underwent one sterilizing 0.2-μm filtration and aseptic filling. The purified vector preparation was stored at –80°C. The produced vector lots were characterized as described in table S2. Physical titer was measured by means of enzyme-linked immunosorbent assay (Perkin Elmer, Applied Biosystem, Foster City,

California) for the detection of HIV-1 gag p24 capsid protein. Infectious titer was measured through transduction of a human T cell line with serial dilutions of vector and calculation of the copies of integrated vector per cell by quantitative PCR.

HSC Isolation and Transduction

For in Vitro Experiments

Healthy donor (HD) bone marrow $CD34^+$ cells were purchased from Lonza (Basel, Switzerland) or obtained after written informed consent according to standard ethical procedure and with approval of the San Raffaele Institute Ethical Committee (protocol TIGET-01). $CD34^+$ cells from three MLD patients not enrolled in the gene therapy trial—diagnosed on the basis of clinical symptoms, ARSA activity, and genetic analysis—were similarly obtained after written informed consent (protocol LDM1) at the time of diagnostic or therapeutic procedures. $CD34^+$ cells were purified from mononuclear cells by means of positive selection with immunomagnetic beads according to the manufacturer's procedure (Miltenyi Biotec, Bergisch-Gladbach, Germany). Soon after purification or thawing, $CD34^+$ cells were placed in culture on retronectin-coated non–tissue culture–treated wells (T100A Takara) in CellGro SCGM medium (2001 CellGenix) at a concentration of 1×10^6 cells/ml in the presence of cytokines [interleukin-3 (IL-3, 60 ng/ml), thrombopoietin (TPO, 100 ng/ml), stem cell factor (SCF, 300 ng/ml), and Flt3 ligand (Flt3-L, 300 ng/ml); PeproTech, Rocky Hill, New Jersey] for 24 hours of prestimulation. Cells were then transduced with ARSA LV [at a multiplicity of infection (MOI) of 100] for 14 hours. In the protocol that foresees two rounds of transduction, selected for clinical application, cells were washed for 10 hours in CellGro SCGM medium additioned with cytokines and underwent a second hit of transduction in the same conditions as the first. At the end of transduction, cells were counted and collected for clonogenic assays, flow cytometry, and in vivo studies. Remaining cells were plated in Iscove's modified Dulbecco's medium (IMDM) –10% fetal bovine serum (FBS) with cytokines (IL-3, 60 ng/ml; IL-6, 60 ng/ml; SCF, 300 ng/ml) and cultured for a total of 14 days. Thereafter, cells were collected for molecular and biochemical studies.

For Patients' Treatment

Please refer to fig. S2. Total bone marrow was collected from the iliac crests under sterile conditions and using general anesthesia, on day –4, according to an internal standard operating procedure. The total collected volume was estimated according to the content of $CD34^+$ cells evaluated by previous bone marrow aspiration; on average, 20 to 25 ml/kg patient's body weight was collected. The harvested bone marrow—collected in a dedicated bag, sealed, and identified—was then transferred to MolMed S.p.A and kept in sterile conditions in a refrigerator at 4°C for 24 hours. $CD34^+$ cells were then purified on day –3 from mononuclear cells by means of positive selection with immunomagnetic beads according to the manufacturer's procedure (Miltenyi Biotec, Bergisch-Gladbach, Germany) in GMP conditions. The purified cells were cultured in retronectin-coated VueLife bags (American Fluoroseal, Gaithersburg, Maryland) in serum-free medium supplemented with GMP-grade cytokines and exposed twice to GMP-grade–purified vector at multiplicity of infection of 100, for a total culture time of 60 hours. At the end of the transduction procedure, the transduced $CD34^+$ cells were harvested, washed with Cell Grow medium, and resuspended in saline solution at the concentration of 2×10^6 to 10×10^6/ml for patient's infusion. At the end of transduction, a fraction of the cells was collected for clonogenic assays, flow cytometry, and in vitro culture, as above. Cells were kept at 4°C up to the time of infusion, upon batch release according to quality control tests [results are available at infusion for viability, immunophenotype, endotoxin, large T Ag DNA, and mycoplasma (table S4)].

Patients' Conditioning

Patients received a total of 14 body weight–based doses of intravenous busulfan, given every 6 hours from day –4 to day –1. The busulfan plasmatic levels were monitored with serial sampling following first and fifth infusion. The doses after the 5th and 10th were adjusted, if needed, according to plasmatic Busulfan levels with an ideal AUC of range 4200-5600 μg/L*hour, target 4800 μg/L*hour. The interval between the end of the last intravenous busulfan dose and final product infusion was ≥24 hours in order to allow safe infusion of the stem cells. At day 0, after premedication with clorfeniramine (0.25 mg/kg, max dose 10 mg) or equivalent drug, the resuspended $CD34^+$ cell product was infused intravenously through the central catheter.

During hospitalization, patients were cared for in an isolation unit and received supportive therapy according to local standards.

Isolation of Hematopoietic Subpopulations from Patients' Peripheral Blood and Bone Marrow

Starting from mononuclear cells (MNCs) obtained from Lymphoprep gradient, human bone marrow and peripheral blood subpopulations were obtained through positive selection of the following markers (Miltenyi Biotec microbeads): CD34, CD13, CD15, CD56, CD19, CD3, glycophorin A (GLYA), and CD61 from the BM, and CD15, CD14, CD56, CD19, and CD3 from PB, according to manufacturer's procedures. Purity of each subpopulation was checked by means of flow-cytometry. Data are reported in table S11.

Clonogenic Assay (CFC)

The CFC assay was performed by means of plating in methylcellulose medium (human MethoCult; StemCell Technologies) either 800 to 1000 $CD34^+$ cells/ml or 1.25×10^4 to 1×10^6 MNCs/ml purified from BM or PB. After 14 days of culture, colonies were counted, distinguishing myeloid and erythroid origin, and plucked for molecular analysis.

Quantitative PCR

Genomic DNA was extracted from $CD34^+$ liquid culture, peripheral blood mononuclear cells (PBMCs), MNCs, PB, and BM subpopulations of MLD patient samples with QIAamp DNA Blood Micro and Mini Kits (Qiagen, Hilden, Germany). Single colonies plucked from the CFC assay were digested for 4 hours at 37°C in Lysis Buffer (Lauryl Ether 0.1%, TRIS/hydrochloride (HCL) 10 mM, 100 μg/ml Proteinase K). After proteinase K inactivation (10 min at 95°C), lysates were centrifuged at 13,000 revolutions per min at 4°C for 15 min.

LV sequences were detected by means of quantitative PCR on 25 to 50 ng of total genomic DNA or 10 μl of lysate supernatants by using previously described primers and probe (*22*).

Absolute quantifications were plotted on standard curves prepared with serial dilutions of genomic DNA or cell lysate from a T cell clone containing 1 copy HIV/cell.

Engraftment of the transduced cells was evaluated by means of quantitative PCR on individual colonies from CFC assay performed on either PB- or BM-derived cells and expressed as percentage (%) of LV^+ (VCN ≥ 0.5) colonies on total tested colonies (≥ 250 cells/colony).

Analysis of Vbeta Repertoire

The analysis of Vbeta repertoire of the T cell receptor was performed on 50 μl of patients' total PB according to the manufacturing procedure described in the V Beta kit; Beckman Coulter (823497) (Fullerton, California). 10000 events were acquired with FACS Canto II (BD-Biosciences, Europe) and then analyzed with FlowJo (TreeStar, Ashland, Oregon). The percentage of each Vbeta population was compared with the range of expression obtained from the analysis of a pool of 85 healthy donors provided by the manufacturer.

Immunophenotype Analysis

Analysis of the immunophenotype of patients' total PB and BM was performed by Laboraf (Ospedale San Raffaele) as described by internal SOPs.

ARSA Activity Determination

p-Nitrocatechol Sulfate (PNCS)

$CD34^+$ liquid culture, PBMCs, MNCs, PB, and BM subpopulations of MLD patients and healthy donors were resuspended in sodium acetate trihydrate 0.05 M (500,000 cells in 25 μl). Samples were then sonicated and centrifuged, and the supernatant was collected for ARSA activity and protein quantification (Bradford assay; Biorad #500-0006) (Hercules, California). ARSA activity was detected with PNCS as substrate, as described, loading a maximum concentration of

protein extract of 0.3 μg/μl diluted in sodium acetate trihydrate 0.05 M (9).

DEAE-Cellulose Chromatography and 4-Methyl-Umbellipheryl-Sulfate

Cells were harvested, washed in phosphate-buffered saline, and resuspended in 10 mM TRIS/HCl buffer, pH 7.5, containing 0.1% (v/v) Nonidet NP40 detergent (Sigma-Aldrich, St. Louis, Missouri). Cell lysates were subjected to three rounds of sonication. Procedures were carried out at 4°C. Proteins were measured with the Bradford method by using bovine serum albumin as standard.

Similar cell number (500,000 cells) was loaded into a 0.2-ml DEAE chromatography column equilibrated with a 25 mM TRIS/HCl buffer, pH 7.5. The flow rate was 0.2 ml/min. After washing with 5 ml of 25 mM TRIS/HCl buffer plus 50 mM NaCl, pH 7.5, enzyme activity retained by the column was eluted by 2.5 ml TRIS/HCl buffer plus 250 mM NaCl, pH 7.5 (starting from fraction n.5). Fractions (0.5 ml) were collected and assayed for the ARSA activity by using the artificial fluorogenic substrate 4-methyl-umbellipheryl-sulfate (MUS) dissolved in 0.05 M Na-acetate/acetic acid buffer, pH 5.5. A volume of 50 μl of test sample was incubated with 100 μL of a 0.01 M solution of substrate respectively in the presence and absence of 125 μM AgNO3 (a specific ARSA inhibitor) at 37°C. Enzymatic reactions were stopped by adding 0.2 M Glycine/NaOH, pH 10.6. Fluorescence of the liberated 4-methylumbelliferone was measured on a Perkin Elmer LS3 spectrofluorimeter (excitation 360 nm, emission 446 nm). ARSA activity was calculated by subtracting the value obtained in the presence of AgNO3 [arylsulfatase B (ARSB) activity] from that measured in the absence of the inhibitor (ARSA+ARSB activity) (*45*).

Sulphatide Assay

Sulfatide (5 mM) (Matreya, St. Pleasant Gap, Pennsylvania) was resuspended in cloroform:methanol:water (2:1:0.1), dried overnight at room temperature, and resuspended in the ARSA enzymatic buffer [100 mM Na/acetate, pH 4.5, containing 20 mM MnCl2 and taurodeoxyxholate (100 mg/50 μl)]. For the reaction (100 μl total volume), 0.003 mU ARSA were added to 21 nmol sulfatide at 37°C for 24 hours. The assay was stopped with 0.85 ml cloroform:methanol:water (1:1) plus 0.85 50 mN sulfuric acid and 0.170 ml Azure A [0.4 mg/ml]. After a centrifugation at 300 g × 5 min, the lower phase was recovered, and the absorbance measured at 650 nm in a microplate reader (GDV DV-990BV6). The naomoles of sulfatide hydrolyzed by ARSA were calculated by subtracting the value measured in the presence of the enzyme respect to a reference assay performed in the absence of ARSA.

In Situ Hybridization and Immunofluorescence

Cells were grown on polyornithine-coated glass coverslips (0.01% solution, Sigma-Aldrich Corp, Italy) 72 hours in IMDM 10% FBS medium and then fixed with 4% paraformaldehyde (PFA) solution.

An antisense 598–base pair digoxigenin-labeled oligonucleotide complementary to W-Pre mRNA sequence and a control sense sequence were produced .The in situ protocol was modified from (*46*). Cells were treated with prehybridization protocol and incubated overnight at 37°C with 0.5 μg/ml probe. The probe was detected by sheep anti Digoxigenin 1:500 (Roche Applied Science, Penzberg, Germany) overnight 4°C.

Immunofluorescence on ARSA-hemagglutinin (HA) (9)–transduced Hela cells and on patients' and healthy donors' PB cells or HeLa cells was performed overnight at 4°C by using rabbit anti–Human Lamp1 1:100 (Abcam), goat anti–Human ARSA 1:50 (Abnova), and/or rat anti-HA 1:100 (Roche Applied Science). Secondary antibodies were incubated 1:500 for 1 hour at RT as follows: donkey anti–sheep Alexa488, donkey anti–goat Alexa546, donkey anti–rat Alexa488, and donkey anti–rabbit Alexa647. Nuclei were counterstained with 4′,6-diamidino-2-phenylindole. Images were acquired with Leica (Solms, Germany) TCS SP2 laser scanning confocal with 63× oil objective.

Rag2$^{-/-}$ Il2rγ$^{-/-}$ Mice Transplantation and Engraftment Evaluation

Rag2$^{-/-}$ Il2rγ$^{-/-}$ mice were obtained from the Central Institute for Experimental Animals, Nogawa, Japan and maintained in our animal facility according to approved protocols. Three-day-old mice were sublethally irradiated (40,000 μGy/m^2) 24 hours before intravenous injection of untransduced and unmanipulated or transduced CD34$^+$ cells. Eight to 12 weeks after the transplantation, mice were killed and hematopoietic organs (bone marrow, spleen, and thymus) were collected after intracardiac PBS perfusion and processed for fluorescence-activated cell sorting (FACS) analysis. All procedures were performed according to protocols approved by the Animal Care and Use Committee of the San Raffaele Scientific Institute (IACUC #325) and communicated to the Ministry of Health and local authorities according to Italian law.

Flow Cytometry

Patients' samples—subpopulation analysis

From each sample, 5000 cells were washed and resuspended in blocking buffer (PBS with 5% FBS 2% BSA Fc Block 1:100), then 1 μl of the following human-specific conjugated antibodies were added: APC-conjugated anti-CD56, PE-conjugated anti-CD34, anti-CD13 and anti-glycophorinA, TC-conjugated anti-CD19, and anti-CD3, FITC-conjugated anti-CD15 and anti-CD61, PB-conjugated anti-CD14 under unstained control (DAKO, Denmark; BD-Pharmigen, Europe).

Rag2$^{-/-}$ IL2rγ$^{-/-}$ mice—engraftment evaluation

From each sample, 250,000 cells were washed and resuspended in blocking buffer (PBS with 5% FBS 2% BSA Fc Block 1:100), then 0.5 μl of the following human-specific conjugated antibodies were added: APC-conjugated anti-CD45, PE-conjugated anti-CD34, anti-CD13, anti-CD4, anti-CD11b and TC-conjugated anti-CD19, anti-CD8, anti-CD3 under control of relative IgG isotype control (DAKO; BD-Biosciences).

After 20 min on ice, cells were washed, resuspended in PBS 2% FBS, 1% PFA for cytometric analysis. Of 100,000 events, 3000 were acquired with FACS Canto II (BD-Biosciences, Europe) and then analyzed by FlowJo (TreeStar, Ashland, Oregon). During quadrant analysis, only fluorescence that excluded >99.9% of isotype control events was considered to be specific.

Vector Integration Site Analysis

A detailed description of the materials and methods used for vector integration site analysis is reported in the supplementary materials, materials and methods section.

References and Notes

1. J. Aicardi, *Diseases of the Nervous System in Childhood* (Mac Keith Press, London, ed. 2, 1998).
2. A. Biffi, G. Lucchini, A. Rovelli, M. Sessa, Metachromatic leukodystrophy: An overview of current and prospective treatments. *Bone Marrow Transplant.* **42**, S2–S6 (2008). doi: 10.1038/bmt.2008.275; pmid: 18978739
3. A. Biffi, P. Aubourg, N. Cartier, Gene therapy for leukodystrophies. *Hum. Mol. Genet.* **20**, R42–R53 (2011). doi: 10.1093/hmg/ddr142; pmid: 21459776
4. W. Krivit, J. H. Sung, E. G. Shapiro, L. A. Lockman, Microglia: The effector cell for reconstitution of the central nervous system following bone marrow transplantation for lysosomal and peroxisomal storage diseases. *Cell Transplant.* **4**, 385–392 (1995). doi: 10.1016/0963-6897(95)00021-O; pmid: 7582569
5. A. M. Rovelli, C. G. Steward, Hematopoietic cell transplantation activity in Europe for inherited metabolic diseases: Open issues and future directions. *Bone Marrow Transplant.* **35**, S23 (2005). doi: 10.1038/sj.bmt.1704839
6. J. J. Boelens, V. K. Prasad, J. Tolar, R. F. Wynn, C. Peters, Current international perspectives on hematopoietic stem cell transplantation for inherited metabolic disorders. *Pediatr. Clin. North Am.* **57**, 123–145 (2010). doi: 10.1016/j.pcl.2009.11.004; pmid: 20307715
7. J. J. Boelens, Trends in haematopoietic cell transplantation for inborn errors of metabolism. *J. Inherit. Metab. Dis.* **29**, 413–420 (2006). doi: 10.1007/s10545-005-0258-8; pmid: 16763911
8. A. Biffi *et al.*, Correction of metachromatic leukodystrophy in the mouse model by transplantation of genetically modified hematopoietic stem cells. *J. Clin. Invest.* **113**, 1118–1129 (2004). pmid: 15085191
9. A. Biffi *et al.*, Gene therapy of metachromatic leukodystrophy reverses neurological damage and deficits in mice. *J. Clin. Invest.* **116**, 3070–3082 (2006). doi: 10.1172/JCI28873; pmid: 17080200
10. I. Visigalli *et al.*, Gene therapy augments the efficacy of hematopoietic cell transplantation and fully corrects mucopolysaccharidosis type I phenotype in the mouse model. *Blood* **116**, 5130–5139 (2010). doi: 10.1182/blood-2010-04-278234; pmid: 20847202
11. B. Gentner *et al.*, Identification of hematopoietic stem cell-specific miRNAs enables gene therapy of globoid cell leukodystrophy. *Sci. Transl. Med.* **2**, 58ra84 (2010). doi: 10.1126/scitranslmed.3001522; pmid: 21084719
12. A. Aiuti *et al.*, Gene therapy for immunodeficiency due to adenosine deaminase deficiency. *N. Engl. J. Med.* **360**, 447–458 (2009). doi: 10.1056/NEJMoa0805817; pmid: 19179314
13. M. Cavazzana-Calvo, A. Fischer, Gene therapy for severe combined immunodeficiency: Are we there yet? *J. Clin. Invest.* **117**, 1456–1465 (2007). doi: 10.1172/JCI30953; pmid: 17549248

14. M. G. Ott *et al.*, Correction of X-linked chronic granulomatous disease by gene therapy, augmented by insertional activation of MDS1-EVI1, PRDM16 or SETBP1. *Nat. Med.* **12**, 401–409 (2006). doi: 10.1038/nm1393; pmid: 16582916
15. L. Naldini, Ex vivo gene transfer and correction for cell-based therapies. *Nat. Rev. Genet.* **12**, 301–315 (2011). doi: 10.1038/nrg2985; pmid: 21445084
16. L. Naldini *et al.*, In vivo gene delivery and stable transduction of nondividing cells by a lentiviral vector. *Science* **272**, 263–267 (1996). doi: 10.1126/science.272.5259.263; pmid: 8602510
17. N. Cartier *et al.*, Hematopoietic stem cell gene therapy with a lentiviral vector in X-linked adrenoleukodystrophy. *Science* **326**, 818–823 (2009). doi: 10.1126/science.1171242; pmid: 19892975
18. S. Hacein-Bey-Abina *et al.*, Insertional oncogenesis in 4 patients after retrovirus-mediated gene therapy of SCID-X1. *J. Clin. Invest.* **118**, 3132–3142 (2008). doi: 10.1172/JCI35700; pmid: 18688285
19. E. Montini *et al.*, Hematopoietic stem cell gene transfer in a tumor-prone mouse model uncovers low genotoxicity of lentiviral vector integration. *Nat. Biotechnol.* **24**, 687–696 (2006). doi: 10.1038/nbt1216; pmid: 16732270
20. E. Montini *et al.*, The genotoxic potential of retroviral vectors is strongly modulated by vector design and integration site selection in a mouse model of HSC gene therapy. *J. Clin. Invest.* **119**, 964–975 (2009). doi: 10.1172/JCI37630; pmid: 19307726
21. A. Capotondo *et al.*, Safety of arylsulfatase A overexpression for gene therapy of metachromatic leukodystrophy. *Hum. Gene Ther.* **18**, 821–836 (2007). doi: 10.1089/hum.2007.048; pmid: 17845130
22. S. Scaramuzza *et al.*, Preclinical safety and efficacy of human CD34$^+$ cells transduced with lentiviral vector for the treatment of Wiskott-Aldrich syndrome. *Mol. Ther.* **21**, 175–184 (2013). doi: 10.1038/mt.2012.23; pmid: 22371846
23. R. L. Koul *et al.*, Late infantile metachromatic leucodystrophy in two siblings. *Indian Pediatr.* **31**, 694–698 (1994).pmid: 7896397
24. S. Yatziv, A. Russell, An unusual form of metachromatic leukodystrophy in three siblings. *Clin. Genet.* **19**, 222–227 (1981). doi: 10.1111/j.1399-0004.1981.tb00702.x; pmid: 6115727
25. T. Satoh *et al.*, Metachromatic leukodystrophy. Report of siblings with the juvenile type of metachromatic leukodystrophy. *Acta Pathol. Jpn.* **38**, 1041–1051 (1988). pmid: 3188912
26. A. Biffi *et al.*, Metachromatic leukodystrophy-mutation analysis provides further evidence of genotype-phenotype correlation. *Clin. Genet.* **74**, 349–357 (2008). doi: 10.1111/j.1399-0004.2008.01058.x; pmid: 18786133
27. C. Kehrer, G. Blumenstock, C. Raabe, I. Krägeloh-Mann, Development and reliability of a classification system for gross motor function in children with metachromatic leucodystrophy. *Dev. Med. Child Neurol.* **53**, 156–160 (2011). doi: 10.1111/j.1469-8749.2010.03821.x; pmid: 21087233
28. S. Groeschel *et al.*, Metachromatic leukodystrophy: Natural course of cerebral MRI changes in relation to clinical course. *J. Inherit. Metab. Dis.* **34**, 1095–1102 (2011). doi: 10.1007/s10545-011-9361-1; pmid: 21698385
29. A. Biffi *et al.*, Lentiviral vector common integration sites in preclinical models and a clinical trial reflect a benign integration bias and not oncogenic selection. *Blood* **117**, 5332–5339 (2011). doi: 10.1182/blood-2010-09-306761; pmid: 21403130
30. U. Abel *et al.*, Real-time definition of non-randomness in the distribution of genomic events. *PLoS ONE* **2**, e570 (2007). doi: 10.1371/journal.pone.0000570; pmid: 17593969
31. G. P. Wang *et al.*, Dynamics of gene-modified progenitor cells analyzed by tracking retroviral integration sites in a human SCID-X1 gene therapy trial. *Blood* **115**, 4356–4366 (2010). doi: 10.1182/blood-2009-12-257352; pmid: 20228274
32. F. Ginhoux *et al.*, Fate mapping analysis reveals that adult microglia derive from primitive macrophages. *Science* **330**, 841–845 (2010). doi: 10.1126/science.1194637; pmid: 20966214
33. J. Priller *et al.*, Targeting gene-modified hematopoietic cells to the central nervous system: Use of green fluorescent protein uncovers microglial engraftment. *Nat. Med.* **7**, 1356–1361 (2001). doi: 10.1038/nm1201-1356; pmid: 11726978
34. A. Capotondo *et al.*, Brain conditioning is instrumental for successful microglia reconstitution following hematopoietic stem cell transplantation. *Proc. Natl. Acad. Sci. U.S.A.* **109**, 15018–15023 (2012). doi: 10.1073/pnas.1205858109; pmid: 22923692
35. K. Araya *et al.*, Localized donor cells in brain of a Hunter disease patient after cord blood stem cell transplantation. *Mol. Genet. Metab.* **98**, 255–263 (2009). doi: 10.1016/j.ymgme.2009.05.006; pmid: 19556155
36. K. Allers *et al.*, Evidence for the cure of HIV infection by CCR5Δ32/Δ32 stem cell transplantation. *Blood* **117**, 2791–2799 (2011). doi: 10.1182/blood-2010-09-309591; pmid: 21148083
37. S. J. Howe *et al.*, Insertional mutagenesis combined with acquired somatic mutations causes leukemogenesis following gene therapy of SCID-X1 patients. *J. Clin. Invest.* **118**, 3143–3150 (2008). doi: 10.1172/JCI35798; pmid: 18688286
38. S. Hacein-Bey-Abina *et al.*, A serious adverse event after successful gene therapy for X-linked severe combined immunodeficiency. *N. Engl. J. Med.* **348**, 255–256 (2003). doi: 10.1056/NEJM200301163480314; pmid: 12529469
39. S. Hacein-Bey-Abina *et al.*, LMO2-associated clonal T cell proliferation in two patients after gene therapy for SCID-X1. *Science* **302**, 415–419 (2003). doi: 10.1126/science.1088547; pmid: 14564000
40. S. Stein *et al.*, Genomic instability and myelodysplasia with monosomy 7 consequent to EVI1 activation after gene therapy for chronic granulomatous disease. *Nat. Med.* **16**, 198–204 (2010). doi: 10.1038/nm.2088; pmid: 20098431
41. D. Zychlinski *et al.*, Physiological promoters reduce the genotoxic risk of integrating gene vectors. *Mol. Ther.* **16**, 718–725 (2008). doi: 10.1038/mt.2008.5; pmid: 18334985
42. D. J. Russell *et al.*, The gross motor function measure: A means to evaluate the effects of physical therapy. *Dev. Med. Child Neurol.* **31**, 341–352 (1989). doi: 10.1111/j.1469-8749.1989.tb04003.x; pmid: 2753238
43. R. G. Voigt *et al.*, Concurrent and predictive validity of the cognitive adaptive test/clinical linguistic and auditory milestone scale (CAT/CLAMS) and the Mental Developmental Index of the Bayley Scales of Infant Development. *Clin. Pediatr. (Phila.)* **42**, 427–432 (2003). doi: 10.1177/000992280304200507; pmid: 12862346
44. C. Mattioli *et al.*, Sedation for children with metachromatic leukodystrophy undergoing MRI. *Paediatr. Anaesth.* **17**, 64–69 (2007). doi: 10.1111/j.1460-9592.2006.02002.x; pmid: 17184435
45. S. Martino *et al.*, Expression and purification of a human, soluble Arylsulfatase A for Metachromatic Leukodystrophy enzyme replacement therapy. *J. Biotechnol.* **117**, 243–251 (2005). doi: 10.1016/j.jbiotec.2005.01.018; pmid: 15862354
46. G. V. Childs, In situ hybridization with nonradioactive probes. *Methods Mol. Biol.* **123**, 131–141 (2000). pmid: 10547766
47. A. Aiuti *et al.*, *Science* **341**, 1233151 (2013). doi: 341,1233151

Acknowledgments: This work was supported by Fondazione Telethon (TIGET grant B2 and F3), the European Union (EU) Seventh Framework Program (FP7)–HEALTH F2-2010-241622 [Therapeutic Challenge in Leukodystrophies (LEUKOTREAT)], the European Leukodystrophy Foundation (ELA 2007-00515), and Italian Ministry of Health (Progetto Giovani Ricercatori GR-2008-57) to A.B.; Fondazione Telethon (TIGET grant D2), the EU FP7-HEALTH (GA 222878 PERSIST), the European Research Council (ERC) (Advanced Grant 249845 TARGETINGGENETHERAPY), and the Italian Ministry of Health to L.N.; Fondazione Telethon (TIGET grant D1 and core grant), Association for International Cancer Research (AICR 09-0784), and Italian Ministry of Health (Progetto Giovani Ricercatori GR-2007-684057) to E.M.; and the Italian Higher Institute of Health (Italia-USA Collaborative Program on Rare Diseases) to M.S. We thank the medical and nursing staff of the TIGET Pediatric Clinical Research Unit, Pediatric Immunohematology and Bone Marrow Transplant Unit; R. Miniero, R. Fiori, P. Silvani, and L. Sacchi for critical help with patient management; L. Callegaro, S. Di Nunzio, M. Bonopane, G. Tomaselli, and the TIGET clinical trial office for trial management; P. Massariello and other MolMed staff for help with patient cell manipulation; I. Spiga for ARSA gene mutation analysis; S. Gerevini for initial brain MRI studies; P. Aubourg for patient referral and, together with N. Cartier, for sharing the original ALD HSC-GT IS data set; D. Redaelli and S. Acquati for molecular and biochemical studies; F. Morena for biochemical studies; A. Capotondo for studies on the MLD mouse model; M. Marini and D. Cesana for technical help on LAM-PCR amplification and bioinformatics; M. Gabaldo for support with project management; G. Royal, L. King, and F. Govani for help with 454-pyrosequencing and sequence data management; and J. Appleby for advice and support. We are especially indebted to F. Pasinelli for unremitting support of this project and to the patients who joined the trial and their families for their commitment and endurance. We dedicate this work to the memory of all MLD patients and their families who accompanied us in the long path from preclinical studies to clinical testing. C.B. is Chief Executive Officer and Chairman of the Scientific Advisory Board of MolMed S.p.A., a biotechnology company focused on research, development, and clinical validation of new cancer therapies. L.N. is an inventor of several patents on lentiviral vector technology that are owned by the Salk Institute and Cell Genesis and are licensed to Lentigen. L.N. is entitled to receive royalties from one of these patents (U.S. Patent No. 6,013,516 with the Salk Institute).

Supplementary Materials

www.sciencemag.org/cgi/content/full/science.1233158/DC1
Materials and Methods
Figs. S1 to S22
Tables S1 to S19
References (*48*–*60*)

26 November 2012; accepted 25 June 2013
Published online 11 July 2013;
10.1126/science.1233158

Groundwater Arsenic Contamination Throughout China

Luis Rodríguez-Lado,[1]* Guifan Sun,[2] Michael Berg,[1] Qiang Zhang,[2] Hanbin Xue,[1] Quanmei Zheng,[2] C. Annette Johnson[1]†

Arsenic-contaminated groundwater used for drinking in China is a health threat that was first recognized in the 1960s. However, because of the sheer size of the country, millions of groundwater wells remain to be tested in order to determine the magnitude of the problem. We developed a statistical risk model that classifies safe and unsafe areas with respect to geogenic arsenic contamination in China, using the threshold of 10 micrograms per liter, the World Health Organization guideline and current Chinese standard for drinking water. We estimate that 19.6 million people are at risk of being affected by the consumption of arsenic-contaminated groundwater. Although the results must be confirmed with additional field measurements, our risk model identifies numerous arsenic-affected areas and highlights the potential magnitude of this health threat in China.

China faces groundwater quality problems of enormous proportions from both industrial and natural sources (*1*). Populations at risk of exposure to excessive levels of arsenic, a natural groundwater contaminant, have been emerging since the 1960s (*2*–*7*). With the exception of Guizhou province, where endemic arsenicosis is mainly due to coal burning (*7*, *8*), most cases of water-related arsenic poisoning have occurred in arid regions of the northern provinces, probably because of the scarcity of clean water for cooking and drinking from sources other than groundwater.

Apart from geothermal and mining environments, two main environmental conditions are known to be linked to natural arsenic enrichment in groundwater systems (*9*): (i) aerobic alkaline environments in closed basins in arid and semi-arid regions, where high pH leads to alkaline desorption of arsenic from mineral oxides, and (ii) aquifers under strongly reducing conditions, where the release of arsenic is related to reductive dissolution of arsenic-bearing iron (hydr)oxides in sediments. Numerous studies in China have related arsenic-enriched groundwater to reducing conditions (*10*–*16*), particularly in arid regions, where such conditions in alluvial and lacustrine aquifer sediments are often concomitant with high alkalinity and/or salinity. In other areas, such as Taiwan, arsenic release has also been associated with anoxic aquifers (*17*). The few studies reporting arsenic measurements in oxic aquifers in China (*18*–*20*) indicate that arsenic concentrations in oxic groundwaters are mostly below 10 μg liter^{-1}.

[1]Eawag, Swiss Federal Institute of Aquatic Science and Technology, 8600 Dübendorf, Switzerland. [2]Department of Occupational and Environmental Health, School of Public Health, China Medical University, 92 Bei Er Road, Heping District, 110001 Shenyang, China.

*Present address: Departamento de Edafoloxía e Química Agrícola, Universidade de Santiago de Compostela, Fac. de Bioloxía, Campus Vida, 15782 Santiago de Compostela (A Coruña), Spain.

†Corresponding author. E-mail: annette.johnson@eawag.ch

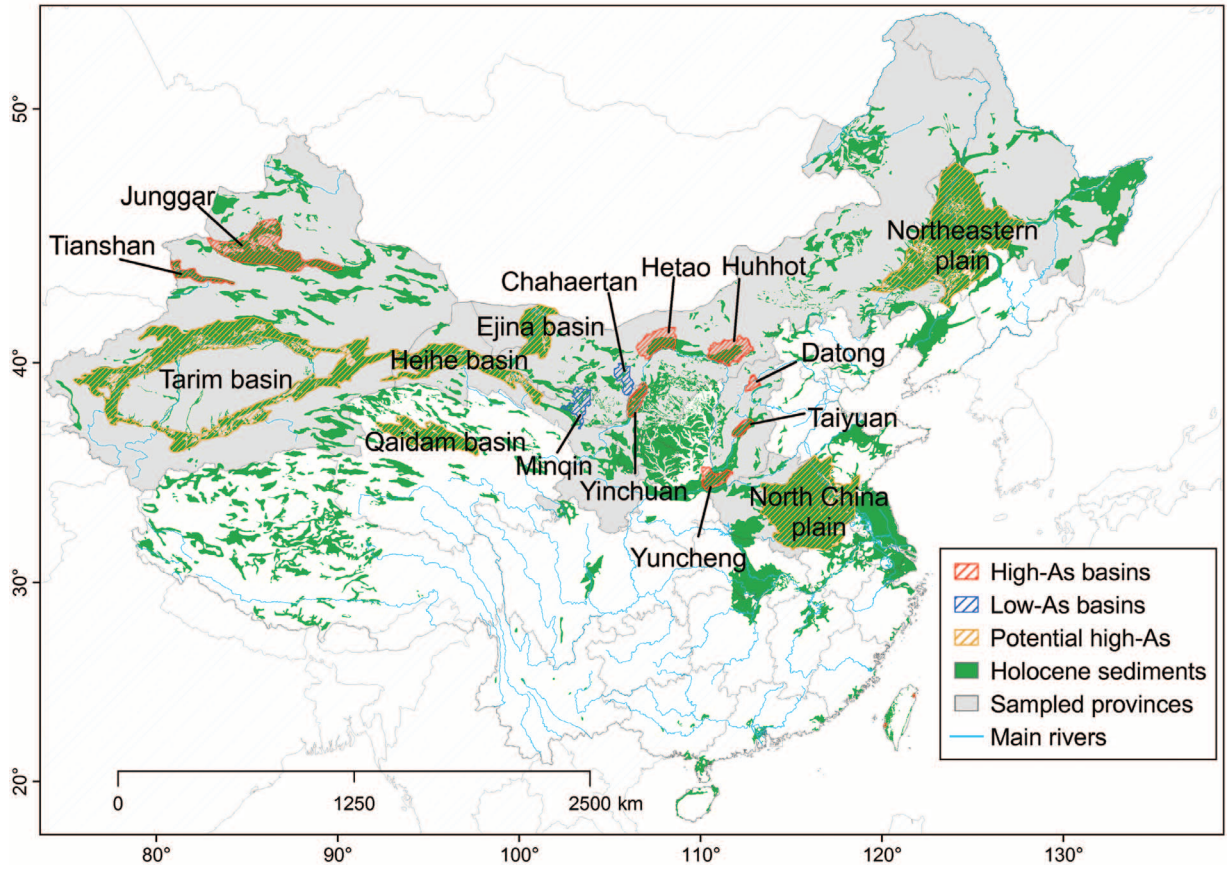


Fig. 1. Location of known and potential arsenic-affected basins in China. Areas with high levels of arsenic (As) are generally characterized by Holocene sediments (green), where large basins may be affected.

Between 2001 and 2005, the Chinese National Survey Program, conducted by the Chinese Ministry of Health, tested some 445,000 wells in 20,517 villages of 292 counties (12% of all counties in China) for arsenic contamination. In almost 5% of wells, arsenic levels were higher than the former Chinese standard of 50 μg liter^{-1}, and about 10,000 individuals were found to be affected by arsenicosis in known and suspected endemic areas (*21*). Screening of wells has continued, and it has been estimated that 5.6 million people are exposed to high concentrations of arsenic in drinking water (>50 μg liter^{-1}) and that some 14.7 million are exposed to arsenic concentrations of >10 μg liter^{-1} (*22*). Because of the sheer size of China, it will take several decades to complete the screening of millions of wells to determine the spatial occurrence and magnitude of arsenic contamination throughout the country.

Here, we present a predictive model that uses survey data and geological and hydrogeochemical parameters as proxies of processes that affect arsenic solubility in groundwater aquifers to identify safe and unsafe areas with respect to geogenic groundwater arsenic contamination. The model was validated with an independent data set and a cut-off probability value of 0.46 (see supplementary materials), revealing fairly good agreement (Cohen's kappa = 0.51), with 77% of the samples correctly classified in the high- and low-risk classes. The model sensitivity (ability to correctly classify samples with arsenic concentrations of >10 μg liter^{-1}) and specificity (ability to correctly classify samples with arsenic concentrations of ≤10 μg liter^{-1}) were 83% and 75%, respectively, which indicates good performance for the prediction of both safe and unsafe areas with respect to arsenic. The model uncertainty is predominantly low (fig. S5) but exceeds 0.5 in the sparsely inhabited sand deserts.

Previous studies in Southeast Asia have identified a relatively small number of geological and hydrogeochemical parameters as significant spatial predictors that can be used to characterize the regional distribution of high arsenic (*23*–*26*). Holocene sediments, for example, have been found to be strongly associated with arsenic contamination. Such coincidence can also be observed in areas reported to suffer from arsenic contamination in China (Fig. 1). We initially considered 16 environmental proxies, in the form of 30 arc sec (~1 km^2) digital raster maps, as potential factors for identifying areas affected by geogenic arsenic hazard. Only eight proxies were significantly linked to the regional distribution of high arsenic occurrence and were used, together with 2668 georeferenced arsenic measurements, to develop an ensemble model with binomial logistic regression as the base classifier (see supplementary materials). The model (Fig. 2A) forecasts that the area at risk of groundwater arsenic contamination (>10 μg liter^{-1}) may encompass more than 580,000 km^2, and it pinpoints elevated arsenic concentrations in regions where endemic arsenic poisoning has already been detected (*27*–*30*). Large areas such as Tarim basin (Xinjiang), Ejina basin (Inner Mongolia), Heihe basin (Gansu), Qaidam basin (Qinghai), the Northeastern plain (Inner Mongolia, Jilin, and Liaoning), and the North China plain (Henan and Shandong) were identified as being potentially affected, although these results must be confirmed with additional field measurements.

The mean model coefficients (table S1) indicate a positive correlation of Holocene sediments, soil salinity, fine subsoil texture, topographic wetness index (TWI; see supplementary materials), and density of rivers with high arsenic, and a negative contribution of slope, distance to rivers, and gravity. Holocene sediments, soil salinity, subsoil texture, and TWI were significant in most of the ensemble members, highlighting their relative importance in predicting the occurrence of groundwater arsenic in relation to the remaining variables. This is consistent with the conditions found in most studies performed in high-risk areas in China, such as Xinjiang province (model sensitivity = 85%) and Hetao-Huhhot basin (model sensitivity = 95%), where high arsenic tends to be associated with the anoxic environments of poorly drained aquifers in young sediments with flat topography and high salinity (Fig. 2B) (*16*). The model also performed well for oxic aquifers, such as Minqin basin, Chahaertan oasis, and Liao-Ho basin (Fig. 2B, areas 3 and 4). Surveys in these areas (*21*, *22*) revealed that these aquifers bear low arsenic concentrations, as correctly predicted by our model with an accuracy ranging from 83 to 98%.

We categorized areas on the probability map as low-risk ($P \leq 0.46$) and high-risk ($P > 0.46$), and cross-referenced the map with a population distribution map for the year 2000. This yielded an estimate of 19,580,000 people in China who live in high-risk areas, mainly in Xinjiang, Inner Mongolia, Henan, Shandong, and Jiangsu provinces (Fig. 3). This may be an overestimation of

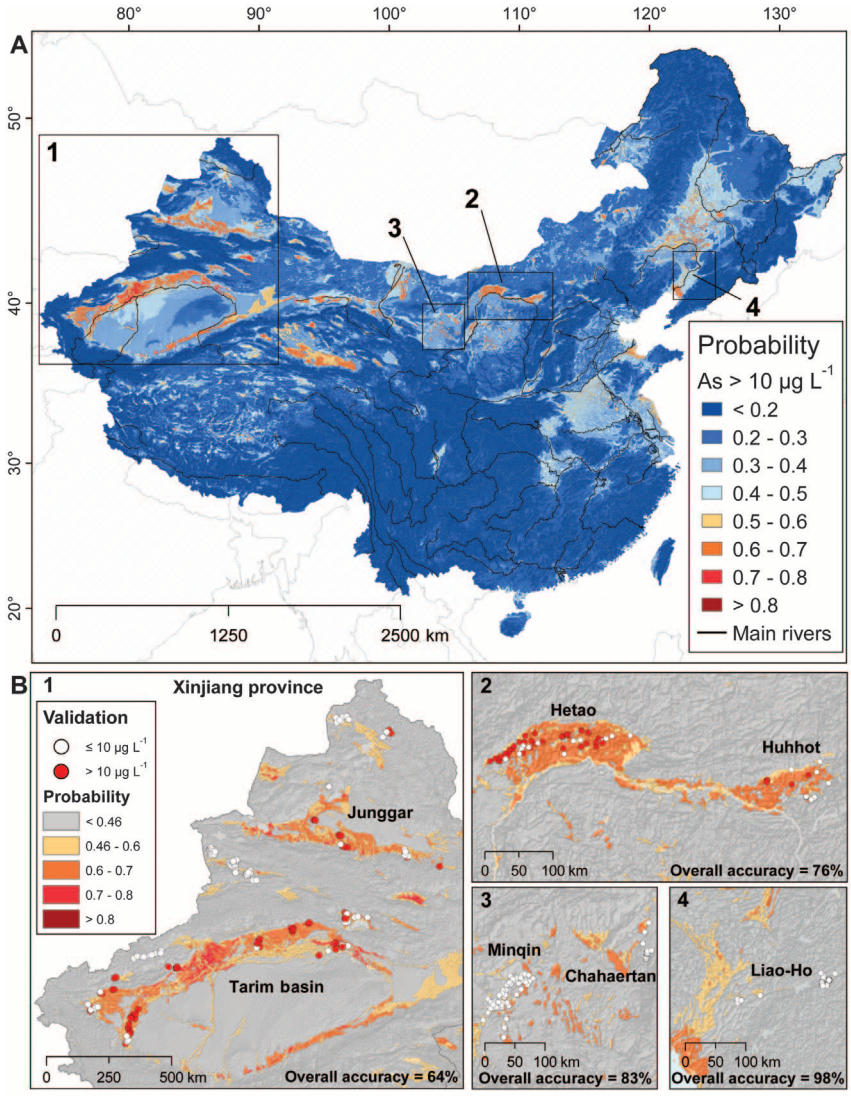


Fig. 2. Arsenic predictive map of China. (**A**) Modeled probability of arsenic concentrations exceeding the 10 μg liter^{-1} threshold in groundwaters. Boxes indicate regions shown in (B). (**B**) Basins used to describe the model performance.

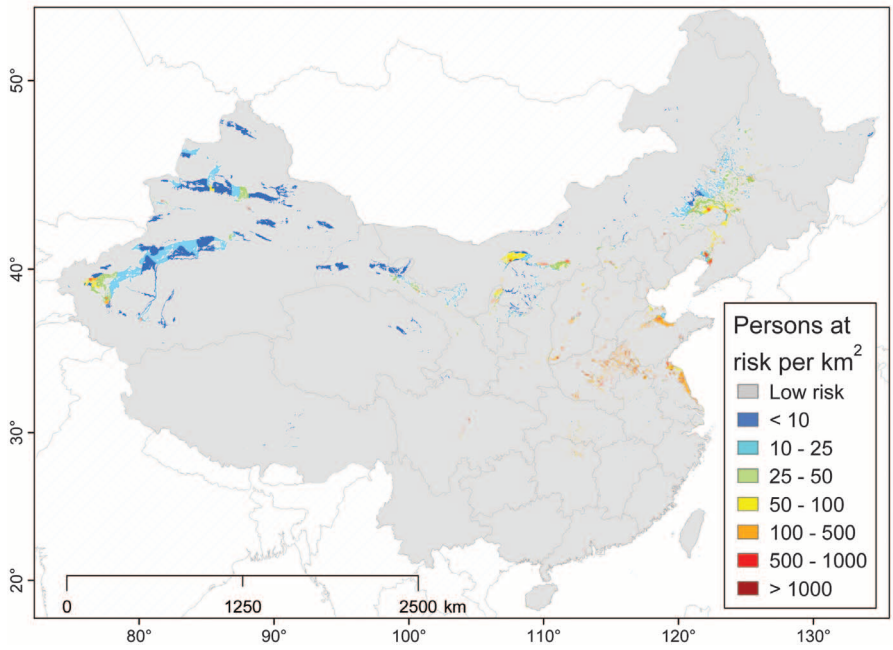


Fig. 3. Estimated Chinese population at potential risk of exposure to arsenic concentrations of >10 μg liter^{-1}. Calculation is based on the model results and population density estimates.

the actual population at risk, because treated and piped water may be used in some places, but water use statistics are not available. However, most of the arsenic-affected areas in China correspond to arid or semiarid regions, where groundwater is the predominant source of drinking water.

Our approach complements traditional groundwater quality surveys, which are expensive and time-consuming. The model requires only a small number of geospatial parameters to provide a preliminary assessment of affected areas, reducing the area that needs to be screened. It may also be appropriate for use in other parts of the world, especially in arid regions such as northwestern Argentina and Chile, where high arsenic concentrations have been reported, or in countries such as Mongolia, Kazakhstan, and Kyrgyzstan, where risk assessments for groundwater arsenic contamination have not yet been performed.

References and Notes

1. J. Qiu, *Science* **334**, 745–745 (2011).
2. G. Sun, *Toxicol. Appl. Pharmacol.* **198**, 268–271 (2004).
3. G. Sun, Y. Xu, Q. Zheng, S. Xi, *Kaohsiung J. Med. Sci.* **27**, 377–381 (2011).
4. J. X. Guo *et al.*, *J. Environ. Sci. Health A* **42**, 1853–1858 (2007).
5. S. Li, T. Xiao, B. Zheng, *Sci. Total Environ.* **421-422**, 31–40 (2012).
6. W. P. Tseng *et al.*, *J. Natl. Cancer Inst.* **40**, 453–463 (1968).
7. Y. Jin, C. Liang, G. He, J. Cao, *J. Hygiene Res.* **32**, 519–540 (2003).
8. J. Liu *et al.*, *Environ. Health Perspect.* **110**, 119–122 (2002).
9. P. L. Smedley, D. G. Kinniburgh, *Appl. Geochem.* **17**, 517–568 (2002).
10. Y. Deng, Y. Wang, T. Ma, *Appl. Geochem.* **24**, 587–599 (2009).
11. H. Guo, Y. Wang, *J. Geochem. Explor.* **87**, 109–120 (2005).
12. H. Guo, B. Zhang, G. Wang, Z. Shen, *Chem. Geol.* **270**, 117–125 (2010).
13. L. H. Zhang, Q. H. Guo, in *Water-Rock Interaction Volumes 1 & 2*, T. D. Bullen, Y. Wang, Eds. (Taylor & Francis, London, 2007), pp. 1299–1303.
14. P. L. Smedley, M. Zhang, G. Zhang, Z. Luo, *Appl. Geochem.* **18**, 1453–1477 (2003).
15. H. Hagiwara, J. Akai, K. Terasaki, T. Yoshimura, H. Luo, *Appl. Geochem.* **26**, 380–393 (2011).
16. X. Xie *et al.*, *Chemosphere* **90**, 1878–1884 (2013).
17. J.-J. Lee, C.-S. Jang, C.-W. Liu, C.-P. Liang, S.-W. Wang, *Environ. Sci. Technol.* **43**, 6662–6668 (2009).
18. M. Currell, I. Cartwright, M. Raveggi, D. Han, *Appl. Geochem.* **26**, 540–552 (2011).
19. W. M. Edmunds, J. Ma, W. Aeschbach-Hertig, R. Kipfer, D. P. F. Darbyshire, *Appl. Geochem.* **21**, 2148–2170 (2006).
20. B. E. O. Dochartaigh, A. M. MacDonald, *Groundwater Degradation in the Chahaertan Oasis, Alxa League, Inner Mongolia* (British Geological Survey, Nottingham, 2006).
21. G. Yu, D. Sun, Y. Zheng, *Environ. Health Perspect.* **115**, 636–642 (2007).
22. G. F. Sun *et al.*, in *Arsenic Exposure and Health Effects IV*, W. R. Chappell, C. O. Abernathy, R. L. Calderon, Eds. (Elsevier, Amsterdam, 2001), pp. 79–85.
23. M. Amini *et al.*, *Environ. Sci. Technol.* **42**, 3669–3675 (2008).
24. L. R. Lado, D. Polya, L. Winkel, M. Berg, A. Hegan, *Appl. Geochem.* **23**, 3010–3018 (2008).
25. L. Winkel, M. Berg, M. Amini, S. J. Hug, C. A. Johnson, *Nat. Geosci.* **1**, 536–542 (2008).
26. L. H. E. Winkel *et al.*, *Proc. Natl. Acad. Sci. U.S.A.* **108**, 1246–1251 (2011).
27. J. Bian, J. Tang, L. Zhang, H. Ma, J. Zhao, *J. Geochem. Explor.* **112**, 347–356 (2012).
28. S. Han, H. Zhang, M. Zhang, *Geochim. Cosmochim. Acta* **74**, A378 (2010).
29. M. N. Mead, *Environ. Health Perspect.* **113**, A378–A386 (2005).
30. Y. Xia, J. Liu, *Toxicology* **198**, 25–29 (2004).

Acknowledgments: Supported by the Sino-Swiss Science and Technology Cooperation Program of the Swiss State Secretariat for Education and Research (project IZLCZ2 123971), the National Science and Technology Pillar Program of China during the 11th Five-Year Plan Period (contract grant no. 2006BAI06B04), and the External Cooperation Program of the Chinese Academy of Sciences. We thank G.-B. Jiang and J. Shi of the Research Center for Eco-Environmental Sciences, Beijing, for support and data collection in the initial phase of the project. L.R.-L. also acknowledges the Isidro Parga Pondal research program from the Xunta de Galicia (Spain) for current financial support. Additional data are available at www.eawag.ch/repository/remarc.

Supplementary Materials

www.sciencemag.org/cgi/content/full/341/6148/866/DC1
Materials and Methods
Figs. S1 to S5
Tables S1 to S7
References (*31*–*50*)

6 March 2013; accepted 19 June 2013
10.1126/science.1237484

Hillslopes Record the Growth and Decay of Landscapes

Martin D. Hurst,[1,2]* Simon M. Mudd,[1] Mikael Attal,[1] George Hilley[3]

Earth's surface archives the combined history of tectonics and erosion, which tend to roughen landscapes, and sediment transport and deposition, which smooth them. We analyzed hillslope morphology in the tectonically active Dragon's Back Pressure Ridge in California, United States, to assess whether tectonic uplift history can be reconstructed using measurable attributes of hillslope features within landscapes. Hilltop curvature and hillslope relief mirror measured rates of vertical displacement caused by tectonic forcing, and their relationships are consistent with those expected when idealizing hillslope transport as a nonlinear diffusion process. Hilltop curvature lags behind relief in its response to changing erosion rates, allowing growing landscapes to be distinguished from decaying landscapes. Numerical modeling demonstrates that hillslope morphology may be used to infer changes in tectonic rates.

Hillslope morphology is a first-order indicator of landscape change, with great potential for investigating landscapes in tectonically active settings (*1*–*3*). Under the condition that erosion rates have adjusted to tectonic uplift, landscape morphology can be used to infer uplift rates (*4*). Until recently, efforts have focused on inferring rates of base-level fall from channel profiles; hillslopes were generally considered insensitive to rapid base-level fall because

they become invariantly steep and planar in such a context (*5*). Advances in the quality of digital topographic data have recently led to new techniques allowing interpretation of hillslope morphology as a first-order indicator of change in boundary conditions, even in rapidly uplifted landscapes (*1*–*3*). In the limiting case that channels respond more rapidly to changes in uplift rates than do hillslopes, the history of tectonic rates may be faithfully archived in the profile form of hillslopes (*6*). Hilltop curvature (C_{HT}) and mean hillslope gradient (S) are expected to vary predictably with relative base-level lowering rates (hereafter equated with tectonic uplift rate, U), provided that hilltops remain soil-mantled (*2*, *7*).

We studied hillslope morphology at the Dragon's Back Pressure Ridge (DBPR), located along the San Andreas Fault (SAF) in California, United States. Small catchments (<400 m long) trending perpendicular to the fault are cut into poorly consolidated sediments of the Paso Robles formation that are readily transportable as soil (*8*). Geological mapping reveals that these sediments are progressively folded as a monocline to the northwest. Surface structures exposed within the North American Plate and magnetotelluric profiles suggest that the SAF is offset in the shallow subsurface and that this offset remains stationary with respect to the North American Plate. Taken together, these observations indicate that flat-lying sediments southwest of the DBPR are progressively deformed as strike-slip motion moves them into and through the deformation zone created by this offset (Fig. 1A). Topography along the DBPR reflects translation through the fixed uplift zone at a rate equal to the mean slip rate along the SAF (33 mm year^{-1}), allowing a space-for-time substitution to analyze topography as a result of the integrated uplift history along the landform. As such, uplift increases rapidly from SE to NW along the landform, peaking 1200 m from the SE tip of the ridge [30 thousand years ago (ka)] and declining by 2000 m from that point (60 ka) (Fig. 1A) (*8*). Additionally, it has been demonstrated that the fluvial system rapidly communicates changes in uplift rates to hillslopes, which is a limiting condition required to examine hillslope responses to changing tectonic rates (*8*).

In steep, rapidly eroding terrain, hillslope gradient is often invariant (*5*, *9*), an observation consistent with geomorphic transport models in which sediment flux increases nonlinearly with hillslope gradient and tends to infinity as the gradient approaches a critical slope, S_C (*2*, *10*, *11*). When tectonic uplift is balanced by surface lowering rates (hereafter referred to as a steady-state relationship), a relationship can be derived from this flux law between two dimensionless topographic measures: (i) an apparent dimensionless erosion rate E^* and (ii) dimensionless relief R^* (*7*) (supplementary materials)

$$E^* = \frac{2C_{HT}L_H}{S_C} \quad (1)$$

$$R^* = \frac{S}{S_C};\ S < S_C \quad (2)$$

where L_H is horizontal hillslope length. Changes in E^* and R^* are primarily driven by changes in C_{HT} and S, respectively. As E^* becomes large, R^* asymptotically approaches unity, indicating that mean slopes approach S_C at high uplift rates (Fig. 2A, dashed line). When the steady-state assumption is violated, deviation from the steady-state relationship (Fig. 2A, dashed line) has been hypothesized to reflect the adjustment of hillslope profiles to changes in relative base-level lowering rates (*6*). Therefore, we calculate E^* and R^* from high-resolution topographic data (see the supplementary materials for details) by quantifying S, C_{HT}, and L_H to reveal landscape history in relation to changing uplift (*2*).

S, C_{HT}, and L_H all increase in response to increased erosion rates (Fig. 1). S attains maximum values by 900 m (27 ka) along the landform and remains high until 2700 m (82 ka), suggesting that S is limited by landsliding in these areas as previously observed (*8*). By 750 m (23 ka), L_H increases to 30 m and remains approximately constant until 2700 m (82 ka). Uplift rates are high (>1 mm year^{-1}) at 900 to 1800 m (27 to 55 ka); in this zone, C_{HT} increases to a maximum value 750 m (23 ka) after uplift has declined.

We used S, C_{HT}, and L_H to calculate E^* and R^*, fixing $S_C = 0.8$ so that R^* cannot exceed unity (S should not exceed S_C). We observed systematic deviations between the measured values and those expected for steady-state hillslopes (Fig. 2A). Initially, increasing S elevates R^* and increasing L_H and C_{HT} causes E^* to rise. R^* does not notably

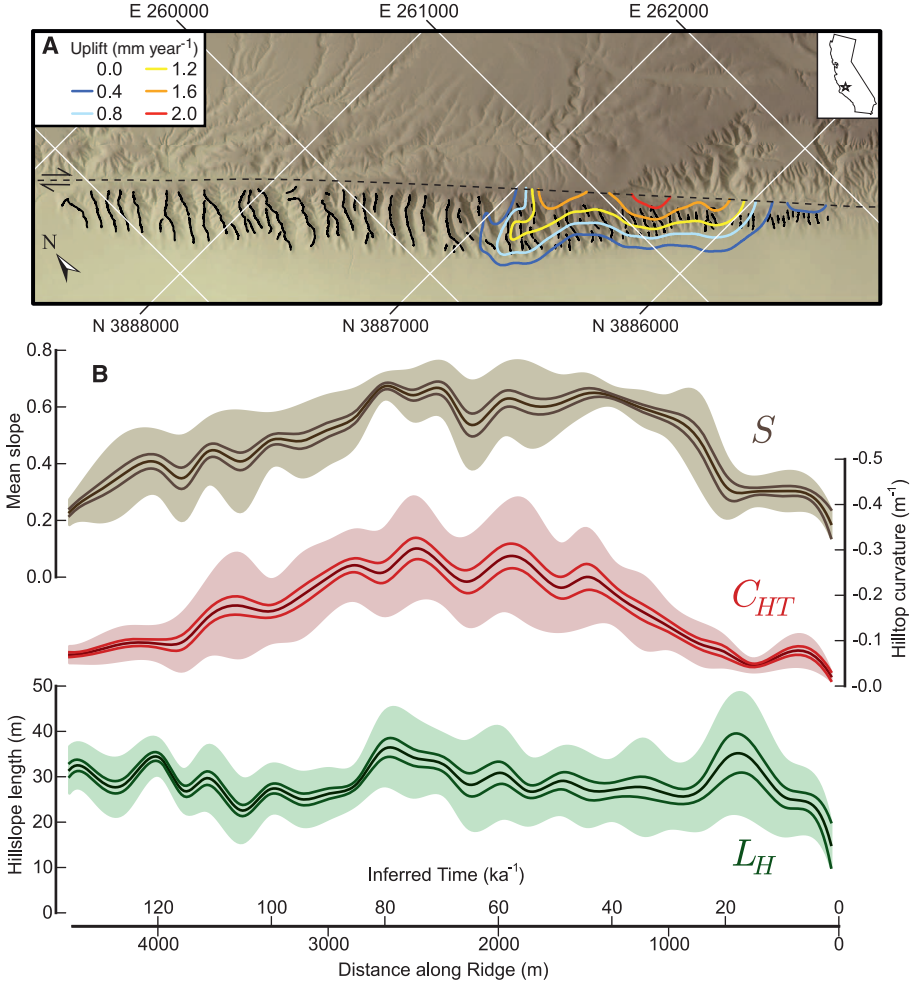


Fig. 1. Study site and hillslope morphology. (**A**) Shaded relief image of the DBPR adjacent to the SAF [Universal Transverse Mercator zone, 11N projection; with eastings (E) and northings (N) given in meters]. Contours show the distribution of surface uplift derived by geological mapping of deformed sedimentary beds (*8*), and black lines depict mapped hilltops. (**B**) Distribution of surface metrics sampled from hilltops in (A). Shaded regions show standard deviations, and solid lines are standard errors about bin means. The space-for-time substitution is based on a slip rate of 0.033 m year^{-1} on the SAF (*8*). S appears limited by 900 m along the DBPR, whereas C_{HT} continues to increase, suggesting rising erosion rates.

[1]School of Geosciences, University of Edinburgh, Drummond Street, Edinburgh EH8 9XP, UK. [2]British Geological Survey, Keyworth, Nottingham NG12 5GG, UK. [3]Department of Geological and Environmental Sciences, Stanford University, 397 Panama Mall, Stanford, CA 94305–2210, USA.

*Corresponding author. E-mail: mhurst@bgs.ac.uk

increase after 25 ka as hillslope gradient approaches S_C. Increasing C_{HT} raises E^* even after uplift ceases at 55 ka. From 80 ka onward, both E^* and R^* decline gradually; however, E^* values are larger for a given R^* value than would be predicted based on the steady-state model. This pattern suggests that changes in C_{HT} (and hence E^*) lag behind S (and hence R^*). The result is tectonically induced hysteresis in hillslope form: high-relief, low-C_{HT} and low-relief, high-C_{HT} hillslopes are associated with active and waning tectonic uplift, respectively.

We constructed a one-dimensional numerical model of hillslope evolution to determine whether the observed hysteresis could be explained by the lag in hillslope response to changes in base-level lowering rates (supplementary materials). The model used a time-dependent uplift pulse idealized as a Gaussian function with the timing (t_{max}*), standard deviation (t_{std}*), and magnitude (U_{max}*) of uplift treated as model parameters. L_H and the transport coefficient D (supplementary materials) were fixed for the modeled hillslope. A Monte Carlo approach was used to find the most likely combination of these parameters according to the misfit between values of R^* and E^* derived from the DBPR topography and those calculated at corresponding model-time values in the forward model.

The resulting distribution of apparent uplift is shown in Fig. 3A. Dimensionalization of the best-fit modeled uplift field uses $D = 0.0086$ m^2 year^{-1} as previously derived for the study site (*12*), and the similarity in magnitude of modeled U with the independently derived mapped uplift field (*8*) supports this value. The model reasonably explains the distribution of hillslope morphology, as shown by the similarity between E^* derived from topography and the modeled hillslope through time (Fig. 3B). Although first-order features of hillslopes within the DBPR were captured using the model, several key features remain unexplained.

First, the inferred U^* distribution implicitly equates changes in base-level lowering rate with changes in rock uplift rate. Channels adjust rapidly but not instantaneously to the waning of uplift (*8*). This delayed channel response introduces an additional 15 to 20 ka ($t^* = 0.14$ to 0.19) lag between changes in uplift and relative base-level fall along hillslopes, similar to the offset between their mapped uplift field and the most likely distribution of U^* derived from the model (Fig. 3A). The modeled t_{std}* values were larger than those observed, with apparent uplift distributed throughout the model run (Fig. 3A).

Second, peak E^* values are smaller than E^* derived from the topography (Fig. 3B). This probably reflects the choice of a modeled Gaussian uplift pulse that is smoother than the documented uplift distribution at the DBPR.

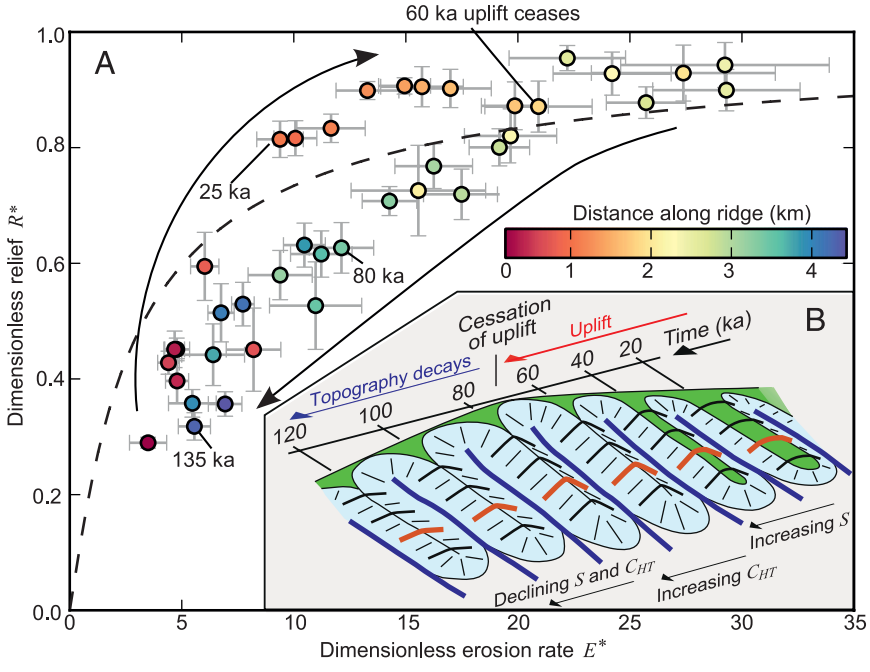


Fig. 2. Hysteresis in hillslope morphology. (**A**) Variation in E^* and R^* with distance toward the NW along the DBPR. The dashed line indicates the theoretical relationship for steady-state hillslopes. Error bars are propagated from standard errors in Fig. 1. The space-for-time substitution is based on a slip rate of 0.033 m a^{-1} on the SAF (*8*). The morphological evolution of hillslopes is distinct for adjustment during uplift versus relaxation after uplift has ceased. (**B**) Schematic diagram illustrating landscape response to the onset and conclusion of uplift and the expected distribution of E^* versus R^*. Values for E^* versus R^* reflect hillslope profiles highlighted in red on the schematic plot. Uplift triggers increased erosion rates in channels that dissect the original surface. A wavelike signal propagates onto the hillslopes, causing steepening (20 to 40 ka). Subsequently, the hilltops respond by becoming sharper (60 to 80 ka). At 60 ka, uplift ceases and channel slopes decrease (*8*). Hillslope gradients and hilltop curvature both reduce gradually in response.

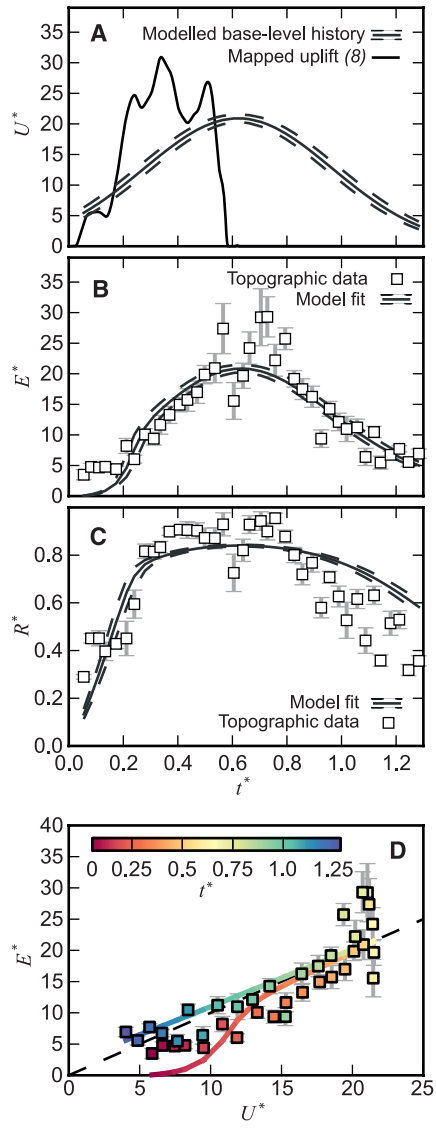


Fig. 3. Modeled uplift. (**A**) Distribution of U^* as a function of t^*. The solid black line represents the mapped uplift field normalized according to eq. S3C (using $D = 0.0086$ m^2 year^{-1} (*12*) and $L_H = 30$ m) and a slip rate of 0.033 m year^{-1}. The gray line is the Gaussian function for apparent uplift (base-level fall), providing the best fit to observed topography from probability densities with mean values (±1σ) of U_{max}* = 20.89 (±0.6), t_{max}* = 0.621 (±0.001), and t_{std}* = 0.490 (±0.015). (**B**) Distribution of E^* through t^*: topography-derived (eq. 5SB) and modeled E^* (Pearson's correlation test gives $R^2 = 0.78$). (**C**) Distribution of modeled and measured R^* through t^*. (**D**) E^* from topography and modeled hillslopes as a function of model-derived apparent uplift U^* through t^*. Hysteresis is recorded so that during accelerating uplift and topographic growth E^* lags behind U^*, whereas during landscape relaxation E^* lags behind a declining U^*.

Third, toward the NW end of the DBPR [beyond 2700 m (80 ka)], R^* is generally smaller than model predictions (Fig. 3C). The mismatch could be due to high transport rates in the study area associated with processes that are not replicated in the model, such as debris flows, landslides, and erosion by overland flow (fig. S2), which have been interpreted as a possible cause for variation in channel concavities within and beyond the uplift zone (*8*).

Finally, we integrated the modeling results with field observations in a conceptual framework for the temporal evolution of the DBPR (Fig. 2B). Accelerated uplift drives erosional adjustment that propagates into a landscape. Channel erosion ensues, with a concomitant delay in hillslope response, so relief can grow without a commensurate change in C_{HT} and thus E^*, leading to data lying above the steady-state E^* versus R^* curve. Once uplift stops, channels rapidly become gentler (*8*), whereas again hillslopes and hilltops are slower to respond, leading to points lying below the steady E^* versus R^* curve. This hysteresis has important implications for the interpretation of transient hillslopes, providing a means to discriminate between growing and decaying landscapes based on hillslope topography alone.

Our findings highlight the potential to distinguish active faults in remote settings, quantify the distribution of fault-related uplift, and delineate zones with high landslide risk (i.e., zones with high uplift rate, steep landscape, and/or proximity to active faults). Such an approach will be best suited to landscapes where hillslopes have a response time that is longer than that of the channel network, but not so long that channels effectively become decoupled from their base level. Alternatively, where the response time of the channel network is very long, hillslopes may be able to track spatial variation in relative base levels (*2*) and provide a complementary test to channel-based erosion rate metrics.

References and Notes

1. R. A. DiBiase, A. M. Heimsath, K. X. Whipple, *Earth Surf. Process. Landf.* **37**, 855–865 (2012).
2. M. D. Hurst, S. M. Mudd, R. Walcott, M. Attal, K. Yoo, *J. Geophys. Res. Earth Surf.* **117**, F02017 (2012).
3. M. D. Hurst, S. M. Mudd, K. Yoo, M. Attal, R. Walcott, *J. Geophys. Res. Earth Surface* **118**, 832 (2013).
4. A. C. Whittaker, *Lithosphere* **4**, 160–164 (2012).
5. R. A. DiBiase, K. X. Whipple, A. M. Heimsath, W. B. Ouimet, *Earth Planet. Sci. Lett.* **289**, 134–144 (2010).
6. S. M. Mudd, D. J. Furbish, *J. Geophys. Res. Earth Surf.* **112**, F03S18 (2007).
7. J. J. Roering, J. T. Perron, J. W. Kirchner, *Earth Planet. Sci. Lett.* **264**, 245–258 (2007).
8. G. E. Hilley, J. R. Arrowsmith, *Calif. Geol.* **36**, 367 (2008).
9. S. A. Binnie, W. M. Phillips, M. A. Summerfield, L. K. Fifield, *Geology* **35**, 743 (2007).
10. D. J. Andrews, R. C. Bucknam, *J. Geophys. Res.* **92**, 12857 (1987).
11. J. J. Roering, J. W. Kirchner, W. E. Dietrich, *Water Resour. Res.* **35**, 853–870 (1999).
12. J. R. Arrowsmith, D. D. Rhodes, D. D. Pollard, *J. Geophys. Res.* **103**, 10141 (1998).

Acknowledgments: This work was supported by a National Environmental Research Council grant (NE/G524128/1) awarded to M.D.H. and by grant NE/H001174/1 and a grant from the Carnegie Trust for the Universities of Scotland to S.M.M.. Thanks to J. Roering, D. Lague, and M. Ellis for helpful discussions. Three anonymous reviewers provided comments that greatly improved the manuscript. Data are available in either the supplementary materials or at the Community Surface Dynamics Modeling System (http://csdms.colorado.edu/wiki/Main_Page).]

Supplementary Materials

www.sciencemag.org/cgi/content/full/341/6148/868/DC1
Materials and Methods
Figs. S1 to S4
References (*13*–*19*)

11 June 2013; accepted 30 July 2013
10.1126/science.1241791

Mapping Tectonic Deformation in the Crust and Upper Mantle Beneath Europe and the North Atlantic Ocean

Hejun Zhu[1]* and Jeroen Tromp[1,2]

We constructed a three-dimensional azimuthally anisotropic model of Europe and the North Atlantic Ocean based on adjoint seismic tomography. Several features are well correlated with historical tectonic events in this region, such as extension along the North Atlantic Ridge, trench retreat in the Mediterranean, and counterclockwise rotation of the Anatolian Plate. Beneath northeastern Europe, the direction of the fast anisotropic axis follows trends of ancient rift systems older than 350 million years, suggesting "frozen-in" anisotropy related to the formation of the craton. Local anisotropic strength profiles identify the brittle-ductile transitions in lithospheric strength. In continental regions, these profiles also identify the lower crust, characterized by ductile flow. The observed anisotropic fabric is generally consistent with the current surface strain rate measured by geodetic surveys.

Minerals that constitute the Earth's crust and upper mantle, such as amphibole and olivine, are highly anisotropic in terms of seismic wavespeeds. Deformation induced by tectonic activity can align the fast axes of these minerals with the directions of flow or principal extension (*1*). This process of lattice preferred orientation leads to a directional and polarization dependence of seismic wavespeeds. Seismic anisotropy has been observed within the crust, lithosphere, and asthenosphere at various scales (*2*–*6*), providing important constraints on past and present deformation within Earth's interior (*7*–*9*).

The European continent has undergone extensive tectonic deformation since the Archaean and was especially heavily reworked by Meso-Cenozoic volcanism and subduction (*10*, *11*). Geodetic surveys have detected substantial deformation due to the convergence of the Eurasian, African, and Arabian Plates (*12*). Most seismic studies in this area have focused on mapping lateral heterogeneities in compressional (*11*) and shear wavespeeds (*13*). Anisotropic images either come from investigations at the global scale (*14*) or local studies limited to a relatively small region (*6*).

Here we present an azimuthally anisotropic model of Europe and the North Atlantic Ocean, constructed based on adjoint tomography. We collected 26,581 three-component seismograms from 190 earthquakes recorded by 745 seismographic stations (supplementary text S1). We used spectral-element (*15*) and adjoint methods (*16*–*18*) to numerically calculate synthetic seismograms and Fréchet derivatives with respect to radial and azimuthal anisotropic model parameters (*19*, *20*) in fully three-dimensional (3D) Earth models (supplementary text S4). Frequency-dependent phase and amplitude measurements of three-component surface waves with periods between 25 and 100 s were used to constrain structure at depths shallower than 200 to 250 km (supplementary text S3). A new anisotropic model of Europe and the North Atlantic Ocean, called EU_{60}, was obtained after 10 preconditioned conjugate gradient iterations (*21*).

Both isotropic shear wavespeed and the anisotropic fast axis reveal numerous features correlated with tectonic activity in the region (Fig. 1). Along the North Atlantic Ridge (NAR), the shear wavespeed is relatively slow (<−3%) down to a depth of 250 km. The fast axis is perpendicular to the ridge system, in agreement with the extensional direction of this divergent plate boundary.

In the western Mediterranean, the east-west–oriented fast direction runs parallel to the opening trajectory of the Algero-Provençal and Tyrrhenian Seas, induced by slab roll-back and migration of the Calabrian and Apennines arcs starting ~30 million years ago (*11*). This strong azimuthal anisotropy correlates with a large shear wavespeed reduction (~−4%) down to depths in excess of 200 km, suggesting intensive deformation and asthenospheric flow associated with trench

[1]Department of Geosciences, Princeton University, Princeton, NJ, USA. [2]Program in Applied and Computational Mathematics, Princeton University, Princeton, NJ, USA.

*Corresponding author. E-mail: hejunzhu@princeton.edu

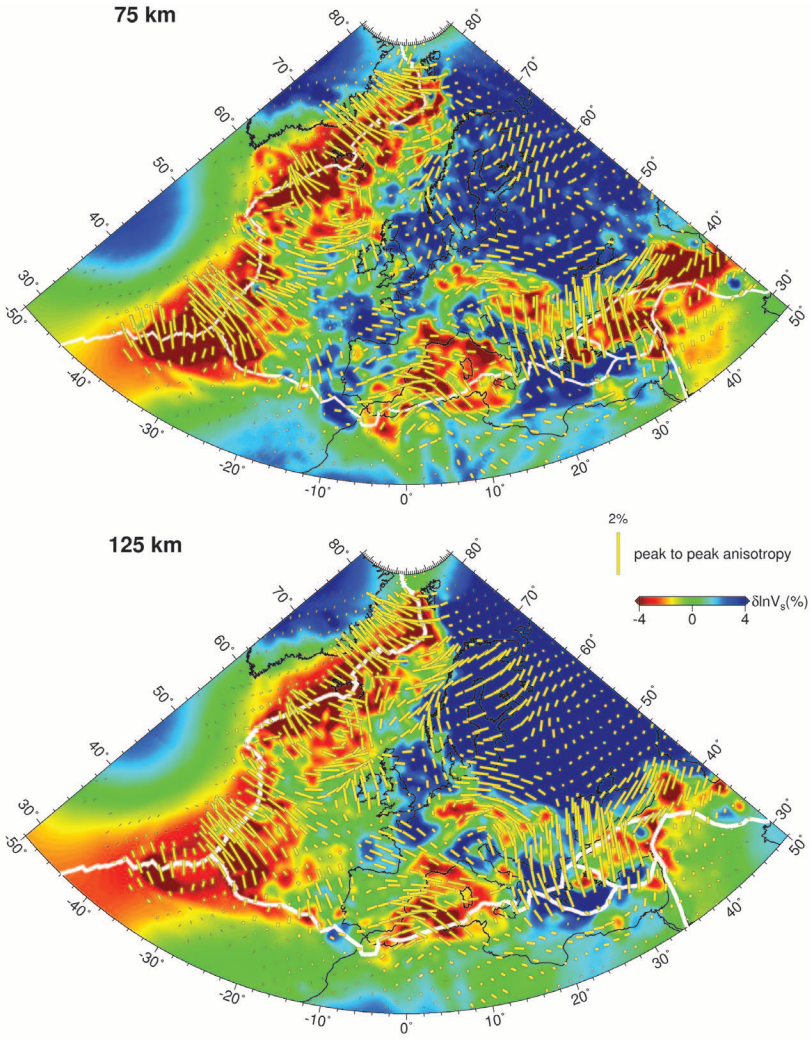


Fig. 1. Isotropic shear wavespeed and azimuthal anisotropy in model EU$_{60}$. The top and bottom panels illustrate horizontal cross sections of relative perturbations in isotropic shear wavespeed and azimuthal anisotropy at depths of 75 and 125 km, respectively. Relative perturbations in shear wavespeed are calculated with respect to 1D reference model STW105 (*28*). The direction and magnitude of the fast axis are given by the orientation and length of the yellow bars. White lines denote global plate boundaries (*29*).

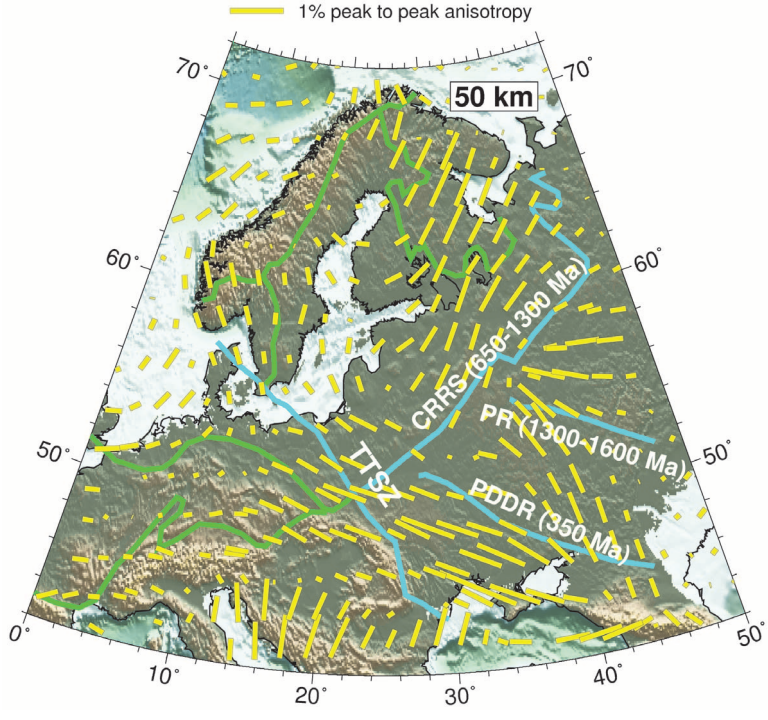


Fig. 2. Azimuthal anisotropy within the EEC at a depth of 50 km. Yellow bars represent the direction and strength of the fast axis. Green lines denote tectonic boundaries modified from (*24*). Cyan lines show the locations of ancient rift systems and suture zones modified from (*24*). CRRS, Central Russia Rift System; PR, Pachelma Rift; PDDR. Pripyat-Dnieper-Donets Rift. The age of each rift event is given according to (*24*).

retreat. Beneath central Europe, the fast direction shows a strong correlation with the arcuate shape of the fast Alpine anomaly down to a depth of 200 km.

The old and stable East European Craton (EEC) is imaged as a fast shear wavespeed anomaly (~+4%) down to depths in excess of 250 km (*22*). Around its border, there are striking azimuthally anisotropic fabrics associated with the accretion of this craton since the Paleozoic era. To the northwest, the Caledonian Orogeny along the western coast of Scandinavia is dominated by a nearly northeast-southwest fabric within the depth ranging from 75 to 150 km, which changes abruptly to a weak east-west trend beneath the Baltic Shield (BS).

On the western border of the EEC, there is a prominent contrast in isotropic shear wavespeed separating the Precambrian East European Platform (EEP) from Phanerozoic central and western Europe, namely the Tornquist-Teisseyre Suture Zone (TTSZ) (*23*). The fast axis runs parallel to the trend of this suture zone from Denmark to the Black Sea. To the west of the TTSZ, the anisotropic fabric follows the strike of several remarkably slow wavespeed anomalies associated with the Bohemian Massif, the Central Slovakian Volcanic Field, and the Pannonian Basin (*22*). The anisotropic strength is relatively weak to the east of the TTSZ at depths greater than 125 km.

Along the southern border of the EEP, northward motion of the Arabian Plate encounters the stable EEC, where its trajectory turns from northerly to east-westerly and contributes to the counterclockwise rotation of the Anatolian Plate (Fig. 1). Furthermore, the Aegean is revealed as a strong slow anomaly, and the fast direction changes from northeast-southwest in the north to north-south in the south, resulting from the westward motion of Anatolia and retreat of the Hellenic trench. Across the fast wavespeed anomaly of the Hellenic arc, the fast axis changes abruptly from trench-normal in the north to trench-parallel in the south, indicating retreat of the Hellenic trench since the Mid-Eocene (*6*).

Although the shear wavespeed structure of the EEC is relatively simple as compared to that of central and western Europe, it exhibits lateral and depth variations in the direction and strength of anisotropy at depths shallower than 200 km (Fig. 1 and fig. S3), in agreement with investigations of anisotropic layering within the continental lithosphere beneath North America (*3*–*5*). Tectonic boundaries, such as the Paleozoic Orogenies and the TTSZ, as well as some ancient rift systems, are superimposed on the anisotropic field within the BS and EEP at a depth of 50 km

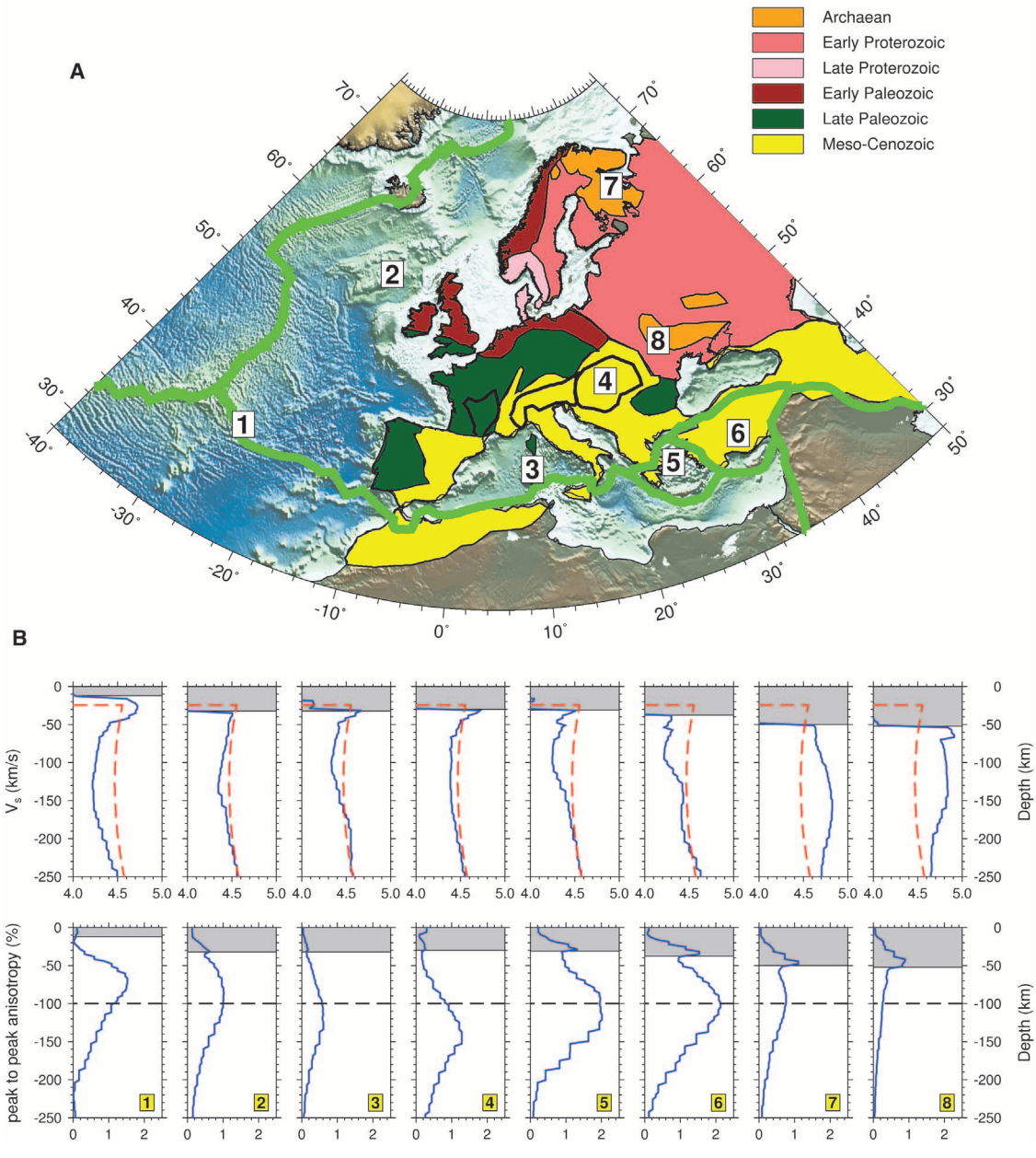


Fig. 3. 1D profiles of isotropic shear wavespeed and peak-to-peak anisotropic strength at locations 1 to 8. (**A**) Simplified tectonic map of the European continent, modified from (*24*). Colors denote the age of each tectonic province. Green lines refer to global plate boundaries (*29*). (**B**) 1D profiles of isotropic shear wavespeed V_s (upper panel) and peak-to-peak anisotropic strength (bottom panel) at locations 1 to 8 in (A). Red dashed lines in the upper panel represent wavespeed profiles from 1D reference model STW105 (*28*). Gray boxes indicate crustal thickness from model EPCrust (*30*). Black dashed lines in the bottom panels denote a reference depth of 100 km.

(Fig. 2). The anisotropic fabric follows the trends of these ancient rift systems, such as the Pachelma Rift, the Central Russia Rift System, and the Pripyat-Dnieper-Donets Rift (*24*), which are at least 350 million years old. This azimuthally anisotropic pattern might originate from a "frozen-in" fabric in the lower crust during Precambrian rifting (*8*), which is preserved owing to relatively low temperatures and a lack of subsequent tectonic activity within the interior of the EEC.

We compared 1D radial profiles of isotropic shear wavespeeds and peak-to-peak anisotropic strength for oceanic and continental lithospheres (Fig. 3). For typical oceanic regions (profiles 1 to 3), strong shear wavespeed reductions are resolved beneath the oceanic lithosphere (from 70 to nearly 200 km), indicating the regime of the ductile asthenosphere. Anisotropy within the crust and lithosphere is relatively weak as compared to that in the asthenosphere. The peak-to-peak anisotropic strength first increases monotonically with depth, exceeding more than 1%, and then steadily decreases with depth below its maximum value. When profiles 1 to 3 are compared, it appears that the depth of maximum anisotropy increases with the thickness of the oceanic plate. Substantial anisotropy underlying a weakly anisotropic oceanic lithosphere may reflect a slow spreading rate and strong shear at the base of the Atlantic Plate, an asthenosphere drag mode in contrast to the plate drag mode of the Pacific Ocean. The anisotropic strength profiles for oceanic lithosphere are consistent with mineral physics experiments focused on the transition from brittle to ductile deformation (*25*), with weak anisotropy in the brittle oceanic crust and lithosphere underlain by a ductile region that exhibits substantial anisotropy (*26*, *27*). The depth of maximum anisotropic strength is nearly 150 km beneath the Pannonian Basin, as demonstrated in profile 4, reflecting substantial deformation beneath this strong slow anomaly (Fig. 1).

In contrast, two peaks in anisotropic strength are observed beneath the Aegean Sea and Anatolian Plate in profiles 5 and 6, one within the lower crust and a second at nearly 100 km depth. These features agree with laboratory investigations of lithospheric strength beneath continents, namely, a "sandwich" model with brittle-ductile-brittle-ductile transitions (*25*). The brittle upper crust is revealed as a regime with relatively weak anisotropy. The first peak indicates ductile flow within the lower crust, which may be related to the frozen-in fabric induced by paleo-extensions in the Miocene (*6*). The strong secondary peak is related to current mantle flow associated with the retreat of the Hellenic trench and the counter-

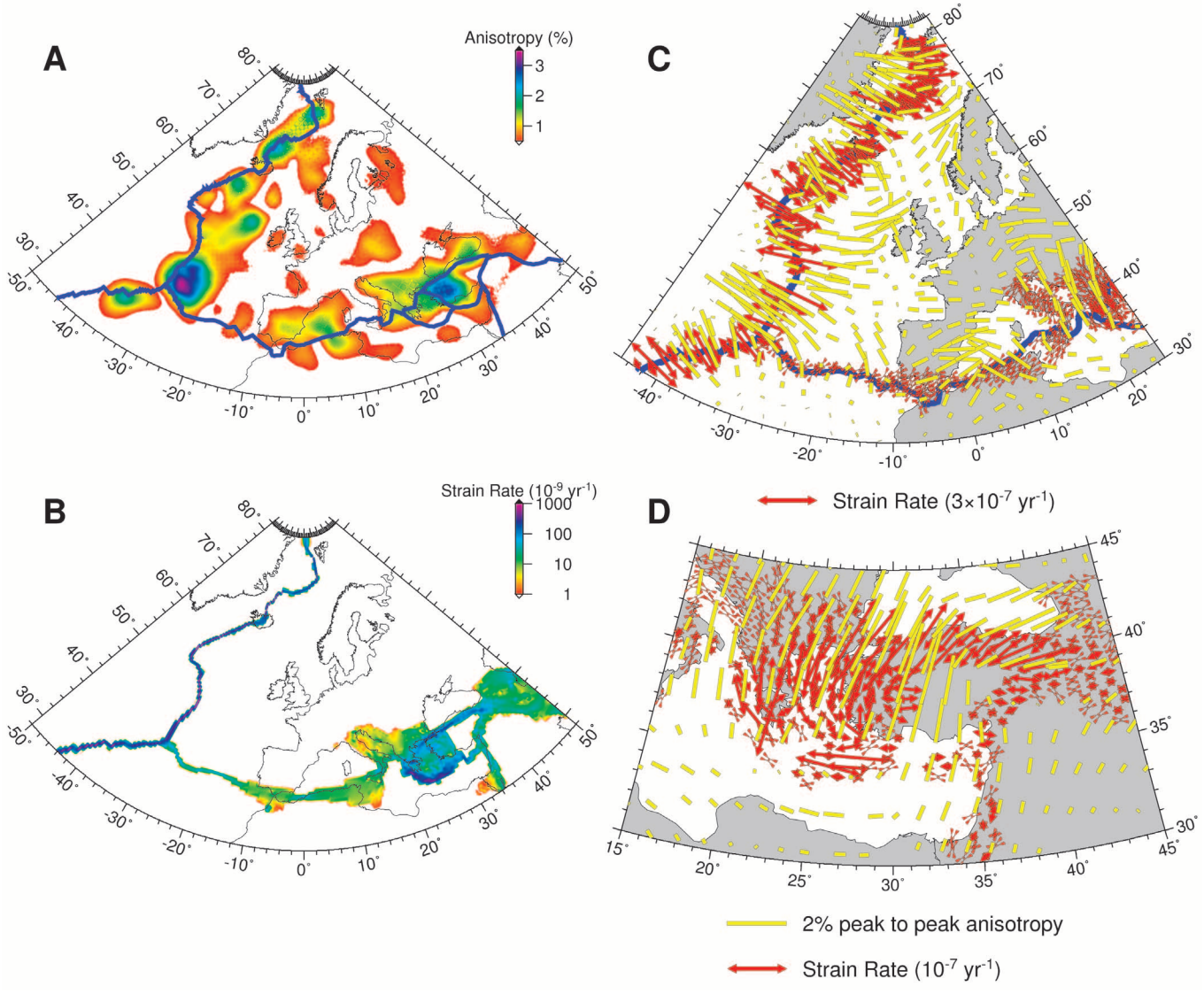


Fig. 4. Comparisons between surface-wave azimuthal anisotropy and current strain-rate field (*12*). (**A**) Contours of peak-to-peak anisotropic strength at a depth of 75 km. (**B**) Contours of the second invariant of the strain-rate field measured at Earth's surface, based on geodetic surveys (*12*). (**C** and **D**) Comparisons between azimuthal anisotropy at a depth of 75 km and the extensional component of strain rate beneath the NAR (C) and the Anatolian/Aegean (D). Yellow and red bars represent the fast axis and the extensional component of the current strain-rate field, respectively. Blue lines in (A) and (C) denote global plate boundaries (*29*).

clockwise rotation of the Anatolian Plate (Fig. 1). The strain rate in this region is on the order of 10^{-7} year^{-1} (*12*), which is sufficient to align the fast axis of olivine with the direction of asthenospheric flow (*1*). These two peaks are accommodated by a transition zone with relatively modest anisotropy.

In profiles 7 and 8, the BS and EEP exhibit large positive shear wavespeed anomalies down to depths in excess of 250 km, corresponding to the fast wavespeed lid underlying continents. The strength profiles involve strong azimuthal anisotropy within the lower crust, in agreement with the location of the ductile lower crust, where the orientation of the fast axis aligns with ancient rift systems (Fig. 2). The anisotropic strength within the lithosphere of the EEC is relatively weak as compared to that in the oceanic lithosphere (profiles 1 to 3) and the continental lithosphere beneath Anatolia (profile 6), which may be indicative of a plunging axis of symmetry owing to relatively small shear underlying this old and stable continent (*14*). Such dipping anisotropy is not accommodated by our current model parameterization.

Geodetic surveys provide direct constraints on deformation at Earth's surface, which may be compared with deformation inferred from surface-wave azimuthal anisotropy. Contours of peak-to-peak anisotropic strength and the second invariant of the strain rate field (*12*) exhibit intensive deformation along the NAR, the western Mediterranean, the Aegean Sea, and the Anatolian Plate (Fig. 4, A and B). The direction of the fast axis from surface-wave tomography and the extensional component of the current strain-rate field beneath the NAR and the Aegean Sea are in good agreement (Fig. 4, C and D). For instance, both run perpendicular to the NAR and reflect counterclockwise rotation of Anatolian lithosphere. Moreover, the transition from trench-normal to trench-parallel patterns beneath the Hellenic arc is observed in both fields (Fig. 4D). These comparisons imply that it is appropriate to use these surface-wave azimuthal anisotropic images (both strength and direction) to infer deformation state and history.

References and Notes

1. S. Zhang, S. Karato, *Nature* **375**, 774–777 (1995).
2. F. Simons, R. Hilst, J. Montagner, A. Zielhuis, *Geophys. J. Int.* **151**, 738–754 (2002).
3. F. Marone, B. Romanowicz, *Nature* **447**, 198–201 (2007).
4. H. Yuan, B. Romanowicz, *Nature* **466**, 1063–1068 (2010).
5. F. Lin, M. Ritzwoller, Y. Yang, M. Moschetti, M. Fouch, *Nat. Geosci.* **4**, 55–61 (2011).
6. B. Endrun, S. Lebedev, T. Meier, C. Tirel, W. Friederich, *Nat. Geosci.* **4**, 203–207 (2011).
7. L. Vinnik, L. Makeyeva, A. Milev, A. Usenko, *Geophys. J. Int.* **111**, 433–447 (1992).
8. P. Silver, *Annu. Rev. Earth Planet. Sci.* **24**, 385–432 (1996).
9. J. Park, V. Levin, *Science* **296**, 485–489 (2002).
10. S. Goes, W. Spakman, H. Bijwaard, *Science* **286**, 1928–1931 (1999).
11. M. J. R. Wortel, W. Spakman, *Science* **290**, 1910–1917 (2000).
12. C. Kreemer, W. Holt, A. Haines, *Geophys. J. Int.* **154**, 8–34 (2003).
13. R. Schivardi, A. Morelli, *Geophys. J. Int.* **185**, 469–484 (2011).
14. E. Debayle, B. Kennett, K. Priestley, *Nature* **433**, 509–512 (2005).
15. D. Komatitsch, J. Tromp, *Geophys. J. Int.* **139**, 806–822 (1999).
16. A. Tarantola, *Geophysics* **49**, 1259–1266 (1984).
17. J. Tromp, C. Tape, Q. Y. Liu, *Geophys. J. Int.* **160**, 195–216 (2005).
18. C. Tape, Q. Y. Liu, A. Maggi, J. Tromp, *Science* **325**, 988–992 (2009).
19. M. Smith, F. Dahlen, *J. Geophys. Res.* **78**, 3321–3333 (1973).
20. J. Montagner, H. Nataf, *J. Geophys. Res.* **91**, 511 (1986).
21. R. Fletcher, C. Reeves, *Comput. J.* **7**, 149–154 (1964).
22. H. Zhu, E. Bozdag, D. Peter, J. Tromp, *Nat. Geosci.* **5**, 493–498 (2012).
23. A. Zielhuis, G. Nolet, *Science* **265**, 79–81 (1994).
24. I. Artemieva, H. Thybo, M. Kaban, in *European Lithosphere Dynamics*, D. G. Gee, R. A Stephenson, Eds. (Geological Society of London, London, 2006), pp. 11–41.
25. D. Kohlstedt, B. Evans, S. Mackwell, *J. Geophys. Res.* **100**, 17,587 (1995).
26. G. Ekström, A. Dziewonski, *Nature* **394**, 168–172 (1998).
27. Y. Gung, M. Panning, B. Romanowicz, *Nature* **422**, 707–711 (2003).
28. B. Kustowski, G. Ekström, A. Dziewonski, *J. Geophys. Res.* **113**, B06306 (2008).
29. P. Bird, *Geochem. Geophys. Geosyst.* **4**, 1027 (2003).
30. I. Molinari, A. Morelli, *Geophys. J. Int.* **185**, 352–364 (2011).

Acknowledgments: This research is supported by NSF grants 1063057 and 1112906. The observed seismic waveforms used in this study were collected from the Incorporated Research Institutions for Seismology (www.iris.edu), Observations and Research Facilities for European Seismology (www.orfeus-eu.org), and the Kandilli Observatory (www.koeri.boun.edu.tr). The open-source spectral-element software package SPECFEM3D_GLOBE and the seismic measurement software package FLEXWIN used in this study are freely available for download via the Computational Infrastructure for Geodynamics (www.geodynamics.org).

Supplementary Materials

www.sciencemag.org/cgi/content/full/science.1241335/DC1
Materials and Methods
Figs. S1 to S11
References (*31–39*)

3 June 2013; accepted 29 July 2013
Published online 8 August 2013;
10.1126/science.1241335

Abundant Porewater Mn(III) Is a Major Component of the Sedimentary Redox System

Andrew S. Madison,[1]*† Bradley M. Tebo,[2] Alfonso Mucci,[3] Bjørn Sundby,[3,4] George W. Luther III[1]

Soluble manganese(III) [Mn(III)] can potentially serve as both oxidant and reductant in one-electron-transfer reactions with other redox species. In near-surface sediment porewater, it is often overlooked as a major component of Mn cycling. Applying a spectrophotometric kinetic method to hemipelagic sediments from the Laurentian Trough (Quebec, Canada), we found that soluble Mn(III), likely stabilized by organic or inorganic ligands, accounts for up to 90% of the total dissolved Mn pool. Vertical profiles of dissolved oxygen and dissolved and solid Mn suggest that soluble Mn(III) is primarily produced via oxidation of Mn(II) diffusing upwards from anoxic sediments with lesser contributions from biotic and abiotic reductive dissolution of MnO_2. The conceptual model of the sedimentary redox cycle should therefore explicitly include dissolved Mn(III).

Manganese (Mn), a trace element essential for life, is involved in many biogeochemical redox processes. In marine and freshwater sediments, Mn is ubiquitous and abundant, exists in multiple oxidation states, and is rapidly cycled between these states. Electron transfers between manganese oxidation states are coupled to reactions that affect the carbon, nitrogen, sulfur, oxygen, and iron (Fe) cycles (*1–4*).

In environmental systems, Mn exists in three oxidation states—Mn(II), Mn(III), and Mn(IV)—but conceptual models of the biogeochemical Mn cycle are based on the notion that only two forms of Mn dominate in natural aquatic environments: particulate Mn(III,IV) oxides and soluble Mn(II). Traditionally, soluble Mn(III) is not considered important in aqueous redox reactions and has been ignored in studies of sediments and in diagenetic modeling (*2*, *5–12*). Yet, Mn(III) can be stabilized in solution when complexed by organic or inorganic ligands such as the siderophore desferrioxamine B (DFOB) (*13*), pyrophosphate (*14*), citrate (*15*), and pyoverdine (*16*). These complexes have thermodynamic stability constants similar to that of the analogous Fe(III) complex (*13*). Soluble Mn(III) complexes, often the dominant dissolved Mn species, have been detected in the suboxic water columns (a region in which the concentrations of O_2 and H_2S are below the detection limits of most analytical techniques) of the Black Sea, Chesapeake Bay, and Baltic Sea (*17–20*). Studies of soluble Mn(III)

[1]School of Marine Science and Policy, University of Delaware, Lewes, DE 19958, USA. [2]Division of Environmental and Biomolecular Systems, Oregon Health and Science University, Beaverton, OR 97006, USA. [3]GEOTOP and Department of Earth and Planetary Sciences, McGill University, Montreal, Quebec H3A 0E8, Canada. [4]Institut des sciences de la mer de Rimouski, Université du Québec à Rimouski, Rimouski, Québec G5L 3A1, Canada.

*Corresponding author. E-mail: andrew_madison@golder.com
†Present address: Golder Associates Inc., 200 Century Parkway, Suite C, Mt. Laurel, NJ 08054, USA.

have been limited to suboxic water columns (*17*–*20*) for methodological reasons, so we have little or no knowledge about soluble Mn(III) in sediment porewaters. Nevertheless, we do know that the nature of the sedimentary environment should favor the production and stabilization of Mn(III) owing to stable redox gradients and elevated concentrations of Mn and dissolved organic matter, which can supply organic ligands. A spectrophotometric method previously optimized for sediment porewaters (*21*) was used to determine the concentration and speciation of dissolved Mn. We analyzed duplicate undisturbed sediment cores recovered in July 2010 at four stations along the Laurentian Trough on a seaward transect from Station 23 (fig. S1) in the Lower St. Lawrence Estuary (LSLE) to Cabot Strait (Station Cabot) at the mouth of the Gulf of St. Lawrence.

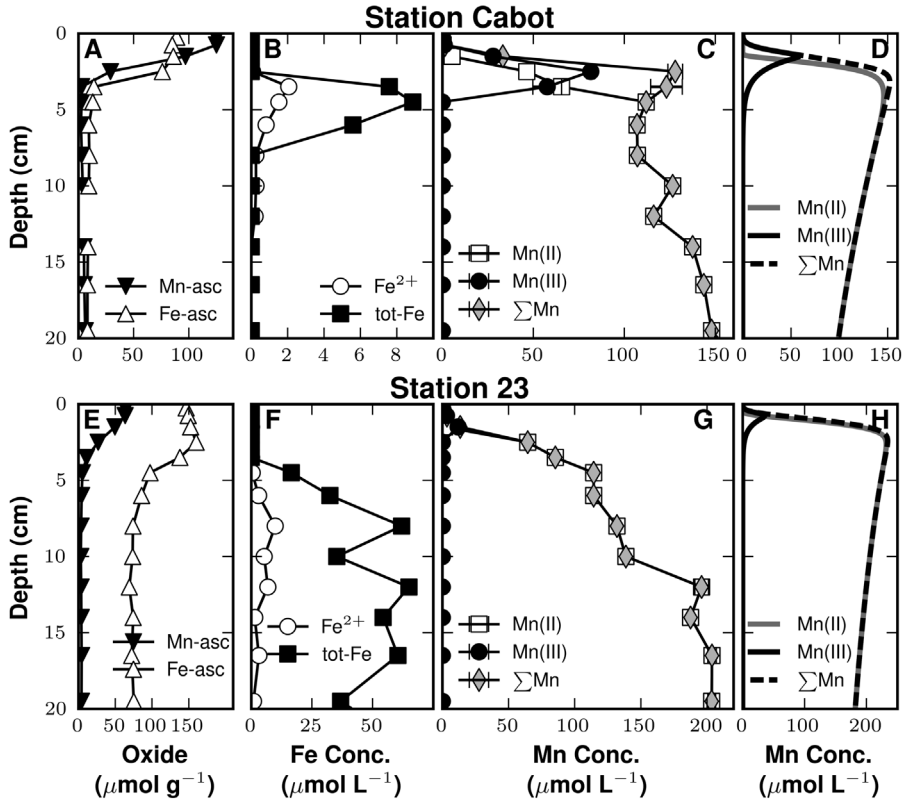


Fig. 1. Mn and Fe sedimentary porewater and solid-phase profiles. From left to right: (**A** and **E**) ascorbate-extractable solid metal content, (**B** and **F**) soluble Fe species, (**C** and **G**) soluble Mn species, and (**D** and **H**) Mn species concentrations at Station Cabot (upper panels) and Station 23 (lower panels) calculated with a diagenetic model. The model simulation agrees well with the measured Mn speciation and total concentration data. In the original diagenetic model (*24*), soluble Mn(III) and Fe(III) species were not considered, and the modeled total Mn concentrations were displaced 2 cm above the experimental data. The natural, porewater Mn(III) complexes are stronger than the Mn(III)-pyrophosphate complex but weaker than the Mn(III)-DFOB complex.

In each core (fig. S2), the O_2 concentration decreased sharply across the sediment-water interface and became undetectable [3 μM detection limit (DL)] at depths ranging from 0.4 cm (Station 23) to 0.8 cm (Station Cabot) below the sediment surface. Sulfide was not detected (0.1 μM DL) in any discrete porewater sample, nor was it detected during microelectrode profiling in the upper 5 to 10 cm of cores analyzed in previous studies (*22*). The surface layer of all cores was enriched in ascorbate-extractable manganese (Mn-oxides) (Fig. 1 and figs. S3 and S4). Dissolved manganese was not detected in the shallowest sampling interval (0 to 0.5 cm) at any of the stations, but was detected above the 0.1 μM detection limit below this depth interval. All soluble Mn(III) profiles displayed a subsurface maximum within the 0.5 to 5.0 cm interval. The highest soluble Mn(III) concentrations were measured at stations Cabot (82 μM; Fig. 1A) and CE (41 μM; fig. S4), where soluble Mn(III) accounted for up to 84% of the total dissolved Mn pool. Comparison with microelectrode O_2 profiles indicate that O_2 (>3 to 25 μM) and soluble Mn(III) coexist within the 0.5 to 1.0 cm depth interval. Lower concentrations of dissolved Mn(III) were detected at stations 23 (12 μM; Fig. 1G) and 16 (20 μM; fig. S4), but Mn(III) still accounted for up to 90% of the soluble Mn pool. Below the Mn(III) maximum in all profiles, Mn(II) concentrations increased to 50 to 250 μM and became

Table 1. Rates of Mn(III) production and loss via the pathways described in the text (reactions 1 to 5), and their relative importance expressed as percentage of total production and total loss at four stations in the St. Lawrence Estuary and Gulf. The downward O_2 flux can account for the production of Mn(III) and subsequent oxidation of upward-diffusing Mn(III). The rates are theoretical maxima and first-order estimates as the calculations do not consider consumption of O_2 or Fe(II) in other reactions, including separate reactions in the Mn cycle.

Mn(III) production pathways

Station	Mn(III) production rate (mmol m^{-2} day^{-1})	Percentage of total Mn(III) production by:	
		Mn(II) + O_2	Mn(IV) + Fe(II)
23	0.020	Up to 100%	No overlap of Mn(IV) and Fe(II)
Cabot	0.075	68%	6.6%
CE	0.051	Up to 100%	5.7%
16	0.017	No O_2 data collected	0.3%

Mn(III) loss pathways

Station	Mn(III) loss rate (mmol m^{-2} day^{-1})	Percentage of total Mn(III) loss	
		Mn(III) + O_2	Mn(III) + Fe(II)
23	0.020	Up to 100%	No overlap of Mn(III) and Fe(II)
Cabot	0.075	Up to 100%	13%
CE	0.051	Up to 100%	31%
16	0.017	No O_2 data collected	0.5%

the dominant Mn species. The rate of Mn(III) complexation by the porphyrin was $4.76 \times 10^{-3} \pm 1.39 \times 10^{-3}$ s^{-1} for the unknown Mn(III) complexes detected in porewater. The porphyrin complexation rates of Mn(III) in Mn(III)-pyrophosphate and Mn(III)-DFOB are $2.06 \times 10^{-2} \pm 2.13 \times 10^{-3}$ s^{-1} and ~2×10^{-5} s^{-1}, respectively (*21*). The St. Lawrence data indicate that the unknown Mn(III) complexes detected are more stable than Mn(III)-pyrophosphate but not as stable as Mn(III)-DFOB.

The soluble Mn(III) profiles in the sediments display a concentration maximum near the oxic-suboxic interface, in agreement with the pattern observed in water-column studies (*17*, *18*). In all depth profiles, the Mn(III) concentration peak is situated below the zone enriched in ascorbate-extractable Mn-oxides and above the Mn(II) peak. This pattern suggests that soluble Mn(III) intermediates are produced via one-electron–transfer reactions involving MnO_2 with reductants and Mn(II) with oxidants and stabilized by ligands. Soluble Mn(III) intermediates could form by at least four pathways: (i) abiotic (*13*) and enzymatic (*2*) oxidation of Mn(II) with O_2 (reaction 1); (ii) MnO_2 reduction by Fe(II) (reaction 2 and fig. S5), H_2S, and FeS, particularly when MnO_2 is in excess to these reductants; (iii) microbial dissimilatory MnO_2 reduction coupled to organic-matter mineralization (reaction 3) (*23*); and (iv) release of Mn from photosystem II components during organic-matter decomposition (*17*).

$$\text{Pathway 1}: 4Mn^{2+} + O_2 + 4H^+ \xrightarrow{L(\text{ligand})} 4Mn^{3+}\text{-L} + 2H_2O \quad (1)$$

$$\text{Pathway 2}: MnO_2 + Fe^{2+} + 4H^+ \xrightarrow{L} Fe^{3+}\text{-L} + Mn^{3+}\text{-L} + 2H_2O \quad (2)$$

$$\text{Pathway 3}: (CH_2O)_x + 4MnO_2 \xrightarrow{L} 4Mn^{3+}\text{-L} + CO_2 + H_2O \text{ (unbalanced)} \quad (3)$$

To assess the relative importance of these pathways, we calculated the fluxes of soluble Mn(III), Mn(II), O_2, and Fe(II) from the porewater profiles, assuming that transport occurs by molecular diffusion (see supplementary materials). We estimated the production rate of Mn(III) as the sum of the upward and downward Mn(III) fluxes from the concentration maximum (Table 1), and we compared this estimate to the Mn(III) production rate(s) that can be supported by the diffusive fluxes of individual reactants [Mn(II), O_2, Fe(II)]. These first-order estimates ignore the effects of bioturbation on transport. The highest Mn(III) production rate was found at Station Cabot (0.075 mmol m^{-2} day^{-1}); the lowest rate was at Station 16 (0.017 mmol m^{-2} day^{-1}). Comparing the Mn(III) production rates to the fluxes of the reactants and accounting for the proper reaction stoichiometry, we found that oxidation of Mn(II) by O_2 (pathway 1; reaction 1) is the dominant Mn(III) production pathway in the Lawrentian Trough sediments as it accounts for up to 100% of the Mn(III) production at stations 23 and CE and up to 68% at Station Cabot.

Laboratory voltammetry experiments (fig. S7) reveal that Mn(III) intermediates also form during the reduction of MnO_2 by Fe(II) in the presence of DFOB, producing a Fe(III)-DFOB peak at approximately –0.50 V and a Mn(III)-DFOB peak at –1.19 V (pathway 2; reaction 2), but the calculated Fe(II) flux (Table 1) indicates that this pathway could account for a maximum of only 6.4% of the total Mn(III) production at Station Cabot and even less at the other stations. At Station Cabot, the two Mn(III) production pathways account for up to 75% (reaction 1 = 68%, reaction 2 = 7%) of the calculated Mn(III) production so about a quarter of the Mn(III) detected at Station Cabot must be produced via other pathways.

In all cores, the decrease in Mn oxide concentration with depth in the upper centimeters coincides with an increase in soluble Mn(III) (Fig. 1 and figs. S3 and S4). This overlap indicates a potential link between dissimilatory MnO_2 reduction and Mn(III) production (pathway 3; reaction 3) (*23*). Biogeochemical models indicate that anaerobic respiration of MnO_2 accounts for 16% of total organic-matter mineralization at Station Cabot (*24*). Recently, soluble Mn(III) was shown to form by pathway 3 in experiments using a strain of *Shewenella putrefaciens* (*23*). Pathway 3 likely accounts for a portion of the ~25% Mn(III) production rate deficit observed at Station Cabot (deficit = 100% – reaction 1 – reaction 2).

With our present detection limit, it is not possible to assess the flux of Mn(III) across the sediment-water interface due to diffusion and/or bioturbation (*25*, *26*). Although our method could not detect Mn in the overlying water, maintaining a long-term mass balance for Mn requires a minor flux of dissolved Mn out of the sediment (*27*). The oxygen profiles show a pronounced change in curvature near or just below 0.5-cm depth (fig. S2), which is indicative of an increased consumption rate of oxygen at this depth. At stations 23, CE, and Cabot, soluble Mn(III) was depleted below the 100 nM detection limit in the shallowest sampling interval (0 to 0.5 cm), but overlapped with O_2 below 0.5-cm depth, suggesting that oxidation by O_2 inhibits Mn(III) from reaching the sediment-water interface. The oxidation reaction can be described as

$$4Mn^{3+}\text{-L} + O_2 + 4H^+ \xrightarrow{L} 4Mn(IV)_{(S)} + 2H_2O + L \quad (4)$$

Using reaction 4 and comparing the calculated fluxes of O_2 and Mn(III), we estimated (Table 1) that the supply of O_2 is more than sufficient to oxidize the upward flux of Mn(III) at stations 23, CE, and Cabot. Thus, oxidation of Mn(III) by O_2 is likely the principal removal mechanism of Mn(III) in surface sediments.

Below the soluble Mn(III) concentration maximum, Mn(III) can be reduced to Mn(II) via two pathways: (i) bacterial reduction (*14*, *23*) and (ii) abiotic reduction with reductants such as Fe(II) and H_2S (*14*, *17*, *28*). Porewater H_2S was not detected in the first 10 cm of any of the cores and is not likely to be the reductant, but the deepest point at which soluble Mn(III) was detected at stations CE, 16, and Cabot coincides with the

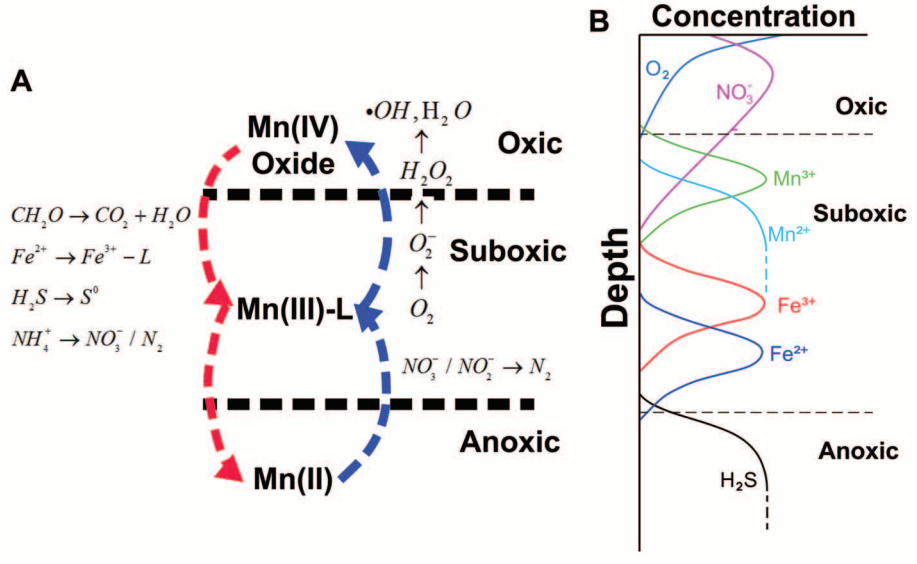


Fig. 2. Idealized update of the Mn cycle and sedimentary porewater redox profile. (**A**) The Mn cycle with one-electron Mn reactions explicitly included. O_2, present at trace concentration levels in the suboxic zone, is a potential Mn^{2+} oxidant (*31*, *32*). Nitrate and nitrite are also potential Mn^{2+} oxidants, but these reactions have not been confirmed in sediment studies; likewise, ammonium is a potential reductant for MnO_2 (*4*, *28*). (**B**) An update of the Froelich *et al.* (*5*) paradigm for sediment biogeochemistry with Mn(III) and Fe(III) included as major components of the cycles.

depth where upward migrating Fe(II) was first detected. Given the calculated fluxes of Mn(III) and Fe(II) and the 1:1 stoichiometry in reaction 5, we estimated that up to 31% of Mn(III) can be reduced by Fe(II) at Station CE (Table 1).

$$Mn^{3+}\text{-L} + Fe^{2+} \rightarrow Mn^{2+} + Fe^{3+}\text{-L} \quad (5)$$

At stations Cabot (13%) and 16 (0.5%), this reduction pathway is less important. Although these results imply that abiotic Mn(III) reduction is important for Mn(III) removal, it is not the most important anoxic removal pathway. Nevertheless, it does have important implications for the Fe cycle, as the downward flux of Mn(III) is sufficient to oxidize the entire upward flux of Fe(II). This pathway, along with several others (*29*, *30*), also leads to soluble and/or colloidal organic Fe(III) production as shown in Fig. 1 and figs. S3 and S4 [Fe(III) = Fe_{total} – Fe(II)]. The reduction of Mn(III) by Mn-reducing bacteria, such as *S. putrefaciens* (*14*, *23*), likely accounts for the consumption of the remaining (69 to 99.5%) downward flux of Mn(III). Prior studies found a linear correlation between Mn(III) reduction and carbon oxidation (*14*, *23*), so this pathway could have implications for organic-matter mineralization. For these reasons, we have revised the current sedimentary redox paradigm (*5*) to include the above Mn(III) production and removal pathways (Fig. 2). We have also added reactions 1 and 4, as well as an unknown generalized Mn(III) microbial reduction pathway (see supplementary materials), to an established biogeochemical model of sediment diagenesis (*24*). The model results (Fig. 1, A and H) reproduce the position and shape of the soluble Mn(III) peak.

Our findings have broad implications for understanding Mn cycling in sediments. First, the current sedimentary redox model (*5*) should be revised to accommodate soluble Mn(III) and Fe(III) species. A proposed revision should highlight the importance of one-electron–transfer reactions for the Mn cycle (Fig. 2A) and explicitly consider dissolved Mn(III) and Fe(III) (Fig. 2B). Second, because Mn(III) can act as either an electron acceptor or an electron donor, the reduction-oxidation capacity of the soluble Mn pool in sediments has been underestimated. For (hemi)pelagic sediments, it appears that oxidation of Mn(II) by O_2 is an important pathway to soluble Mn(III). Soluble Mn(III) intermediates are also produced during dissimilatory MnO_2 reduction upon organic-matter mineralization and during abiotic reduction of MnO_2 by reductants such as Fe(II) and H_2S. Soluble Mn(III) is likely to be ubiquitous in sediment porewaters, where it would facilitate key electron-transfer processes in global biogeochemical cycles.

References and Notes

1. B. L. Lewis, W. M. Landing, *Deep-Sea Res.* **38**, S773–S803 (1991).
2. B. M. Tebo, *Deep-Sea Res. A, Oceanogr. Res. Pap.* **38**, S883–S905 (1991).
3. G. W. Luther III, *Geomicrobiol. J.* **22**, 195–203 (2005).
4. G. W. Luther, *Aquat. Geochem.* **16**, 395–420 (2010).
5. P. Froelich *et al.*, *Geochim. Cosmochim. Acta* **43**, 1075–1090 (1979).
6. S. Emerson *et al.*, *Geochim. Cosmochim. Acta* **46**, 1073–1079 (1982).
7. R. C. Aller, *Philos. Trans. R. Soc. Lond. A* **331**, 51–68 (1990).
8. T. J. Shaw, J. M. Gieskes, R. A. Jahnke, *Geochim. Cosmochim. Acta* **54**, 1233–1246 (1990).
9. K. S. Johnson *et al.*, *Science* **257**, 1242–1245 (1992).
10. L. N. Neretin, C. Pohl, G. Jost, T. Leipe, F. Pollehne, *Mar. Chem.* **82**, 125–143 (2003).
11. A. Schippers, L. N. Neretin, G. Lavik, T. Leipe, F. Pollehne, *Geochim. Cosmochim. Acta* **69**, 2241–2252 (2005).
12. W. B. Homoky *et al.*, *Geochim. Cosmochim. Acta* **75**, 5032–5048 (2011).
13. O. W. Duckworth, G. Sposito, *Environ. Sci. Technol.* **39**, 6037–6044 (2005).
14. J. E. Kostka, G. W. Luther, K. H. Nealson, *Geochim. Cosmochim. Acta* **59**, 885–894 (1995).
15. K. J. Klewicki, J. J. Morgan, *Environ. Sci. Technol.* **32**, 2916–2922 (1998).
16. D. L. Parker, G. Sposito, B. M. Tebo, *Geochim. Cosmochim. Acta* **68**, 4809–4820 (2004).
17. R. E. Trouwborst, B. G. Clement, B. M. Tebo, B. T. Glazer, G. W. Luther III, *Science* **313**, 1955–1957 (2006).
18. E. Yakushev, S. Pakhomova, K. Sørenson, J. Skei, *Mar. Chem.* **117**, 59–70 (2009).
19. O. Dellwig, B. Schnetger, H. J. Brumsack, H. P. Grossart, L. Umlauf, *J. Mar. Syst.* **90**, 31–41 (2012).
20. B. Schnetger, O. Dellwig, *J. Mar. Syst.* **90**, 23–30 (2012).
21. A. S. Madison, B. M. Tebo, G. W. Luther 3rd, *Talanta* **84**, 374–381 (2011).
22. P. Anschutz, B. Sundby, L. Lefrancois, G. W. Luther III, A. Mucci, *Geochim. Cosmochim. Acta* **64**, 2751–2763 (2000).
23. H. Lin, N. H. Szeinbaum, T. J. Dichristina, M. Taillefert, *Geochim. Cosmochim. Acta* **99**, 179–192 (2012).
24. B. P. Boudreau, A. Mucci, B. Sundby, G. W. Luther, N. Silverberg, *J. Mar. Res.* **56**, 1259–1284 (1998).
25. S. Mulsow, B. P. Boudreau, J. N. Smith, *Limnol. Oceanogr.* **43**, l–9 (1998).
26. S. Katsev, G. Chaillou, B. Sundby, A. Mucci, *Limnol. Oceanogr.* **52**, 2555–2568 (2007).
27. B. Sundby, N. Silverberg, R. Chesselet, *Geochim. Cosmochim. Acta* **45**, 293–307 (1981).
28. G. W. Luther III, B. Sundby, B. L. Lewis, P. J. Brendel, N. Silverberg, *Geochim. Cosmochim. Acta* **61**, 4043–4052 (1997).
29. G. W. Luther III, J. E. Kostka, T. M. Church, B. Sulzberger, W. Stumm, *Mar. Chem.* **40**, 81–103 (1992).
30. M. Taillefert, A. B. Bono, G. W. Luther, *Environ. Sci. Technol.* **34**, 2169–2177 (2000).
31. B. G. Clement, G. W. Luther III, B. M. Tebo, *Geochim. Cosmochim. Acta* **73**, 1878–1889 (2009).
32. N. P. Revsbech *et al.*, *Limnol. Oceanogr. Methods* **7**, 371–381 (2009).

Acknowledgments: This work was funded by grants from the Chemical Oceanography Division of the National Foundation to G.W.L. (OCE-1155385 and OCE-1031272) and B.M.T. (OCE-1031200 and OCE-1154307), and from the Natural Sciences and Engineering Research Council of Canada (NSERC) through Discovery and Ship-time grants to A.M. and B.S. Raw data are presented in the supplementary materials.

Supplementary Materials

www.sciencemag.org/cgi/content/full/341/6148/875/DC1
Materials and Methods
Supplementary Text
Figs. S1 to S7
Tables S1 and S2
References (*33*–*45*)

3 June 2013; accepted 29 July 2013
10.1126/science.1241396

14-Step Synthesis of (+)-Ingenol from (+)-3-Carene

Lars Jørgensen,[1]* Steven J. McKerrall,[1]* Christian A. Kuttruff,[1] Felix Ungeheuer,[1] Jakob Felding,[2] Phil S. Baran[1]†

Ingenol is a diterpenoid with unique architecture and has derivatives possessing important anticancer activity, including the recently Food and Drug Administration–approved Picato, a first-in-class drug for the treatment of the precancerous skin condition actinic keratosis. Currently, that compound is sourced inefficiently from *Euphorbia peplus*. Here, we detail an efficient, highly stereocontrolled synthesis of (+)-ingenol proceeding in only 14 steps from inexpensive (+)-3-carene and using a two-phase design. This synthesis will allow for the creation of fully synthetic analogs of bioactive ingenanes to address pharmacological limitations and provides a strategic blueprint for chemical production. These results validate two-phase terpene total synthesis as not only an academic curiosity but also a viable alternative to isolation or bioengineering for the efficient preparation of polyoxygenated terpenoids at the limits of chemical complexity.

Structurally complex, polyoxygenated terpenoids and their derivatives constitute a medicinally vital class of natural products used in a myriad of different therapeutic areas such as oncology (Taxol, Bristol-Myers Squibb), immunology (prednisone), and infectious diseases (artemisinin) (*1*). Despite the promise of complex terpenoids as drug molecules, their utility has been hampered by a number of challenges to development (*2*). In particular, many plant-derived terpenoid natural products, such as Taxol and artemisinin, suffer from a combination of low isolation yields, inconsistent isolation procedures, and nonrenewable natural sources (*3*, *4*). In the case of Taxol, plant cell culture technology overcame low-yielding isolation (*3*), whereas in the case of artemisinin, collaborations between scientists in genetic engineering and chemical synthesis hold promise for providing a consistent supply (*4*, *5*). These seminal works in the biological production of natural products have led to a widely held presumption that bioengineering

[1]Department of Chemistry, The Scripps Research Institute, 10550 North Torrey Pines Road, La Jolla, CA 92037, USA. [2]External Discovery, LEO Pharma A/S, Industriparken 55, 2750 Ballerup, Denmark.

*These authors contributed equally to this work.
†Corresponding author. E-mail: pbaran@scripps.edu

is superior to organic synthesis in the production of all complex terpenoids (*6*, *7*). Further, it has even been claimed that metabolic engineering is favored in the production of "natural products, particularly active pharmaceutical ingredients (APIs), some of which are too complex to be chemically synthesized" in a meaningful way (*7*). We repudiate these claims and present a case study in which chemical synthesis provides an approach to a structurally complex and medicinally relevant terpenoid that is both amenable to analog synthesis and concise enough to finally make chemical production possible.

A particularly chemically and biologically important terpene is ingenol (**1**, Fig. 1), a plant-derived diterpenoid first isolated by Hecker in 1968 from *Euphorbia ingens* (*8*). Its structure was elucidated through x-ray crystallography (*9*), showing a unique *in,out*-[4.4.1]bicycloundecane core, which is considerably more strained than the typical out,out configuration (*10*). In addition to its intriguing structure, ingenol esters also possess important anticancer activity in animal models and anti-HIV activity in vitro (*11*–*13*), deriving from their interaction with protein kinase C (*14*). In particular, ingenol mebutate [Picato (LEO Pharma), **2**] was recently Food and Drug Administration–approved as a first-in-class treatment for actinic keratosis (*15*), a precancerous skin condition, and has completed phase II clinical trials for the topical treatment of basal cell carcinomas (*16*). Although ingenol mebutate (**2**) is highly suited for topical applications, it is degraded through rapid ester migration and hydrolysis (*17*). These characteristics preclude systemic administration in the treatment of a broader range of cancers and are not easily addressed by available synthetic modifications of the natural product.

Currently the supply of ingenol mebutate (**2**) is limited to direct isolation (the current commercial source) and semisynthesis from ingenol (*17*, *18*). Direct isolation yields only 1.1 mg of **2** per kg of *E. peplus* (*19*), thus requiring an immense amount of plant material to achieve large-scale production. The semisynthesis requires isolation of ingenol, which, although available in a more abundant yield of 275 mg of **1** per kg of dried seeds of *E. lathyris* (*20*), still presents a dearth of material. For comparison, the isolation of artemisinin—where limited supply drives price instability—provides around 5 g per kg of dried leaves of *Artemisia annua* (*21*). In addition, engineering ingenol biosynthesis faces considerable challenges because the biosynthetic pathway is nontrivial and largely unknown [vide infra, and (*22*)]. Indeed, only the production of casbene (**4**, Fig. 2A) has been expressed in nonnative hosts, with a low titer of 31 mg/l (*23*). The above considerations led LEO Pharma, developer of Picato, to initiate a partnership with our group to design and implement a total synthesis of ingenol that would simultaneously be amenable to the creation of analogs and, more importantly, short enough to make commercial synthesis possible.

The structure and biological activity of ingenol (**1**) have motivated tremendous interest from synthetic organic chemists over the past 30 years (*24*). During that time, chemists have completed three total syntheses (*25*–*27*), one formal synthesis (*28*), and numerous approaches to the bicyclic core (*24*). Although these landmark efforts achieved elegant syntheses of **1**, those routes required between 37 and 45 steps, precluding their use in accessing synthetic analogs in meaningful quantities. As such, we required a much more concise, direct approach.

In light of the challenge of the in,out system in **1**, inspiration was sought from the biosynthesis of ingenane terpenoids (Fig. 2A). Their biosyntheses begin with the production of geranylgeranyl pyrophosphate (**3**) and its cyclization to casbene (**4**) by casbene synthase. Beyond **4**, the biosynthetic pathway remains speculative; however, the presence of a variety of intermediately cyclized natural products suggests discrete cyclizations to lathyrane, tigliane, and lastly ingenane skeletons (*22*). To the best of our knowledge, enzymes responsible for these later transformations for use in bioengineering have not been identified. The conversion from a tigliane skeleton, such as phorbol (**5,** Fig. 2B), to an ingenane skeleton should proceed through a 1,2-pinacol rearrangement, as shown with putative intermediate **6**. Cha has demonstrated this type of rearrangement by leveraging the strain of an epoxide (*29*) to overcome thermodynamic forces (vide infra). On the other hand, a vinylogous retropinacol rearrangement of ingenol (**1**) has also been observed (*30*), suggesting that the strain of the in,out system thermodynamically

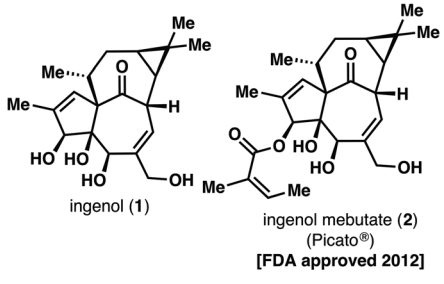


Fig. 1. Ingenol (1) and ingenol mebutate (2).

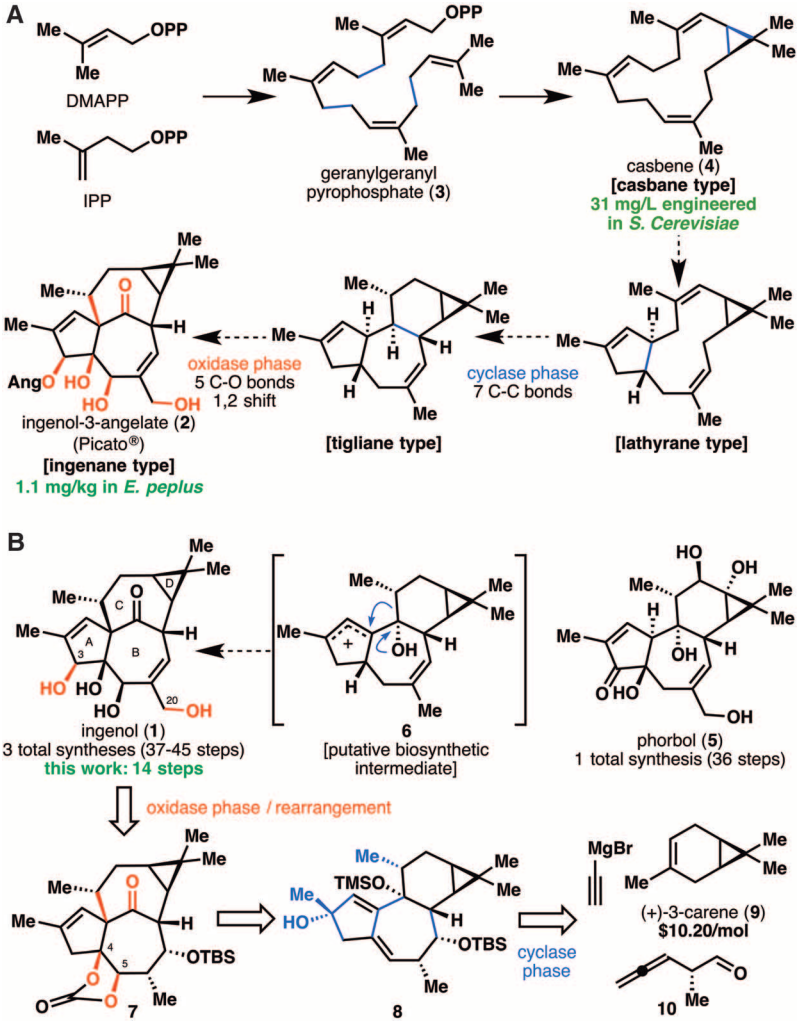


Fig. 2. Biosynthetic inspiration and retrosynthetic analysis. (**A**) Biosynthesis and bioengineering of ingenane diterpenoids. Ang is *Z*-2-methyl-2-butenoate. (**B**) Two-phase approach to ingenol.

favors the reverse reaction. Nevertheless, we viewed the vinylogous pinacol rearrangement, however challenging, as a key structurally simplifying disconnection, reducing the highly strained, bridged ring system into an angularly fused ring system.

A two-phase design consisting of a cyclase phase and an oxidase phase was chosen (*31*). The cyclase phase would establish the precursor tigliane carbon skeleton, and the oxidase phase would install the four hydroxyl groups and rearrange the tigliane skeleton to an ingenane skeleton (Fig. 2B). The retrosynthetic plan thus begins with the strategic removal of oxidized functionality in the oxidase phase. The alcohols at C-3 and C-20 were removed in anticipation that allylic oxidations would enable their installation (*32*). Indeed, Wood has demonstrated the feasibility of C-20 oxidation in his total synthesis of **1** (*27*). To conclude the oxidase phase, the remaining two alcohols (C-4 and C-5) and the in,out-bicyclic system in **7** arise from a stereoselective dihydroxylation of the corresponding olefin and a vinylogous pinacol rearrangement, respectively. In the cyclase phase, intermediate diene **8** was traced back to the commodity chemical (+)-3-carene (**9**, $10.20/mol), in which the dimethyl cyclopropane would serve as a stereochemistry-controlling element, ethynyl magnesium bromide, and aldehyde **10**. Our hypothesis was that this route would provide rapid, scalable access to diene **8**, which would serve as a key intermediate for both efficient preparation of ingenol and divergent access to ingenol analogs in sufficient quantity for drug development.

The synthesis begins with the transformation of **9** into a suitable intermediate for the installation of the C-11 methyl group and the coupling with **10** (Fig. 3). Chlorination of **9** with *N*-chlorosuccinimide (NCS), followed by ozonolysis, gave chloroketone **11** in 48% yield over two steps (22.5-g scale). The requisite methyl group could be installed through a reductive alkylation; however, the corresponding methyl ketone proved configurationally unstable and formed azeotropes with a variety of solvents, complicating its isolation. It was found that a one-pot procedure for reductive alkylation and aldol reaction provided superior isolated yield and eliminated handling of the challenging methyl ketone. Thus, **11** was treated with lithium naphthalenide followed by hexamethylphosphoramide (HMPA) and methyl

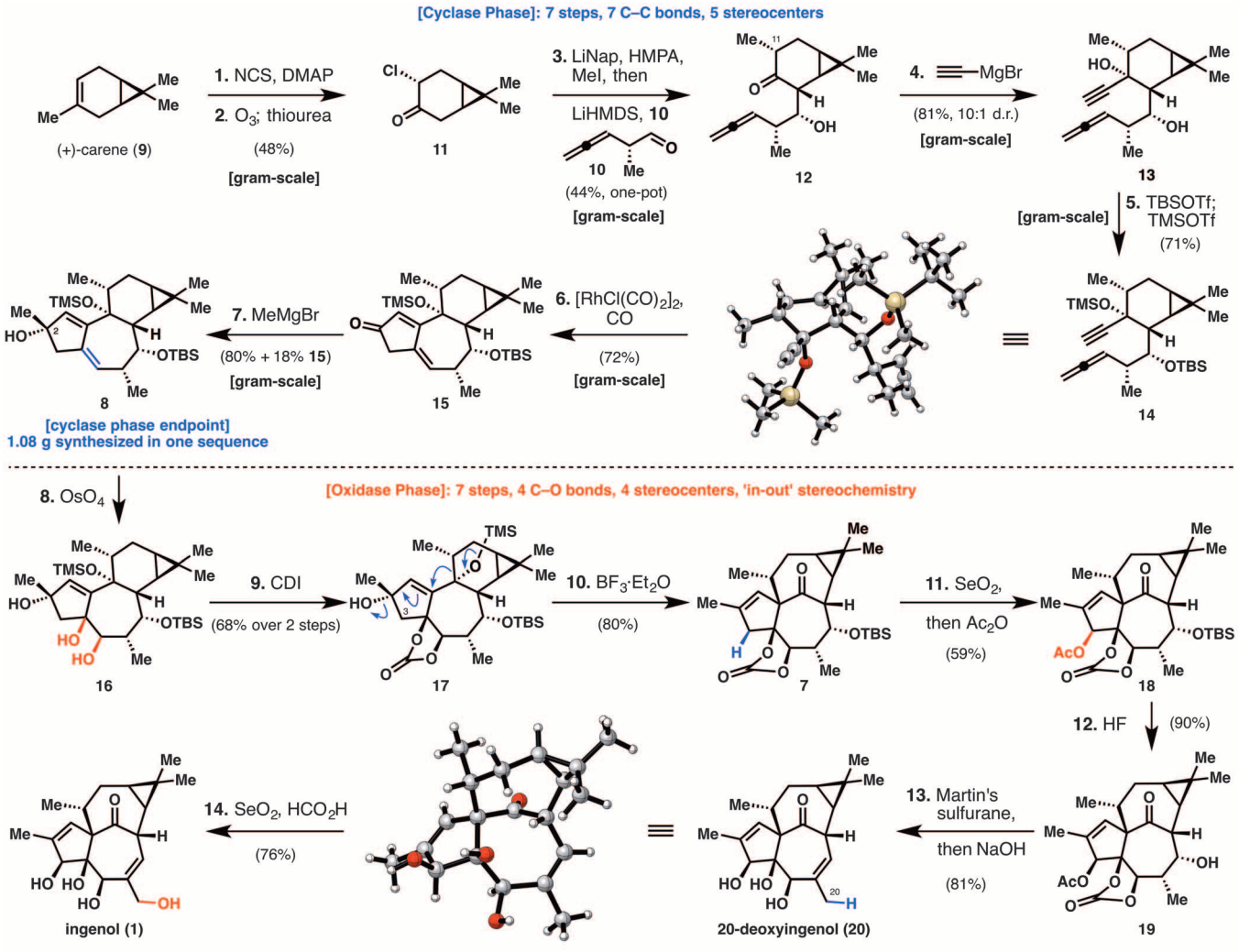


Fig. 3. Reaction sequence for the total synthesis of ingenol (1). Reagents and conditions are as follows: Reaction 1. NCS [3.0 equivalents (equiv.)], *N,N*-dimethylaminopyridine (DMAP) (0.1 equiv.), CH_2Cl_2, room temperature (r.t.), 3 hours. Reaction 2. O_3, CH_2Cl_2/MeOH; thiourea (1.6 equiv.), 2 hours, 48% over two steps. Reaction 3. Lithium naphthalenide (~2 equiv.), MeI (10 equiv.), HMPA/tetrahydrofuran (THF), –78°C to r.t., 1.5 hours; LiHMDS (1.25 equiv.), **10** (2.0 equiv.), –78°C, 4 hours, 44%. Reaction 4. Ethynylmagnesium bromide (5.0 equiv.), THF, –78° to –15°C, 3 hours, 81%. Reaction 5. TBSOTf (2.0 equiv.), Et_3N (4.0 equiv.), CH_2Cl_2, 0°C, 30 min; TMSOTf (2.0 equiv.), Et_3N (4.0 equiv.), 0°C, 1.5 hours, 71%. Reaction 6. $[RhCl(CO)_2]_2$ (0.1 equiv.), *p*-xylene, 140°C, 12 hours, 72%. Reaction 7. Methylmagnesium bromide (4.1 equiv.), THF, –78° to 0°C, 30 min, 80% + 18% **15**. Reaction 8. OsO_4 (1.5 equiv.), pyridine, r.t., 12 hours; 1:1 aqueous Na_2SO_3/THF, r.t., 12 hours. Reaction 9. CDI (5.0 equiv.), DMAP (0.1 equiv.), CH_2Cl_2, r.t., 8 hours, 64% over 2 steps. Reaction 10. BF_3•Et_2O (10.0 equiv.), CH_2Cl_2, –78° to –40°C, 30 min, then Et_3N/MeOH, 80%. Reaction 11. SeO_2 (5.0 equiv.), dioxane, 80°C, 14 hours; Ac_2O (20.0 equiv.), DMAP (0.1 equiv.), pyridine (40.0 equiv.), r.t., 1 hour, 59%. Reaction 12. HF (60.0 equiv.), CH_3CN, 50°C, 10 hours, 90%. Reaction 13. Martin's sulfurane (6.0 equiv.), $CHCl_3$, 80°C, 3 hours, then NaOH, THF, 1 hour, 81%. Reaction 14. SeO_2 (10.0 equiv.), 2:1 dioxane/formic acid, 80°C, 1.25 hours, then NaOH, 76%.

iodide. The excess methyl iodide was removed by distillation, and subsequent addition of lithium bis (trimethylsilyl)amide (LiHMDS) and **10**—derived from 2-iodoxybenzoic acid (IBX) oxidation of the corresponding alcohol (*33*)—delivered aldol product **12** as a single diastereomer in 44% yield (6.4-g scale).

Treatment of **12** with ethynyl magnesium bromide provided diol **13** in 81% yield as a 10:1 mixture of diastereomers (3.0-g scale). This initial four-step sequence rapidly assembles **13**, the substrate for the key Pauson-Khand cyclization, by setting four contiguous stereocenters and forming three carbon–carbon bonds. Under known conditions (*34*) for the Pauson-Khand cyclization, **13** decomposed rapidly. The alcohols were identified as problematic functionalities and were protected by sequential, one-pot treatment with *tert*-butyldimethylsilyl triflate (TBSOTf) and trimethylsilyl triflate (TMSOTf) to deliver **14** in 72% yield (2.7-g scale). Unexpectedly, **14** crystallized upon cooling, and x-ray crystallographic analysis unambiguously confirmed the desired stereochemistry. Aided by the pioneering studies of Brummond and others on allenic Pauson-Khand reactions (*34*), cyclization of **14** was effected by treatment with 10 mole percent (mol %) $[RhCl(CO)_2]_2$ under a CO atmosphere to provide dienone **15** in 72% yield (1.5-g scale). The use of degassed and anhydrous solvent under high dilution (0.005 M) conditions proved essential to the high yield of this reaction.

Installation of the C-2 methyl group was achieved by treatment of **15** with methylmagnesium bromide to give **8**, the cyclase phase end point, in 80% yield with an additional 18% recovered **15** (1.3-g scale). By using the described route, 1.08 g of **8** was prepared in a single sequence. The cyclase phase proceeded in only seven steps from **9** to generate five stereocenters and form seven carbon–carbon bonds, illustrating the strategic value of targeting a minimally oxidized core structure and using powerful carbon–carbon bond–forming methodologies.

The oxidase phase began with the dihydroxylation of **8**. Unfortunately, catalytic dihydroxylation was ineffective on **8**, and only starting material or overoxidation product was obtained under numerous conditions used. Dihydroxylation of the desired olefin could be realized through the use of stoichiometric OsO_4, followed by reductive hydrolysis, to deliver the requisite diol **16** as a single stereoisomer. The crude diol **16** was protected with *N*,*N*-carbonyldiimidazole (CDI) to deliver carbonate **17** in 68% yield over two steps (100-mg scale). With **17** in hand, conditions were developed for the pivotal vinylogous pinacol rearrangement. Initial results were disappointing because **17** was unreactive or underwent elimination under conditions used. However, it was discovered that reaction temperature plays a crucial role. The desired pinacol rearrangement could ultimately be effected by treating **17** with BF_3•Et_2O (where Et indicates an ethyl group) in CH_2Cl_2 at –78° to –40°C, followed by quenching with Et_3N and MeOH (Me, methyl), to set the strained in,out stereochemistry and produce ingenane **7** in 80% yield (191-mg scale). These results, in light of previous reports of the retropinacol rearrangement (*30*) of ingenol (**1**), suggest competing kinetic and thermodynamic factors. Efforts to understand the dynamics of this reaction and its implications for ingenol (**1**) biosynthesis are ongoing.

The C-3 alcohol was installed by allylic oxidation with SeO_2, followed by in situ protection as the acetate, to deliver **18** as a single diastereomer in 59% yield (128-mg scale). Removal of the TBS group with HF gave alcohol **19** in 90% yield (82-mg scale). An x-ray crystal structure, obtained by conversion of **19** to the *para*-bromobenzoate **21**, unambiguously confirmed the stereochemistry of both the alcohol triad and the *in,out* bicyclic system (Fig. 4A). Alcohol elimination and global deprotection were achieved by treatment with Martin's sulfurane, followed by basic hydrolysis, to provide crystalline 20-deoxyingenol (**20**) in 80% yield (23-mg scale). Installation of the final C-20 alcohol was accomplished by using Shibuya's conditions for allylic oxidation (*35*)—which produced higher conversion, without overoxidation, than Wood's conditions (*27*)—to deliver **1** in 76% yield (10-mg scale). Synthetic **1** and **20** were spectroscopically identical to naturally obtained material. Thus, the oxidase phase consists of seven steps, which install the congested tetraol moiety and use a biomimetic rearrangement to generate the all-carbon quaternary stereocenter and in,out stereochemistry. The use of late-stage oxidations to introduce the four alcohols, particularly those that involve functionalization of activated C–H bonds, greatly increases the step economy of the synthesis (*36*).

A synthesis of **1** was achieved in 14 steps and 1.2% overall yield (73% average per step) from **9**. This compares favorably with the 1.1 mg/kg [0.0011% weight/weight (w/w)] isolation yield of **2** (*18*) and the 275 mg/kg (0.028% w/w) isolation yield of **1** (*19*). Salient features of the current route include (i) a four-step sequence transforming **9** into stereochemically complex **13**, (ii) a catalytic allenic Pauson-Khand reaction producing the core carbon skeleton, (iii) a seemingly improbable (*30*) vinylogous pinacol rearrangement setting the requisite in,out stereochemistry, and (iv) sequential, chemoselective oxidation reactions installing the alcohol tetrad. A notable feature of the synthesis is excellent redox economy, evidenced by the absence of nonstrategic redox manipulations (*37*). Additionally, the approach provides gram quantities of key intermediate **8**, which serves as a point of divergence for the synthesis of analogs of **2** (vide infra). Such studies are ongoing, and the current synthesis is being scaled up in conjunction with LEO Pharma to produce large quantities of intermediate **8** for use in analog preparation.

This synthesis of **1** is not without limitations. In particular, the oxidase phase relies on the use of stoichiometric quantities of toxic oxidants (OsO_4 and SeO_2) to install the alcohol functionality. A first step to address these issues is a catalytic dihydroxylation of dienone **15** (Fig. 4B), which uses 5 mol % OsO_4 in the presence of citric acid, to deliver diol **22** in 88% yield (180-mg scale). The use of these conditions on the dihydroxylation of **8** gave decomposition, however, and retailoring the synthesis to use **22** requires a change in protecting group strategy. These challenges point to limitations in existing chemical methods for oxidation (*31*), and additional efforts to address the scalability of the oxidase phase are ongoing.

The oxidase phase shown is designed to yield **1**; however, by using the predictable oxidase reactivity exemplified above, intermediate **8** can be diverted to a variety of ingenanes of varying oxidation and substitution patterns to address the pharmacological challenges to oral dosing of **2**. By altering the oxidase phase, we can

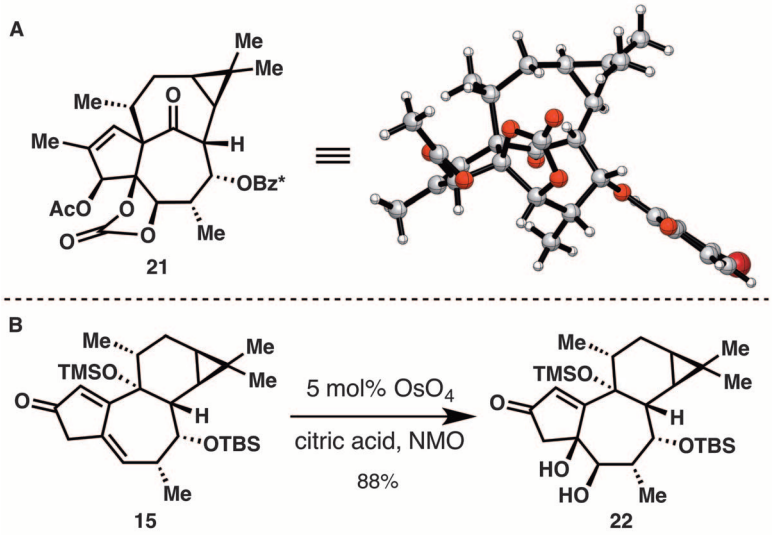


Fig. 4. Stereochemical confirmation and preliminary catalytic dihydroxylation. (**A**) X-ray crystal structure of **21**. Bz* is *p*-bromobenzoate. (**B**) Catalytic dihydroxylation of **15**. OsO_4 (0.05 equiv.), *N*-methylmorpholine *N*-oxide (NMO) (2.0 equiv.), citric acid (2.0 equiv.), 1:1 *t*-BuOH/H_2O, r.t., 24 hours, 88%.

produce analogs of **2** differing in the alcohol functionalities (C-3, C-4, C-5, and C-20) to better understand the structure-activity relationship of ingenanes.

The synthesis of ingenol (**1**) presented herein illustrates the power of two-phase logic to deliver an efficient, concise synthesis even in architecturally complex settings. The usefulness of the two-phase approach will undoubtedly continue to expand as new methods for C–C bond formation and C–H oxidation are developed. Furthermore, this report provides a strong rebuttal to the presumption that chemical synthesis is ill-equipped to deal with the preparation of structurally complex terpenoid drug molecules. Rather, in this instance, total chemical synthesis holds promise as the best method to both prepare ingenol mebutate (**2**) and enable the development of therapeutic analogs with broader utility in the treatment of human diseases.

References and Notes

1. F. E. Koehn, G. T. Carter, *Nat. Rev. Drug Discov.* **4**, 206–220 (2005).
2. I. Raskin *et al.*, *Trends Biotechnol.* **20**, 522–531 (2002).
3. P. G. Mountford, in *Green Chemistry in the Pharmaceutical Industry*, P. J. Dunn, A. S. Wells, M. T. Williams, Eds. (Wiley, Weinheim, Germany, 2010), pp. 145–160.
4. C. J. Paddon *et al.*, *Nature* **496**, 528–532 (2013).
5. C. Zhu, S. P. Cook, *J. Am. Chem. Soc.* **134**, 13577–13579 (2012).
6. J. D. Keasling, A. Mendoza, P. S. Baran, *Nature* **492**, 188–189 (2012).
7. J. D. Keasling, *Science* **330**, 1355–1358 (2010).
8. E. Hecker, *Cancer Res.* **28**, 2338–2349 (1968).
9. K. Zechmeister *et al.*, *Tetrahedron Lett.* **11**, 4075–4078 (1970).
10. R. W. Alder, S. P. East, *Chem. Rev.* **96**, 2097–2112 (1996).
11. S. M. Ogbourne *et al.*, *Cancer Res.* **64**, 2833–2839 (2004).
12. M. Fujiwara *et al.*, *Antimicrob. Agents Chemother.* **40**, 271–273 (1996).
13. A. Vasas, D. Rédei, D. Csupor, J. Molnár, J. Hohmann, *Eur. J. Org. Chem.* **2012**, 5115–5130 (2012).
14. C. M. Hasler, G. Acs, P. M. Blumberg, *Cancer Res.* **52**, 202–208 (1992).
15. U.S. Food and Drug Administration, *2012 Novel New Drugs Summary* (FDA, Washington, DC, 2013); www.fda.gov/downloads/Drugs/DevelopmentApprovalProcess/DrugInnovation/UCM337830.pdf.
16. G. Siller *et al.*, *Australas. J. Dermatol.* **51**, 99–105 (2010).
17. "European public assessment report: Picato" [European Medicines Agency (EMA) publication 650464, London, 2012]; www.ema.europa.eu/docs/en_GB/document_library/EPAR_-_Public_assessment_report/human/002275/WC500135329.pdf.
18. X. Liang, G. Grue-Sørensen, A. K. Petersen, T. Högberg, *Synlett* **23**, 2647–2652 (2012).
19. J. Hohmann, F. Evanics, L. Berta, T. Bartók, *Planta Med.* **66**, 291–294 (2000).
20. G. Appendino, G. C. Tron, G. Cravotto, G. Palmisano, J. Jakupovic, *J. Nat. Prod.* **62**, 76–79 (1999).
21. V. Hale, J. D. Keasling, N. Renninger, T. T. Diagana, *Am. J. Trop. Med. Hyg.* **77** (suppl.), 198–202 (2007).
22. R. J. Schmidt, *J. Linn. Soc. Bot.* **94**, 221–230 (1987).
23. J. Kirby *et al.*, *Phytochemistry* **71**, 1466–1473 (2010).
24. I. Kuwajima, K. Tanino, *Chem. Rev.* **105**, 4661–4670 (2005).
25. J. D. Winkler, M. B. Rouse, M. F. Greaney, S. J. Harrison, Y. T. Jeon, *J. Am. Chem. Soc.* **124**, 9726–9728 (2002).
26. K. Tanino *et al.*, *J. Am. Chem. Soc.* **125**, 1498–1500 (2003).
27. A. Nickel *et al.*, *J. Am. Chem. Soc.* **126**, 16300–16301 (2004).
28. K. Watanabe *et al.*, *J. Org. Chem.* **69**, 7802–7808 (2004).
29. O. L. Epstein, J. K. Cha, *Angew. Chem. Int. Ed.* **44**, 121–123 (2004).
30. G. Appendino *et al.*, *Eur. J. Org. Chem.* **1999**, 3413–3420 (1999).
31. K. Chen, P. S. Baran, *Nature* **459**, 824–828 (2009).
32. A. Nakamura, M. Nakada, *Synthesis* **45**, 1421–1451 (2013).
33. T. Konegawa, Y. Ohtsuka, H. Ikeda, T. Sugai, H. Ohta, *Synlett* **1997**, 1297–1299 (1997).
34. K. M. Brummond *et al.*, *Org. Lett.* **4**, 1931–1934 (2002).
35. K. Shibuya, *Synth. Commun.* **24**, 2923–2941 (1994).
36. P. A. Wender, V. A. Verma, T. J. Paxton, T. H. Pillow, *Acc. Chem. Res.* **41**, 40–49 (2008).
37. N. Z. Burns, P. S. Baran, R. W. Hoffmann, *Angew. Chem. Int. Ed.* **48**, 2854–2867 (2009).

Acknowledgments: Financial support for this work was provided by LEO Pharma. The Carlsberg Foundation and the Danish Council for Independent Research (Technology and Production Sciences) provided postdoctoral fellowships for L.J., and the Alexander von Humboldt Foundation provided a postdoctoral fellowship for C.A.K. We are grateful to A. Rheingold and C. E. Moore (University of California, San Diego) for x-ray crystallographic analysis and G. Siuzdak (the Scripps Research Institute) for mass spectrometry assistance. We thank H. Bladh (LEO Pharma) for valuable discussions and LEO Pharma for generous donations of natural 20-deoxyingenol and ingenol. Metrical parameters for the structures of compounds **14**, **20**, and **21** are available free of charge from the Cambridge Crystallographic Data Centre under reference numbers CCDC-943074, 943076, and 943075, respectively. A provisional patent application has been filed and is available under patent application no. U.S. 61/829,861.

Supplementary Materials

www.sciencemag.org/cgi/content/full/science.1241606/DC1
Materials and Methods
Supplementary Text
Figs. S1 to S4
Tables S1 to S7
Data

7 June 2013; accepted 18 July 2013
Published online 1 August 2013;
10.1126/science.1241606

Mapping of Functional Groups in Metal-Organic Frameworks

Xueqian Kong,[1,2]* Hexiang Deng,[3,4]*† Fangyong Yan,[1,4]* Jihan Kim,[4]‡ Joseph A. Swisher,[1,4] Berend Smit,[1,3,4] Omar M. Yaghi,[3,4,5]§ Jeffrey A. Reimer[1,2]§

We determined the heterogeneous mesoscale spatial apportionment of functional groups in a series of multivariate metal-organic frameworks (MTV-MOF-5) containing BDC (1,4-benzenedicarboxylate) linkers with different functional groups—B (BDC-NH_2), E (BDC-NO_2), F [(BDC-$(CH_3)_2$], H [BDC-$(OC_3H_5)_2$], and I [BDC-$(OC_7H_7)_2$]—using solid-state nuclear magnetic resonance measurements combined with molecular simulations. Our analysis reveals that these methods discern between random (EF), alternating (EI and EHI), and various cluster (BF) forms of functional group apportionments. This combined synthetic, characterization, and computational approach predicts the adsorptive properties of crystalline MTV-MOF systems. This methodology, developed in the context of ordered frameworks, is a first step in resolving the more general problem of spatial disorder in other ordered materials, including mesoporous materials, functionalized polymers, and defect distributions within crystalline solids.

A strategy for optimizing the properties of synthetic crystalline materials is to deliberately introduce heterogeneity by increasing the number of constituents (*1*). This approach can be compromised by the dual challenges of phase separation, lack of order, or both. Multivariate metal-organic frameworks (MTV-MOFs) can meet this challenge by incorporating multiple linkers that bear different functional groups into the same crystal, which creates a heterogeneous interior (*2*). This heterogeneity can enhanced selectivity for carbon dioxide (CO_2) capture and hydrogen uptake relative to mixtures of pure materials. On a fundamental level, these materials present characterization challenges, in that there are no experimental techniques that can elucidate the intermingling of functional groups that characterizes the heterogeneity within the crystalline MTV-MOFs. For example, this "heterogeneity problem" is intractable for diffraction methods (x-ray, neutron, and electron) and remains unexamined with other characterization methods. We show that multidimensional solid-state nuclear magnetic resonance (SSNMR) combined with molecular simulations can be used to generate three-dimensional (3D) maps of the apportionment of functional groups (Fig. 1) within and between the pores of MTV-MOF-5. These MTV-MOFs adopt MOF-5 structure containing BDC (1,4 benzenedicarboxylate) linkers with different functional groups–B (BDC-NH2), E (BDC-NO2), F [(BDC-(CH3)2], H [BDC-(OC3H5)2], and I [BDC-(OC7H7)2]. This method can be applied to other ordered or disordered systems to

[1]Department of Chemical and Biomolecular Engineering, University of California, Berkeley, CA 94720, USA. [2]Environmental Energy Technologies Division, Lawrence Berkeley National Laboratory, Berkeley, CA 94720, USA. [3]Department of Chemistry, University of California, Berkeley, CA 94720, USA. [4]Materials Sciences Division, Lawrence Berkeley National Laboratory, Berkeley, CA 94720, USA. [5]NanoCentury KAIST Institute and Graduate School of Energy, Environment, Water, and Sustainability (World Class University), Daejeon 305-701, Republic of Korea.

*These authors contributed equally to this work.
†Present address: College of Chemistry and Molecular Sciences, Wuhan University Luojiashan, Wuhan, 430072 China.
‡Present address: Department of Chemical and Biomolecular Engineering, Korea Advanced Institute of Science and Technology, 291 Daehak-ro Yuseong-gu, Daejeon, 305-701 Korea.
§Corresponding author. E-mail: yaghi@berkeley.edu (O.M.Y.); reimer@berkeley.edu (J.A.R.)

map the distributions of functional groups, ligands, particles, or defects.

Our analysis indicates that, depending on the combination of various kinds of functionality and their ratios, three distinct apportionments of those functionalities exist: random, alternating, and clustered. Upon discerning these apportionments, we can then predict and explain (i) the CO_2 adsorption isotherm and the observed differences in selectivity, (ii) the changes in apportionment of functionalities as a function of composition and functionality ratio, and (iii) the apportionment in ternary functionality mixtures based on their binary NMR data.

Different interactions between linkers can lead to different apportionment scenarios. Linkers with preferential interactions with each other form clusters, whereas linkers with preferential interactions with different linkers lead to alternating structures. Linkers with no preferences give a random structure. The SSNMR distance measurements represent an average of pairwise interactions throughout the entire sample and thus reflect the average nature of apportionments. The matching of these NMR-derived average distances with Monte Carlo and molecular dynamics simulations allows us to uncover these various apportionment scenarios. We invoked two separate strategies for distance measurements in the MTV-MOF system: 2D correlation experiments (*3*, *4*) and rotational-echo double-resonance (REDOR) NMR (*5*–*9*). The former method enjoys broad applicability in polymer science (*4*), yet was inconclusive in the present study (*10*). The latter method proved to be decisive.

The REDOR NMR method provides a quantitative measure of distances between atoms. A pairwise measurement of the distance between two spectroscopically resolved nuclear spins and, hence, the corresponding atoms might seem an unlikely way to assess the apportionment of the functionalities of linkers because of the large number of possible linker configurations. The key to recovering apportionment of the functional groups from this measurement, however, is in how one considers the averaging of point-to-point distances over the entire sample.

In the REDOR method, a period of multinuclear irradiation is incrementally increased so that the pairwise coupling between NMR-active isotopes evolves to yield "decay curves,". These curves are governed by the dipolar coupling constant between two spins (*i* and *j*), which is proportional to $1/r_{ij}^3$, where r_{ij} is their internuclear distance (*11*). We selectively labeled the spins at different linkers—for example, ^{13}C on linker X and ^{15}N on linker Y—to probe the intermolecular separation of these linkers. If the linkers are close, the average coupling is large and the decay is rapid; that is, a fast decay means that most of the linkers are in close proximity. Figure 2 provides a sketch of how these decay curves depend on the apportionment of functionalities for the different scenarios possible in MTV-MOF-5-BF. Indeed, faster decay is expected for the scenarios in the order of alternating, random, small, and large clusters (Fig. 2B).

To measure the REDOR curves, we ^{15}N labeled, in the case of MTV-MOF-5-BF, each amine group of linker B and measured its coupling to ^{13}C spins of the methyl groups [19 parts per million (ppm)]. Figure 2C shows the ^{13}C spectra measured in a $^{13}C\{^{15}N\}$ REDOR experiment at a given recoupling time with and without ^{15}N dipolar modulation, *S* and S_0, respectively. The S/S_0 ratio for the resonance at 19 ppm is plotted against a series of recoupling times to give S/S_0 decay data and shown in Fig. 3A. Similar data were obtained for MTV-MOF-5-EF, EI, and EHI and are overlaid on the predicted REDOR curves (Fig. 3A).

The apportionment can be derived from a model if we assume that linkers with different functional groups are predisposed to have different neighbor preferences and that we can express these preferences as effective interaction energies. A Monte Carlo simulation (*12*) is then conducted whereby linkers between metal sites are randomly exchanged in a simulated lattice structure; a new apportionment is accepted according to the energy difference between the new and old apportionment. In this way, the effective interaction energies

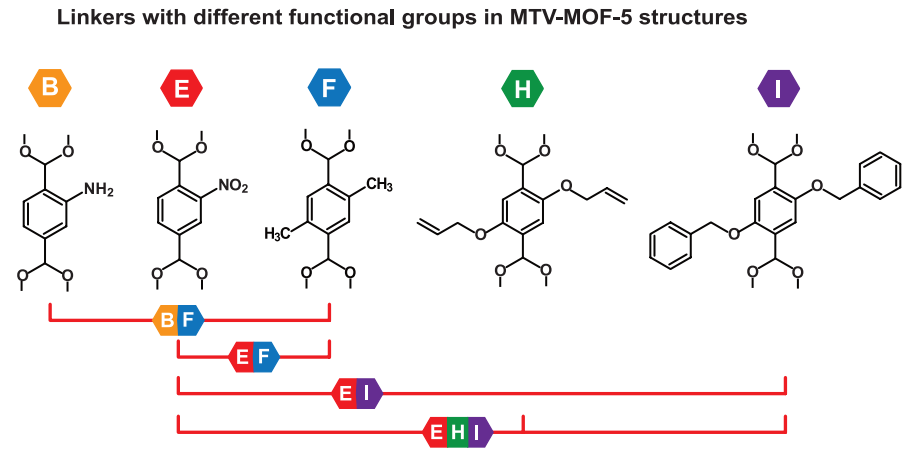


Fig. 1. MTV-MOF-5 linkers. Six linkers are combined with a Zn_4O "secondary building unit" to form an MTV-MOF-5. We use the linkers B, E, F, H, and I. Each linker has the same length but differs by their functional groups so that they can be interchanged to form a material with the same crystal lattice but different apportionment of the linkers. The amino and nitro groups on linker B and E, respectively, were 100% isotopically enriched with ^{15}N, whereas all other nuclei are present at natural isotopic abundance.

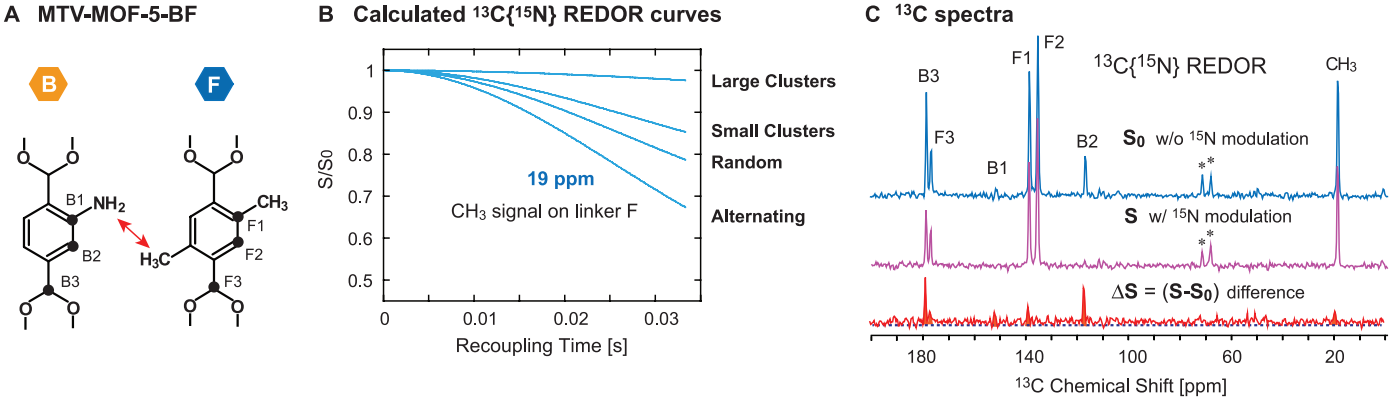


Fig. 2. Solid-state NMR results for MTV-MOF-5-BF. (**A**) The arrow represents the specific distance measured by our REDOR experiments. (**B**) Molecular dynamics simulations of the $^{13}C\{^{15}N\}$ REDOR S/S_0 decay curves for different BF apportionments. (**C**) A suite of $^{13}C\{^{15}N\}$ REDOR experiment at a given recoupling time. Blue, the ^{13}C spectrum taken without ^{15}N dipolar modulation, S_0; pink, the ^{13}C spectrum with ^{15}N dipolar modulation, *S*; red, the difference spectrum ΔS obtained by subtracting *S* from S_0. *, Spinning side bands.

determine the apportionment in a lattice model for which many configurations are generated using conventional Monte Carlo methods. The different apportionments lead to the distinct REDOR curves because these scenarios result in different average distances between atoms on different functional groups. In an alternating system, the majority of ^{13}C (on linker X)–^{15}N (on linker Y) are paired next to each other, and we observed fast decay. In a clustered system, the number of neighboring ^{13}C-^{15}N pairs is far less, and the REDOR S/S_0 decay is relatively flat. A quantitative measure of the REDOR curves was obtained by taking the apportionments of the functional groups from our lattice simulations and replacing the lattice model by the corresponding all-atom model. The subsequent molecular dynamics optimization provided the ensemble average of $1/r^3$ for all labeled pairs from which we computed the REDOR curves. Both the experiments and the simulation show that the decay was not sensitive to temperature. Figure 3B shows that for different materials, we could obtain a quantitative match with experimental data for the different apportionment scenarios, which yield materials that are visually quite different. For example, the EF linkers had a random distribution, the EI linkers were alternating, and clusters were formed for the BF linkers. To rationalize these results, we carried out density functional theory (DFT) calculations (*10*) to address the effect of functional group identity on the energy of formation of the metal-linker complex (table S3). Because of the electronegative -NO_2 group, the E linker has the least favorable energy of formation. This accounts for why we have been unable to synthesize a pure E MTV-MOF and why binary and ternary MTV-MOFs have a lower linker E content compared with their synthesis solution (table S1). The implication of these DFT calculations for apportionment is that the structural building units will minimize the number of E linkers, resulting in an apportionment biased toward an alternating structure. The B linker differentiates itself from others in that this linker can form hydrogen bonds both with other B linkers and with the synthesis solvent (*13*). One therefore would anticipate clustering in solution as an antecedent for the formation of clusters in the MTV-MOF.

With these apportionments, we can predict the adsorption properties of these materials. Figure 4 shows that the experimental isotherms of MTV-MOF-5-EI and EHI agree well with the ones derived from our best-fit models to the REDOR data and that alternative apportionments of large clusters fail to describe the adsorption isotherms. We can also use this result to rationalize the surprising enhancement of the selectivity for CO_2 over carbon monoxide (CO) observed in the MTV-MOF-5-EHI material compared with the single-linker MOF-5 material (*2*). The MOF-5 with E linkers lacks selectivity, while the ones with I linkers are too bulky and therefore block the pores. The combination of the two in an alternating functionality apportionment, however, creates the highly selective adsorption sites and sufficient pore space that are responsible

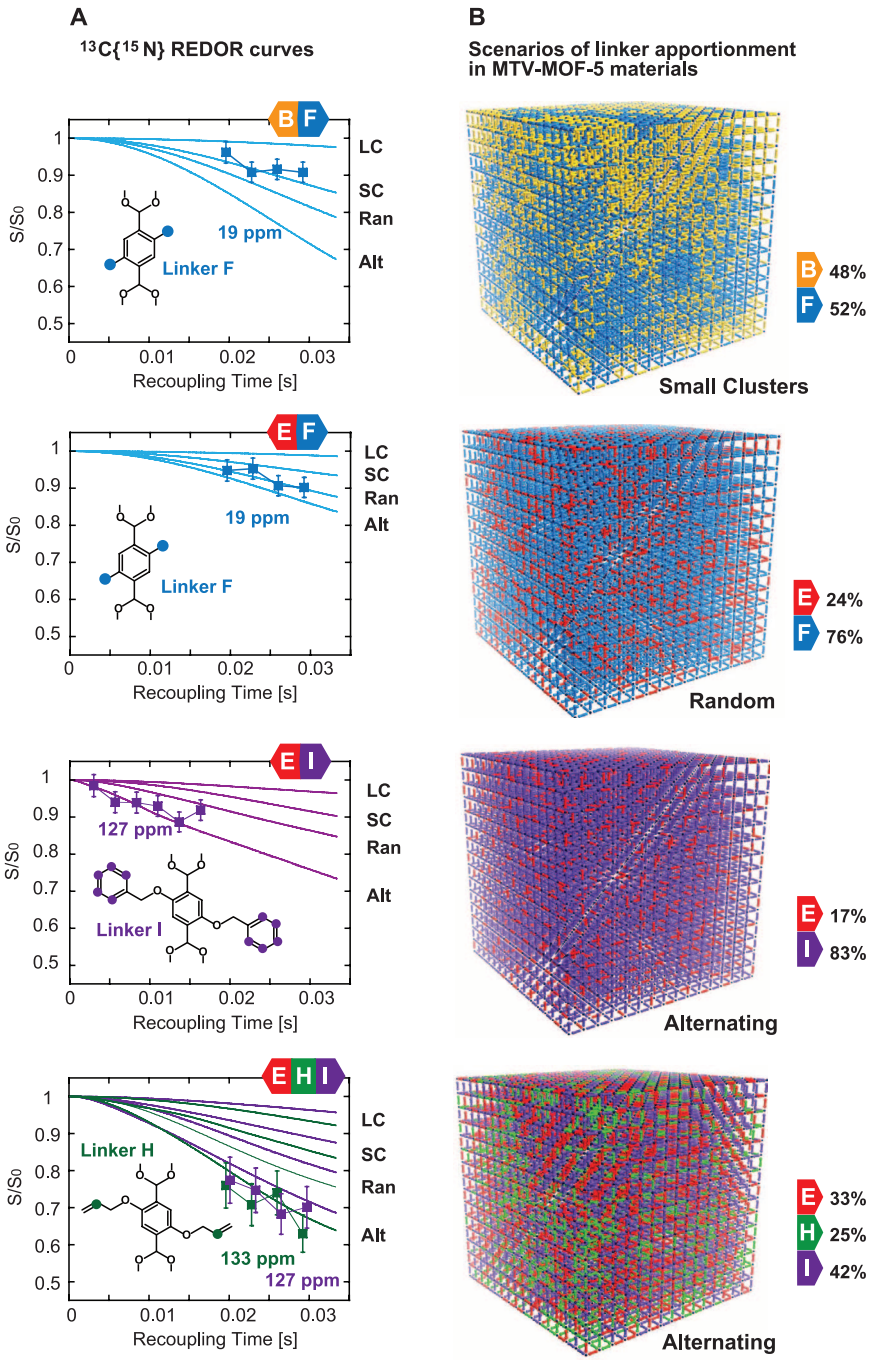


Fig. 3. REDOR results and apportionments. (**A**) Experimental $^{13}C\{^{15}N\}$ REDOR curves (squares) are compared with the molecular dynamics simulations for the different linker apportionments, large clusters (LC), small clusters (SC), random (Ran), and alternating (Alt). (**B**) The derived apportionments for the different MTV-MOF-5s. Yellow, linker B; blue, linker F; red, linker E; purple, linker I; green, linker H.

for the fourfold enhancement of the selectivity observed previously but unexplained (*2*).

Until now, we have used the effective interaction energies as fitting parameters for the NMR REDOR curves. We surmise that these effective energies describe the underlying interactions of the linkers during the formation of the MOF. We can use this model to predict the apportionment. For example, we successfully predicted the apportionments and corresponding REDOR curves of compositions that were not yet synthesized (fig. S17). In addition, we predicted the effect of changes in the linker composition and the ternary linker apportionment on the basis of only binary interaction parameters (tables S6 and S7).

Our strategy to resolve apportionment in a disordered system consists of three parts: the synthesis of systems with disorder distributed upon an ordered lattice (in the present study MTV-MOFs); experimental measurement of pairwise

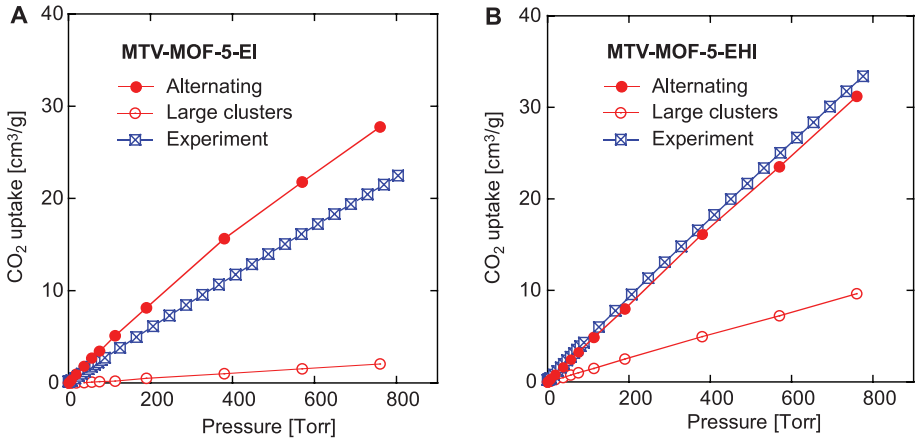


Fig. 4. CO_2 adsorption isotherms. (**A**) MTV-MOF-5-EI and (**B**) MTV-MOF-5-EHI. Experimental (blue) and simulated (red) at 298 K. Solid circles correspond to simulated isotherms for those linker apportionments that best fit the REDOR experiments. For reference, we have added simulation results for a large-cluster apportionment.

distances (here via NMR REDOR); and a computational method that allows us to directly simulate the disorder. This strategy may be employed for many issues in materials engineering, such as defect distributions in crystals and functional group distributions in block copolymers. It is our current vision to design and synthesize materials with crafted heterogeneity so as to carry out complex molecular operations such as recognizing, sorting, and counting substrates.

References and Notes

1. J. Hemminger *et al.*, *From Quanta to the Continuum: Opportunities for Mesoscale Science* (U.S. Department of Energy, Washington, DC, 2012).
2. H. Deng *et al.*, *Science* **327**, 846–850 (2010).
3. J. Jeener, B. H. Meier, P. Bachmann, R. R. Ernst, *J. Chem. Phys.* **71**, 4546–4553 (1979).
4. K. Schmidt-Rohr, H. W. Spiess, *Multidimensional Solid-State NMR and Polymers* (Academic Press, San Diego, CA, 1994).
5. T. Gullion, J. Schaefer, *J. Magn. Reson.* **81**, 196–200 (1989).
6. S. D. Cady *et al.*, *Nature* **463**, 689–692 (2010).
7. L. Cegelski *et al.*, *J. Am. Chem. Soc.* **132**, 16052–16057 (2010).
8. C. P. Jaroniec, B. A. Tounge, C. M. Rienstra, J. Herzfeld, R. G. Griffin, *J. Magn. Reson.* **146**, 132–139 (2000).
9. E. A. Louie, P. Chirakul, V. Raghunathan, S. T. Sigurdsson, G. P. Drobny, *J. Magn. Reson.* **178**, 11–24 (2006).
10. Materials and methods are available as supplementary materials on *Science* Online.
11. K. T. Mueller, *J. Magn. Reson. A* **113**, 81–93 (1995).
12. D. Frenkel, B. Smit, *Understanding Molecular Simulation from Algorithms to Applications* (Academic Press, San Diego, CA, 2002).
13. S. Loos, W. Seichter, E. Weber, F. Mertens, *Acta Crystallogr. Sect. E Struct. Rep. Online* **68**, o2501 (2012).

Acknowledgments: This research was supported through the Center for Gas Separations Relevant to Clean Energy Technologies, an Energy Frontier Research Center funded by the U.S. Department of Energy, Office of Science, Office of Basic Energy Sciences under award DE-SC0001015, and the synthesis effort (H.D.) was partially supported by BASF SE (Ludwigshafen, Germany). For all computations, we used the resources of the National Energy Research Scientific Computing Center (NERSC). We thank W. Morris, C. Stevens, and H. Furukawa for their invaluable assistance.

Supplementary Materials

www.sciencemag.org/cgi/content/full/science.1238339/DC1
Materials and Methods
Supplementary Text
Figs. S1 to S31
Tables S1 to S12
References (*14*–*42*)

26 March 2013; accepted 3 July 2013
Published online 25 July 2013;
10.1126/science.1238339

Microscopic Evidence for Liquid-Liquid Separation in Supersaturated $CaCO_3$ Solutions

Adam F. Wallace,[1,2,3]* Lester O. Hedges,[1,2] Alejandro Fernandez-Martinez,[1,4] Paolo Raiteri,[5] Julian D. Gale,[5] Glenn A. Waychunas,[1] Stephen Whitelam,[2] Jillian F. Banfield,[1,6] James J. De Yoreo[2,7,8]*

Recent experimental observations of the onset of calcium carbonate ($CaCO_3$) mineralization suggest the emergence of a population of clusters that are stable rather than unstable as predicted by classical nucleation theory. This study uses molecular dynamics simulations to probe the structure, dynamics, and energetics of hydrated $CaCO_3$ clusters and lattice gas simulations to explore the behavior of cluster populations before nucleation. Our results predict formation of a dense liquid phase through liquid-liquid separation within the concentration range in which clusters are observed. Coalescence and solidification of nanoscale droplets results in formation of a solid phase, the structure of which is consistent with amorphous $CaCO_3$. The presence of a liquid-liquid binodal enables a diverse set of experimental observations to be reconciled within the context of established phase-separation mechanisms.

Calcium carbonate ($CaCO_3$) has been intensely studied over the past century, and its most stable polymorph at ambient conditions, calcite, is often cited as a model of classical crystal growth behavior (*1*). However, findings from titration, ultracentrifugation (*2*, *3*), and cryogenic transmission electron microscopy (cryo-TEM) (*3*, *4*) now suggest that the onset of $CaCO_3$ mineralization—nucleation—contradicts classical expectations. In the classical picture, nucleation is a stochastic process in which thermal fluctuations induce the formation of clusters that are unstable with respect to dissolution. Clusters increase in both size and free energy until a threshold is crossed, whereupon the energy gained by forming the bulk material overcomes the penalty for creating an interface, and growth proceeds spontaneously. Contrasting with this classical picture, recent observations of long-lived nanometer-sized clusters present before nucleation have led to a predominant view of $CaCO_3$ formation in which the nucleation pathway is "nonclassical" (*2*, *3*, *5*–*8*), involving prenucleation clusters that are stable (or metastable) with respect to both dissolution and growth. In this model, bulk $CaCO_3$ forms primarily through aggregation of these clusters.

An alternative route to mineralization, liquid-liquid separation, has also been proposed based on light scattering, electron microscopy, and nuclear magnetic resonance (NMR) (*9*–*11*). This hypothesis is supported by experimental work documenting the formation of liquid magnesium sulfate ($MgSO_4$) at high temperature (*12*), as well as the known persistence of a polymer-stabilized liquid

[1]Earth Sciences Division, Lawrence Berkeley National Laboratory, Berkeley, CA 94720, USA. [2]The Molecular Foundry, Lawrence Berkeley National Laboratory, Berkeley, CA 94720, USA. [3]Department of Geological Sciences, University of Delaware, Newark, DE 19716, USA. [4]Institut des Sciences de la Terre (ISTerre), Université de Grenoble 1, CNRS, 38041 Grenoble, France. [5]Nanochemistry Research Institute, Department of Chemistry, Curtin University, Post Office Box U1987, Perth, WA 6845, Australia. [6]Department of Earth and Planetary Science, University of California, Berkeley, Berkeley, CA 94720, USA. [7]Materials Sciences Division, Lawrence Berkeley National Laboratory, Berkeley, Berkeley, CA 94720, USA. [8]Physical Sciences Division, Pacific Northwest National Laboratory, Richland, WA 99352, USA.

*Corresponding author. E-mail: afw@udel.edu (A.F.W.); james.deyoreo@pnnl.gov (J.J.D.Y.)

$CaCO_3$ phase under ambient conditions (*13*). A recent study using NMR to quantify the diffusion of ions in solution after the introduction of calcium (*11*) concluded that a bicarbonate-rich liquid phase may exist at pH = 8.5. However, because the measurements quantified the diffusion of ion species in a bulk sense only, the inhibited mobility of the bicarbonate ions could not be unambiguously assigned to the formation of cluster species over ion-pairs; moreover, the proclivity of calcium ions to structure water and influence the overall solution viscosity with increasing concentration could not be addressed. Thus, conclusive experimental evidence that the clusters observed at the onset of $CaCO_3$ mineralization are liquid does not exist, and the relationship between the prenucleation clusters and the hypothesized liquid phase remains unclear, as does the size distribution and thermodynamic character of clusters themselves (*8*, *14*).

Owing to the challenges faced by experimental approaches in directly quantifying the energetics of transient nanoscale cluster species that form during the nucleation process, we used molecular dynamics simulations to investigate whether initially formed clusters are stable or unstable relative to the solution and to explore their formation pathways. Earlier simulations (*5*, *6*, *15*, *16*) used high ion concentrations in order to increase the frequency of ion association events and facilitate sampling of the energy landscape within time scales accessible with unbiased simulations (*5*, *15*). After formation, the clusters generated in this manner were transferred to lower concentration environments in order to demonstrate their stability at more experimentally relevant conditions (*5*). These results show that the earliest formed clusters adopt low-density chain, ring, and branched structures. However, in the high-concentration limit growth proceeds at the diffusion limit, with barriers opposing ion attachment on par with the ambient thermal energy ~k_BT, where k_B is the Boltzmann constant and T is temperature. Application of biased sampling methods—designed to limit the amount of time the system spends exploring local features of the energy landscape (metadynamics)—found that compact crystalline states could be stable at sizes as small as ~2 to 4 nm (*16*), although their free energy relative to ions in solution was not determined.

Neither of the aforementioned approaches shed light on the evolution of the initial hydrated clusters to more compact dense states, which is the key to understanding the pathway to nucleation and the stability of the prenucleation clusters. We explored cluster stability, structure, and the nucleation pathway by introducing simulation techniques that are capable of determining the nature of equilibrated $CaCO_3$ cluster species directly at the low concentrations used experimentally. We used the Kawska-Zahn method (*17*), modified to allow for solvation during all steps, to grow hydrated clusters into a size regime (~1.5 to 2 nm in diameter) that overlaps with cryo-TEM–based observations of prenucleation clusters, while temperature-based replica-exchange molecular dynamics (*18*, *19*) was used to hasten the exploration of the energy landscape and minimize the tendency of the system to become kinetically trapped in local energy minima during the early stages of nucleation and growth (*20*).

In agreement with previous studies (*5*, *15*), our simulations show that low-density configurations are observed for small clusters; however, such arrangements give way to more condensed states very rapidly with further ion additions (Fig. 1A). The dynamic character of the clusters is quantified through determination of the constituent ion diffusivities (*20*). For all cluster sizes investigated, we obtained diffusive characteristics that were inconsistent with the solid state. Plotted as a function of cluster size, ion diffusivities fell largely within the range of self-diffusivities expressed by several common solvents (Fig. 1B) (*21*) and were markedly higher than in bulk amorphous calcium carbonate (ACC) and calcite, indicating that the clusters are droplets of a dense ion-rich liquid phase of $CaCO_3(nH_2O)$. The ion diffusivities decrease as the dense liquid phase grows; however, the rate of decline gradually abates and approaches a constant value characteristic of the "bulk" liquid phase. The leveling off of the ion diffusivity is accompanied by a

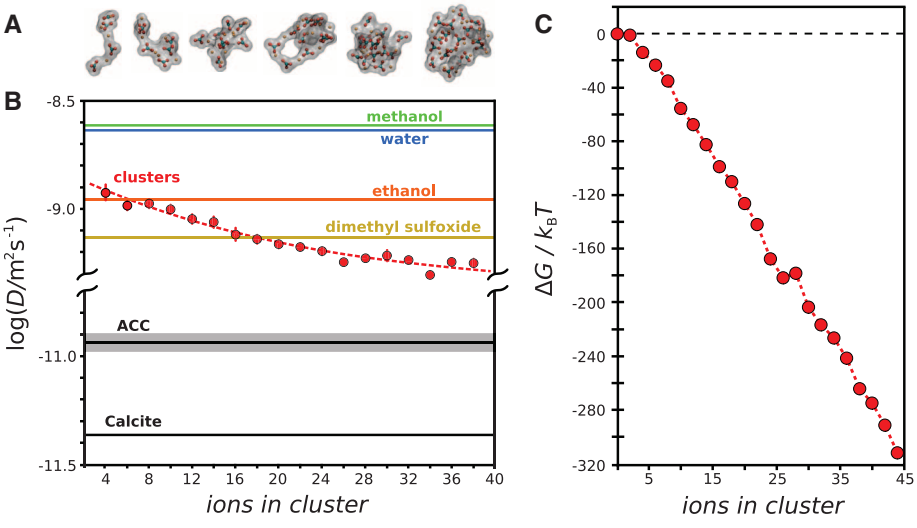


Fig. 1. Structural, dynamical, and energetic properties of $CaCO_3$ clusters. (**A**) Snapshots taken from replica-exchange molecular dynamics simulations showing the evolution of polymeric cluster configurations toward denser structures at larger sizes. (**B**) Plot showing the diffusivity of calcium ions within the cluster species at various stages of growth compared with two solid phases of $CaCO_3$, calcite, and ACC (from simulation) and the self-diffusivities (experimental) of several common solvents. The error bars represent the mean ± SEM for n = 6 simulation trajectories at each cluster size. (**C**) The free energy of the solvated ions as a function of cluster size determined at $[Ca^{2+}] = [CO_3^{2-}] = 0.015$ mol/L using the method of Lin and coworkers (*30*). The symbols represent the mean ± SEM for n = 240 free energy calculations at each cluster size.

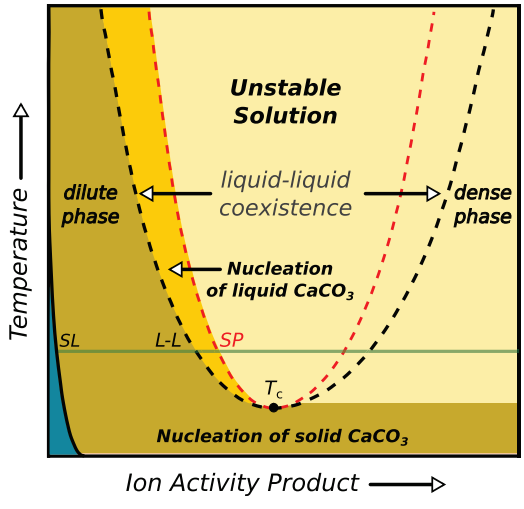


Fig. 2. Schematic representation of the phase relationships in the $CaCO_3$-H_2O system. The green horizontal line represents a constant temperature slice through the stability fields as the solution ion activity product is increased. The solubility of all polymorphs is represented by a single solubility line (SL), which bounds the blue undersaturated solution field. This simplification highlights that the solid phases of $CaCO_3$ (calcite, aragonite, vaterite, and presumably ACC) all display the same general retrograde solubility behavior. Indirect nucleation of the solid phases proceeds to the high concentration side of the dashed black liquid-liquid coexistence line (L-L). The bright yellow phase field bounded by the L-L line and the dashed red spinodal line (SP) indicates the conditions in which nucleation of the dense liquid phase is possible. In the region bounded by the spinodal line, the solution is unstable to fluctuations, and liquid-liquid separation proceeds spontaneously.

gradual increase in the average coordination of calcium by carbonate ions, and a smooth crossover in the most probable coordination number from 2 to 3 that culminates at ~26 ions (fig. S1). However, as evidenced by a plot of the average Ca-C coordination number against the ion diffusivity (fig. S2), the structural and dynamical properties of the clusters are correlated and smoothly trending, suggesting that the formation of the dense liquid is not marked by an abrupt transition in cluster character (supplementary text).

A plot of the free energy versus cluster size (Fig. 1C) displays an entirely downhill free energy landscape, except for a possible slight increase at 26 ions that is correlated with the gradual evolution of the Ca-C coordination number from 2 to 3 (*20*). However, the upturn in free energy is within the statistical confidence of our analysis. Moreover, if real it represents a thermodynamic impedance to the formation of the dense liquid phase of less than ~8 k_BT (20 kJ/mol at 300 K) at the simulated conditions ($[Ca^{2+}] = [CO_3^{2-}] = 0.015$ mol/L), which is not sufficient to halt the growth of the clusters. Therefore, the most salient result of the free energy analysis is the observation that the free energy decreases monotonically with cluster size.

The observed free energy landscape, combined with the absence of a substantial repulsive barrier opposing cluster association (*6*), is characteristic of a solution that has exceeded its stability limit and is undergoing a spontaneous phase separation by means of spinodal decomposition (*22*). The accessibility of the spinodal region at relatively modest concentrations has considerable consequences for the mineralization process. Thermodynamically, it indicates that a liquid-liquid coexistence line exists between the dense liquid phase and the ion-poor solution phase (Fig. 2), so that the two liquids are in a state of metastable equilibrium with respect to solid $CaCO_3$ phases over a wide range of solution conditions.

The existence of this dense liquid phase enables both conventional ion-by-ion and cluster-mediated crystallization pathways to be described in terms of established phase separation models, without invoking nonclassical constructs. The schematic representation of the presumptive phase relationships within the system (Fig. 2) displays regions in composition and temperature space in which both direct and indirect crystallization mechanisms are possible. The exact relationships

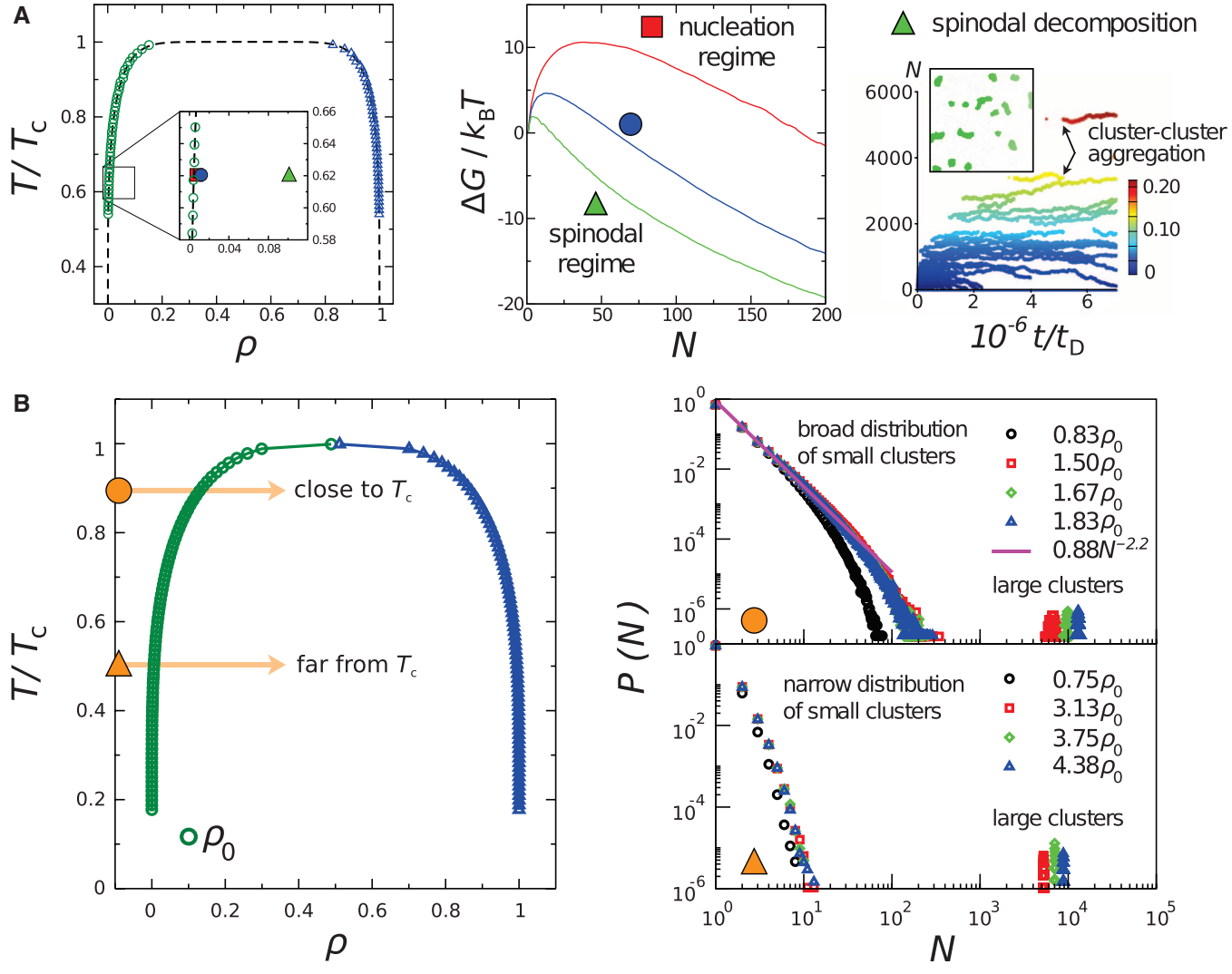


Fig. 3. Classical liquid-liquid phase separation can generate coexisting populations of small and large clusters. (**A**) (Left) Temperature-density phase diagram for the two-dimensional (2D) Ising lattice gas (fig. S3 and movies S1 to S3). (Center) The free energy barrier to phase change diminishes with supersaturation. (Right) In the small-barrier (spinodal) regime, an evolving cluster population is generated (inset, snapshot). The distribution of cluster sizes (colored according to how much of the system's mass the clusters contain) versus time (t_D is the characteristic time for a monomer to diffuse a length equal to its diameter) is shown at each point. (**B**) (Left) Phase diagram for the 3D Ising lattice gas. (Right) Equilibrated cluster size distributions after the completion of phase separation carried out at a range of densities near (top) and far from (bottom) the critical temperature. ρ_0 is the binodal density. Near the critical temperature, a broad distribution of small clusters coexists with the largest products of phase change. Small clusters are seen even in undersaturated solution. Because of lattice artifacts, cluster size distributions from the Ising model can only be compared with experimental distributions on a qualitative level (*24*) (supplementary text).

are a complex function of chemical factors (such as pH, ionic strength, concentration, composition, and temperature) and may shift substantially depending on environmental conditions. Based on the retrograde solubility exhibited by solid $CaCO_3$ phases, the known behavior of $MgSO_4$ at high temperatures (*12*), and the interpretations of Faatz *et al*. (*9*), the binodal orientation is likely concave up. A solution with a composition falling within the ion-poor solution field of the phase diagram is thermodynamically favored to nucleate one of the crystalline phases of $CaCO_3$. However, in practice the thermodynamic barriers opposing nucleation in this regime are predicted to be well in excess of 100 k_BT (*23*), preventing homogeneous nucleation from occurring on observable time scales.

As the ion activity product increases (at constant temperature), the liquid-liquid coexistence line is encountered, and homogeneous nucleation of the dense liquid phase becomes possible. Dense liquid formation on short time scales is more likely than direct crystallization because the excess free energy of the solution-liquid interface is considerably reduced relative to the solution-crystal interface, resulting in a lower thermodynamic barrier to liquid-liquid separation than to crystallization. As the ion-activity product is increased even further, the spinodal line is crossed. This point marks the limit of solution stability and the point at which the barrier opposing nucleation becomes comparable with the ambient thermal energy; infinitesimal fluctuations in the density of ions in solution give rise to clusters that are thermodynamically unstable with respect to growth, and a macroscopic quantity of the dense liquid phase emerges.

The predicted liquid-liquid separation also provides a mechanism for generating clusters of various sizes, as a generic consequence of the spatial correlations that result from particle interactions (*24*). We demonstrate this mechanism within the Ising lattice gas, a canonical model of phase change that enables exploration of the general dynamics of solutions driven out of equilibrium independent of system-specific chemical details (*25*, *26*). The results exhibit a number of features that are consistent with experimental observations.

First, in the spinodal regime hierarchical cluster-cluster association generates a population of large clusters. These clusters form on a monotonically decreasing free energy landscape (Fig. 3A and fig. S3) akin to the results of the atomistic simulations (Fig. 1C) and therefore have no special thermodynamic status. At the ion concentrations characteristic of the experiments in (*2*, *3*, *9*), the mean radius $R(t)$ of this population of clusters should evolve rapidly as $R(t) \sim 100\ \text{nm}\ (t/\text{s})^{1/3}$ (*27*). Although the initial microscopic phase observed by Faatz *et al*. (*9*) is not clearly identifiable as either liquid or solid, the evolution of the particle size distribution as displayed in their Figs. 1B and 2 is consistent with this expectation.

Second, a population of small clusters emerges alongside the rapidly growing products of spinodal decomposition (Fig. 3B) (*24*). These clusters are similar in character to those that form from undersaturated solutions; they appear rapidly and persist throughout the spinodal process. After phase separation, the small cluster population is stable in a statistical sense. The binodal exerts a considerable amount of influence over the resulting size distribution, which broadens—because of a reduction in the cluster-solution interfacial tension (*24*, *28*)—with increasing proximity to the critical temperature [Faatz *et al*. (*9*) estimated that the critical temperature is close to room temperature on the basis that the number density of large clusters tended toward zero at ~10°C]. These results are consistent with those of Pouget *et al*. (*3*), who observed large particles coexisting with a persistent population of much smaller clusters (0.7 to 1.1 nm). Although Pouget *et al*. attributed the larger-size fraction to ACC, the low-dose electron diffraction technique used may not be able to distinguish between a cryogenically frozen liquid phase and a bonafide amorphous solid. Therefore, a conventional liquid-liquid phase separation mechanism can account for a richly structured fluid of clusters of sizes qualitatively similar to those seen experimentally, both small (*2*, *3*) and large (*3*, *9*).

To discern whether the liquid clusters identified in this study are reasonable models for the nanoscopic species observed at the onset of phase separation, a model of solid ACC was constructed by randomly aggregating clusters of the dense liquid phase and thereafter reducing the water content, by a simulated dehydration process, to be commensurate with that of amorphous hydrated $CaCO_3$ (*20*). The local order within the model ACC structure was quantified through calculation of the total pair distribution function and compared with the results of x-ray scattering measurements for validation. This approach is distinct from the previous effort to model the structure with reverse Monte Carlo methods (*29*) because the structure is derived from an assembly and dehydration process that mimics a plausible growth mechanism.

The model pair distribution function is distinct from those for the crystalline $CaCO_3$ polymorphs, which are ordered indefinitely beyond the 15 Å radius that comprises the coherent x-ray scattering length in ACC and is also in general registry with the experimentally measured distribution function (Fig. 4). The most evident differences between the model and experimental structures arise at small radial distances (O-H and C-O distances) at which the experimental signal is most subject to interference from Fourier transformation. Additionally, the Ca-O peak centered at ~2.4 Å is slightly split in the model structure, showing the presence of two peaks arising from nearest neighbor oxygen contacts in water molecules and carbonate ions. However, the major features of the experimental pair distribution function are reproduced. Although the model structure

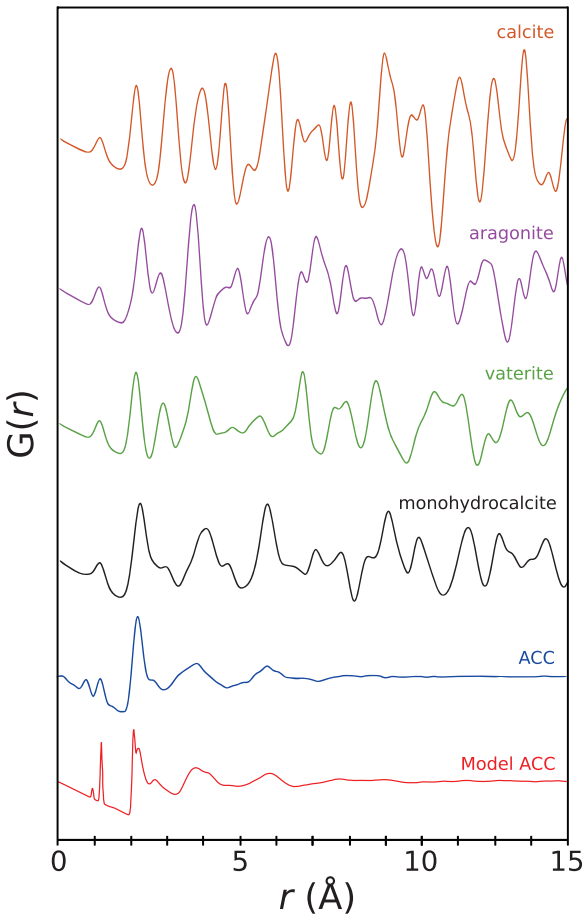


Fig. 4. Local order in the $CaCO_3$ polymorphs. The total x-ray pair distribution functions of crystalline and amorphous polymorphs of $CaCO_3$ are compared with that of the model ACC structure produced through aggregation of the cluster species identified in this study.

is by no means unique or exact, the general correspondence of the model and experimental structures supports the notion that ACC forms by means of ion-rich liquid cluster aggregation (*2*, *3*), followed by dehydration and solidification.

Recent experimental results on $CaCO_3$ mineralization have shifted the focus of research toward exploration of prenucleation clusters as the crucial precursor species during the mineral formation process (*2*, *3*, *5*–*8*). Although sedimentation coefficients obtained from seminal analytical ultracentrifugation experiments (*2*, *3*) were initially believed to provide evidence that the prenucleation cluster population was long-lived and narrowly distributed, more recent interpretations (*8*, *14*) suggest that they represent an average over an unknown distribution of clusters detected over the course of many hours. This latter view is supported by sample-to-sample variations that are larger than the apparent cluster size distributions themselves (*3*), as well as cryo-TEM results (*3*) revealing both small (~0.7 to 1.1 nm) and large (30 to 250 nm) clusters and cluster coalescence.

The findings reported here demonstrate that if the atomic potentials widely used to simulate the behavior of the $CaCO_3$ system are accurate, then the system should exhibit a liquid-liquid binodal, and this phase behavior will result in cluster dynamics that are consistent with the above ultracentrifugation and TEM observations, as well as those based on light scattering and NMR (*9*–*11*). Although the phase separation mechanism depends on where the system lies relative to the binodal, our molecular dynamics simulations suggest that the spinodal line is easily accessible within the range of supersaturations spanned by laboratory experiments. Further, on the basis of our Ising model simulations, we would also expect a population of small clusters to coexist with large clusters produced by spinodal decomposition. Although we cannot make quantitative predictions for experimental cluster size distributions, we predict that this distribution of small clusters broadens on approaching the critical temperature (*9*). Upon crossing the spinodal, growth and coalescence of the dense liquid clusters is predicted, and their dehydration produces an amorphous solid exhibiting a structure that is consistent with that determined experimentally for ACC.

On the basis of these findings, we argue that liquid-liquid phase separation can explain the behavior of calcium and carbonate-bearing solutions within the context of established mechanisms without negating long-standing physical concepts (*8*). Thus, obtaining experimental data that can distinguish stable prenucleation clusters from those produced through liquid-liquid separation is of the utmost importance.

References and Notes

1. H. H. Teng, P. M. Dove, C. A. Orme, J. J. De Yoreo, *Science* **282**, 724–727 (1998).
2. D. Gebauer, A. Völkel, H. Cölfen, *Science* **322**, 1819–1822 (2008).
3. E. M. Pouget *et al.*, *Science* **323**, 1455–1458 (2009).
4. J. Rieger *et al.*, *Faraday Discuss.* **136**, 265–277, discussion 309–328 (2007).
5. R. Demichelis, P. Raiteri, J. D. Gale, D. Quigley, D. Gebauer, *Nat. Commun.* **2**, 590 (2011).
6. P. Raiteri, J. D. Gale, *J. Am. Chem. Soc.* **132**, 17623–17634 (2010).
7. D. Gebauer *et al.*, *Angew. Chem. Int. Ed. Engl.* **49**, 8889–8891 (2010).
8. D. Gebauer, H. Cölfen, *Nano Today* **6**, 564–584 (2011).
9. M. Faatz, F. Gröhn, G. Wegner, *Adv. Mater.* **16**, 996–1000 (2004).
10. S. E. Wolf, J. Leiterer, M. Kappl, F. Emmerling, W. Tremel, *J. Am. Chem. Soc.* **130**, 12342–12347 (2008).
11. M. A. Bewernitz, D. Gebauer, J. Long, H. Cölfen, L. Gower, *Faraday Discuss.* **159**, 291–312 (2012).
12. X. Wang, I.-M. Chou, W. Hu, R. C. Burruss, *Geochim. Cosmochim. Acta* **103**, 1–10 (2013).
13. L. B. Gower, D. J. Odom, *J. Cryst. Growth* **210**, 719–734 (2000).
14. *Faraday Discuss.* **155**, 139–180 (2012).
15. G. A. Tribello, F. Bruneval, C. Liew, M. Parrinello, *J. Phys. Chem. B* **113**, 11680–11687 (2009).
16. D. Quigley, C. L. Freeman, J. H. Harding, P. M. Rodger, *J. Chem. Phys.* **134**, 044703 (2011).
17. A. Kawska, J. Brickmann, R. Kniep, O. Hochrein, D. Zahn, *J. Chem. Phys.* **124**, 024513 (2006).
18. S. Chaudhury, M. A. Olson, G. Tawa, A. Wallqvist, M. S. Lee, *J. Chem. Theory Comput.* **8**, 677–687 (2012).
19. Y. Sugita, Y. Okamoto, *Chem. Phys. Lett.* **314**, 141–151 (1999).
20. Materials and methods are available as supplementary materials on *Science* Online.
21. J. Wang, T. Hou, *J. Comput. Chem.* **32**, 3505–3519 (2011).
22. J. W. Cahn, J. E. Hilliard, *J. Chem. Phys.* **31**, 688–699 (1959).
23. Q. Hu *et al.*, *Faraday Discuss.* **159**, 509 (2012).
24. N. Sator, *Phys. Rep.* **376**, 1–39 (2003).
25. K. Binder, H. Müller-Krumbhaar, *Phys. Rev. B* **9**, 2328–2353 (1974).
26. D. Stauffer, A. Coniglio, D. Heermann, *Phys. Rev. Lett.* **49**, 1299–1302 (1982).
27. E. D. Siggia, *Phys. Rev. A* **20**, 595–605 (1979).
28. T. Vicsek, F. Family, *Phys. Rev. Lett.* **52**, 1669–1672 (1984).
29. A. L. Goodwin *et al.*, *Chem. Mater.* **22**, 3197–3205 (2010).
30. S.-T. Lin, P. K. Maiti, W. A. Goddard 3rd, *J. Phys. Chem. B* **114**, 8191–8198 (2010).

Acknowledgments: This work was performed at the Lawrence Berkeley National Laboratory in support of the Center for Nanoscale Control of Geologic CO_2, an Energy Frontier Research Center, and was carried out at the Molecular Foundry, a Scientific User Facility, both of which are funded by the U.S. Department of Energy (DOE), Office of Science, Office of Basic Energy Sciences under contract DE-AC02-05CH11231. Use of the Advanced Photon Source, an Office of Science User Facility operated for the DOE Office of Science by Argonne National Laboratory, was supported by the DOE under contract DE-AC02-06CH11357. This research used resources of the National Energy Research Scientific Computing Center, which is supported by the Office of Science of the DOE under contract DE-AC02-05CH1123 and the Lawrencium computational cluster resource provided by the IT Division at the Lawrence Berkeley National Laboratory (supported by the Director, Office of Science, Office of Basic Energy Sciences, of the DOE under contract DE-AC02-05CH11231). J.D.G. and P.R. thank the Australian Research Council for funding under grant DP0986999 and iVEC/National Computational Infrastructure for computing resources.

Supplementary Materials

www.sciencemag.org/cgi/content/full/341/6148/885/DC1
Materials and Methods
Supplementary Text
Figs. S1 to S3
References (*31*–*60*)
Movies S1 to S3

1 October 2012; accepted 24 June 2013
10.1126/science.1230915

Molecular Mechanism for Plant Steroid Receptor Activation by Somatic Embryogenesis Co-Receptor Kinases

Julia Santiago, Christine Henzler, Michael Hothorn*

Brassinosteroids, which control plant growth and development, are sensed by the leucine-rich repeat (LRR) domain of the membrane receptor kinase BRASSINOSTEROID INSENSITIVE 1 (BRI1), but it is unknown how steroid binding at the cell surface activates the cytoplasmic kinase domain of the receptor. A family of somatic embryogenesis receptor kinases (SERKs) has been genetically implicated in mediating early brassinosteroid signaling events. We found a direct and steroid-dependent interaction between the BRI1 and SERK1 LRR domains by analysis of their complex crystal structure at 3.3 angstrom resolution. We show that the SERK1 LRR domain is involved in steroid sensing and, through receptor–co-receptor heteromerization, in the activation of the BRI1 signaling pathway. Our work reveals how known missense mutations in BRI1 and in SERKs modulate brassinosteroid signaling and the targeting mechanism of BRI1 receptor antagonists.

Plants have membrane-integral receptor kinases that sense diverse extracellular signals including steroid hormones (*1*), peptides (*2*), and proteins (*3*). The steroid receptor kinase BRI1, which controls plant growth and development (*4*), binds the hormone brassinolide (BL) with its LRR ectodomain (*5*–*8*). BL binding to BRI1 causes ordering of a ~70-residue island domain that, together with the LRR core, may form a docking platform for a co-receptor protein (*7*, *8*). The size of the envisioned interaction surface and its proximity to the membrane suggest that the SERK family of plant receptor kinases are likely co-receptor candidates. SERK1 and SERK3 are genetic components of the brassinosteroid signaling

Structural Plant Biology Lab, Friedrich Miescher Laboratory of the Max Planck Society, Spemannstraße 39, Tübingen 72076, Germany.

*Corresponding author. E-mail: mhothorn@tuebingen.mpg.de

pathway (*9*–*12*). BRI1 and SERK3 associate in a ligand-dependent manner (*13*), and this interaction can be disrupted by the BRI1 inhibitor protein BKI1 (*14*). The BRI1 and SERK3 kinase domains transphosphorylate each other upon steroid sensing (*13*).

To study the interaction between BRI1 and SERK family proteins, we first characterized the *bri1$_{sud1}$* gain-of-function allele (*15*) in molecular detail. A 2.5 Å crystal structure of bri1$_{sud1}$ (table S1) shows that the Gly^{643} → Glu point mutation is involved in the stabilization of the island domain, a structural motif that we previously suggested to be crucial for the interaction with the co-receptor (*8*) (Fig. 1A). Glu^{643} in bri1$_{sud1}$ contributes to a hydrogen-bonding network in the island domain β sheet, which is part of the hormone binding pocket (green in Fig. 1A). The bri1$_{sud1}$-BL complex indicates that bri1$_{sud1}$ cannot signal independent of ligand, but rather stabilizes the hormone-bound state of the receptor. Consistent with this observation, we found that *bri1$_{sud1}$* plants are only partially resistant to the brassinosteroid biosynthesis inhibitor brassinazole (*16*) (Fig. 1B).

We next produced the isolated SERK1 ectodomain (residues 24 to 213) by secreted expression in insect cells and obtained crystals after mutating two of the five N-glycosylation sites (Asn^{115} → Asp, Asn^{163} → Gln). A 1.5 Å crystal structure of SERK1 (table S1) revealed the presence of five LRRs and the canonical N- and C-terminal capping motifs found in plant LRR proteins (*7*, *8*, *17*) (Fig. 1C). The size of the SERK1 LRR domain is in good agreement with the size of the envisioned docking platform in BRI1.

We took advantage of the bri1$_{sud1}$ mutation to form biochemically stable ternary complexes containing bri1$_{sud1}$, SERK1, and the steroid hormone, purified by size exclusion chromatography. The isolated LRR domains of both bri1$_{sud1}$ and SERK1 eluted as apparent monomers from the size exclusion column, whereas the retention time of a bri1$_{sud1}$-BL-SERK1 complex corresponded to a heterodimer at physiological cell wall pH (pH 4.5 to 6; Fig. 1, D and E). Complex formation was BL-dependent, which suggests that the direct physical interaction of the BRI1 and SERK1 ectodomains is mediated by the hormone itself (Fig. 1, D and E). Similar complexes could be formed using the wild-type BRI1 ectodomain, but we were unable to crystallize them (fig. S1).

Crystals of a bri1$_{sud1}$-BL-SERK1 complex diffracted to 3.3 Å resolution. The structure was solved by molecular replacement, using the isolated bri1$_{sud1}$ and SERK1 LRR domains as search models (table S1). The asymmetric unit contained two highly similar bri1$_{sud1}$-BL-SERK1 complexes [fig. S2; root mean square deviation (RMSD) = 0.7 Å comparing 893 corresponding C_α atoms]. SERK1 bound to the previously suggested docking platform in BRI1 (*8*), using the inner surface

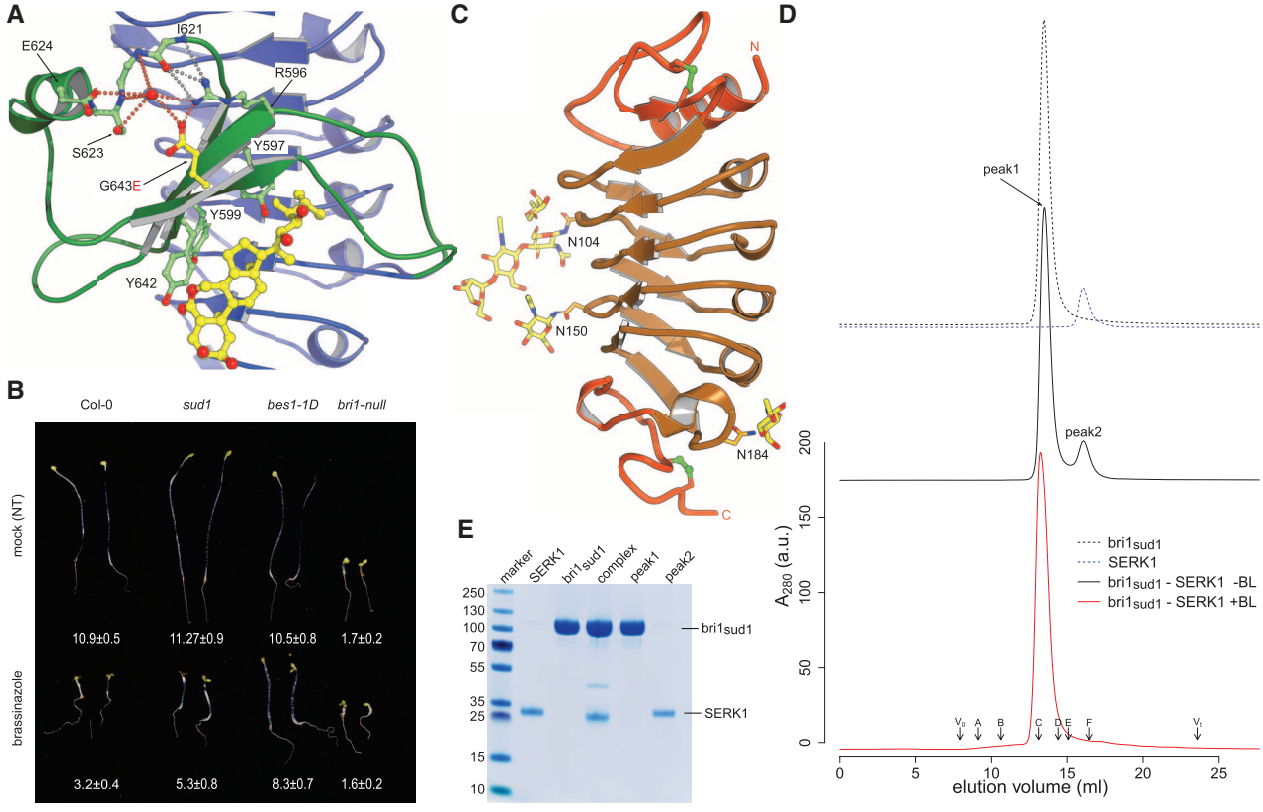


Fig. 1. The BRI1 and SERK1 ectodomains interact upon steroid sensing. (**A**) The hormone binding pocket in bri1$_{sud1}$ with the LRR core (blue), the island domain (green), BL (yellow), and island domain Tyr^{597}, Tyr^{599}, and Tyr^{642} contributing to the BL binding pocket in green (sticks). Polar interactions between island domain Arg^{596} and the main-chain oxygen and nitrogen from Ile^{621} are in gray. Additional contacts by Glu^{643} in bri1$_{sud1}$ to Ser^{623} and Glu^{624} (red) are mediated by a water molecule (red sphere). (**B**) *bri1$_{sud1}$* plants show reduced hypocotyl growth in the presence of the BL biosynthesis inhibitor brassinazole (1 μM). Hypocotyl length is in mm ± SD (n = 30); NT, nontreated. Controls (Col-0, *bes1-1D*, and a *bri1-null* allele) are shown alongside. (**C**) Ribbon diagram of the SERK1 ectodomain with N- and C-terminal caps (orange), the LRR core (gold), disulfide bridges (green), and N-glycosylation sites in yellow (sticks). (**D**) Analytical size exclusion chromatography traces: BL-bound bri1$_{sud1}$ elutes as a monomer (black dotted line), as does the isolated SERK1 LRR domain (blue dotted line). The bri1$_{sud1}$-BL-SERK1 complex elutes as an apparent heterodimer (red line); a mixture of bri1$_{sud1}$ and SERK1 in the absence of BL yields two isolated peaks that correspond to monomeric bri1$_{sud1}$ and SERK1, respectively (black line). Void (V_0) and total volume (V_t) are shown, together with elution volumes for molecular mass standards (A, thyroglobulin, 669 kD; B, ferritin, 440 kD; C, aldolase, 158 kD; D, conalbumin, 75 kD; E, ovalbumin, 44 kD; F, carbonic anhydrase, 29 kD). The calculated molecular masses for the bri1$_{sud1}$ and SERK1 peaks are ~125 and ~35 kD, respectively; purified bri1$_{sud1}$ and SERK1 are ~110 and ~30 kD. A_{280}, absorbance at 280 nm. (**E**) SDS–polyacrylamide gel electrophoresis (PAGE) analysis of peak elution fractions from the experiments shown in (D). Single-letter abbreviations for amino acid residues: E, Glu; G, Gly; I, Ile; N, Asn; R, Arg; S, Ser; Y, Tyr.

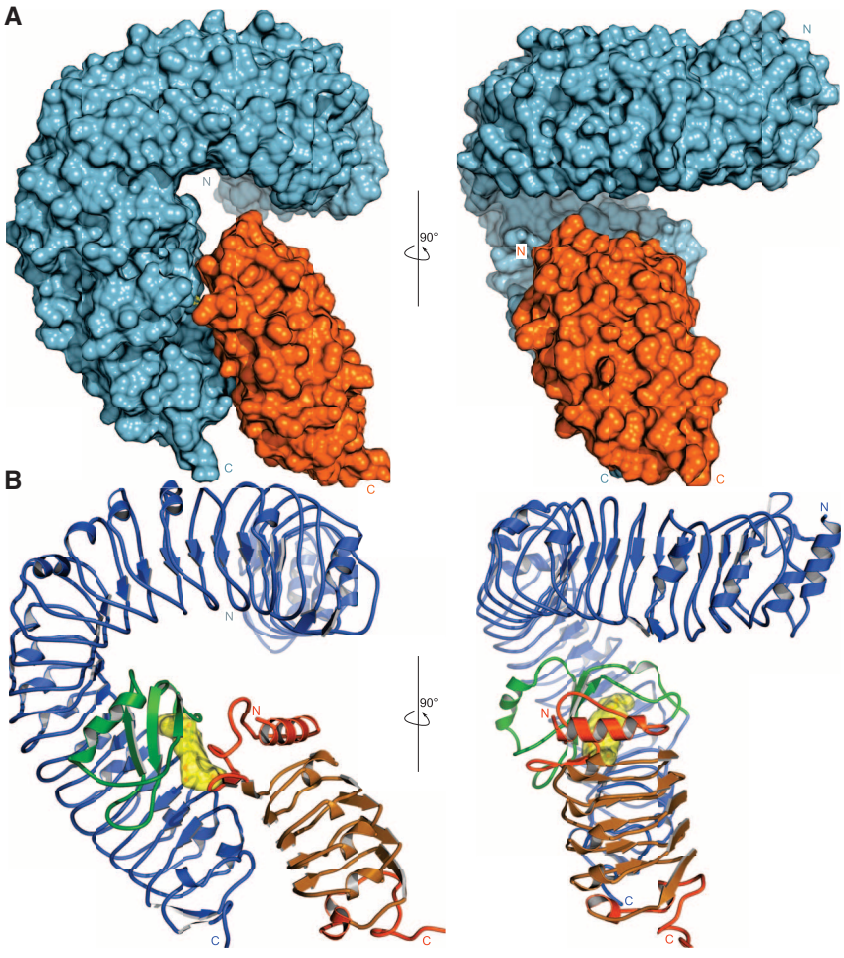


Fig. 2. Architecture of the ternary bri1$_{sud1}$-BL-SERK1 complex. (**A**) Side and 90°-rotated front views of the complex, with the bri1$_{sud1}$ (blue) and SERK1 (orange) LRR domains in surface representation. (**B**) Corresponding ribbon diagrams of the bri1$_{sud1}$ LRR domain (blue), the BRI1 island domain (green), and the SERK1 LRR domain (orange); BL is in yellow (surface representation). The co-receptor ectodomain binds to the lower end of the BRI1 superhelix, bringing the C termini of both ectodomains, which connect to the membrane helices and to the cytoplasmic kinase domains, into proximity.

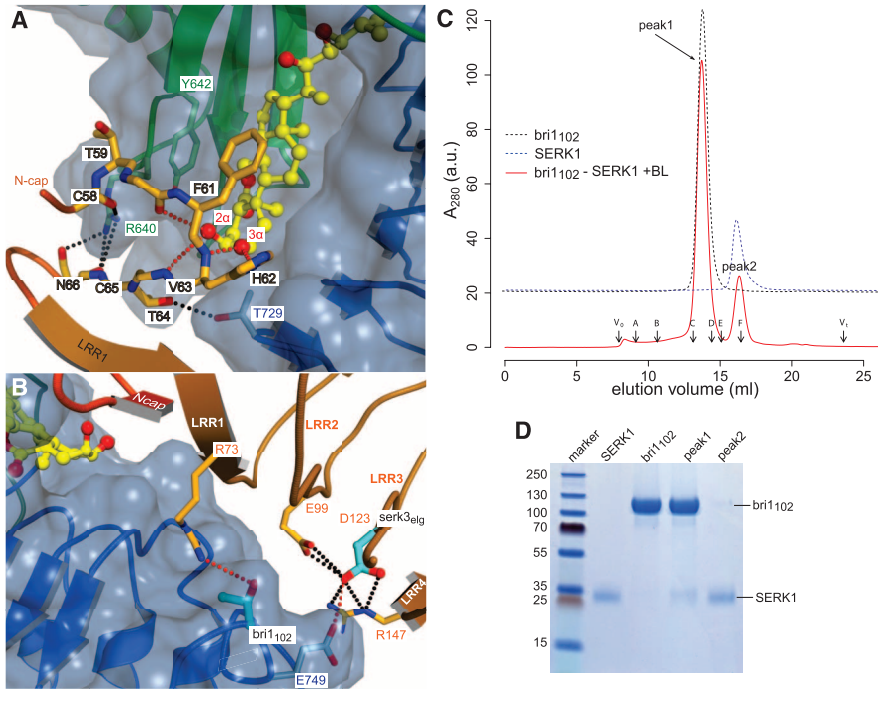


Fig. 3. Ligand chemistry and genetic missense alleles validate the BRI1-SERK1 complex interface. (**A**) The N-terminal capping domain of SERK1 directly contacts the BRI1 steroid binding pocket and the 2α,3α-diol moiety of BL. Shown is a molecular surface of BRI1, with the LRR core depicted in blue and the island domain in green. Parts of the SERK1 N-cap and LRR 1 are shown as ribbon diagram (orange). Main-chain hydrogen-bond interactions of SERK1 N-cap residues (Cys^{58}, Cys^{65}, and Asn^{66}) with island domain BRI1 residue Arg^{640} are depicted as dotted lines (black). SERK1 residues Phe^{61} and His^{62} are shown alongside with interactions to the 2α and 3α OH groups in BL shown in red. Another hydrogen-bond interaction is between SERK1 residue Thr^{64} and Thr^{729} in BRI1 LRR 25. (**B**) Known genetic BRI1 and SERK1 alleles map to the complex interface. Thr^{750} (cyan) in the BRI1 C-terminal cap contacts the conserved SERK1 residue Arg^{73} and is mutated to Ile in the BRI1 loss-of-function mutant *bri1-102*. SERK1 residue Asp^{123} is centrally located in the complex interface (cyan) and establishes contacts with Glu^{749} in the BRI1 C-terminal cap. The serk3$_{elg}$ gain-of-function allele, which causes mutation of the corresponding Asp^{122} to Asn, may further stabilize the complex interface. (**C**) Analytical size exclusion chromatography traces of BL-bound bri1$_{102}$, which elutes as a monomer (black dotted line), as does the isolated SERK1 LRR domain (blue dotted line). A mixture of bri1$_{102}$, BL, and SERK1 elutes as two isolated peaks, which suggests that the Thr^{750} → Ile mutation destabilizes the complex (red line; compare Fig. 1D). (**D**) SDS-PAGE analysis of peak elution fractions from the experiments shown in (C). Single-letter abbreviations for amino acid residues: C, Cys; D, Asp; E, Glu; F, Phe; H, His; N, Asn; R, Arg; T, Thr; V, Val; Y, Tyr.

of its LRR domain (Fig. 2). Superposition with the isolated $bri1_{sud1}$ and SERK1 ectodomains revealed no structural rearrangements upon complex formation (RMSD = 1 Å comparing 743 corresponding $bri1_{sud1}$ C_α atoms, RMSD = 0.6 Å comparing 185 corresponding SERK1 C_α atoms, respectively). The small complex interface (buried surface area ~850 $Å^2$) involves residues originating from the BRI1 island domain, from BRI1 LRR 25, and from SERK1 LRRs 1 to 4 (Fig. 2 and Fig. 3).

In contrast to previously described animal innate immunity receptor complexes (*18*, *19*), LRR capping domains are involved in the formation of the BRI1-SERK1 complex: The N-terminal cap of SERK1 folds on top of the BRI1 steroid binding pocket, where it establishes contacts with the BRI1 island domain (green in Fig. 3A), with BRI1 LRR 25 (BRI1 residues 726 to 729; Fig. 3A and fig. S5, in blue) and with the hormone itself. Here, SERK1 residue Phe^{61} (which appears disordered in the isolated SERK1 structure) makes a stacking interaction with the C ring of the hormone, while the neighboring histidine establishes hydrogen bonds with the 2α,3α-diol moiety of brassinolide (Fig. 3A and figs. S3A and S4). Our complex structure thus provides an explanation for the BL-dependent interaction of BRI1 and SERK1 (Fig. 1, D and E, and fig. S1) and for the critical role of the 2α and 3α hydroxyls in brassinosteroid bioactivity (*20*, *21*). These results are consistent with observations that a 2,3-acetonide form of BL acts as a brassinosteroid pathway antagonist (*22*). We speculate that this compound still binds to BRI1 (*8*) but disrupts the interaction with the co-receptor ectodomain, thereby blocking BRI1 activation (*13*, *22*) (fig. S3).

The C-terminal cap of BRI1 also contributes to complex formation by establishing contacts with residues originating from SERK1 LRRs 1 to 4 (Fig. 3B and figs. S4 and S5). Major nonpolar interactions are provided by SERK1 residues Tyr^{97}, Tyr^{101}, Tyr^{125}, and Phe^{145} as well as by residue Met^{745} in the BRI1 C-terminal cap (fig. S5). An extensive hydrogen-bonding network is centered around BRI1 C-terminal cap residue Glu^{749}, which is contacted by SERK1 residues Glu^{99}, Asp^{123}, and Arg^{147} from SERK1 LRRs 2, 3, and 4, respectively (Fig. 3B and fig. S5). Acidic residues in the complex interface titrate in the pH range relevant in the plant cell wall (Fig. 1, D and E, and fig. S1). All SERK1 interface residues are highly conserved among the known BRI1-interacting SERK family members from *Arabidopsis* and rice and in other small LRR receptor kinases (fig. S4).

The presence of two known genetic alleles in the outlined complex interface allowed us to validate our structural model. The strong loss-of-function allele *bri1-102* (Thr^{750} → Ile; cyan in Fig. 3B; see also fig. S5) (*23*), which does not affect steroid binding (*24*), mapped to the center of the BRI1-SERK1 interface, forming a hydrogen bond with SERK1 residue Arg^{73}. Mutation of the respective threonine to isoleucine destabilized the complex (Fig. 3, C and D), which explains the strong phenotype (*23*). A gain-of-function mutation ($serk3_{elg}$, Asp^{122} → Asn) (*25*) mapped to Asp^{123} in SERK1 (cyan in Fig. 3B; see also fig. S5). SERK1 Asp^{123} is part of the hydrogen-bonding network described above, and its mutation to Asn may allow for the formation of additional interactions with the BRI1 C-terminal cap. A more stable association of $serk3_{elg}$ with the receptor BRI1 would explain the behavior of this mutant, which displays a gain-of-function growth phenotype and more strongly associates with BRI1 upon steroid binding in vivo, even when the co-receptor kinase domain is catalytically inactive (*25*).

Taken together, our findings define the activation mechanism for a plant LRR receptor kinase, in which a shape-complementary co-receptor protein forms an integral part of the receptor's ligand-binding pocket. Our pharmacologically (*21*, *22*, *24*) and genetically (*11*, *12*, *23*, *25*) validated BRI1-BL-SERK1 complex structure suggests that BL acts as a "molecular glue" promoting association of the receptor with its co-receptor, which may trigger interaction of their kinase domains and subsequent activation of the signaling pathway (*13*). A similar activation mechanism has been suggested for soluble plant hormone receptors (*26*, *27*). However, we emphasize that in the context of the full-length proteins, the transmembrane segments as well as the cytoplasmic kinase domains might play additional roles in receptor–co-receptor heteromerization and activation (*13*, *14*). Also, our experiments cannot address the oligomeric state of BRI1-SERK signaling complexes at the plasma membrane, but rather define a minimal signaling unit required for receptor activation.

The interaction surface with BRI1 occupies only ~10% of SERK1's total accessible surface area (blue in fig. S6). We used these sequence fingerprints to identify other putative BRI1 co-receptors (fig. S4). When mapping their overall sequence conservation to the molecular surface of SERK1 (orange in fig. S6), we found conserved surface patches that are much larger than required for the interaction with BRI1. SERK family co-receptors mediate the activation not only of BRI1 but of other plant receptor kinases that sense very different ligands (*28*–*30*). We hypothesize that SERKs harbor several distinct, partially overlapping, but conserved surface patches, which allow them to establish specific interactions with different receptor kinases and, potentially, their ligands. In line with this idea, the *$serk3_{elg}$* mutant acts as a gain-of-function allele in brassinosteroid signaling (*25*), whereas it behaves as a loss-of-function mutant in the FLAGELLIN-SENSING 2 pathway (*25*). Plant invertase/pectin methylesterase inhibitor proteins provide another example where distinct surface areas on a common structural scaffold allow for interaction with different protein targets (*31*). The widespread use of multifunctional SERKs in plant membrane signaling could enable signaling cross-talk directly at the level of ligand sensing at the cell surface and may orchestrate the plant's response to external stimuli (*15*).

References and Notes

1. J. Li, J. Chory, *Cell* **90**, 929–938 (1997).
2. M. Ogawa, H. Shinohara, Y. Sakagami, Y. Matsubayashi, *Science* **319**, 294 (2008).
3. L. Gómez-Gómez, T. Boller, *Mol. Cell* **5**, 1003–1011 (2000).
4. Z.-Y. Wang, M.-Y. Bai, E. Oh, J.-Y. Zhu, *Annu. Rev. Genet.* **46**, 701–724 (2012).
5. Z. He *et al.*, *Science* **288**, 2360–2363 (2000).
6. T. Kinoshita *et al.*, *Nature* **433**, 167–171 (2005).
7. J. She *et al.*, *Nature* **474**, 472–476 (2011).
8. M. Hothorn *et al.*, *Nature* **474**, 467–471 (2011).
9. J. Li *et al.*, *Cell* **110**, 213–222 (2002).
10. K. H. Nam, J. Li, *Cell* **110**, 203–212 (2002).
11. X. Gou *et al.*, *PLoS Genet.* **8**, e1002452 (2012).
12. R. Karlova *et al.*, *Plant Cell* **18**, 626–638 (2006).
13. X. Wang *et al.*, *Dev. Cell* **15**, 220–235 (2008).
14. Y. Jaillais *et al.*, *Genes Dev.* **25**, 232–237 (2011).
15. Y. Belkhadir *et al.*, *Proc. Natl. Acad. Sci. U.S.A.* **109**, 297–302 (2012).
16. T. Asami *et al.*, *Plant Physiol.* **123**, 93–100 (2000).
17. A. Di Matteo *et al.*, *Proc. Natl. Acad. Sci. U.S.A.* **100**, 10124–10128 (2003).
18. M. S. Jin *et al.*, *Cell* **130**, 1071–1082 (2007).
19. J. Y. Kang *et al.*, *Immunity* **31**, 873–884 (2009).
20. T. G. Back, R. P. Pharis, *J. Plant Growth Regul.* **22**, 350–361 (2003).
21. T. G. Back, L. Janzen, R. P. Pharis, Z. Yan, *Phytochemistry* **59**, 627–634 (2002).
22. T. Muto, Y. Todoroki, *Bioorg. Med. Chem.* **21**, 4413–4419 (2013).
23. D. M. Friedrichsen, C. A. Joazeiro, J. Li, T. Hunter, J. Chory, *Plant Physiol.* **123**, 1247–1256 (2000).
24. Z. Y. Wang, H. Seto, S. Fujioka, S. Yoshida, J. Chory, *Nature* **410**, 380–383 (2001).
25. Y. Jaillais, Y. Belkhadir, E. Balsemão-Pires, J. L. Dangl J. Chory, *Proc. Natl. Acad. Sci. U.S.A.* **108**, 8503–8507 (2011).
26. X. Tan *et al.*, *Nature* **446**, 640–645 (2007).
27. L. B. Sheard *et al.*, *Nature* **468**, 400–405 (2010).
28. D. Chinchilla *et al.*, *Nature* **448**, 497–500 (2007).
29. B. Schwessinger *et al.*, *PLoS Genet.* **7**, e1002046 (2011).
30. M. Roux *et al.*, *Plant Cell* **23**, 2440–2455 (2011).
31. M. Hothorn, W. Van den Ende, W. Lammens, V. Rybin, K. Scheffzek, *Proc. Natl. Acad. Sci. U.S.A.* **107**, 17427–17432 (2010).

Acknowledgments: We thank Y. Jaillais and M. Jinek for comments on the manuscript, J. Martinez for help with data collection, A. Pauluhn for providing beam time and staff members of beamline PXII (Swiss Light Source, Villigen, Switzerland), Y. Jaillais for *$bri1_{sud1}$* and GABI_13E10 transgenic lines, and M. Blazquez for *bes1-1D*. Atomic coordinates and structure factors have been deposited in the Protein Data Bank with accession codes 4LSA ($bri1_{sud1}$), 4LSC (SERK1), and 4LSX ($bri1_{sud1}$-BL-SERK1). Supported by the Max Planck Society, a Federation of European Biochemical Societies long-term fellowship (J.S.), and an International Human Frontier Science Program Organization Career Development Award (M.H.). M.H. and Joanne Chory (Salk Institute) are inventors on a patent application filed by the Salk Institute for Biological Studies entitled "Structure of the Brassinosteroid Receptor BRI1, and Modulation of BRI1 Signaling" (patent 20130007910).

Supplementary Materials

www.sciencemag.org/cgi/content/full/science.1242468/DC1
Materials and Methods
Figs. S1 to S6
Table S1
References (*32*–*45*)

26 June 2013; accepted 29 July 2013
Published online 8 August 2013;
10.1126/science.1242468

Titration of Four Replication Factors Is Essential for the *Xenopus laevis* Midblastula Transition

Clara Collart,[1,2] George E. Allen,[1] Charles R. Bradshaw,[1] James C. Smith,[2] Philip Zegerman[1,3]*

The rapid, reductive early divisions of many metazoan embryos are followed by the midblastula transition (MBT), during which the cell cycle elongates and zygotic transcription begins. It has been proposed that the increasing nuclear to cytoplasmic (N/C) ratio is critical for controlling the events of the MBT. We show that four DNA replication factors—Cut5, RecQ4, Treslin, and Drf1—are limiting for replication initiation at increasing N/C ratios in vitro and in vivo in *Xenopus laevis*. The levels of these factors regulate multiple events of the MBT, including the slowing of the cell cycle, the onset of zygotic transcription, and the developmental activation of the kinase Chk1. This work provides a mechanism for how the N/C ratio controls the MBT and shows that the regulation of replication initiation is fundamental for normal embryogenesis.

The early cell divisions in many metazoa are rapid and maintained by maternally supplied products. Bulk zygotic transcription begins at the midblastula transition (MBT), also referred to as the start of the maternal-zygotic transition (MZT) (*1*), and is accompanied by the onset of cell movement, the activation of cell cycle checkpoints, and the elongation and asynchrony of cell divisions (*2*–*6*). This elongation of the cell cycle is coincident with a reduction in the density and synchrony of DNA replication initiation events (*7*–*9*), leading to the possibility that replication factors themselves might be important regulators of cell cycle duration during development. To test this hypothesis, we measured the abundance of replication initiation factors in *Xenopus laevis* embryos. Components of the first step of replication initiation, a process called "licensing" or prereplicative complex (pre-RC) assembly, remained constant or increased in abundance during embryogenesis (Fig. 1A, Orc1 and Mcm2, 4, 5, and 7).

After pre-RC formation, two kinases are required to assemble active replisomes, cyclin-dependent kinase (CDK) and Dbf4-dependent kinase (DDK). The abundance of the noncatalytic subunit of DDK, which in *Xenopus* embryos is Drf1 (Dbf4-related factor 1), becomes greatly reduced by the time of gastrulation (*10*, *11*). Both the mRNA and protein levels of three other replication factors—*cut5*, *treslin*, and *recq4*—also decreased during embryogenesis (Fig. 1A and fig. S1). Treslin and RecQ4 are orthologs of Sld3 and Sld2, the CDK targets required for replication initiation in yeast, whereas Cut5 is the ortholog of their interaction partner Dpb11 (*12*–*14*). Reduction in the levels of these replication factors during early cell divisions suggested that their abundance might be a determinant of embryonic replication initiation rates. To investigate this, we added

[1]Wellcome Trust/Cancer Research UK Gurdon Institute, The Henry Wellcome Building of Cancer and Developmental Biology, University of Cambridge, Cambridge CB2 1QN, UK. [2]Medical Research Council, National Institute for Medical Research, The Ridgeway, Mill Hill, London NW7 1AA, UK. [3]Department of Zoology, The Henry Wellcome Building of Cancer and Developmental Biology, University of Cambridge, Cambridge CB2 1QN, UK.

*Corresponding author. E-mail: p.zegerman@gurdon.cam.ac.uk

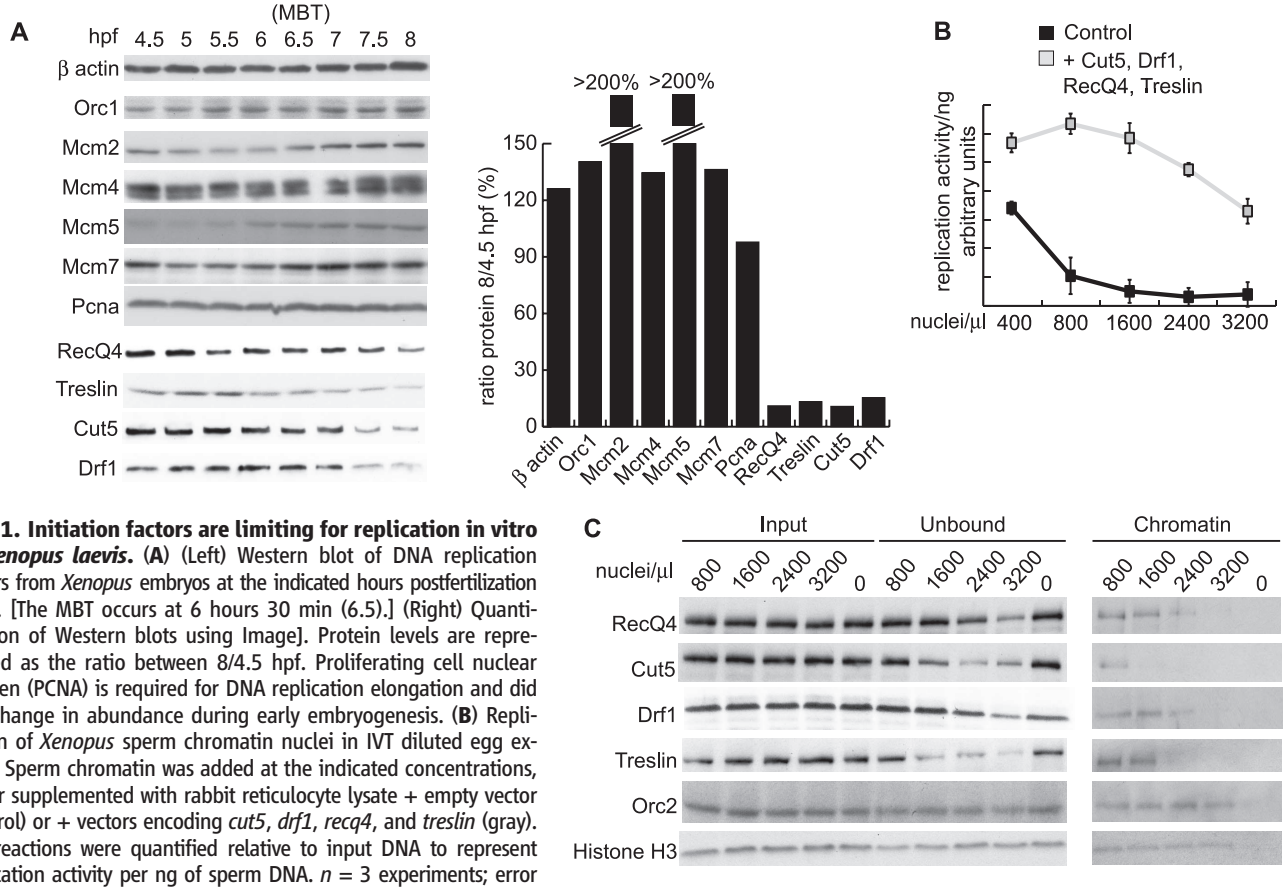


Fig. 1. Initiation factors are limiting for replication in vitro in *Xenopus laevis*. (**A**) (Left) Western blot of DNA replication factors from *Xenopus* embryos at the indicated hours postfertilization (hpf). [The MBT occurs at 6 hours 30 min (6.5).] (Right) Quantification of Western blots using Image]. Protein levels are represented as the ratio between 8/4.5 hpf. Proliferating cell nuclear antigen (PCNA) is required for DNA replication elongation and did not change in abundance during early embryogenesis. (**B**) Replication of *Xenopus* sperm chromatin nuclei in IVT diluted egg extract. Sperm chromatin was added at the indicated concentrations, either supplemented with rabbit reticulocyte lysate + empty vector (control) or + vectors encoding *cut5*, *drf1*, *recq4*, and *treslin* (gray). The reactions were quantified relative to input DNA to represent replication activity per ng of sperm DNA. $n = 3$ experiments; error bars show mean ± SD. (**C**) Western blot of chromatin binding of replication factors at increasing sperm nuclei to extract ratios. *Xenopus* sperm nuclei of the indicated ratios were replicated for 15 min in undiluted egg extract. Input and chromatin unbound fractions were equally loaded by volume, and the chromatin fractions were normalized to the same DNA concentration.

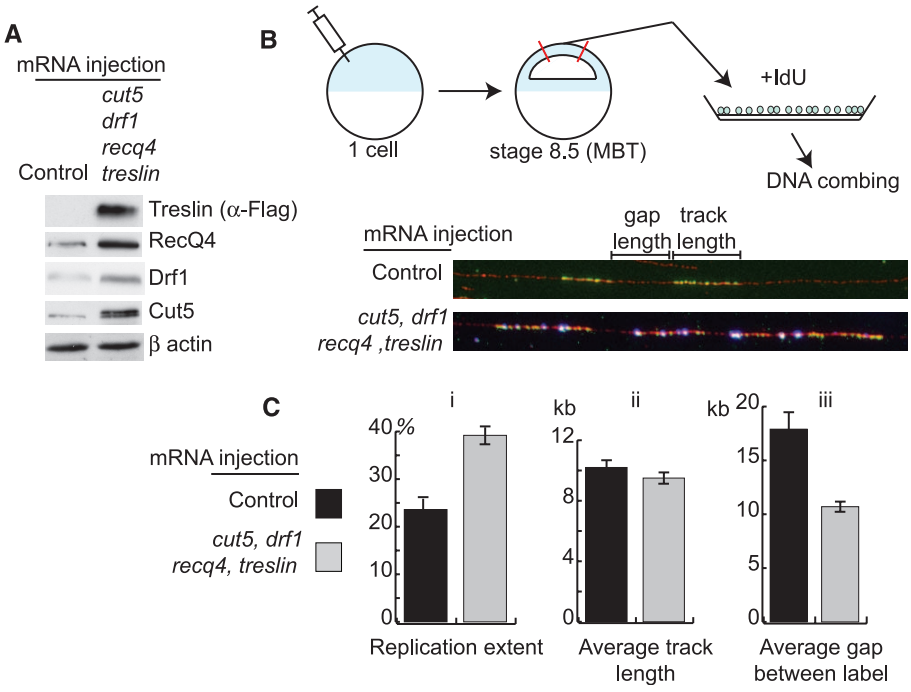


Fig. 2. Cut5, Drf1, RecQ4, and Treslin are limiting for replication in vivo in *Xenopus laevis*. (**A**) Western blot from stage 9 (post-MBT) embryos injected at the one-cell stage either with water (control) or with 300 pg mRNA each of *treslin*, *cut5*, *recq4*, and *drf1*. (**B**) (Top) Schematic representation of experimental design. *Xenopus* embryos were injected at the one-cell stage, as in (A) in the animal pole. At 6.5 hpf (stage 8.5), animal caps were cut and their cells were dissociated. The cells were given a pulse with IdU and incorporation was visualized by anti-IdU immunofluorescence after stretching DNA onto slides (bottom). DNA, red; IdU, green. (**C**) Analysis from (B) of (i) replication extent (%), (ii) average IdU track length (kb), and (iii) average gap between label (kb). $n = 96$ and 93 fibers for control and overexpressing embryos, respectively.

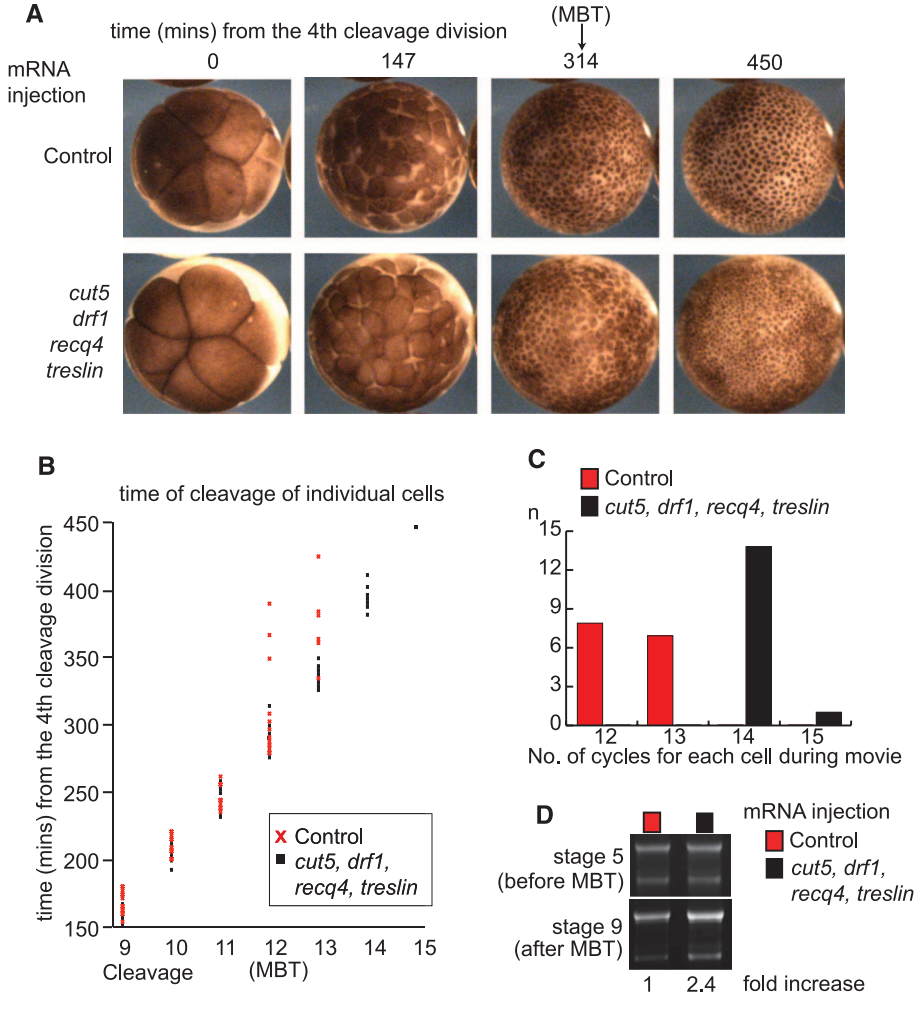


Fig. 3. Overexpression of Cut5, Drf1, RecQ4, and Treslin causes extra rapid cell divisions after the MBT. (**A**) Images taken from a time-lapse movie (movie S1) of embryos injected at the one-cell stage, as in Fig. 2A. Cleavage 4 at the 16-cell stage was set to time zero. (**B**) Fifteen individual cells from the embryos in movie S1 were followed through early divisions until 450 min after cleavage 4. Each time point corresponds to the cleavage of an individual cell. Cleavages 1 to 8 are excluded for simplicity. (**C**) Representation of the number of cell cycles each cell in (B) undergoes until 450 min after cleavage 4. (**D**) Embryos were injected as in (A), and half the DNA content of a single embryo at stages 5 and 9 was loaded onto an agarose gel and stained with ethidium bromide. This gel is representative of triplicate repeats. DNA amount at stage 9 was quantified using ImageJ and fold increase relative to control is represented.

in vitro–translated (IVT) RecQ4, Treslin, Cut5, and Drf1 to *Xenopus* egg extracts and analyzed the replication of sperm nuclei in vitro. Increased expression of these proteins in extracts resulted in a corresponding increase in DNA synthesis when these factors were overexpressed in combination (fig. S2, A to E). Furthermore, increasing the nuclei:extract ratio, to mimic the increasing N/C ratio of the early embryo, caused an exponential decline in DNA synthesis, which was suppressed by overexpression of RecQ4, Treslin, Cut5, and Drf1 (Fig. 1B and fig. S2C). In addition, whereas neither the pre-RC component Orc2 nor histone H3 were titrated out from extracts or on chromatin at increasing nuclei:extract ratios (Fig. 1C) (*15*), RecQ4, Cut5, Drf1, and Treslin were depleted from extracts (unbound) and less abundant on chromatin at nuclei:extract ratios that resulted in reduced replication activity (Fig. 1C and fig. S2F). We conclude that these four factors are limiting for DNA synthesis rates in *Xenopus* egg extracts in a N/C ratio–dependent manner.

To determine whether these factors are limiting for replication initiation in vivo, we increased the levels of all four factors in embryos by injection of mRNA into the fertilized egg (Fig. 2A). To analyze replication rates directly, we dissected the animal caps of embryos at stage 8.5 (MBT), dissociated the cells, and pulse-labeled replication forks with 5′-iododeoxyuridine (IdU) (Fig. 2B, top). Anti-IdU immunofluorescence of labeled DNA stretched onto slides (Fig. 2B, bottom) revealed that overexpression of RecQ4, Treslin, Drf1, and Cut5 resulted in an almost twofold increase in total replication (Fig. 2C, i). The length of the IdU incorporation tracks remained constant after overexpression of the four factors (Fig. 2C, ii), suggesting that replication elongation was not affected. By contrast, the gap between labels was reduced nearly twofold by overexpression of these factors (Fig. 2C, iii), which is indicative of an increase in origin firing. From this analysis, we conclude that RecQ4, Treslin, Drf1, and Cut5 are limiting for the frequency of initiation at the MBT in *Xenopus* embryos.

A major transition at the MBT is the lengthening of the cell cycle (*4*, *16*). To test the importance of these limiting replication factors for cell cycle control at the MBT, we analyzed time-lapse movies of injected *Xenopus laevis* embryos (movie S1). In control embryos, rapid synchronous divisions occurred until the MBT at cycle 12, after which cell divisions slowed and became asynchronous (Fig. 3, A to C, and fig. S3), as previously described (*17*). In embryos that overexpress RecQ4, Treslin, Drf1, and Cut5, the rapid, synchronous cell divisions continued beyond cycle 12 (Fig. 3, A to C, and fig. S3), and as a result these embryos had a considerably greater number of cells (Fig. 3A) and a higher DNA content after the MBT (Fig. 3D).

In accordance with a direct role for the N/C ratio in the titration of these factors in embryos, we observed a dose dependency between the levels of overexpression of these factors and the number of rapid cell cycles that were induced after the MBT (fig. S4). Furthermore, partial depletion of RecQ4, Treslin, Drf1, and Cut5 had the opposite effect as the overexpression and resulted in longer cell cycles at the MBT (fig. S5C). We conclude that the titration of at least four replication factors—RecQ4, Treslin, Drf1, and Cut5—controls cell cycle length at the MBT in *Xenopus laevis*.

Shortening of the cell cycle at the MBT by overexpression of these limiting factors is unlikely due to indirect effects on the cell-autonomous developmental clock (*18*, *19*) because the timing of Cyclin E degradation was unaffected in injected embryos (fig. S6A). We also investigated whether the limiting factors affected the checkpoint kinase Chk1, which becomes transiently activated at the time of the MBT (*2*, *3*, *6*). The combined overexpression of RecQ4, Treslin, Drf1, and Cut5 together caused much earlier activation of Chk1 in *Xenopus* embryos (fig. S6, B and E).

We have previously shown that increasing the rates of replication initiation in budding yeast leads to checkpoint activation by the transient depletion of nucleotides (*20*). Because it has been shown that deoxyribonucleotide levels are reduced at the onset of the MBT in *Xenopus laevis* (*21*), we wondered whether the early activation of Chk1 upon overexpression of RecQ4, Treslin, Drf1, and Cut5 is due to the premature depletion of nucleotides. To test this, we coinjected a fourfold excess (200 pmols) of deoxynucleotide triphosphates (dNTPs) into the fertilized egg (*22*). Whereas injection of dNTPs alone had no effect on the developmental activation of Chk1 (fig. S6C), coinjection of dNTPs together with overexpression of the four factors greatly reduced the activation of Chk1, particularly at the time of the MBT (fig. S6D). This suggests that the developmental activation of Chk1 is, at least in part, caused both by the depletion of initiation factors and by limiting dNTP levels at the MBT. Coinjection of dNTPs together with the four factors, although partially suppressing the developmental Chk1 activation, did not affect the continuation of rapid cell divisions in these embryos (fig. S7). This indicates that overexpression of RecQ4, Treslin, Drf1, and Cut5 sustains rapid cell divisions at the MBT independently of Chk1 activation levels.

Previous studies have suggested that elongation of the cell cycle is a requirement for the onset of zygotic transcription (*23*). To address directly the importance of coordinating replication with the onset of transcription, we analyzed the *Xenopus laevis* transcriptome by high-throughput sequencing of staged embryos. Overexpression of limiting replication factors delayed the expression of a large number of genes at the MBT (fig. S8). Therefore, the regulation of replication initiation densities and cell cycle length at the MBT is a primary event that controls the timely transcription of a subset of genes in *Xenopus* embryos. As is the case in flies (*24*), the dynamics of expression of

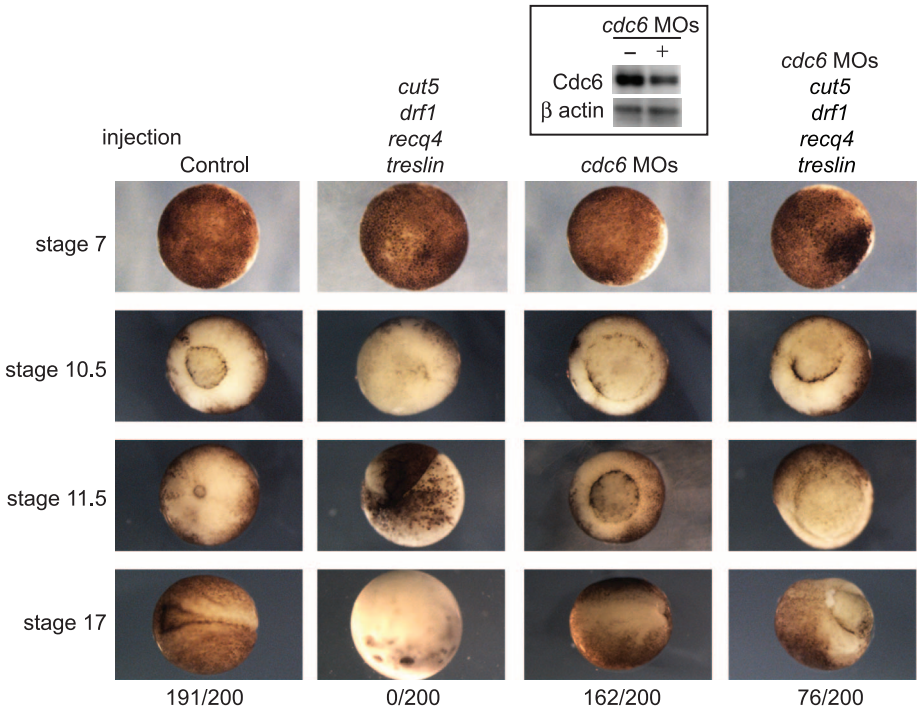


Fig. 4. Increasing interorigin distances at the MBT is critical for gastrulation and neurulation. Images of embryos injected with water (control, first column); *treslin*, *cut5*, *recq4*, and *drf1* mRNA (second column); *cdc6* morpholinos (MOs, third column); and embryos injected with a mixture of the *cdc6* morpholinos and mRNA for *treslin*, *cut5*, *recq4*, and *drf1* (fourth column). Stage 7, pre-MBT; 10.5, gastrulation; 11.5, midgastrulation; 17, neurula. The number of embryos out of 200 surviving at stage 17 is indicated at the bottom. (**Top**) Western blot of knockdown of Cdc6 after morpholino injection.

several genes remained unaffected by the extra rapid cell cycles (fig. S8A), underlining that several mechanisms regulate mRNA abundance at the MBT (*1*).

To understand the physiological importance of the regulation of DNA replication during development, we analyzed the phenotype of embryos overexpressing RecQ4, Treslin, Drf1, and Cut5. Embryos that overexpress these four factors failed to complete gastrulation and blastopore closure at stage 10.5 (Fig. 4) and underwent cell death by stage 17 (neurula), showing that titration of these factors is critical for embryogenesis.

If this developmental defect upon overexpression of RecQ4, Treslin, Drf1, and Cut5 is indeed due to increased rates of initiation, we hypothesized that a partial reduction in origin licensing might suppress this phenotype. Injection of embryos with morpholinos against the pre-RC component *cdc6* resulted in partial depletion of the Cdc6 protein (Fig. 4, top), and although this caused a slight delay in blastopore closure, 81% of these morpholino-injected embryos reached the neurula stage (Fig. 4). However, coinjection of these *cdc6* morpholinos together with overexpression of RecQ4, Treslin, Drf1, and Cut5 partially rescued the ability of these embryos to undergo gastrulation, and 38% of embryos survived until stage 17. This indicates that the developmental deficiency caused by overexpression of RecQ4, Treslin, Drf1, and Cut5 is at least in part due to the resulting increase in replication initiation. The *cdc6* morpholinos in combination with the overexpression of limiting initiation factors not only partially rescued the embryonic defect but also restored normal cell cycle elongation and Chk1 activation at the MBT (fig. S9). Together, these experiments demonstrate that the regulation of replication initiation rates is necessary for several of the critical events of the MBT and for normal development in *Xenopus laevis*.

This study provides a mechanistic basis for the hypothesis put forward 30 years ago that passive depletion of limiting factors by the N/C ratio is the primary mechanism controlling events at the MBT (*4*). We speculate that the interplay between the limiting replication factors RecQ4, Treslin, Drf1, and Cut5, together with Chk1 activation and CDK inactivation, forms a feedback loop (fig. S10), which in accordance with work in flies (*3*, *6*, *25*, *26*) underlies how *S*-phase length is regulated during development across eukaryotes.

References and Notes

1. W. Tadros, H. D. Lipshitz, *Development* **136**, 3033–3042 (2009).
2. K. Shimuta *et al*., *EMBO J.* **21**, 3694–3703 (2002).
3. O. C. Sibon, V. A. Stevenson, W. E. Theurkauf, *Nature* **388**, 93–97 (1997).
4. J. Newport, M. Kirschner, *Cell* **30**, 675–686 (1982).
5. J. Newport, M. Kirschner, *Cell* **30**, 687–696 (1982).
6. P. Fogarty *et al*., *Curr. Biol.* **7**, 418–426 (1997).
7. O. Hyrien, C. Maric, M. Méchali, *Science* **270**, 994–997 (1995).
8. S. L. McKnight, O. L. Miller Jr., *Cell* **12**, 795–804 (1977).
9. A. B. Blumenthal, H. J. Kriegstein, D. S. Hogness, *Cold Spring Harb. Symp. Quant. Biol.* **38**, 205–223 (1974).
10. T. S. Takahashi, J. C. Walter, *Genes Dev.* **19**, 2295–2300 (2005).
11. T. Silva, R. H. Bradley, Y. Gao, M. Coue, *J. Biol. Chem.* **281**, 11569–11576 (2006).
12. A. Kumagai, A. Shevchenko, A. Shevchenko, W. G. Dunphy, *J. Cell Biol.* **193**, 995–1007 (2011).
13. K. Matsuno, M. Kumano, Y. Kubota, Y. Hashimoto, H. Takisawa, *Mol. Cell. Biol.* **26**, 4843–4852 (2006).
14. M. N. Sangrithi *et al*., *Cell* **121**, 887–898 (2005).
15. J. Walter, J. W. Newport, *Science* **275**, 993–995 (1997).
16. B. A. Edgar, C. P. Kiehle, G. Schubiger, *Cell* **44**, 365–372 (1986).
17. J. Newport, M. Dasso, *J. Cell Sci. Suppl.* **1989** (suppl. 12), 149–160 (1989).
18. J. A. Howe, J. W. Newport, *Proc. Natl. Acad. Sci. U.S.A.* **93**, 2060–2064 (1996).
19. R. S. Hartley, J. C. Sible, A. L. Lewellyn, J. L. Maller, *Dev. Biol.* **188**, 312–321 (1997).
20. D. Mantiero, A. Mackenzie, A. Donaldson, P. Zegerman, *EMBO J.* **30**, 4805–4814 (2011).
21. L. Vastag *et al*., *PLoS ONE* **6**, e16881 (2011).
22. H. R. Woodland, R. Q. Pestell, *Biochem. J.* **127**, 597–605 (1972).
23. D. Kimelman, M. Kirschner, T. Scherson, *Cell* **48**, 399–407 (1987).
24. X. Lu, J. M. Li, O. Elemento, S. Tavazoie, E. F. Wieschaus, *Development* **136**, 2101–2110 (2009).
25. A. W. Shermoen, M. L. McCleland, P. H. O'Farrell, *Curr. Biol.* **20**, 2067–2077 (2010).
26. M. L. McCleland, A. W. Shermoen, P. H. O'Farrell, *J. Cell Biol.* **187**, 7–14 (2009).

Acknowledgments: We are grateful to T. Takahashi, J. Walter, V. Costanzo, J. Diffley, H. Takisawa, and R. Laskey for reagents. DNA combing analysis was performed with assistance from V. Gaggioli. We are grateful to J. Pines, R. Laskey, and members of the Zegerman group for critical reading of this manuscript and S. Di Talia for discussions. P.Z. is funded by AICR 10-0908. J.C.S. and C.C. were supported by the Wellcome Trust and by the UK Medical Research Council (programme no. U117597140). All authors acknowledge the core support provided by CRUK C6946/A14492 and the Wellcome Trust 092096.

Supplementary Materials

www.sciencemag.org/cgi/content/full/science.1241530/DC1
Materials and Methods
Figs. S1 to S10
Movie S1
Reference (*27*)

5 June 2013; accepted 23 July 2013
Published online 1 August 2013;
10.1126/science.1241530

SGK196 Is a Glycosylation-Specific *O*-Mannose Kinase Required for Dystroglycan Function

Takako Yoshida-Moriguchi,[1] Tobias Willer,[1] Mary E. Anderson,[1] David Venzke,[1] Tamieka Whyte,[2] Francesco Muntoni,[2] Hane Lee,[3] Stanley F. Nelson,[3] Liping Yu,[4] Kevin P. Campbell[1]*

Phosphorylated *O*-mannosyl trisaccharide [*N*-acetylgalactosamine–β3-*N*-acetylglucosamine–β4-(phosphate-6-)mannose] is required for dystroglycan to bind laminin-G domain–containing extracellular proteins with high affinity in muscle and brain. However, the enzymes that produce this structure have not been fully elucidated. We found that glycosyltransferase-like domain–containing 2 (GTDC2) is a protein O-linked mannose β 1,4-*N*-acetylglucosaminyltransferase whose product could be extended by β 1,3-*N*-acetylgalactosaminyltransferase2 (B3GALNT2) to form the *O*-mannosyl trisaccharide. Furthermore, we identified SGK196 as an atypical kinase that phosphorylated the 6-position of *O*-mannose, specifically after the mannose had been modified by both GTDC2 and B3GALNT2. These findings suggest how mutations in GTDC2, B3GALNT2, and SGK196 disrupt dystroglycan receptor function and lead to congenital muscular dystrophy.

Posttranslational modification of proteins via stringently regulated biosynthetic pathways extends their range of function. Defects in the posttranslational modification of the dystroglycan (DG) protein are common to a variety of congenital muscular dystrophies (CMDs)—including Walker-Warburg syndrome (WWS), Fukuyama CMD, muscle-eye-brain disease, and certain types of limb-girdle muscular dystrophy—and result in the malfunction of DG as an extracellular matrix (ECM) receptor (*1*). DG is composed of a transmembrane β subunit and a cell-surface α subunit (*2*). α-DG serves as a receptor for laminin-G domain–containing ECM ligands, including laminin, perlecan, agrin, and neurexin (*2*), which involves various types of glycosylation of its mucin domain. In particular, phosphorylation at the 6-position of an *O*-mannose of the trisaccharide [*N*-acetylgalactosamine (GalNAc)–β3-*N*-acetylglucosamine (GlcNAc)–β4-mannose]

[1]Howard Hughes Medical Institute, Department of Molecular Physiology and Biophysics, Department of Neurology, Department of Internal Medicine, University of Iowa Roy J. and Lucille A. Carver College of Medicine, 4283 Carver Biomedical Research Building, 285 Newton Road, Iowa City, IA 52242–1101, USA. [2]Dubowitz Neuromuscular Centre, Division of Neuroscience, Institute of Child Health and Great Ormond Street Hospital for Children, London, UK. [3]Department of Human Genetics, David Geffen School of Medicine, University of California, Los Angeles, CA 90095, USA. [4]Medical Nuclear Magnetic Resonance Facility, University of Iowa Roy J. and Lucille A. Carver College of Medicine, B291 Carver Biomedical Research Building, 285 Newton Road, Iowa City, IA 52242–1101, USA.

*Corresponding author. E-mail: kevin-campbell@uiowa.edu

produces a branch chain that is ultimately extended with repeating disaccharides [–α3-glucuronic acid (GlcA)–β3-xylose (Xyl)–] synthesized by like-acetylglucosaminyltransferase (LARGE), enabling α-DG to bind ECM ligands (*3*, *4*). Mutations in several known and putative glycosyltransferases cause DG-related disorders. Recently, genetic studies of the DG-related diseases CMD and cobblestone lissencephaly identified several new causative genes, including *isoprenoid synthase domain containing* (*ISPD*) (*5*), *transmembrane protein 5* (*TMEM5*) (*6*), β*1,3-N-acetylglucosaminyltransferase* (*B3GNT1*) (*7*), *glycosyltransferase-like domain containing 2* (*GTDC2*) (*8*), β*3-N-acetylgalactosaminyltransferase2* (*B3GALNT2*) (*9*), and *SGK196* (*10*). However, the functions of the genes' products remain largely unknown.

O-Mannosyl glycosylation of α-DG is initiated by the endoplasmic reticulum (ER)–resident protein *O*-mannosyl transferase 1/2 complex (POMT1/2), which adds mannose to Ser/Thr residues (*11*). To help to clarify the functions of the recently identified causative proteins, we examined their subcellular localization. GTDC2 was present in the ER (Fig. 1A), suggesting that it might modify the above-described *O*-mannose. Thus, we synthesized a peptide corresponding to the mucinlike domain of human α-DG (residues 316 to 329), in which Thr^{317} was modified by *O*-mannose but the remaining Thr/Ser residues were replaced with Ala. The glycopeptide was incubated with c-Myc–tagged GTDC2 (GTDC2-Myc) purified from human embryonic kidney (HEK) 293 cell lysates, as well as various nucleotide sugars. Matrix-assisted laser desorption-ionization time-of-flight mass spectrometry (MALDI-TOF/MS) analysis suggested that GTDC2-Myc transferred *N*-acetylhexosamine to the glycopeptide (fig. S1). Repetition of this assay using uridine 5′-diphosphate (UDP)–GlcNAc

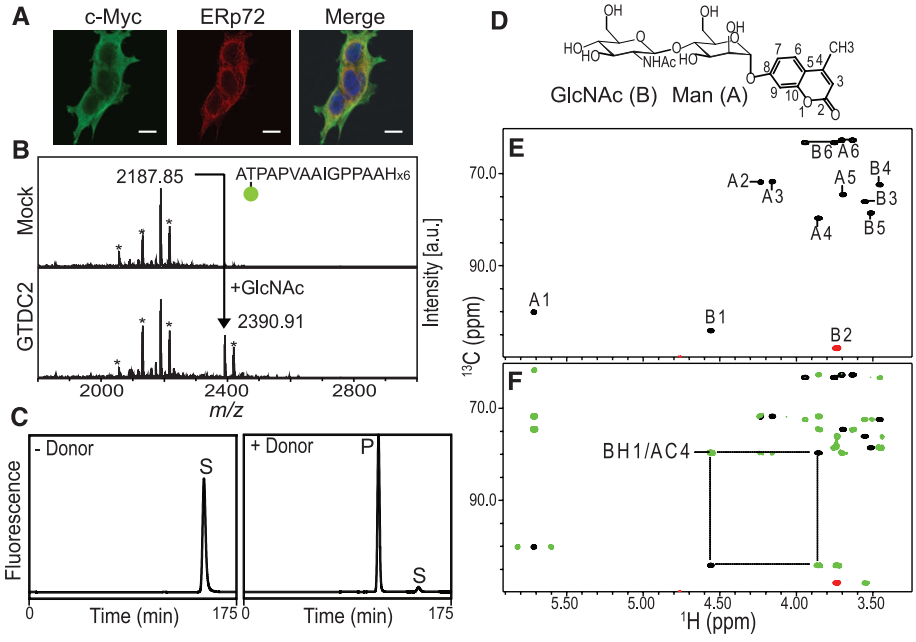


Fig. 1. GTDC2 has a protein *O*-linked mannose β1,4-*N*-acetylglucosaminyltransferase activity. (**A**) HEK293 cells expressing c-Myc–tagged GTDC2 were stained with anti-Myc (green), ERp72 (ER marker, red), and 4′,6-diamidino-2-phenylindole (DAPI, nuclei, blue). Scale bars indicate 10 μm. (**B**) The product of the GTDC2 in vitro assay when a DG-derived peptide modified with *O*-linked mannose and UDP-GlcNAc were used as substrates was analyzed by MALDI-TOF/MS. A, Ala; G, Gly; H, His; I, Ile; P, Pro; T, Thr; V, Val. a.u., arbitrary units; *m/z*, mass to charge ratio. (**C**) Reactant of the GTDC2dTM assay using Man–α-MU and UDP-GlcNAc was separated on Superdex Peptide 10/300 (GE Healthcare) columns. S, unreacted acceptor substrate. P, enzymatic product. (**D**) Structure of the product in (C), with the sugar subunits labeled A and B. HMQC (**E**) and overlay (**F**) of the HMQC (black and red) and HMBC (green) spectra of the product. Assigned cross-peaks are labeled with a first letter representing the subunit [as designated in (D)], and the rest of the label represents the position on that subunit. The red peak in (E) is the folded peak. ppm, parts per million.

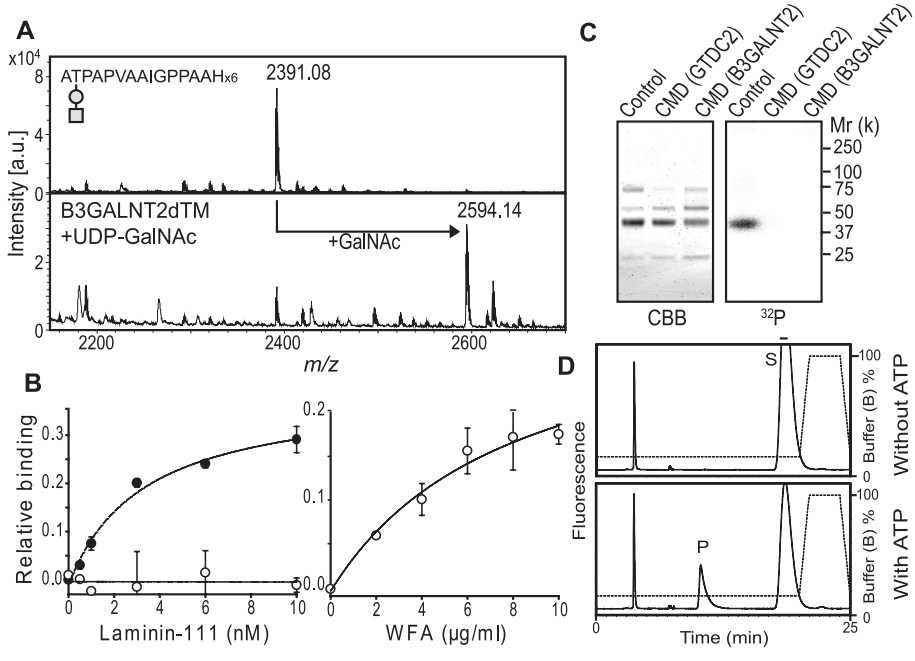


Fig. 2. Mutations in GTDC2 and B3GALNT2 cause defects in the synthesis of phosphorylated α-DG. (**A**) The product of the B3GALNT2dTM in vitro assay using the product depicted in Fig. 1B and UDP-GalNAc as substrates was analyzed by MALDI-TOF/MS. (**B**) Laminin (open circles, left) and WFA (open circles, right) binding to DG-derived peptide modified with the GalNAc–β3-GlcNAc–β4-mannose was measured by solid-phase assay (n = 3). The trisaccharide-modified peptide produced by the GTDC2dTM and B3GALNT2dTM reactions was conjugated to maleimide-activated plates. The peptide modified with mannose was used for background subtraction. Wild-type muscle glycoproteins (solid circles) served as positive control in the laminin-binding assay. Error bars indicate SD. (**C**) Fc-tagged DGFc340 was produced in [^{32}P]-orthophosphate–labeled fibroblasts derived from a control individual and GTDC2- or B3GALNT2-mutated patients. DGFc340 was isolated from the culture medium by using protein-A agarose, separated by SDS–polyacrylamide gel electrophoresis, stained with Coomassie brilliant blue (CBB), and analyzed by phosphorimaging ([^{32}P]). Mr, relative molecular mass. (**D**) Reactants of rabbit brain total membrane fraction incubated with ATP and GalNAc–β3-GlcNAc–β4-Man–α-MU at 37°C for 6 hours were separated on a C18 reverse-phase column. S, unreacted acceptor substrate. P, enzymatic product.

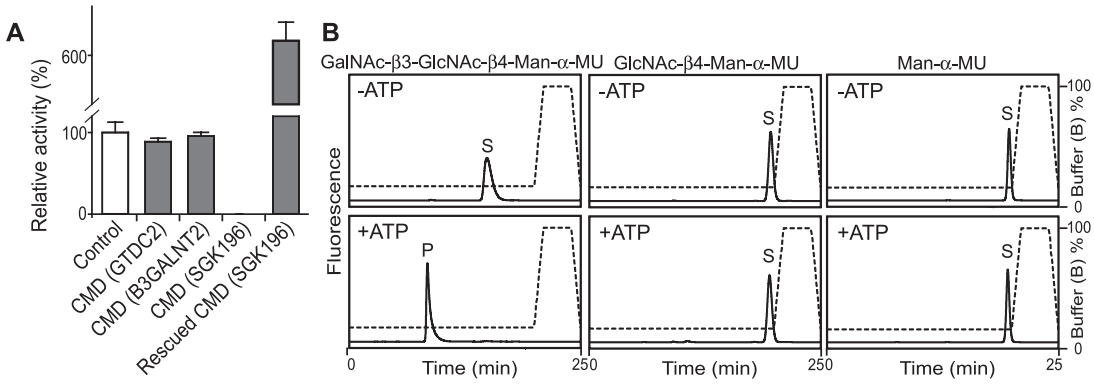


Fig. 3. SGK196 phosphorylates GalNAc–β3-GlcNAc–β4-Man. (**A**) Cell lysates from control fibroblasts and fibroblasts derived from patients with a mutation in SGK196, GTDC2, or B3GALNT2, as well as SGK196 patient–derived fibroblasts ectopically expressing SGK196-Myc-DDK, were subjected to a kinase assay using GalNAc–β3-GlcNAc–β4-Man–α-MU. Data obtained from three individual experiments are shown, with error bars indicating SD. (**B**) Reactants from a phosphorylation assay in which SGK196-Myc-DDK was used were separated on a C18 reverse-phase column. GalNAc–β3-GlcNAc–β4-Man–α-MU (left), GlcNAc–β4-Man–α-MU (middle), or Man–α-MU (right) was used as acceptor in the absence (top) or presence (bottom) of ATP.

(Fig. 1B) or UDP-GalNAc (fig. S2) as the donor confirmed that the transfer was specific to GlcNAc and that it did not occur when GTDC2-Myc carrying a mutation found in a CMD patient was used (fig. S2). Next, we prepared a secreted form of GTDC2 (lacking the transmembrane domain; GTDC2dTM) in HEK293 cells (fig. S3) and conducted the transfer assay by using fluorescently labeled mannoside (4-methylumbelliferyl–α-D-mannoside; Man–α-MU) as the acceptor. The product was purified by gel filtration (Fig. 1C) and then analyzed by nuclear magnetic resonance (NMR). The ^{1}H and ^{13}C resonances of the product were assigned by using heteronuclear multiple quantum coherence (HMQC) and heteronuclear 2-bond correlation (H2BC) spectra (fig. S4; Fig. 1, D and E; table S1). Rotating-frame Overhauser enhancement (ROE) data (fig. S5) confirmed that GlcNAc has a beta configuration. A BH1/AC4 cross-peak detected by the heteronuclear multiple bond correlation (HMBC) spectrum (Fig. 1F) indicated that the GlcNAc was linked to the 4-position of the mannose. Thus, GTDC2 possesses a protein *O*-mannose β1,4-*N*-acetylglucosaminyltransferase activity.

Human *B3GALNT2*, mutations in which cause WWS (*9*), has been cloned on the basis of its β3-glycosyltransferase motifs. This enzyme is thought to act as a β1,3-*N*-acetylgalactosaminyltransferase that uses β-linked GlcNAc as its acceptor in vitro (*12*). However, the GalNAc–β3-GlcNAc–β sequence had not been found in mammals when the gene was cloned, leaving the biological importance of this enzyme unclear. α-DG contains an *O*-mannosyl glycan (GalNAc–β3-GlcNAc–β4-Man), with the mannose phosphorylated at the 6-position (*3*). The ECM-ligand–binding moiety of α-DG extends from this phosphate residue (*3*). To test whether B3GALNT2 and GTDC2 act coordinately on *O*-mannose to synthesize this trisaccharide, we prepared a secreted form of B3GALNT2 (B3GALNT2dTM) (fig. S6) and incubated this protein with UDP-GalNAc and the GlcNAc–β4-Man-*O*-peptide produced by the GTDC2dTM reaction. MALDI-TOF/MS analysis confirmed that B3GALNT2 could transfer a GalNAc residue to the acceptor (Fig. 2A), suggesting that

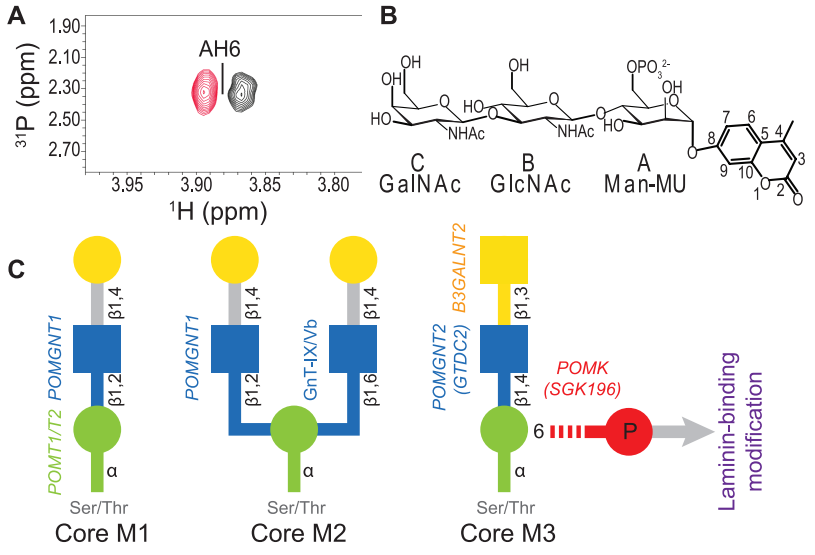


Fig. 4. SGK196 phosphorylates the 6-position of *O*-mannose. (**A**) The ^{31}P/^{1}H correlation spectroscopy spectrum of the product depicted in Fig. 3B when GalNAc–β3-GlcNAc–β4-Man–α-MU was used as the acceptor. Assigned cross-peaks were labeled as described in Fig. 1 by using the subunit designation indicated in (B). (**B**) Structure of the phosphorylated product, with sugar subunits labeled A to C. (**C**) Model of α-DG glycan structures. Proposed classification of each *O*-mannosyl core structure is indicated at bottom. Enzymes responsible for forming the respective linkages are indicated at left; those identified as causing (POMT1/2, POMGNT1 and 2, B3GALNT2, and POMK) DG-related disorders are indicated in italics. Green circle, Man; blue square, GlcNAc; yellow circle, Gal; yellow square, GalNAc; red circle, phosphate.

B3GALNT2 and GTDC2 can synthesize GalNAc–β3-GlcNAc–β4-Man. CMD patients who have mutations in these genes produce α-DG with pathological defects in ECM binding (*8*, *9*). We next used a solid-phase laminin-binding assay to test whether the GalNAc–β3-GlcNAc–β-terminus contributes directly to the binding of α-DG to ECM ligands. Whereas the GalNAc–β3-GlcNAc–β4-Man–modified peptide exhibited significant affinity for *Wisteria floribunda* lectin (WFA, which recognizes terminal GalNAc residues), this was not the case for laminin-111 (Fig. 2B). Next we asked whether a defect in synthesis of the GalNAc–β3-GlcNAc–β-terminus prevented *O*-mannose from being further modified by phosphorylation. We expressed Fc-tagged recombinant DG (DGFc340), which contains the region in which the functional modification occurs (*13*), in [^{32}P]-orthophosphate–labeled control fibroblasts and CMD patient fibroblasts with mutations in GTDC2 or B3GALNT2 (Fig. 2C). Indeed, the cells from the CMD patients did not produce [^{32}P]-phosphorylated DGFc340, indicating that phosphorylation of the α-DG *O*-mannose is inhibited by lack of the GalNAc–β3-GlcNAc–β-terminus from the mannose.

To understand how the *O*-glycan on α-DG is phosphorylated, we synthesized fluorescently labeled GalNAc–β3-GlcNAc–β4-Man by using GTDC2dTM, B3GALNT2dTM, and the acceptor Man-α-MU. We first tested adenosine triphosphate (ATP) as a phosphate donor, by performing the assay on total membrane fractions obtained from rabbit brain with GalNAc–β3-GlcNAc–β4-Man–α-MU

as the acceptor. Separation of the reactant on a C18 column revealed that GalNAc–β3-GlcNAc–β4-Man–α-MU (Fig. 2D) was phosphorylated in the presence of ATP. We further separated the ER and Golgi complex in mouse liver membrane fractions and found that the phophorylation activity resided in the ER fractions (fig. S7). Causative proteins of DG-related disorders whose functions remain unknown include fukutin (FKTN), fukutin-related protein (FKRP), TMEM5, ISPD, and SGK196. Among these, only SGK196 shares homology with known protein kinases, although it is believed to be inactive because of the high divergence of its putative kinase domains from the consensus sequence (*14*). We tested its phosphorylation activity in lysates from control fibroblasts and CMD patient fibroblasts with mutations in SGK196, GTDC2, or B3GALNT2. The activity toward GalNAc–β3-GlcNAc–β4-Man–α-MU was lacking only in the SGK196-mutated cells, and this loss was rescued by ectopic expression of c-Myc-DDK (FLAG)–tagged SGK196 (SGK196-Myc-DDK) (Fig. 3A). When SGK196-Myc-DDK produced in HEK293 cells was incubated with ATP and/or Man–α-MU derivatives, SGK196 exhibited significant phosphorylation activity toward GalNAc–β3-GlcNAc–β4-Man–α-MU. Moreover, this activity was not observed when GlcNAc–β4-Man–α-MU or Man–α-MU was used as the acceptor (Fig. 3B). Phosphorylated GalNAc–β3-GlcNAc–β4-Man–α-MU was not detected when SGK196-Myc-DDK carrying a mutation (Leu^{137}→Arg^{137}) found in a CMD patient (*10*) was used in the assay (fig. S8). To elucidate the enzymatic properties of SGK196, we produced a soluble form of SGK196 (SGK196dTM, fig. S9). Its phosphorylation activity depended on divalent ions with an apparent Michaelis constant for ATP of 4.1 ± 1.4 μM (fig. S10). To pinpoint which hydroxyl group of the trisaccharide is phosphorylated by SGK196, we isolated the product obtained in the experiment depicted in Fig. 3B and analyzed its structure by NMR. The ^{1}H and ^{13}C resonances of the product were assigned on the basis of HMQC, HMBC, and H2BC spectra (fig. S11 and table S2), and the anomeric configurations were determined by ROE (fig. S12). The BH1/AC4 and CH1/BC3 cross-peaks detected in the HMBC spectrum confirmed that the GalNAc and GlcNAc residues were attached to GlcNAc and Man via β1-3 and β1-4 linkages, respectively (fig. S11). The phosphate group added by SGK196 was attached to the 6-position of the mannose residue (Fig. 4, A and B).

We have shown that GTDC2 has a protein *O*-mannose β1,4-*N*-acetylglucosaminyltransferase activity, which leads us to designate it as POMGNT2, and that GTDC2 and B3GALNT2 can synthesize a GalNAc–β3-GlcNAc–β-terminus at the 4-position of protein *O*-mannose. SGK196 phosphorylated the 6-position of *O*-mannose by using ATP, and on this basis we propose to designate it as a protein *O*-mannose kinase (POMK). Because SGK196 lacks certain residues required for catalysis by kinases (*14*), the mechanism used to catalyze the phosphotransfer reaction is unclear. SGK196 exhibited the phosphorylation activity only when the GalNAc–β3-GlcNAc–β-terminus was linked to the 4-position of *O*-mannose, indicating that this disaccharide serves as the substrate recognition motif of SGK196. This strict specificity of SGK196 may explain why mutations in GTDC2 and B3GALNT2 cause DG-related disorders although their product does not directly recognize the ECM ligand. Because multiple types of *O*-mannosyl glycans exist, we propose to designate the *O*-mannosyl glycan structures as cores M1 to M3 (Fig. 4C). Although the sialylated core M1 of DG was originally proposed to be responsible for binding to ligands in the ECM (*15*), recent glycomics analysis suggests that proteins besides DG are subject to modification of sialylated cores M1 and M2 (*16*). The fact that LARGE alone could not modify phosphorylated GalNAc–β3-GlcNAc–β4-Man–α-MU by using UDP-Xyl and UDP-GlcA as substrate (fig. S13) suggests that CMD causative proteins (FKRP, FKTN, TMEM5, and B3GNT1) besides LARGE are likely to contribute to maturation of the ECM-binding moiety on the phosphorylated core M3 glycan.

References and Notes

1. D. E. Michele *et al.*, *Nature* **418**, 417–421 (2002).
2. R. Barresi, K. P. Campbell, *J. Cell Sci.* **119**, 199–207 (2006).
3. T. Yoshida-Moriguchi *et al.*, *Science* **327**, 88–92 (2010).
4. K. Inamori *et al.*, *Science* **335**, 93–96 (2012).
5. T. Willer *et al.*, *Nat. Genet.* **44**, 575–580 (2012).
6. S. Vuillaumier-Barrot *et al.*, *Am. J. Hum. Genet.* **91**, 1135–1143 (2012).
7. K. Buysse *et al.*, *Hum. Mol. Genet.* **22**, 1746–1754 (2013).
8. M. C. Manzini *et al.*, *Am. J. Hum. Genet.* **91**, 541–547 (2012).
9. E. Stevens *et al.* UK10K Consortium, *Am. J. Hum. Genet.* **92**, 354–365 (2013).
10. L. T. Jae *et al.*, *Science* **340**, 479–483 (2013); 10.1126/science.1233675.
11. H. Manya *et al.*, *Proc. Natl. Acad. Sci. U.S.A.* **101**, 500–505 (2004).
12. T. Hiruma *et al.*, *J. Biol. Chem.* **279**, 14087–14095 (2004).
13. Y. Hara *et al.*, *Proc. Natl. Acad. Sci. U.S.A.* **108**, 17426–17431 (2011).
14. G. Manning, D. B. Whyte, R. Martinez, T. Hunter S. Sudarsanam, *Science* **298**, 1912–1934 (2002).
15. A. Chiba *et al.*, *J. Biol. Chem.* **272**, 2156–2162 (1997).
16. S. H. Stalnaker *et al.*, *J. Biol. Chem.* **286**, 21180–21190 (2011).

Acknowledgments: We thank all members of the Campbell laboratory, C. M. Brenner, and C. M. Blaumueller for fruitful discussions; Y. Hara for making an adenovirus vector; H. van Bokhoven for providing patient cells; J. R. Levy for helping imaging studies; H. Nguyen for graphical arts; and the University of Iowa Proteomics Facility and Gene Transfer Vector Core for their services. This work was supported in part by a Paul D. Wellstone Muscular Dystrophy Cooperative Research Center grant (1U54NS053672, K.P.C.), the Muscular Dystrophy Campaign, and the Great Ormond Street Hospital Children Charity (F.M.). K.P.C. is an Investigator of the Howard Hughes Medical Institute. The data are included in the paper and the supplementary materials.

Supplementary Materials

www.sciencemag.org/cgi/content/full/science.1239951/DC1
Materials and Methods
Figs. S1 to S13
Tables S1 and S2
References (*17*–*23*)

2 May 2013; accepted 25 July 2013
Published online 8 August 2013;
10.1126/science.1239951

Conformational Motions Regulate Phosphoryl Transfer in Related Protein Tyrosine Phosphatases

Sean K. Whittier,[1] Alvan C. Hengge,[2] J. Patrick Loria[1,3]*

Many studies have implicated a role for conformational motions during the catalytic cycle, acting to optimize the binding pocket or facilitate product release, but a more intimate role in the chemical reaction has not been described. We address this by monitoring active-site loop motion in two protein tyrosine phosphatases (PTPs) using nuclear magnetic resonance spectroscopy. The PTPs, YopH and PTP1B, have very different catalytic rates; however, we find in both that the active-site loop closes to its catalytically competent position at rates that mirror the phosphotyrosine cleavage kinetics. This loop contains the catalytic acid, suggesting that loop closure occurs concomitantly with the protonation of the leaving group tyrosine and explains the different kinetics of two otherwise chemically and mechanistically indistinguishable enzymes.

Molecular motions are crucial for the optimal functioning of enzymes. There has been much debate regarding what role motions play in the enzymatic conversion of substrates to products (*1*, *2*), and recent studies, primarily solution nuclear magnetic resonance (NMR) relaxation experiments, have shown that enzyme motions are critical for optimizing the active site (*3*–*6*), enabling effective substrate or cofactor binding (*7*), and facilitating product dissociation (*8*). These motions often require collective movement of many amino acids over substantial molecular distances (*9*) and are

[1]Department of Molecular Biophysics and Biochemistry, Yale University, 260 Whitney Avenue, New Haven, CT 06520, USA. [2]Department of Chemistry and Biochemistry, Utah State University, 0300 Old Main Hill, Logan, UT 84322, USA. [3]Department of Chemistry, Yale University, 225 Prospect Street, New Haven, CT 06520, USA.

*Corresponding author. E-mail: patrick.loria@yale.edu

indispensible for chemistry. Furthermore, motions appear to have been evolutionarily optimized to accommodate the extreme environments in which enzymes must function (*10*). Often, motions are rate-limiting to enzyme turnover; however, this is mainly via product release, whereas the chemical steps are usually much faster (*11*). As a result, the direct participation of molecular motions in the chemical steps of an enzyme reaction, with few exceptions (*12*, *13*), remains largely untested experimentally.

We addressed this question through a comparison of active-site loop motions in two structurally similar protein tyrosine phosphatases (PTPs) (Fig. 1A and fig. S1A): YopH, a virulence factor from *Yersinia* (*14*), and PTP1B, a human phosphatase that is involved in regulating insulin, leptin, and epidermal growth factor (EGF) signaling (*15*). These enzymes catalyze the cleavage of the tyrosine phosphate monoester (pY) of their protein substrates followed by hydrolysis of the phosphoenzyme intermediate. YopH and PTP1B contain 10-residue WPD (*16*) active-site loops and conserved, eight-residue P-loops. The P-loops bind the phosphate moiety of the substrate and contain the catalytic nucleophiles C403 in YopH and C215 in PTP1B (Fig. 1, C and D). The WPD loop contains an aspartic acid D356 (D181 in PTP1B) that serves as the general acid to protonate the leaving group, such that Tyr leaves as the alcohol rather than the alkoxide (Fig. 1, B to D). The P-loop does not undergo a substantial conformational change during catalysis. However, motions of about 10 Å differentiate the open (apo) and the catalytically competent closed WPD loop (Fig. 1B). The closed WPD loop positions the general acid near the oxygen of the leaving group of the substrate. YopH and PTP1B reactions occur in two steps (Fig. 1D). First, after substrate binds, the WPD loop closes and catalyzes the cleavage ($k_{cleavage}$, where k is the rate constant) of the phosphotyrosine moiety, generating a phosphoenzyme intermediate and a tyrosine peptide. Subsequently, the phosphoenzyme intermediate is hydrolyzed ($k_{hydrolysis}$), regenerating active enzyme and releasing inorganic phosphate. YopH and PTP1B share equivalent chemical mechanisms and transition states for P–O bond cleavage. In both, kinetic isotope effects (KIE) (*17*, *18*) showed the leaving group oxygen to be fully protonated in the transition state for phosphotyrosine cleavage, a conclusion supported by the negligible dependence ($\beta = -0.008$) on leaving group basicity (*19*). Despite very similar substrate interactions and chemical mechanisms, their k_{cat} values, which are partially limited by the rate of hydrolysis of the phosphoenzyme intermediate, are significantly different, with YopH about 20-fold more active than PTP1B for phosphopeptide substrate with temperature-adjusted catalytic rates of 700 to 1000 s^{-1} versus 15 to 30 s^{-1}, respectively, at pH = 6.6 and 293 K (*20*). The cleavage of phosphopeptide is faster than the hydrolysis step, as evidenced by burst kinetics and an observed kinetic solvent deuterium isotope effect on the overall reaction (*21*). Overall, these kinetic data indicate that $k_{cleavage}$ values for YopH and PTP1B range from 1400 to 2000 s^{-1} and 25 to 80 s^{-1}, respectively (methods). Here, we describe the WPD loop motion by solution-phase NMR relaxation dispersion studies and focus on the role of loop closure in the cleavage step.

The apo (ligand-free) forms of PTP1B and YopH behave very differently. We applied ^{15}N-Carr-Purcell-Meiboom-Gill (CPMG) relaxation dispersion experiments to PTP1B (*22*), in which the measured relaxation rate (R_2) depends on the physical parameters for motion, [equilibrium populations p_a/p_b and chemical shift differences ($\Delta\omega$) between the two interconverting conformations and kinetics ($k_{ex} = k_f + k_r$), where ex indicates exchange; f and r indicate forward and reverse rates, respectively and τ_{cp}, which is the delay between ^{15}N 180° pulses (eq. S1). For PTP1B, we have assigned amide resonances for W179, F182, G183, V184, S187, and A189 (*16*) in the WPD loop. Of these, resonances for G183 and S187 are too weak to quantitate, and V184 is partially overlapped precluding further analysis. The remaining WPD loop residues (W179, F182, and A189, fig. S1, B to D) show upward curving CPMG relaxation dispersion (Fig. 2, A to C). The exchange parameters are shown in Table 1. Their individual fits yield similar exchange rates with $k_{ex} \sim 900$ s^{-1}, suggesting concerted loop motion. Therefore, F182 and A189 data were fit to a global model simultaneously at 600 and 800 MHz (Table 1). For these two residues, p_a = 97.5 ± 1.4% (SE) and p_b = 2.5%. Knowledge of p_a and k_{ex} enables determination of $k_f = 22 \pm 5$ s^{-1} and $k_r = 890 \pm 190$ s^{-1}. The larger uncertainties in measured R_2 values for W179 precluded use of eq. S1; however, reliable k_{ex} values = 900 ± 200 s^{-1} and R_{ex} values ($= p_a p_b \Delta\omega^2/k_{ex}$) = 31.4 ± 4.6 s^{-1} are obtained for this residue by using eq. S2 (Fig. 1C). By using p_a = 97.5% determined above, we calculated $\Delta\omega$ for W179 to be 2.8 ± 0.9 parts per million (ppm) (Table 1).

On the basis of the many apo PTP1B crystal structures (*23*), we hypothesized that the major solution conformer is an open WPD loop with a minor population of closed WPD loop, supported by an apo closed crystal structure [Protein Data Bank (PDB) code 1SUG (*24*)] with a closed active site loop. This interconversion between open and closed conformations means that k_f represents the rate for loop closure and k_r the rate for loop opening. Support for this hypothesis comes from measurements of the chemical shift differences between the open and closed WPD loop, which were determined by direct measurement

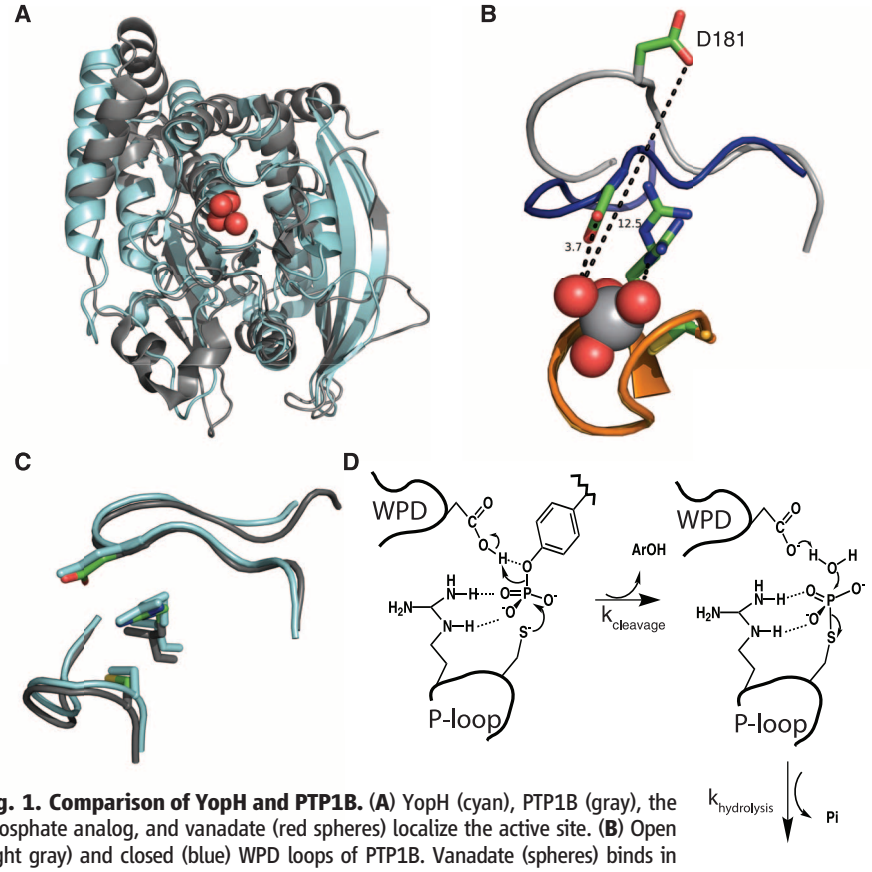


Fig. 1. Comparison of YopH and PTP1B. (**A**) YopH (cyan), PTP1B (gray), the phosphate analog, and vanadate (red spheres) localize the active site. (**B**) Open (light gray) and closed (blue) WPD loops of PTP1B. Vanadate (spheres) binds in the P-loop (orange), with C215 and R221 (*16*) in stick rendering. Movement of D181 is indicated by dashed lines. (**C**) Superposition of closed loops for PTP1B and YopH. The three catalytic residues are shown in stick rendering. (**D**) PTP catalytic reaction of cleavage and hydrolysis. PDB accession numbers for (A) are 2I42 and 3I80.

($\Delta\delta^N_{meas}$) (materials and methods) of the differences in open and closed shifts for the apo and peptide bound (vide infra) enzyme. Moreover, the difference ($\Delta\delta^N_{calc}$) between calculated shifts for the closed conformation based on the crystal structure and the measured shifts for the open conformation was determined. These $\Delta\omega$, $\Delta\delta^N_{meas}$, and $\Delta\delta^N_{calc}$ values are nearly identical for F182, A189, and similarly for W179, whose bound resonance disappears; $\Delta\omega$ and $\Delta\delta^N_{calc}$ are within error (Fig. 3, A and B, fig. S3A, and Table 1). The agreement between these shifts supports the hypothesis that the apo loop converts between a predominantly open conformation with a minor closed state and indicates that the WPD loop in apo PTP1B closes ($k_{close} = k_f = 22 \pm 5\ s^{-1}$) with a rate constant very similar to its $k_{cleavage}$ value of 25 to 80 s^{-1} (see methods) suggesting that, if the enzyme maintained these motions in the substrate-bound state, loop closure occurs simultaneously with protonation of the leaving group substrate.

Distinct from PTP1B, YopH is over an order of magnitude faster in its enzymatic reaction. WPD loop resonances for T358, A359, V360, and S361 were assigned (fig. S4A). In contrast to PTP1B, YopH ^{15}N-CPMG and ^{15}N-$R_{1\rho}$ dispersion curves are flat (fig. S4, B and C) indicating loop motions $\geq 30{,}000\ s^{-1}$. To detect these faster motions, we modified a ^{1}H-$R_{1\rho}$ experiment (*25*) for transverse relaxation-optimized spectroscopy (TROSY) detection (fig. S5) and applied it to YopH. In Fig. 2, D and E, dispersion is observed for loop residues A359 and S361 with global $k_{ex} = 43{,}000 \pm 6200\ s^{-1}$. T358 is overlapped, and V360 had too low signal-to-noise for quantitation. Like PTP1B, our hypothesis is that the WPD loop moves between open and closed conformations, which is supported by the similarity in $\Delta\delta^N_{meas}$ and $\Delta\delta^N_{calc}$ ^{15}N chemical shifts for A359 and S361 (Fig. 3, C and D) and for T358 and V360 (fig. S3, B and C).

The motion of the apo YopH WPD loop is in the fast exchange limit, and therefore other methods are needed to extract $\Delta\omega$ and populations from these data because they appear as the product, $p_a p_b \Delta\omega^2$ in Eq. 1

$$R_{1\rho}/\sin^2\theta = (R_2^0 - R_1) + \frac{\Delta\omega^2 p_A p_B k_{ex}}{\omega_e^2 + k_{ex}^2} \quad (1)$$

To circumvent this limitation, we measured the ^{15}N-R_{ex} values ($R_{ex} = p_a p_b \Delta\omega^2/k_{ex}$) from a ^{15}N TROSY Hahn-echo experiment (*26*) (fig. S6) (for details, see supplementary materials) and used the measured k_{ex} and $\Delta\delta^N_{meas}$ as a proxy for $\Delta\omega$ to give $p_a = 97\%$. A loop-closing rate, $k_{close} = 1240 \pm 280\ s^{-1}$ (Table 1), was calculated for YopH, which is about 1.7-fold greater than its k_{cat} value and similar to $k_{cleavage}$ (1400 s^{-1} to 2000 s^{-1}), suggesting that, like PTP1B, there is intimate involvement of WPD loop closure in the step of pY cleavage. Thus, for two enzymes with very different catalytic rates and identical chemical mechanisms, active-site loop motion in the apo enzyme is tuned to approximate the overall cleavage rate in each. Because the WPD loop must be closed for chemistry to occur, loop closing on the proper time scale will facilitate the chemical reaction.

We formed the complex between PTP1B and an octamer peptide, Ac-DADEXLIP-NH_2 (*16*) (fig. S2A) derived from EGF receptor, where X is difluoromethylphosphono-phenylalanine, a non-cleavable phosphotyrosine mimic. The inhibition constant value of the peptide (high nM, low μM) is similar to the substrate Michaelis constant, indicating that DADEXLIP behaves as a good substrate mimic (*27*). In PTP1B, F182 is significantly exchange-broadened in the peptide-bound form, and the resonance for W179 disappears, preventing further analysis. Both observations indicate a change in loop motions. The ^{15}N-CPMG dispersion curves at 600 and 800 MHz for A189 in peptide-bound PTP1B are noticeably different from apo PTP1B and display pronounced oscillation at low CPMG pulsing frequencies, characteristic of slow conformational exchange

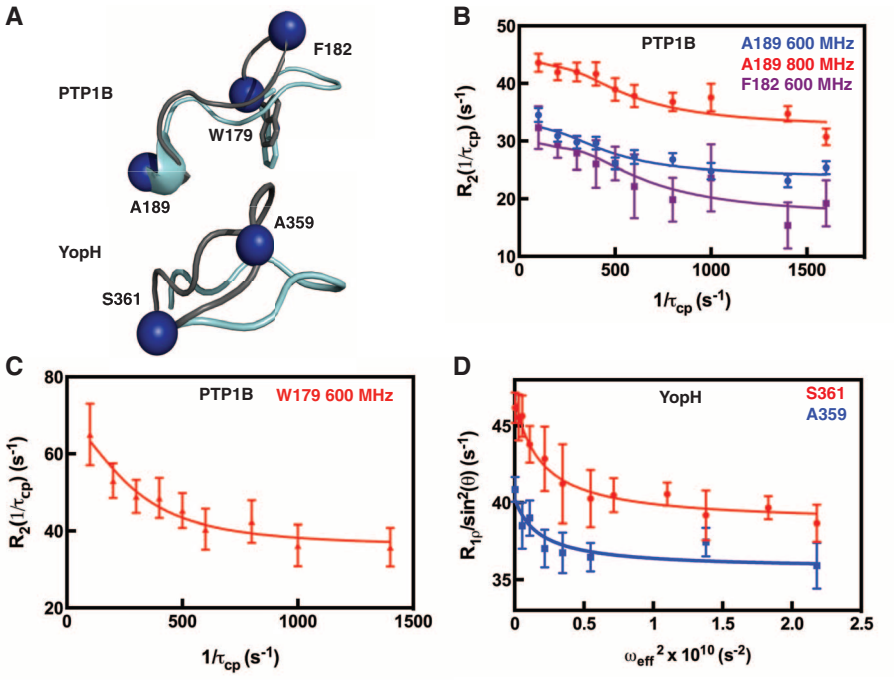


Fig. 2. NMR-detected motions. Open and closed PTP1B and YopH WPD loops (**A**). (**B** and **C**) The ^{15}N-CPMG dispersion curves for A189, F182, and W179. (**D**) TROSY-detected off-resonance ^{1}H-$R_{1\rho}$ dispersion curves for A359 (blue) and S361 (red). Error bars indicate standard errors determined from duplicate measurements.

Table 1. Summary of WPD loop motions. Open/closed loop equilibrium values are derived from p_{open}/p_{closed}. The ^{15}N $\Delta\omega$ values were determined from fits to relaxation dispersion data; ^{15}N $\Delta\delta_{calc}$ values were determined with ShiftX2 as described in the methods; and ^{15}N $\Delta\delta_{meas}$ values were determined from differences in measured chemical shifts between apo and peptide bound enzyme.

Enzyme	k_{ex} (s^{-1})	k_{close} (s^{-1})	k_{open} (s^{-1})	K_{eq}	^{15}N $\Delta\omega$ (ppm)	^{15}N $\Delta\delta_{calc}$ (ppm)	^{15}N $\Delta\delta_{meas}$ (ppm)
PTP1B apo	920 ± 190	22 ± 5	890 ± 190	40	A189: 3.8 ± 0.6	A189: 3.7 ± 0.2	A189: 3.87
					F182: 3.4 ± 1.3	F182: 4.9 ± 1.0	F182: 3.60
					W179: 2.8 ± 0.9	W179: 1.9 ± 0.5	W179: Not determined
PTP1B/peptide	35 ± 5	30 ± 4	4.5 ± 1	0.15	A189: 3.2 ± 0.3	A189: 3.7 ± 0.2	A189: 3.87
YopH apo	43,000 ± 6200	1240 ± 200	42,000 ± 6000	34	Not determined	A359: 3.4 ± 0.4	A359: 3.82
						S361: 6.4 ± 1.2	S361: 3.96
YopH/peptide	1790 ± 240	1770 ± 240	18 ± 2	0.01	A359: 3.5 ± 0.4	A359: 3.4 ± 0.4	A359: 3.82
					S361: 4.5 ± 0.8	S361: 6.4 ± 1.2	S361: 3.96

(Fig. 4A and eq. S3). The A189 $\Delta\omega$ = 1210 ± 130 s^{-1} (3.2 ± 0.3 ppm) is identical to that determined in ligand-free PTP1B (Table 1). The equivalence of $\Delta\omega$ for apo and peptide-bound PTP1B is additional evidence that when substrate occupies the active site, the WPD loop interconverts between major closed and minor open conformations. Further support for this hypothesis comes from a PTP1B ligand-bound crystal structure [3EB1 (*28*)] in which the WPD loop is open, unlike the majority of other bound structures. From these data, we obtain a k_{close} = 30 ± 4 s^{-1} and k_{open} = 5 ± 1 s^{-1}. Thus, loop closure is the same in apo and peptide-bound PTP1B; peptide binding only slows loop opening. The similarity of k_{close} and $k_{cleavage}$ along with KIE data (*17*, *18*) indicating leaving group protonation in the transition state suggests that protonation of the tyrosine occurs concomitantly with loop closure with the proton being delivered by D181 on the WPD loop. Cleavage of phosphotyrosine is followed by hydrolysis of the phosphoenzyme intermediate, which occurs somewhat slower. These NMR data suggest that closing of the WPD loop occurs in close connection with the chemistry of phosphate cleavage and plays an important regulatory role in the overall catalytic cycle.

For YopH bound to peptide, loop motion slows substantially such that the ^{15}N-CPMG dispersion experiment can now be used for characterization, in contrast to apo YopH (Fig. 4B). Global fits of eq. S1 to the dispersion data in Fig. 4B gives $\Delta\omega$ values for A359 and S361 of 1350 ± 150 s^{-1} (3.5 ppm) and 1730 ± 290 s^{-1} (4.5 ppm), which are similar to the apo $\Delta\omega$, $\Delta\delta^N_{meas}$, and $\Delta\delta^N_{calc}$ values, as they are in PTP1B, indicating interconversion between open and closed conformations (Table 1). For the YopH loop, k_{ex} is 1790 ± 240 s^{-1} and p_a is 99%, to give k_{close} = 1770 ± 240 s^{-1} and k_{open} = 18 ± 2 s^{-1}. Like PTP1B, peptide binding to YopH only slows loop opening. Thus, in this faster enzyme k_{close} and $k_{cleavage}$ are similar, again suggesting that loop closure is concerted with protonation of the leaving group tyrosine as part of the cleavage reaction. Unlike the apo and peptide-bound enzymes, the product state mimic, tungstate, dissociates from PTB1B and YopH with identical rate constants (fig. S7 and methods). Thus, once cleavage and hydrolysis are complete, release of product is the same for both enzymes.

These NMR results for YopH are different than observed by other techniques. For apo YopH, Trp fluorescence anisotropy and temperature-jump (T-jump) fluorescent experiments suggest loop kinetics ranging from 3 ns to 3 µs, respectively (*29*, *30*). The former value is consistent with molecular dynamics simulations (*31*) indicating conformational motion between open and partially closed states, unlike our data that show opening and closing times, similar to T-jump experiments, of 22 µs between open and fully closed conformations. Those fluorescence experiments, however, only report on the indole side chain of W179, whereas our NMR data pertain to the motion of the backbone and therefore are more closely connected to the motion of the entire loop. Comparison of YopH loop motion in the bound conformation to other studies is more difficult. We used a peptide, whereas the previous T-jump experiment exploits the fluorescence from *p*-nitrocatechol sulfate; the differences in ligand choice may explain the 50-fold difference in observed loop kinetics in the respective complexes. For PTP1B, there are no available data for comparison.

The data presented for this pair of phosphatases suggest that the tuning of loop motion is closely synchronized with the chemical reaction of phosphotyrosine cleavage. During the femtosecond bond-making and -breaking steps of the enzyme reaction, the WPD loop is static on the time scale observable by NMR. However, our NMR experiments do suggest a contiguous energy landscape for loop motion and catalytic activity and that loop closure is closely coupled to the protonation of the tyrosine leaving group. Additionally, the nature of the occupancy of the active site modulates the WPD loop kinetics and is consistent with the dynamic energy landscape hypothesis of enzyme function (*3*).

A myriad of crucial biological pathways are regulated by posttranslational protein phosphorylation levels. Remarkably, our NMR data for these phophatases suggest that phosphorylation levels can be modulated through control of WPD loop kinetics. The additional Pro residues in the PTP1B loop are potentially responsible for the slower motions. Slower PTP1B loop motions likely reflect the physiological role of PTP1B as a tight regulator of cellular processes, in which its turnover rate must meet the strict growth requirements of the cell. In contrast, the faster loop motion and enzymatic activity in YopH would be beneficial for the rapid disruption of normal cellular pathways that enable this enzyme to participate in and facilitate *Yersinia* infection.

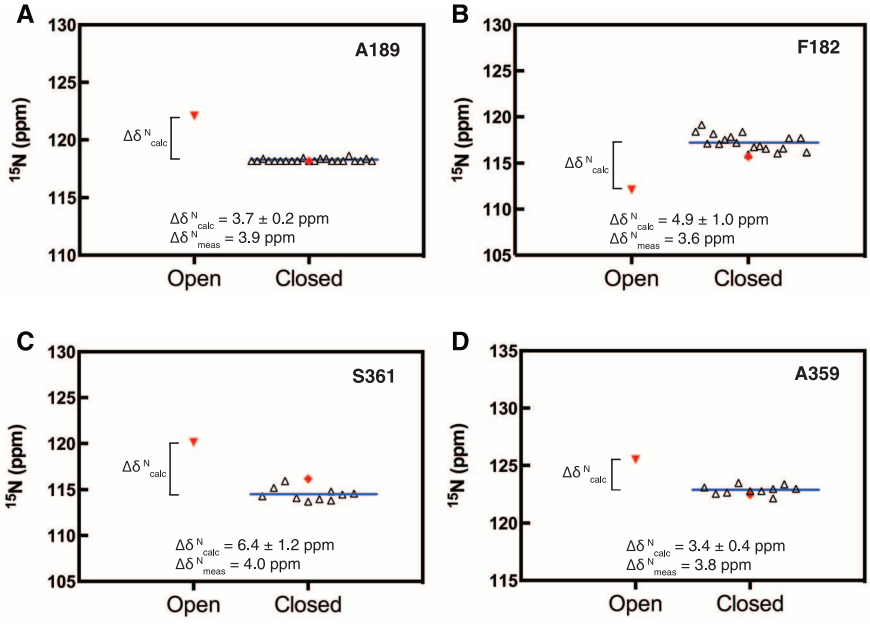


Fig. 3. Chemical shift differences for open and closed WPD loops. For PTP1B (**A** and **B**) and YopH (**C** and **D**), the NMR-measured (red symbols) and calculated (black open symbols) chemical shifts are shown for residues in the WPD loop.

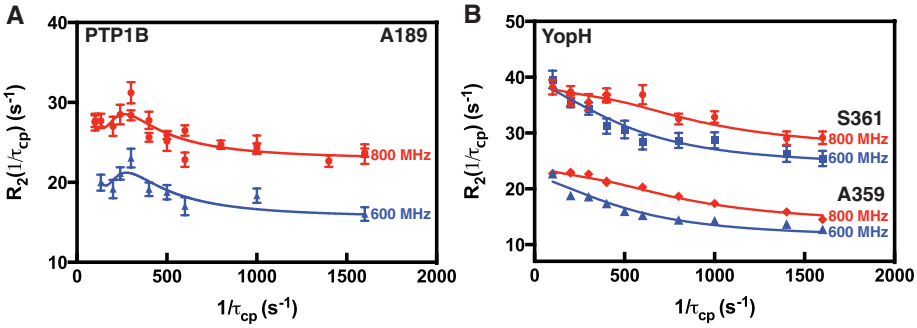


Fig. 4. NMR-detected motions. The ^{15}N-CPMG dispersion analyses for peptide-bound PTP1B (**A**) and YopH (**B**). (A) shows a global fit at 800 and 600 MHz for A189. (B) shows a global fit at 800 (red) and 600 (blue) MHz for A359 and S361 in YopH.

References and Notes

1. S. C. Kamerlin, A. Warshel, *Proteins* **78**, 1339–1375 (2010).
2. A. J. Adamczyk, J. Cao, S. C. Kamerlin, A. Warshel, *Proc. Natl. Acad. Sci. U.S.A.* **108**, 14115–14120 (2011).
3. D. D. Boehr, D. McElheny, H. J. Dyson, P. E. Wright, *Science* **313**, 1638–1642 (2006).
4. S. Rozovsky, A. E. McDermott, *Proc. Natl. Acad. Sci. U.S.A.* **104**, 2080–2085 (2007).
5. E. Z. Eisenmesser *et al*., *Nature* **438**, 117–121 (2005).
6. K. A. Henzler-Wildman *et al*., *Nature* **450**, 838–844 (2007).
7. G. Bhabha *et al*., *Science* **332**, 234–238 (2011).
8. H. Beach, R. Cole, M. L. Gill, J. P. Loria, *J. Am. Chem. Soc.* **127**, 9167–9176 (2005).
9. D. Joseph, G. A. Petsko, M. Karplus, *Science* **249**, 1425–1428 (1990).
10. M. Wolf-Watz *et al*., *Nat. Struct. Mol. Biol.* **11**, 945–949 (2004).
11. R. Desamero, S. Rozovsky, N. Zhadin, A. McDermott, R. Callender, *Biochemistry* **42**, 2941–2951 (2003).
12. D. Antoniou, X. Ge, V. L. Schramm, S. D. Schwartz, *J. Phys. Chem. Lett.* **3**, 3538–3544 (2012).
13. R. G. Silva, A. S. Murkin, V. L. Schramm, *Proc. Natl. Acad. Sci. U.S.A.* **108**, 18661–18665 (2011).
14. R. R. Brubaker, *Clin. Microbiol. Rev.* **4**, 309–324 (1991).
15. Z. Y. Zhang, *Curr. Opin. Chem. Biol.* **5**, 416–423 (2001).
16. Single-letter abbreviations for the amino acid residues are as follows: A, Ala; C, Cys; D, Asp; E, Glu; F, Phe; G, Gly; H, His; I, Ile; K, Lys; L, Leu; M, Met; N, Asn; P, Pro; Q, Gln; R, Arg; S, Ser; T, Thr; V, Val; W, Trp; and Y, Tyr.
17. T. A. Brandão, A. C. Hengge, S. J. Johnson, *J. Biol. Chem.* **285**, 15874–15883 (2010).
18. A. C. Hengge, G. A. Sowa, L. Wu, Z. Y. Zhang, *Biochemistry* **34**, 13982–13987 (1995).
19. Y. F. Keng, L. Wu, Z. Y. Zhang, *Eur. J. Biochem.* **259**, 809–814 (1999).
20. Z. Y. Zhang *et al*., *Proc. Natl. Acad. Sci. U.S.A.* **90**, 4446–4450 (1993).
21. Z. Y. Zhang, *J. Biol. Chem.* **270**, 11199–11204 (1995).
22. J. P. Loria, M. Rance, A. G. Palmer 3rd, *J. Biomol. NMR* **15**, 151–155 (1999).
23. D. Barford, A. J. Flint, N. K. Tonks, *Science* **263**, 1397–1404 (1994).
24. A. K. Pedersen, G. H. Peters, K. B. Møller, L. F. Iversen, J. S. Kastrup, *Acta Crystallogr. D Biol. Crystallogr.* **60**, 1527–1534 (2004).
25. C. Eichmüller, N. R. Skrynnikov, *J. Biomol. NMR* **32**, 281–293 (2005).
26. C. Wang, M. Rance, A. G. Palmer 3rd, *J. Am. Chem. Soc.* **125**, 8968–8969 (2003).
27. T. R. Burke Jr., H. K. Kole, P. P. Roller, *Biochem. Biophys. Res. Commun.* **204**, 129–134 (1994).
28. S. Liu *et al*., *J. Am. Chem. Soc.* **130**, 17075–17084 (2008).
29. L. J. Juszczak, Z. Y. Zhang, L. Wu, D. S. Gottfried, D. D. Eads, *Biochemistry* **36**, 2227–2236 (1997).
30. M. Khajehpour *et al*., *Biochemistry* **46**, 4370–4378 (2007).
31. X. Hu, C. E. Stebbins, *Biophys. J.* **91**, 948–956 (2006).

Acknowledgments: We thank J. Hoch, D. Korzhnev, M. Maciejewski, and G. Armstrong for access to their high-field NMR instruments and G. Khirich for running Monte Carlo simulations. S.K.W., A.C.H., and J.P.L. acknowledge support from grants NIH-T32GM008283, NIH-GM47297, and NSF-MCB1121372.

Supplementary Materials

www.sciencemag.org/cgi/content/full/341/6148/899/DC1
Materials and Methods
Figs. S1 to S7
References (*32*–*52*)

10 June 2013; accepted 29 July 2013
10.1126/science.1241735

Cyclic GMP-AMP Synthase Is an Innate Immune Sensor of HIV and Other Retroviruses

Daxing Gao,[1] Jiaxi Wu,[1] You-Tong Wu,[1] Fenghe Du,[1,2] Chukwuemika Aroh,[3,4] Nan Yan,[3,4] Lijun Sun,[1,2] Zhijian J. Chen[1,2]*

Retroviruses, including HIV, can activate innate immune responses, but the host sensors for retroviruses are largely unknown. Here we show that HIV infection activates cyclic guanosine monophosphate–adenosine monophosphate (cGAMP) synthase (cGAS) to produce cGAMP, which binds to and activates the adaptor protein STING to induce type I interferons and other cytokines. Inhibitors of HIV reverse transcriptase, but not integrase, abrogated interferon-β induction by the virus, suggesting that the reverse-transcribed HIV DNA triggers the innate immune response. Knockout or knockdown of cGAS in mouse or human cell lines blocked cytokine induction by HIV, murine leukemia virus, and simian immunodeficiency virus. These results indicate that cGAS is an innate immune sensor of HIV and other retroviruses.

Although tremendous advances have been made in our understanding of innate immune recognition of many microbial pathogens (*1*–*3*), relatively little is known about innate immune responses against retroviral infections (*4*). Retroviruses were thought to trigger weak or no innate immune responses, which were typically measured through the production of inflammatory cytokines and type I interferons. However, recent research has shown that retroviruses such as HIV can trigger innate immune responses, which are normally masked by viral or host factors (*5*–*8*). For example, TREX1 is a cytosolic exonuclease that degrades DNA derived from HIV or endogenous retroelements, thereby preventing the accumulation of cytosolic DNA, which would otherwise trigger innate immunity (*9*, *10*). Loss-of-function mutations of TREX1 in humans have been closely linked to Aicardi-Goutières syndrome (AGS), a lupus-like disease characterized by elevated expression of inflammatory cytokines and interferon-stimulated genes (*11*).

We have recently identified the enzyme cyclic guanosine monophosphate–adenosine monophosphate (cGAMP) synthase (cGAS) as a cytosolic DNA sensor that triggers the production of type I interferons and other cytokines (*12*, *13*). DNA binds and activates cGAS, which catalyzes the synthesis of a cGAMP isomer from adenosine triphosphate (ATP) and guanosine triphosphate (GTP). This cGAMP isomer, termed 2′3′-cGAMP, which contains both 2′-5′ and 3′-5′ phosphodiester linkages, functions as a second messenger that binds and activates the endoplasmic reticulum protein STING (*14*–*17*). STING then activates the protein kinases IκB kinase (IKK) and TANK-binding kinase 1 (TBK1), which in turn activate the transcription factors nuclear factor κB (NF-κB) and interferon regulatory factor 3 (IRF3) to induce interferons and other cytokines (*18*). Knockdown of cGAS inhibits interferon-β (IFN-β) induction by DNA viruses such as herpes simplex virus 1 (HSV-1) and vaccinia virus (*13*). Because retroviruses generate complementary DNA from the viral RNA by reverse transcription, we hypothesized that cGAS might detect retroviral DNA and trigger innate immune responses.

We used a single-round HIV-1 virus in which its envelope protein was replaced with the glycoprotein of vesicular stomatitis virus (VSV-G), which allows it to infect a large variety of human and mouse cell types (*9*). This virus also expresses green fluorescent protein (GFP), which can be used to monitor viral infection. Infection of the human monocytic cell line THP1 with HIV-GFP led to dimerization of IRF3 (fig. S1A), a hallmark of its activation. Phosphorylation of STAT1 at Tyr-701 was also detected after HIV infection (fig. S1A), indicating that the interferon signaling pathway was activated in the virus-infected cells (*19*). HIV infection led to the induction of IFN-β and the chemokine CXCL10 (fig. S1B), concomitant with the generation of the HIV Gag episomal DNA (fig. S1C). The levels of IFN-β production were proportional to the multiplicity of infection by HIV (fig. S1D). Treatment of HIV-GFP virus with DNase I did not impair its ability to induce IFN-β (fig. S1E), whereas treatment of herring testis DNA (HT-DNA) with DNase I inhibited IFN-β induction (fig. S1F), indicating that IFN-β induction by HIV-GFP was not due to any contaminating DNA. Differentiation of THP1 from monocytes to macrophages by treating the cells with phorbol-12-myristate-13-acetate (PMA) inhibited HIV-GFP infection or replication (fig. S1G) and strongly inhibited IFN-β induction (fig. S1H). Thus, unless otherwise indicated, THP1 cells used in our study were not treated with PMA before HIV infection.

To test whether reverse transcription is required for HIV to activate the innate immune response,

[1]Department of Molecular Biology, University of Texas Southwestern Medical Center, Dallas, TX 75390–9148, USA. [2]Howard Hughes Medical Institute, University of Texas Southwestern Medical Center, Dallas, TX 75390–9148, USA. [3]Department of Internal Medicine, University of Texas Southwestern Medical Center, Dallas, TX 75390–9148, USA. [4]Department of Microbiology, University of Texas Southwestern Medical Center, Dallas, TX 75390–9148, USA.

*Corresponding author. E-mail: Zhijian.Chen@UTSouthwestern.edu

we treated THP1 cells with the HIV reverse transcriptase inhibitors azidothymidine (AZT) and nevirapine (NVP). Both inhibitors blocked IRF3 activation and IFN-β induction by HIV (Fig. 1, A and B). In contrast, the HIV integrase inhibitor raltegravir (RAL) did not affect the activation of this pathway. AZT and NVP, even at high concentrations, did not inhibit IFN-β induction by HT-DNA (fig. S2, A to C), indicating that the inhibitory effects of AZT and NVP were due to their specific inhibition of HIV reverse transcription. These results suggest that the reverse-transcribed HIV DNA is the trigger of IRF3 activation and IFN-β production.

Short-hairpin RNA (shRNA)–mediated knockdown of cGAS or STING in THP1 cells strongly inhibited the induction of IFN-β and CXCL10 and the activation of IRF3 by HIV-GFP (Fig. 1, C and D; and fig. S2, D and E). Control experiments showed that shRNA against luciferase did not inhibit the activation of the pathway and that the shRNA vectors knocked down the intended targets specifically. In particular, the cGAS shRNA knocked down cGAS but not STING (Fig. 1D), and the induction of IFN-β in these cells was rescued by delivering cGAMP into the cells (fig. S2F), indicating that the cGAS shRNA did not have off-target effects in the STING pathway.

Previous studies have shown that VSV-G–pseudotyped HIV-1 strongly induces IFN-β in TREX1-deficient mouse embryonic fibroblasts (MEFs) but not in the wild-type (WT) MEF (*9*). We generated *Trex1*$^{-/-}$ MEF cell lines stably expressing shRNA against cGAS, STING, or luciferase (as a control; fig. S3, A and B). HIV infection induced IFN-β and CXCL10 RNA in the control cells (sh-luciferase) but not in cGAS- or STING-depleted cells (fig. S3, C and D). In contrast, knockdown of cGAS or STING did not affect the induction of IFN-β or CXCL10 by the double-stranded RNA analog poly[I:C].

To obtain definitive evidence for the role of cGAS in the innate sensing of cytosolic DNA and retroviruses, we employed the TALEN technology to disrupt the gene that encodes cGAS (*Mb21d1*); specifically, the region that encodes the catalytic domain, in L929 cells (see methods and fig. S4A) (*20*). Although L929 cells contain three copies of chromosome 9, which harbors the cGAS gene, DNA sequencing of the TALEN-expressing cells identified multiple clones that had deletions in all three chromosomes; three of these clones were chosen for further studies (fig. S4B). All three clones contained deletions in the cGAS locus that generated frameshift mutations (*21*).

All three cGAS mutant cell lines failed to activate IRF3 in response to HT-DNA transfection or HSV-1 (a double-stranded DNA virus) infection (Fig. 2A and fig. S4C). As controls, these cells activated IRF3 normally in response to transfection with poly[I:C] or infection with Sendai virus, an RNA virus. The cGAS mutant cells were also defective in inducing CXCL10 in response to HT-DNA, but this defect was rescued by trans-

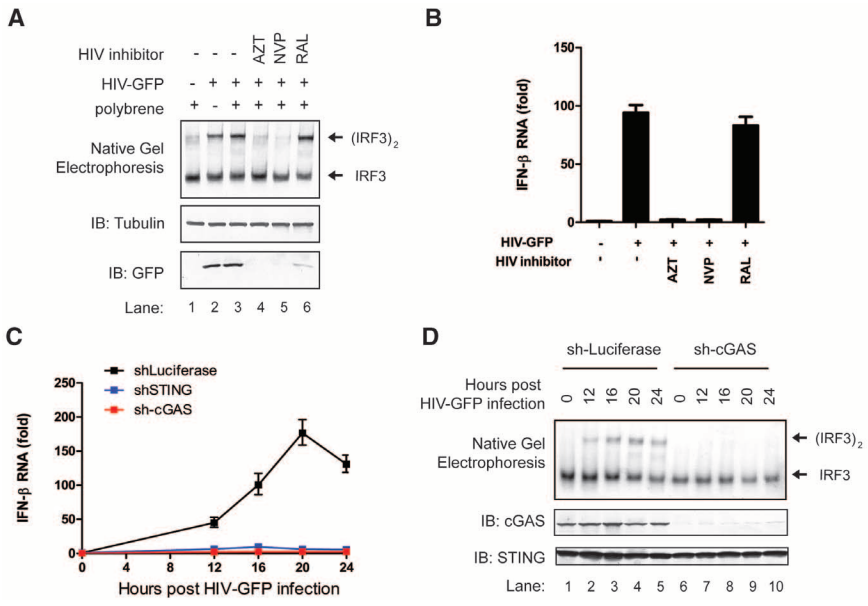


Fig. 1. The cGAS-STING pathway mediates innate immune responses against HIV. (**A** and **B**) THP1 cells were treated with the HIV reverse transcriptase inhibitors AZT and NVP (each at 5 μM) or the integrase inhibitor RAL (at 10 μM) for 30 min before infection with HIV-GFP. 24 hours after infection, cell extracts were analyzed by native gel electrophoresis or SDS–polyacrylamide gel electrophoresis, followed by immunoblotting with indicated antibodies (A), and total RNA was isolated for quantitative reverse transcription polymerase chain reaction (qRT-PCR) (B). (**C** and **D**) THP1 cells stably expressing an shRNA against human cGAS, STING, or luciferase (control) were infected with HIV-GFP for the indicated time, followed by measurement of IFN-β RNA by qRT-PCR (C) and immunoblotting with the indicated antibodies (D). Error bars indicate standard deviations of triplicate measurements. Unless otherwise indicated, data shown in this and all other figures are representative of at least two independent experiments.

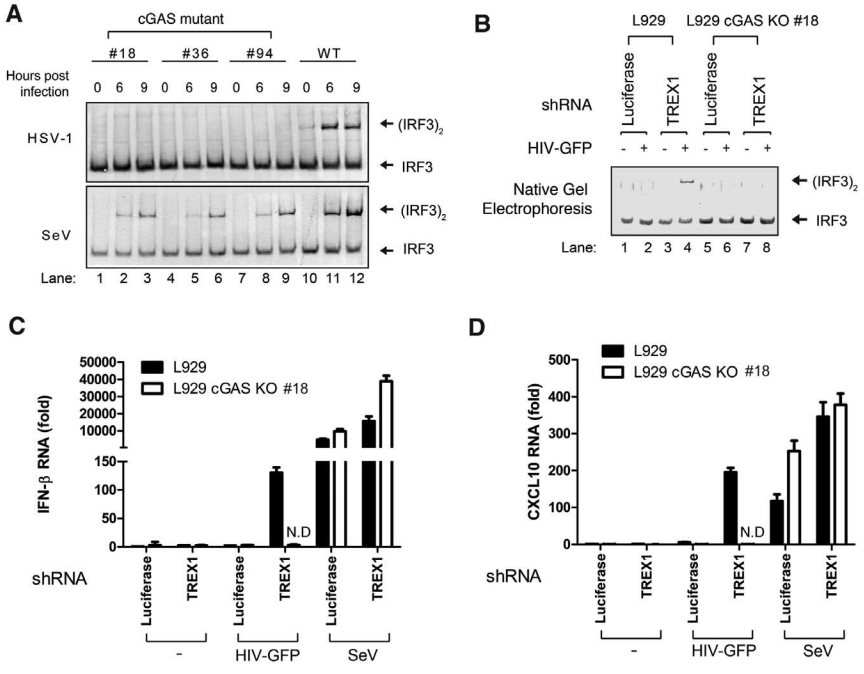


Fig. 2. cGAS is essential for innate immune responses triggered by HIV. (**A**) L929 cell lines harboring various deletions in exon 2 of the cGAS locus were generated by TALEN (see fig. S4). These cells and the parental L929 cells were infected with HSV-1 or Sendai virus (SeV), followed by measurement of IRF3 dimerization. (**B**) L929 cGAS knockout clone 18 and parental L929 cells were stably transfected with shRNA vector targeting TREX1 or luciferase (as a control). These cells were infected with HIV-GFP for 20 hours, followed by an IRF3 dimerization assay. (**C** and **D**) Similar to (B) except that RNA levels of IFN-β (C) and CXCL10 (D) were measured by qRT-PCR. As a control, some cells were also infected with Sendai virus for 12 hours. The error bars indicate standard deviations of triplicate measurements. N.D., nondetectable.

fecting the cells with the mouse cGAS expression plasmid (fig. S4D).

We chose cGAS mutant clone 18 and the parental L929 cells to investigate the role of cGAS in innate immune recognition of HIV infection. In L929 cells stably expressing an shRNA against TREX1, but not the control luciferase, HIV-GFP infection induced IRF3 dimerization and the production of IFN-β and CXCL10 (Fig. 2, B to D; and fig. S4, E and F). In contrast, the L929 cGAS mutant cells failed to mount any detectable immune response to HIV infection even when TREX1 was depleted, demonstrating the essential role of cGAS in immune responses against HIV. The depletion of cGAS did not affect IFN-β or CXCL10 induction by Sendai virus (Fig. 2, C and D).

We have previously shown that HEK293T cells do not express detectable levels of cGAS and STING and thus fail to activate IRF3 in response to DNA transfection or DNA virus infection (*13*). Consistent with an important role of cGAS and STING in retrovirus detection, HIV-GFP infection activated IRF3 and STAT1 in THP1 but not HEK293T cells (fig. S5A). In contrast, Sendai virus activated IRF3 and STAT1 in both cell lines. To determine whether HIV infection leads to the production of endogenous cGAMP in human cells, we prepared lysates from HIV-infected THP1 and HEK293T cells and heated the lysates at 95°C to denature most proteins, which were removed by centrifugation (*12*). The supernatant that potentially contained cGAMP was delivered to THP1 cells that had been permeabilized with the bacterial toxin perfringolysin-O (PFO), and then IRF3 dimerization was assayed by native gel electrophoresis (fig. S5B). The heat-resistant supernatant from HIV-infected THP1, but not HEK293T, cells contained the cGAMP activity that stimulated IRF3 activation in the recipient cells. Furthermore, inhibition of HIV reverse transcription by AZT, DDI (didanosine), or NVP blocked the generation of the cGAMP activity, whereas the HIV integrase inhibitor RAL had no effect (Fig. 3A). HIV-GFP infection in L929-shTrex1 cells also led to generation of the cGAMP activity, which was dependent on cGAS (Fig. 3B). Taken together, these results indicate that HIV infection induces the production of endogenous cGAMP in a manner that depends on cGAS and the reverse transcription of HIV RNA to cDNA.

To test whether HIV infection produces retroviral cDNA in the cytoplasm to activate cGAS, we infected HEK293T cells with HIV-GFP and prepared cytosolic extracts that were then incubated with purified cGAS protein in the presence of ATP and GTP (fig. S5C). Cytosolic extracts from HIV-infected cells, but not from uninfected cells, were able to stimulate cGAS to produce the cGAMP activity that activated IRF3 in permeabilized THP1 cells. Treatment of HEK293T cells with AZT inhibited the generation of the cGAS stimulatory activity. Further analyses showed that the cytoplasm of HIV-infected cells contained the HIV Gag DNA

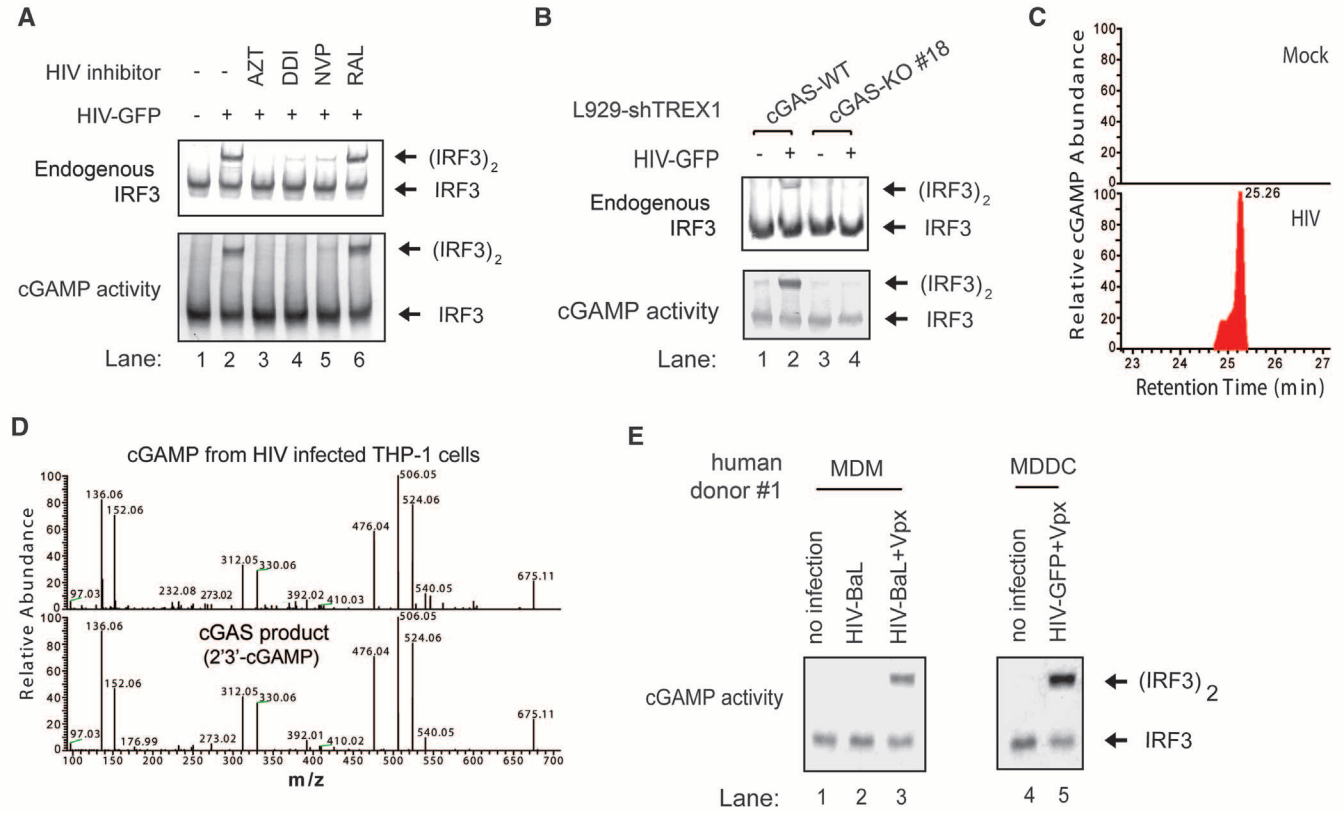


Fig. 3. HIV infection induces the production of cyclic GMP-AMP in human cells. (**A**) THP1 cells were treated with inhibitors of HIV reverse transcriptase (AZT, DDI, and NVP) or integrase (RAL) before infection with HIV-GFP for 24 hours. Cell extracts were prepared for native gel electrophoresis to detect endogenous IRF3 dimer (top panel). Aliquots of the cell extracts were treated at 95°C for 5 min to denature proteins, which were subsequently removed by centrifugation. The cGAMP activity in the supernatant was measured after its delivery into PFO-permeabilized THP1 cells, followed by IRF3 dimerization assay (bottom panel). (**B**) L929 cGAS knockout clone 18 and the parental cells, both stably expressing an shRNA against TREX1, were infected with HIV-GFP for 22 hours. Endogenous IRF3 activation and cGAMP production in the cells were measured as described in (A). (**C**) The heat-resistant supernatants from THP-1 cells without (mock) or with HIV-GFP infection were fractionated by high-performance liquid chromatography using a C18 column, and the abundance of cGAMP was quantitated by mass spectrometry using SRM. (**D**) Comparison of the tandem mass spectrometry spectra of cGAMP isolated from HIV-infected THP-1 cells and that synthesized in vitro by recombinant human cGAS protein. Higher-energy collision dissociation (HCD) was used to fragment the precursor ion ($[M+H]^+$ = 675.107,) and normalized collision energy was set at 25. (**E**) MDMs or MDDCs from a human donor were either untreated or treated with Vpx-VLP for 24 hours before infection with HIV. MDMs were infected with HIV-BaL for 3 days, whereas MDDCs were infected with HIV-GFP for 1 day. The cGAMP activity in these cells was measured as described in (A). Fluorescence-activated cell sorting analysis of HIV infection and measurement of cGAMP abundance by mass spectrometry are shown in fig. S6. The data are representative of three independent experiments involving three human donors.

(fig. S5D) and GFP protein (fig. S5E), both of which were inhibited by AZT.

Quantitative measurement of cGAMP abundance by mass spectrometry using selective reaction monitoring (SRM) provided the direct evidence that cGAMP was produced in HIV-infected, but not mock-treated, THP1 cells (Fig. 3C). Tandem mass spectrometry of the endogenous cGAMP from HIV-infected THP1 cells revealed that it was identical to the cGAS product, 2′3′-cGAMP (Fig. 3D) (*15*).

To test whether HIV infection in primary human immune cells leads to cGAMP production, we infected monocyte-derived macrophages (MDMs) and monocyte-derived dendritic cells (MDDCs) with the clinical HIV-1 isolate HIV-BaL and HIV-GFP, respectively. Previous research has shown that human macrophages and dendritic cells express SAMHD1, a nuclease that hydrolyzes dNTP, thereby inhibiting HIV reverse transcription (*7*, *8*). HIV-2 and simian immunodeficiency virus (SIV) contain the protein Vpx, which targets SAMHD1 for ubiquitin-mediated proteasomal degradation, thus removing this host restriction factor. To facilitate HIV infections in human MDMs and MDDCs, we delivered the SIV Vpx into these cells using a virus-like particle (VLP) before HIV infection (fig. S6, A, B, and D) (*6*). In the presence of Vpx, infection of MDMs and MDDCs with HIV-BaL and HIV-GFP, respectively, led to the generation of cGAMP activity (Fig. 3E). Quantitative mass spectrometry analysis further confirmed the production of 2′3′-cGAMP in HIV-infected MDDCs that expressed Vpx (fig. S6C). The cGAMP activity was consistently observed in MDDCs and MDMs of additional human donors, and this activity was higher in the cells infected with HIV than in those treated with Vpx alone (fig. S6, D to F). These results demonstrate that HIV infection in human macrophages and dendritic cells leads to the generation of cGAMP under conditions that are permissive to viral replication.

Finally, we tested whether cGAS is required for innate immune responses against other retroviruses by infecting L929 and L929-cGAS knockout cell lines with murine leukemia virus (MLV) and SIV. Similar to HIV, MLV and SIV induced IFN-β and CXCL10 RNA in L929 cells depleted of endogenous TREX1, but such induction was completely abolished in the cGAS knockout cells (Fig. 4A-4D). In further support of an essential role of the cGAS-STING pathway in innate immune sensing of retroviruses, knockdown of cGAS or STING in *Trex1*$^{-/-}$ MEF cells strongly inhibited IFN-β induction by MLV and SIV (fig. S7, A to D).

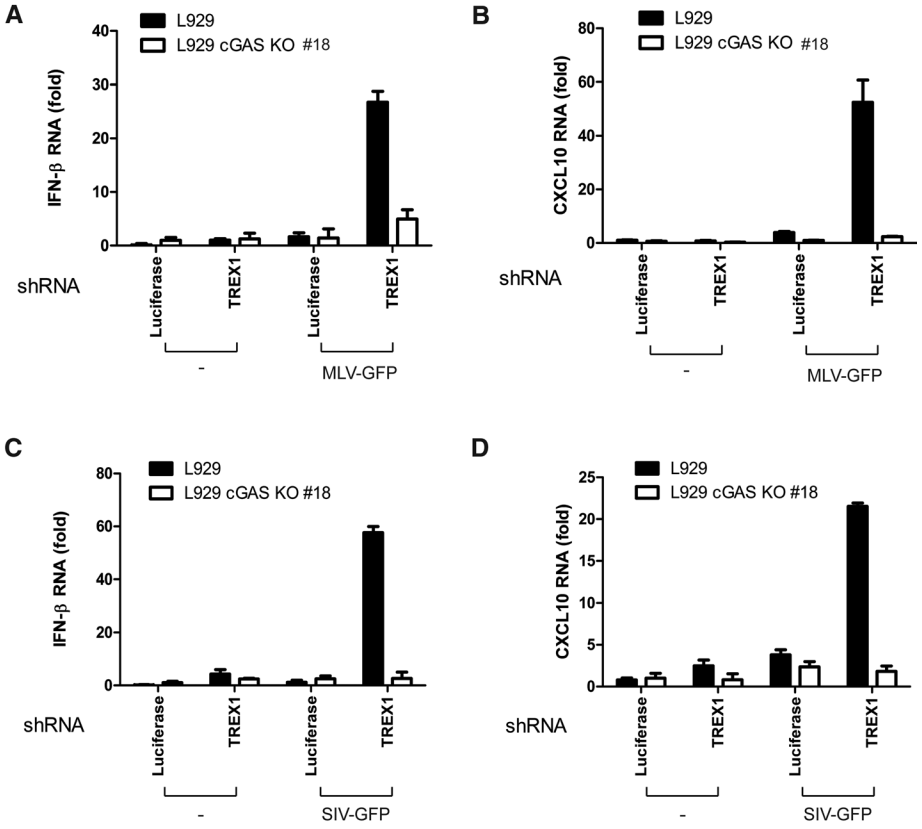


Fig. 4. MLV and SIV activate innate immune responses through cGAS. (**A** and **B**) L929 cGAS knockout (KO) clone 18 and the parental L929 cells stably expressing shRNA against TREX1 or luciferase (control) were infected with MLV-GFP [multiplicity of infection (MOI) = 2] for 20 hours, followed by measurement of IFN-β (A) and CXCL10 (B) RNA by qRT-PCR. (**C** and **D**) Similar to (A) and (B), except that cells were infected with SIV-GFP (MOI = 1.5) for 20 hours.

Here we have demonstrated that cGAS is essential for innate immune responses against HIV, SIV, and MLV, suggesting that cGAS is a general innate immune sensor of retroviral DNA. Although HIV primarily infects human CD4 T cells, it can also enter macrophages and dendritic cells, normally without triggering an overt innate immune response by concealing the viral nucleic acids within the capsid and by limiting the accumulation of viral DNA through co-opting host factors such as TREX1 and SAMHD1 (*8*). The absence of a rigorous innate immune response to HIV in dendritic cells is thought to be a major factor that hampers productive T cell responses and vaccine development (*7*). Our finding that HIV and other retroviruses can induce the production of cGAMP through cGAS under permissive conditions suggests that cGAMP might be used to bypass the block of innate immune responses against HIV. As such, cGAMP could be a candidate vaccine adjuvant for HIV and other pathogens that are adept at subverting the host innate immune system.

References and Notes

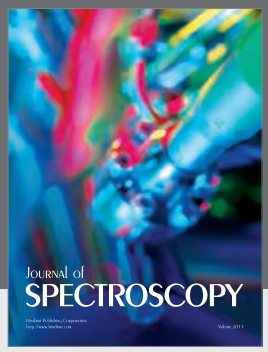
1. A. Iwasaki, R. Medzhitov, *Science* **327**, 291–295 (2010).
2. O. Takeuchi, S. Akira, *Cell* **140**, 805–820 (2010).
3. P. C. Ronald, B. Beutler, *Science* **330**, 1061–1064 (2010).
4. R. Medzhitov, D. Littman, *Nature* **455**, 591 (2008).
5. N. Manel, D. R. Littman, *Cell* **147**, 271–274 (2011).
6. N. Manel *et al.*, *Nature* **467**, 214–217 (2010).
7. J. Luban, *Cell Host Microbe* **12**, 408–418 (2012).
8. N. Yan, Z. J. Chen, *Nat. Immunol.* **13**, 214–222 (2012).
9. N. Yan, A. D. Regalado-Magdos, B. Stiggelbout, M. A. Lee-Kirsch, J. Lieberman, *Nat. Immunol.* **11**, 1005–1013 (2010).
10. D. B. Stetson, J. S. Ko, T. Heidmann, R. Medzhitov, *Cell* **134**, 587–598 (2008).
11. Y. J. Crow *et al.*, *Nat. Genet.* **38**, 917–920 (2006).
12. J. Wu *et al.*, *Science* **339**, 826–830 (2013).
13. L. Sun, J. Wu, F. Du, X. Chen, Z. J. Chen, *Science* **339**, 786–791 (2013).
14. P. Gao *et al.*, *Cell* **153**, 1094–1107 (2013).
15. X. Zhang *et al.*, *Mol. Cell* **51**, 226–235 (2013).
16. E. J. Diner *et al.*, *Cell Rep.* **3**, 1355–1361 (2013).
17. A. Ablasser *et al.*, *Nature* **498**, 380–384 (2013).
18. G. N. Barber, *Immunol. Rev.* **243**, 99–108 (2011).
19. D. E. Levy, J. E. Darnell Jr., *Nat. Rev. Mol. Cell Biol.* **3**, 651–662 (2002).
20. T. Cermak *et al.*, *Nucleic Acids Res.* **39**, e82 (2011).
21. Clone 18 has frameshift mutations in all three chromosomes. In addition to frameshifts, clone 36 harbored a 9–base pair (bp) deletion in one chromosome that removed three amino acids (^{215}MFK^{217}) in the catalytic domain, whereas clone 94 had a 12-bp deletion in one chromosome and an 18-bp deletion in another that removed four (^{214}VMFK^{217}) and six (^{212}FDVMFK^{217}) amino acids in the catalytic domain, respectively. For details, see materials and methods in the supplementary materials.

Acknowledgments: We thank X. Chen for assistance with mass spectrometry. The data presented in this manuscript are tabulated in the main paper and in the supplementary materials. Materials including the cGAS knockout cell lines may be requested upon signing of a materials transfer agreement. This work was supported by NIH grants to Z.J.C. (R01-AI093967) and N.Y. (RO1-AI098569). Z.J.C is an investigator of the Howard Hughes Medical Institute.

Supplementary Materials

www.sciencemag.org/cgi/content/full/science.1240933/DC1
Materials and Methods
Figs. S1 to S7
References

23 May 2013; accepted 29 July 2013
Published online 8 August 2013;
10.1126/science.1240933

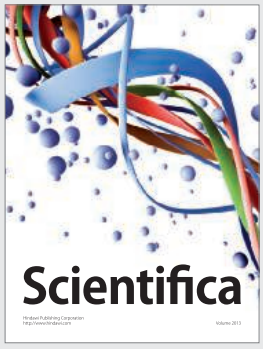










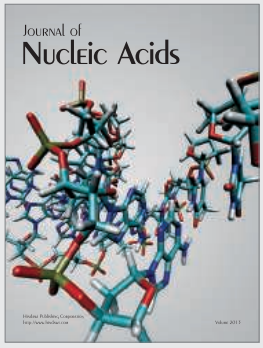




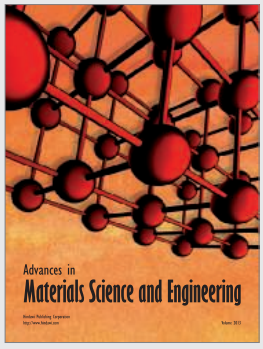


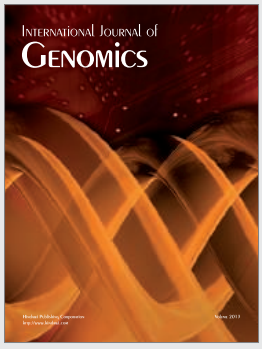
Hindawi

Submit your manuscripts at
http://www.hindawi.com



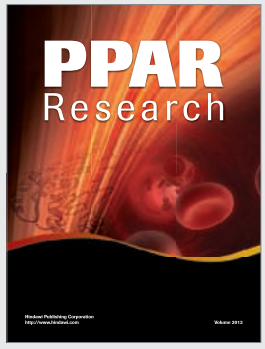


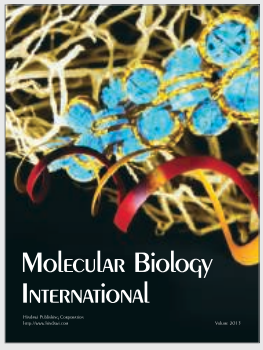


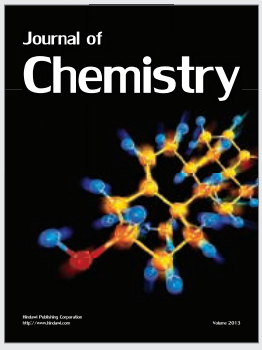


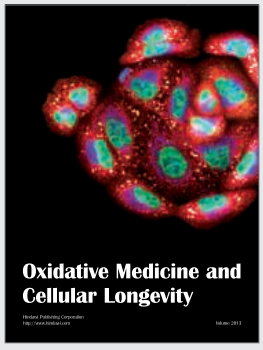


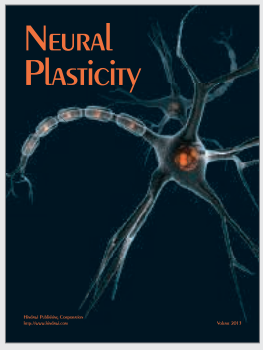


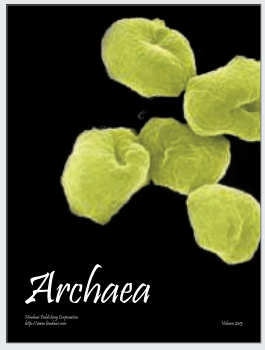














RESEARCH FROM ANYWHERE

START WITH ENDNOTE®

Finally a research tool that is readily available whenever and wherever you need it. Access and manage your *EndNote* library from anywhere, even your iPad, with *EndNoteSync*.

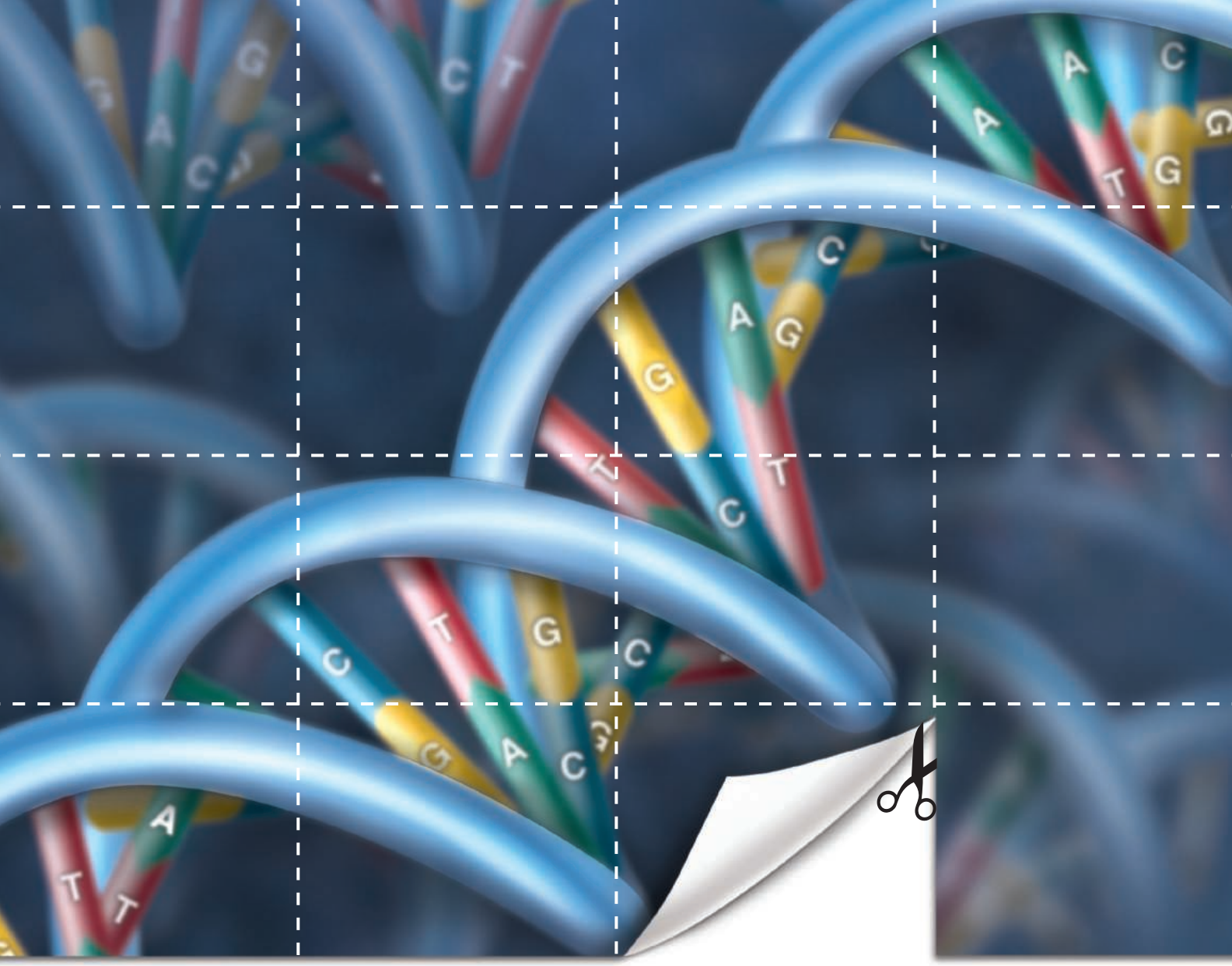
- Find full text for your references in one click.
- Search hundreds of online resources for references and PDFs.
- Watch your references appear as you write with patented *Cite While You Write*® technology.

START AT ENDNOTE.COM

Use Coupon Code: **science13** for exclusive pricing

Available for Windows® and Macintosh®

THOMSON REUTERS™





Cut smarter.

Restriction enzymes from NEB – now with CutSmart™ Buffer

You make smart choices every day. Why stop there? The choice to use restriction enzymes from New England Biolabs is now even easier.

- Choose from > 200 restriction enzymes supplied with a single buffer
- Simplify your double digest reactions
- Reduce your pipetting steps by no longer having to add BSA

Now, that's **Smart!**

Explore the smarter choice at
NEBCutSmart.com

NEW ENGLAND BioLabs® Inc.
enabling technologies in the life sciences



Elevate your PCR research

30 YEARS
PCR DISCOVERY

PCR essentials:

Extraordinarily convenient, high-performing, and innovative end-to-end workflow solutions

Shop PCR essentials at **lifetechnologies.com/elevatepcr**

life technologies™

For Research Use Only. Not for use in diagnostic procedures. © 2013 Life Technologies Corporation. All rights reserved. The trademarks mentioned herein are the property of Life Technologies Corporation and/or its affiliate(s) or their respective owners. CO06514 0713

Introducing the new BD FACSAria™ Fusion

Integrated cell sorting and biosafety.



The fusion of safety, performance, and sorting.

BD

Helping all people live healthy lives

The BD FACSAria™ Fusion cell sorter is built on the solid foundation of patented technologies, exceptional multicolor performance and ease-of-use that was first brought to the world of sorting by the launch of the BD FACSAria™ cell sorter in 2003.

Now this sorting know-how is combined with best-in-class biosafety expertise to create the BD FACSAria Fusion, a fully integrated advanced cell sorter and biosafety solution for research laboratories.

The BD FACSAria Fusion has been verified to meet personnel and product protection standards for a Class II Type A2 biosafety cabinet, the National Sanitation Foundation International Standard 49, the European Standard 12469, and the Australian Standard AS 2252.2–2009.

Choose up to six laser wavelengths and 20 detector positions to measure up to 18 colors simultaneously.

Learn more at **bdbiosciences.com/go/fusion.**

Class 1 Laser Product.
For Research Use Only. Not for use in diagnostic or therapeutic procedures.
BD, BD Logo and all other trademarks are the property of Becton, Dickinson and Company. © 2013 BD
23-15046-01

BD Biosciences
2350 Qume Drive
San Jose, CA 95131
bdbiosciences.com

MEMBRANE PROTEIN INTERACTION DETECTION

Designed to detect novel interaction partners for membrane proteins, the DUALmembrane System can be used to detect pairwise protein interactions, identify novel protein interactions by cDNA library screening, investigate ternary complexes, and map interaction domains. The system is available in both a convenient kit form and as a custom screening service. The DUALmembrane System reliably detects interactions between integral membrane proteins and receptor subunits and co-receptors as well as membrane-associated proteins and soluble proteins. The system is based on the properties of ubiquitin, a small protein modifier that is conserved in all eukaryotes and plays a primary role in protein degradation. The DUALmembrane Kit screens full-length integral membrane proteins for interactions in vivo under the physiological conditions at the membrane, with novel interactions identified through screening of cDNA libraries. The kit also allows easy subcloning of full-length cDNA inserts using *Sfi I* technology.



Dualsystems Biotech

For info: +41-(0)-44-738-50-00 | www.dualsystems.com

HUMAN STEM CELL PLURIPOTENCY

MILLIPLEX MAP Human Stem Cell Pluripotency Magnetic Bead Kits enable the analysis of many different pluripotency biomarkers in a single measurement. The new kits examine protein biomarkers that indicate the potency of stem cells, enabling pluripotent stem cells to be distinguished from multipotent or differentiating cells. These new kits save time and resources by accurately detecting large numbers of pluripotency markers in one measurement. Kits can be used on cultures of induced pluripotent stem cells, human embryonic stem cells, cancer stem cells, or cancer cell lines. Two kits are available for assessing stem cell pluripotency. The MILLIPLEX MAP Human Stem Cell Pluripotency Magnetic Bead Kit 1 monitors the expression of specific transcription factors Oct 3/4, Sox2, Nanog and c-Myc, and the MILLIPLEX MAP Human Stem Cell Pluripotency Magnetic Bead Kit 2 contains seven additional pluripotency-related markers.

EMD Millipore

For info: 800-645-5476 | www.millipore.com

HIGH CONTENT ANALYSIS SOFTWARE

The HCS Studio Software is a suite of high content imaging and analysis applications offering researchers the ability to easily and quickly interact with and analyze cell images and corresponding data. The HCS Studio Software delivers a sophisticated analysis tool with built-in intelligence and enhanced usability to analyze multiple parameters simultaneously. Simple-to-use tools, including icon-driven interfaces, step-by-step workflows and a desktop navigator, enable researchers to gain more knowledge about their cells. The HCS Studio software is the first high-content software to feature an integrated, automated plate handling capability, enabling the Orbitor RS Plate Mover to be used in conjunction with either the ArrayScan XTI High Content Analysis (HCA) Reader or the CellInsight NXT High Content Screening (HCS) Platform. This simple and automated simple plate handling capability delivers the right-sized solution for high-content users who do not need plate scheduling, but rather straightforward movement of plates from stacks to stage.

Thermo Fisher Scientific

For info: 800-874-3723 | www.thermoscientific.com/highcontent

LOW-NOISE DATA ACQUISITION SYSTEM

The next generation Axon Digidata 1550 Low-Noise Data Acquisition System enables the parallel patching of up to eight cells simultaneously to provide better insight of neuronal network function and capture more data points per experiment. This new system extends the precision and quality of the existing Axon Digitizer platform to include a higher sampling rate to monitor rapid responders, combined with enhanced performance in low-noise, high resolution 16-bit data acquisition. The Digidata 1550 Digitizer features eight independent analog output channels to simultaneously send command waveforms to multiple cells at one time, essential for higher throughput toxicology experiments or to study synaptic function in complex neuronal networks. Combined with a sampling rate of up to 500 kHz per channel, the Digidata 1550 Digitizer allows researchers to gather more data points in demanding experiments such as nanopore and bilayer studies.

Molecular Devices

For info: 800-635-5577 | www.moleculardevices.com/digidata

MICROSCOPY DATA ANALYSIS

Focusing on ease of use for routine applications, the latest cellSens software release, version 1.8, offers flexible and user-centric imaging, processing, analysing, and reporting. New and enhanced functions include a fully customizable user interface, precise frame-by-frame sample navigation, and easy one-button switching between wells. For a wide range of life science applications, cellSens provides easy control of the workflow. The software binds together Olympus frames, cameras, and high-quality optics to form complete, highly precise, and user-friendly microscopy systems. The new 'My Functions' window allows users to build their own personal interface by selecting and freely grouping software commands and icons according to individual needs. In addition, the creation of flexible workflow toolbars facilitates repetitive operations. The ability to display only the functions needed on the toolbar and to group common operations in a single tab, enables quick and easy access to the most frequently used tasks while providing a display free from clutter and confusion.

Olympus

For info: +49-40-23773-5913 | www.microscopy.olympus.eu

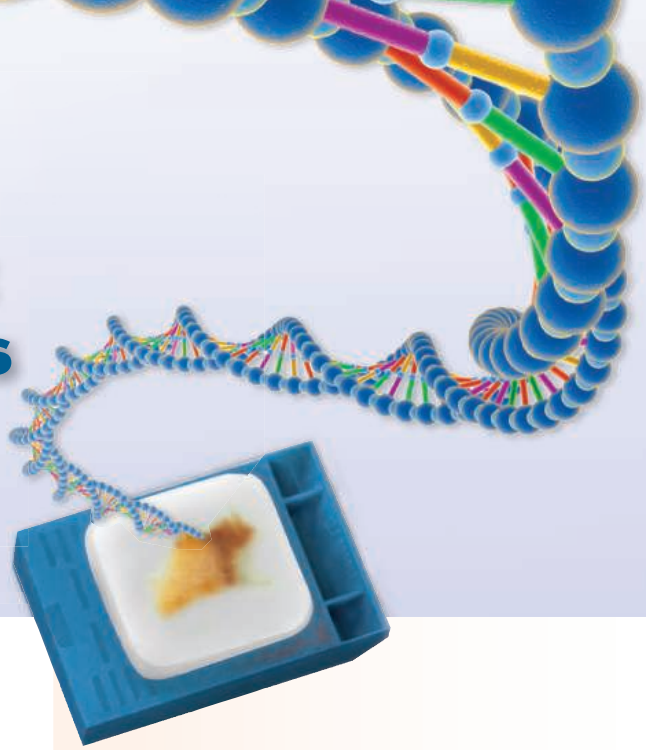
Electronically submit your new product description or product literature information! Go to **www.sciencemag.org/products/newproducts.dtl** for more information.

Newly offered instrumentation, apparatus, and laboratory materials of interest to researchers in all disciplines in academic, industrial, and governmental organizations are featured in this space. Emphasis is given to purpose, chief characteristics, and availability of products and materials. Endorsement by *Science* or AAAS of any products or materials mentioned is not implied. Additional information may be obtained from the manufacturer or supplier.

WEBINAR

Unearthing Hidden Genomic Data in Solid Tumor Samples

Are Your FFPE Samples Revealing All?



Wednesday, September 18, 2013

12 noon Eastern, 9 a.m. Pacific, 5 p.m. UK, 6 p.m. Central Europe

Cancer is a highly complex disease that can encompass multiple genomic alterations in the progression from normal to diseased cell. Recent studies point to the significance of copy number aberrations in the etiology of cancer, with the number and complexity of these aberrations being indicative of overall prognosis. Additionally, the detection and characterization of subclones is also understood to be important for understanding clonal evolution of the cancer and thus patient monitoring and treatment decisions. Genome-wide copy number analysis is a powerful means to understand the genetic basis of solid tumors. With the majority of solid tumors typically stored as formalin-fixed, paraffin-embedded (FFPE) tissue, retrospectively analyzing these samples with available outcome data is a cost-effective route to prognostic and predictive biomarker discovery. Our expert panel will describe their research and discoveries, and how they have overcome the significant challenges of extracting copy number data from often degraded, heterogeneous FFPE samples.

During the webinar, the speakers will:

- Describe how their experimental approaches are expanding our understanding of the genetic basis of solid tumors
- Address some of the technical difficulties of working with FFPE samples
- Discuss the potential implications of their findings in terms of diagnosing, classifying, and treating patients in the future
- Answer your questions live on air!

Webinar sponsored by

affymetrix
Biology for a better world

Speakers



Sarah South, Ph.D.
ARUP Laboratories
Salt Lake City, UT



Torsten Pietsch, M.D.
University of Bonn Medical Center
Bonn, Germany

REGISTER NOW!
webinar.sciencemag.org

Brought to you by the *Science*/AAAS Custom Publishing Office

Science
AAAS

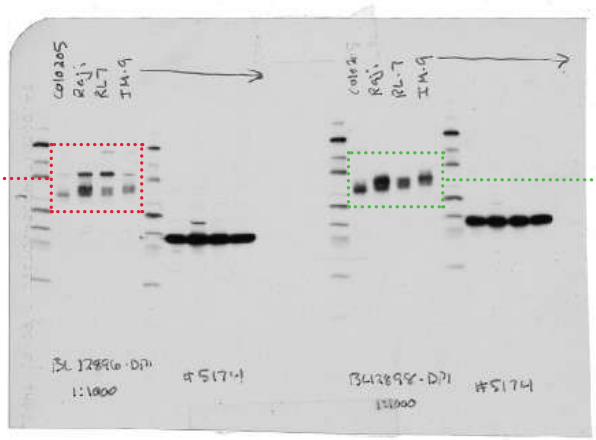
You've carefully designed your experiment.

Taylor Ngo started at CST 8 years ago and is currently in the Molecular Biology group.

Does your antibody measure up?

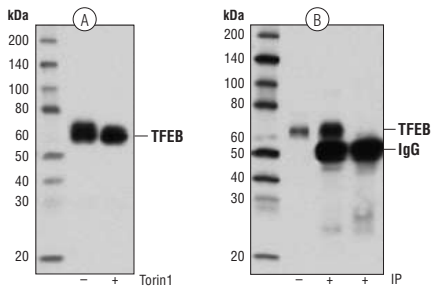
We validate all our antibodies in-house. If it's not specific, it doesn't ship.

REJECTED
Extra Band
Weak Signal



CST APPROVED
Clean Band
Strong Signal

WB analysis of various cell extracts using two development samples at 1:1000 dilution. GAPDH (D16H11) XP® Rabbit mAb #5174 was used as a loading control.



TFEB Antibody #4240: (A) WB analysis of Raji cell extracts, untreated (-) or Torin1-treated, using #4240 (Torin1 treatment induces dephosphorylation). **(B)** IP of TFEB from COLO 205 cells using #4240 (lane 2) or Normal Rabbit IgG #2729 (lane 3). Lane 1 is 10% input.



Please visit our website to request a copy of our new white paper – *A Guide to Successful Western Blotting.*

www.cellsignal.com/successfulWB

Cell Signaling TECHNOLOGY®

© 2013 Cell Signaling Technology, Inc. Cell Signaling Technology® and XP® are trademarks of Cell Signaling Technology, Inc.



Science Careers Advertising

For full advertising details, go to ScienceCareers.org and click For Employers, or call one of our representatives.

Tracy Holmes
Worldwide Associate Director
Science Careers
Phone: +44 (0) 1223 326525

THE AMERICAS
E-mail: advertise@sciencecareers.org
Fax: 202-289-6742

Tina Burks
East Coast/West Coast/South America
Phone: 202-326-6577

Marci Gallun
Midwest/Canada
Phone: 202-326-6582

Candice Nulsen
Corporate
Phone: 202-256-1528

Online Job Posting Questions
Phone: 202-312-6375

EUROPE / INDIA / AUSTRALIA / NEW ZEALAND / REST OF WORLD
E-mail: ads@science-int.co.uk
Fax: +44 (0) 1223 326532

Axel Gesatzki
Phone: +44 (0)1223 326529

Sarah Lelarge
Phone: +44 (0) 1223 326527

Kelly Grace
Phone: +44 (0) 1223 326528

JAPAN
Yuri Kobayashi
Phone: +81-(0)90-9110-1719
E-mail: ykobayas@aaas.org

CHINA / KOREA / SINGAPORE / TAIWAN / THAILAND
Ruolei Wu
Phone: +86-1367-1015-294
E-mail: rwu@aaas.org

All ads submitted for publication must comply with applicable U.S. and non-U.S. laws. *Science* reserves the right to refuse any advertisement at its sole discretion for any reason, including without limitation for offensive language or inappropriate content, and all advertising is subject to publisher approval. *Science* encourages our readers to alert us to any ads that they feel may be discriminatory or offensive.

Science Careers
From the journal *Science* AAAS
ScienceCareers.org

POSITIONS OPEN

POSTDOCTORAL FELLOW POSITIONS
Translational Neuroscience/Optogenetics
University of Pittsburgh

Postdoctoral fellow positions are available in the Ahmari laboratory in the Departments of Psychiatry and Neurobiology at the University of Pittsburgh. The successful candidate(s) will become part of a large, multidisciplinary neuroscience community, and will have ample opportunities for collaboration. These positions are supported by a Burroughs Wellcome Fund Career Award and NIMH grants with goals of discovering the molecular, cellular, and circuit abnormalities underlying OCD and anxiety disorders (see **website: http://www.sciencemag.org/content/340/6137/1234.long**). Projects will require integration of multiple advanced techniques for the analysis and manipulation of neural circuits, including optogenetics, in vivo electrophysiology, in vivo microscopy, viral tract tracing, and rodent behavioral analysis.

The successful candidate(s) should meet the following qualifications: Ph.D. in Neuroscience, Cell Biology/Physiology, Bioengineering, or related field, with a track record of productivity and innovation; Solid background and hands-on experience in optogenetics, electrophysiology, and computational analysis methods is a plus; Experience using genetic and molecular tools to study the nervous system, preferably with behavioral experience in rodents; Creative thinking skills and command of the neuroscience literature; and Ability to work collaboratively with excellent communication skills.

For more information/application please contact **Susanne Ahmari** at **e-mail: sahmari@pitt.edu.** Applications should include curriculum vitae and names/contact information of three professional references.

THE HARVARD MEDICAL SCHOOL

OPPORTUNITIES FOR INFORMATICS
Research at Harvard Medical School

The Biomedical Informatics Research Training (BIRT) Program is a consortium of leading informatics laboratories at Harvard. It is supported by a grant from the National Library of Medicine, National Institutes of Health. For United States citizens and permanent residents, this postdoctoral fellowship provides stipend, tuition, and travel funds. Selected fellows are provided with many opportunities for training, research, interaction, and collaboration. All fellows also pursue the two-year Harvard Medical School Biomedical Informatics MMSc.

The MMSc is a postdoctoral degree program that consists of course work and mentored research. Fellows in our program choose from one of four possible tracks: Clinical Informatics; Population Health Informatics; Imaging Informatics; and Bioinformatics.

To learn more, visit **website: informaticstraining.hms.harvard.edu/.**

In addition to the BIRT program, the Center for Biomedical Informatics (CBMI) offers a number of other training and research opportunities.

For more information about our programs, contact **Katherine Flannery,** Program Manager, CBMI, at **e-mail: katherine_flannery@hms.harvard.edu.**

The Santa Fe Institute's Omidyar **POSTDOCTORAL FELLOWSHIP** offers you transdisciplinary collaboration with leading researchers worldwide, up to three years in residence in Santa Fe, New Mexico. Research and collaboration funds, competitive salary, and generous benefits. A leadership training program and unparalleled intellectual freedom. For details and to apply, please visit our **website: http://www.santafe.edu/ofellowship.**

POSITIONS OPEN

Yale University School of Medicine

POSTDOCTORAL or **RESEARCH ASSOCIATE:** Cell Biology. Position available in the laboratory of **Dr. Stephen G. Waxman** at the Department of Neurology and the Center for Neuroscience and Regeneration Research, Yale University School of Medicine.

Superb opportunity to join a multidisciplinary research group to study the pathophysiology of axonal degeneration and the cellular and molecular mechanisms that mediate pain and axonal degeneration after injury, with focused attention on the contributions of sodium channels. Ongoing work utilizes in vitro and in vivo models of axonal injury.

Candidates should have a strong publication record and intensive training in general molecular and cell biology methods, quantitative morphometric analysis, and cellular imaging techniques.

More information can be found on Yale **website: http://medicine.yale.edu/cnrr/index.aspx**.

Applicants should send curriculum vitae and a list of references to **e-mail: stephen.waxman@yale.edu.**

SIE FOUNDATION POSTDOCTORAL FELLOWSHIP

The University of Colorado-Boulder, the BioFrontiers Institute, and the Linda Crnic Institute for Down Syndrome seek courageous and innovative postdoctoral fellows to ameliorate cognitive, cardiovascular, neurodegenerative or other ill effects of trisomy 21 in affected children. Possible approaches include working with people with Down syndrome, mouse or other animal models of Down syndrome, or cell lines trisomic for chromosome 21. This should be considered an opportunity to apply modern techniques, such as next generation sequencing, induced pluripotent stem cells, or advanced techniques in proteomics, to aid in understanding a very complex syndrome coming from a known but poorly understood genetic alteration, an extra copy of the smallest human chromosome.

Sie Fellows may work in any laboratory on the Boulder campus, and will interact with the entire Boulder bioscience community and with **Dr. Tom Blumenthal** and colleagues at the Crnic Institute at the CU Anschutz Medical Campus in Denver. Sie Fellows will be awarded salaries of $55,000 to $70,000, depending on field, experience, and qualifications, as well as substantial research budgets, and will be encouraged to take the project with them when they start their independent faculty positions.

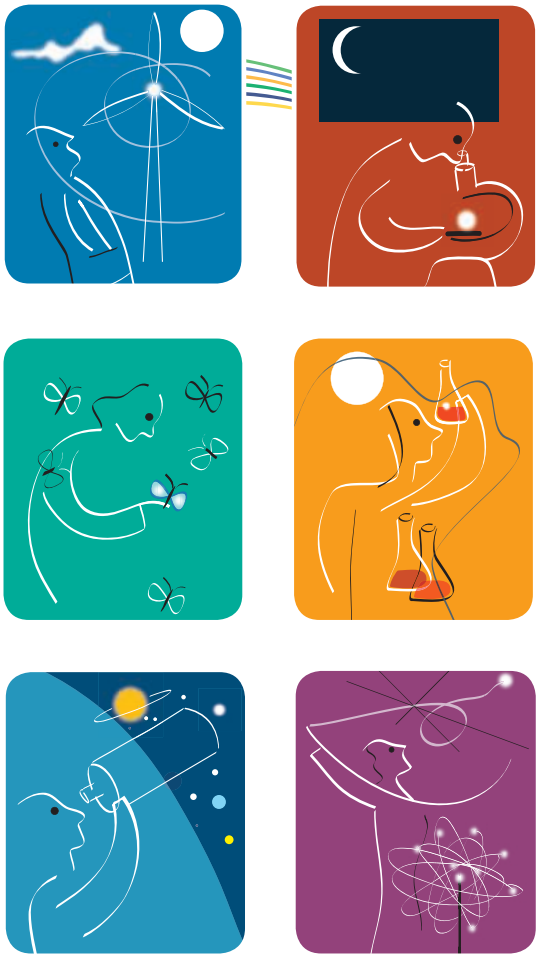
Applicants should have a Ph.D. and/or M.D. degree and no more than three years of prior postdoctoral experience. Applications should include curriculum vitae and a letter describing their interest in Down syndrome research. Applicants should send these materials to **Cait Mobley** (**e-mail: caitlin.mobley@ucdenver.edu**) and should have three letters of recommendation sent directly to the same address.

Help employers find you. Post your resume/cv.

Science Careers
From the journal *Science* AAAS

www.ScienceCareers.org

Postdoc and research **opportunities** in Brazil



About us

Fifty percent of all science created in Brazil is produced in the State of São Paulo. The state hosts three of the most important Latin American universities: USP, UNICAMP and UNESP. Other universities and 19 research institutes are also located in São Paulo, among them the renowned Instituto Tecnológico de Aeronáutica (ITA), Instituto Nacional de Pesquisas Espaciais (INPE) and Laboratório Nacional de Luz Síncrotron, besides most of Brazilian Industrial P&D.

The São Paulo Research Foundation (FAPESP), one of the leading Brazilian agencies dedicated to the support of research, has ongoing programs and support mechanisms to bring researchers from abroad to excellence centers in São Paulo.

The **Young Investigators Awards** is part of FAPESP's strategy to strengthen the State research institutions, favoring the creation of new research groups. See more about it at www.fapesp.br/yia.

FAPESP **Post-Doctoral Fellowship** is aimed at distinguished researchers with a recent doctorate degree and a successful research track record. The fellowship enables the development of research within higher education and research institutions in São Paulo. Postdoc fellowships are available when calls for applications are issued internationally, or as individual fellowships requested on demand.

In the first case, positions are advertised at www.fapesp.br/oportunidades/ and candidates are selected through international competition. In the second, the proposal must represent an addition to a pre-existent research group and should be developed in association with faculty in higher education and research institutions in São Paulo. More information at www.fapesp.br/en/postdoc.

Location: São Paulo, SP, Brazil

Primary Contact Details:
Rua Pio XI, 1500 – Alto da Lapa
05468-901
São Paulo, SP – Brazil
Phone: +55-11-3838-4224
URL: www.fapesp.br

FAPESP 50 YEARS

FAPESP
SÃO PAULO RESEARCH FOUNDATION

POSTDOCTORAL OPPORTUNITIES
Science Careers online @sciencecareers.org

POSTDOC ADVANCEMENT:
MARKETING YOUR VALUE

The postdoctoral appointment is not only a time of exploration and hard work, but also a time to learn and hone critical skills that will enable you to move into a position of independent research. Skills such as leadership and management, teambuilding, communication, fundraising, and even marketing are required to advance, and one must be adept in all of these areas to succeed in this highly competitive economic landscape. There are multiple opportunities for postdocs to not only gain these necessary abilities, but also demonstrate them to current and future employers. The key is keeping a watchful eye out for chances to learn and sharpen your talents and to articulate your value to decision-makers. **By Alaina G. Levine**



fundraising
teambuilding
marketing
management
communication
leadership



Aydin Farajidavar

"You need to be focused on the science, but you also have to have a career perspective in mind. You need to know where you want to go."
—Zoe Cournia

Zoe Cournia is a Greek chemist who received advanced training abroad and desired to return to her home nation for permanent employment as a researcher. After graduating with her Bachelor's degree in chemistry from the University of Athens, she pursued her Ph.D. at Heidelberg University, Germany and postdoctoral training at Yale University in New Haven, Connecticut. To stay connected to her country's academic community while away, she corresponded with her undergraduate mentors and asked for introductions to other scientists. Whenever she came home on holiday, she volunteered to give research talks at her alma mater and elsewhere. Pretty soon, she was receiving invitations from universities across the nation to give seminars. "I may have left the country physically, but I never left the Greek academic system," she says. After five years of notable research which included publishing, presenting, and mentoring combined with connecting with colleagues and lecturing activities in Greece, Cournia landed a job as an investigator (lecturer) in pharmacology and pharmacotechnology at the Biomedical Research Foundation Academy of Athens, Greece.

"You need to be focused on the science, but you also have to have a career perspective in mind," she says. "You need to know where you want to go." A career plan is an important element of any scientist's path, but there must be other aspects associated with it, in addition to significant scientific outputs, especially during these troubled economic times. In Cournia's case, while continuing her research, she also gained skills in project and grant management, networking, marketing, and independent leadership that ultimately helped her obtain the position at the academy.

For every postdoc pining for a professorship, a good rule to follow is to use your current appointment to find and leverage opportunities that will make you extremely attractive to potential employers. Specifically, you have to learn and hone certain skills that hiring committees look for when recruiting talent. It may not always be easy to chip away time in your day to become a better communicator or to solidify your fundraising expertise, but it is necessary to gain a competitive advantage.

Leadership and Management

Becoming a thoughtful, results-oriented leader doesn't happen overnight. "Managing human capital is very difficult," says **Aydin Farajidavar,** assistant professor of electrical and computer engineering at New York Institute of Technology (NYIT). As a postdoc at Georgia Institute of Technology, he was thrust into a position where he had to supervise students in their research group. "The first time I complained to my PI, he said 'welcome to the club!'" But Farajidavar realized the opportunity was precious because it gave him his first chance to really lead the team, something which he knows has helped him succeed in academia.

"As a postdoc, you are seen as a senior member of the group and may be called upon to make a decision or speak up," says **Natalie Lundsteen,** assistant director, Graduate Student Career Services at the Massachusetts Institute of Technology (MIT) Global Education & Career Development. You can leverage this opportunity to strengthen your leadership talents. "Ask your lab continued>

Upcoming Features

Faculty—September 13
Top Employers Survey—October 25
Neuroscience Careers—November 1

CREDIT: (TOP) © ISTOCKPHOTO.COM/ KHALUS; (RIGHT) AYDIN FARAJIDAVAR, DIRECTOR OF IMS LABORATORY AT NYIT, OLD WESTBURY, NY.



Postdoctoral Fellowships in Genomic Biology
at the University of Illinois at Urbana-Champaign

The Institute for Genomic Biology at the University of Illinois at Urbana-Champaign offers a number of fellowships for truly exceptional young scholars who have completed their Ph.D. within the last several years, and are looking for a stimulating and supportive interdisciplinary environment to carry out independent and collaborative research in the field of genomic biology. IGB Fellows will typically spend two years conducting research in one of several research themes in the Institute, and ideally this research will also overlap with two or more of these thematic areas. A personalized mentoring plan will be developed for each Fellow. Visit www.igb.illinois.edu/content/fellows-application for more information about the Institute, the research themes and the application procedures. Annual salary is $50,000. The closing date for all positions is December 1, 2013. Fellows will be announced on or about January 15, 2014.

Biocomplexity
We seek a postdoc with a strong quantitative background to join a multidisciplinary group exploring collective effects in biology from the genome to the ecosystem scale. Ongoing research addresses the emergence of life and the nature of evolution prior to the Last Universal Common Ancestor, the evolution of core cellular machinery in Archaea and other domains of life, the role of horizontal gene transfer in shaping communities of microbes and phages, geomicrobiology, and the systems biology of microbes, biofilms and ecosystems. We are also developing an interest in evolutionary medicine, with special interest in combating the emergence of antibiotic resistance.
(Nigel Goldenfeld, Theme Leader)

Cellular Decision Making in Cancer
We seek an individual with interest in quantitative biology. Our theme faculty members have expertise in single molecule biophysics, genomics and chemical biology. Building on the current strengths on cell death, antiviral signaling, stem cell differentiation, live cell probing of decision making and genome instability modeling, we aim to develop a multiple-scale narrative on how single molecule events in the cell are integrated into the protein networks to determine the cell fate. Cancer is a major focus area of research. (Taekjip Ha, Theme Leader)

Energy Biosciences Institute
The Energy Biosciences Institute (EBI) is an externally funded theme within the IGB. It is the largest industry/academia collaboration to date, currently receiving $500 million over ten years and focusing on the development of second-generation biofuels intended to significantly slow the rate of global climate change. Its research ranges from systems biology of fermentative organisms to quantification of ecosystem services provided by new sustainable biofuel crops. Other areas include development of enzymes of efficient plant biomass depolymerization, biofuel law and social and economic impacts. The EBI also has an interest in geomicrobial approaches to increasing the efficiency of oil extraction. The full range of research can be seen at www.energybiosciences-institute.org. We seek an outstanding candidate across these areas interested in applying genomic biology to understanding and developing opportunities for improving sustainable biofuel production. Research can be at any point in the supply chain from improving feedstocks and their environmental sustainability to producing fuel. The appointee will work in an interdisciplinary laboratory of over 100 exceptional colleagues focused on this challenge. The appointment would also involve collaboration with our partners: UC Berkeley, Lawrence Berkeley National Lab, and BP. (Isaac Cann, Theme Leader)

Genomic Ecology of Global Change
The Fellow will be involved in a cross-disciplinary project investigating how changes in networks of genes affect plant and ecosystem function when challenged by elements of global change, including greater carbon dioxide, ozone, drought, temperature, disease and herbivory. The ideal candidate will have a strong background in plant biology and a record of expertise in molecular biology, genomic ecology, physiology or modeling of gene networks or ecosystem function. The ability to work creatively and productively in a highly interdisciplinary and collaborative environment is essential. (Don Ort, Theme Leader)

Gene Networks in Neural & Developmental Plasticity
We seek a biologist with strong bioinformatics skills and training in one or more of the following areas: gene regulation (especially relating to transcription factor dynamics or epigenomics), evolutionary biology, neuroscience, or systems biology. Applicants with expertise in both experimental biology and bioinformatics will be strongly preferred. The successful candidate will join a multidisciplinary team using systems biology approaches to analyze regulatory mechanisms underlying complex developmental and behavioral phenotypes, and components that may define determinants of inter- and intraspecies diversity. Fellows are expected to conduct research that contributes to the development of theme goals by integrating components from multiple theme members' areas of expertise. (Lisa Stubbs, Theme Leader)

Mining Microbial Genomes
The Fellow will be involved in one of several multidisciplinary projects focused on (1) the discovery, design, and development of novel antibiotics, or (2) the assignment of function to novel enzymes discovered in genome projects. The ideal candidate will have a proven record of expertise in microbially produced natural products and/or enzyme evolution. We are interested in candidates with previous experience in bacterial metabolism, bacterial genetics, molecular biology, biochemistry, enzyme evolution, metabolic engineering, organic synthesis, mass spectroscopy, bioinformatics and/or metagenomics.
(Bill Metcalf, Theme Leader)

Regenerative Biology & Tissue Engineering
The Fellow will be involved in one or more of our multidisciplinary projects related to regenerative biology and harnessing the potential of adult/embryonic stem cells for tissue engineering applications. Of particular interest is leveraging theme expertise in biomaterials fabrication, drug delivery systems, microfluidics-based *in vitro* experimental platforms, and *in vivo* evolutionary biology and regeneration medicine studies. The ideal candidate will have experience in one or more areas of (stem) cell biology, induced pluripotent cell technology, biomaterials, microfluidics, and/or tissue engineering.
(Paul Kenis, Theme Leader)

Synthetic Biology
The Fellow will be involved in one of several multidisciplinary projects focused on the development and application of synthetic biology tools to address challenging problems related to human health and sustainability. The ideal candidate will have a proven record of expertise in synthetic biology, metabolic engineering, protein engineering, mass spectroscopy, laboratory automation, computer aided design, bioinformatics, and plant genetic engineering.
(Huimin Zhao, Theme Leader)

The University of Illinois is an Affirmative Action/ Equal Opportunity Employer
www.igb.illinois.edu

Science Careers online @sciencecareers.org
POSTDOCTORAL OPPORTUNITIES


Yvonne Klaue

advisor if you can take over a project or oversee students," she suggests.

This is exactly what **Yvonne Klaue** did during her postdoc at the University of California, Irvine. When her PI announced he was taking a sabbatical for a year, she offered to run the lab in his absence. Klaue organized regular meetings of the research group, supervised the junior members to ensure they were meeting the lab's mission and goals, handled group communications with other faculty, and even oversaw inventory and budgeting. "No one ever told me how to manage a lab," she says. "I was thrown into it."

As you look for opportunities to reinforce your management experience, recognize that leadership is not limited to managing people and projects. A great leader is one who has vision and the ability to implement that vision with success. Cournia was able to gain and demonstrate this kind of leadership drive by creating a funding source for postdocs to travel to conferences while at Yale. At the time, there was no institutional financial support for non-U.S. citizen postdocs to present at scientific meetings. On her own accord, Cournia approached the Office for Postdoctoral Affairs and helped launch a committee to write a grant proposal to the provost to support the endeavor. The committee ended up raising $20,000 that year and the travel fund became a permanent part of the Yale budget. "There are ways you can demonstrate your leadership potential, your potential to be a doer, and that you are really committed to your career," she urges. "This was essential to my career so I could travel to conferences, so I did it. As an independent researcher, you need to show you can be tough and decisive and that you can take the next step to go forward and be proactive."

There are other opportunities to be found on your campus that can aid you in your career, says **Leslie Beckman,** senior coordinator of special programs in the Office of Postdoctoral Affairs at the University of Texas Health Science Center at Houston (UTHealth). Consider serving on high-profile committees, like the postdoctoral association, or taking on interdisciplinary or even interinstitutional projects that allow you to be seen as a leader. Furthermore, teaching and informal mentoring can also provide you with critical leadership skills.

Teambuilding

As a postdoc, your research group may seem like a functioning team environment. But more often than not, "work is partitioned off into silos but the staff doesn't have to deeply collaborate or rely on team members for success," says **Steven Casper,** Henry E. Riggs Professor of Management and associate dean for faculty development of the Keck Graduate Institute of Applied Life Sciences (KGI). But to transition into a research career where you are the leader, you must have abilities that show you know how to effectively collaborate on and build a winning team. Casper recommends pursuing an internship or a short-term volunteer project in your university "where you have to rely on a division of labor to reach goals," he says. You might consider joining a team through the institution's entrepreneurship program, where students work on business plans and appreciate a postdoc's technical expertise. "Go outside the 'all science zone' and work with highly intelligent people who are in other disciplines than your own," he advises.

Networking plays an important role in building a unit that can accomplish a goal. **Michelle Fennessy,** a postdoctoral fellow in nursing at the University of California, Davis, works at the crossroads of data management, administration, and safety in hospital environments. She realized that to accomplish her research and acquire funding, she would need a multidisciplinary lineup with major credentials behind her. So she actively recruited thought leaders in the field. It took her six months of networking through conferences and leveraging contacts to assemble her dream team, but it was worth it on so many levels, she says. "As a junior investigator, it is important to surround yourself with experts in the field to help mentor you through the process," she notes.

Communication

"Everything we do as faculty requires communication skills," stresses **Wendi Heinzelman,** dean of graduate studies and professor of electrical and computer engineering at the University of Rochester. "You can have the greatest idea but if you don't know how to explain it, it will fall flat on its face."

> **"Everything we do as faculty requires communication skills. You can have the greatest idea but if you don't know how to explain it, it will fall flat on its face."**
> **—Wendi Heinzelman**

The ability to convince others of the importance of your work and why they should engage you, either as an employer, research partner, funder, or mentor, is paramount. You should seek as many opportunities as possible to practice these skills. Start small where the stakes are low, says Lundsteen. Begin by giving a talk in your research group, then move on to a journal group, the department, your postdoc association, and then to a conference. Volunteer to speak in another department besides your own, says **Michael Hadjiargyrou,** chair of life sciences at NYIT. "It forces you to put together a presentation that's targeted for a specific audience," which is vital given that when you interview for an academic job, you may have to give a talk for scientists outside your realm of research or in another department altogether. Hadjiargyrou also recommends seeking out opportunities to address lay people.

Funding

A demonstrated record of finding and acquiring funding is crucial to landing a job in academia, where "you don't just get handed a sack of money," jokes Lundsteen. Working on a grant project signals to the prospective employer that "you are cognizant of the funding and where it comes from," she adds.

So naturally, as a postdoc you should consider applying for grants. Cournia wrote 20 applications and received funding from three. Her hard work and success established to her perspective continued>

CREDIT: COURTESY OF KECK GRADUATE INSTITUTE

Roche Postdoctoral Fellowships (RPFs) in Pharma Research and Early Development

Who we are

At Roche, 82,000 people across 150 countries are pushing back the frontiers of healthcare. Working together, we've become one of the world's leading research focused healthcare groups. Our success is built on innovation, curiosity and diversity, and on seeing each other's differences as an advantage. To innovate healthcare, Roche has ambitious plans to keep learning and growing – and is seeking people who have the same goals for themselves.

The RPF program supports outstanding young scientists focusing on cooperative R&D projects between Roche and international academic institutions. As an RPF, you will receive scientific mentoring from both Roche and its academic partners, and gain valuable research experience from both academic and industrial perspectives. We have currently several Postdoc positions open in the area of Neuroscience, Immunology, Non-clinical safety, and Metabolic Diseases within our Pharma Research and Early Development (pRED) department:

- **Postdoctoral Fellow – Tumor immunology** (Schlieren/Zurich, Switzerland)
- **Postdoctoral Fellow – Resolution of inflammation in metabolic diseases** (Basel, Switzerland & Dublin, Ireland)
- **Postdoctoral Fellow – Intracellular sorting of biotherapeutics at the blood-brain barrier** (Basel, Switzerland & Strasbourg, France)
- **Postdoctoral Fellow – Islet endothelial cell research** (Basel, Switzerland & Dusseldorf, Germany)
- **Postdoctoral Fellow – Evaluation of peptide immunogenicity** (Basel, Switzerland & Penzberg, Germany)
- **Postdoctoral Fellow – Label-Free biomolecular interaction analysis applied to cell cultures** (ETH Zurich, Switzerland)

These positions are sponsored by the Roche Postdoctoral Fellowship program and are initially limited to two years.

Who you are

You're someone who wants to influence your own development. You're looking for a company where you have the opportunity to pursue your interests across functions and geographies, and where a job title is not considered the final definition of who you are, but the starting point.

You have:

- a PhD degree obtained no more than 4 years ago
- research experience in the relevant field with proven track record in the research area
- competency of both, team and independent work, interest in working in a multidisciplinary and multinational environment, fluency in English is required

The next step is yours. To apply online visit www.careers.roche.ch. Please include a CV, a motivation letter and references in your application.

Roche is an Equal Opportunity Employer



Featured Participants

Biomedical Research Foundation Academy of Athens
www.bioacademy.gr

Georgia Institute of Technology
www.gatech.edu

Heidelberg University
www.uni-heidelberg.de/index_e.html

Jet Propulsion Laboratory, California Institute of Technology
www.jpl.nasa.gov

Keck Graduate Institute of Applied Life Sciences (KGI)
www.kgi.edu

Massachusetts Institute of Technology (MIT)
www.mit.edu

New York Institute of Technology (NYIT)
www.nyit.edu

The University of Texas Health Science Center at Houston (UTHealth)
www.uthouston.edu

University of Athens
en.uoa.gr

University of California, Davis
www.ucdavis.edu

University of California, Irvine
www.uci.edu

University of Rochester
www.rochester.edu

Yale University
www.yale.edu

employer that she knew how to manage grants, write reports, and oversee budgets.

Yet "even if you don't get the grant, it is a very useful experience," says Hadjiargyrou. "Grant writing is an art and it takes a long time to hone this skill." Farajidavar secured priceless advice about grant funding practices from his PI, who had served on review panels for several national agencies. "He knew the criteria for scoring," he says, "and he shared his experiences and read my proposals and helped edit them." Farajidavar also asked his advisor if he could accompany him to an NSF workshop to learn the ins and outs of grant writing and meet the program officers. As a postdoc, he applied for five proposals in one year and, although none were funded, he learned another valuable lesson—you can call the program officer and inquire why your application was not selected. The information they provided was an essential factor for his next proposal getting funded.

Approach your advisor about writing a grant and if they don't support it, find another mentor who will, advises Hadjiargyrou. And you don't just have to apply for large-scale grants—consider pursuing small pockets of money that may exist in your department or through the postdoc affairs division of your institution.

Furthermore, as the economics of funding changes, it's in a faculty member's best interest to become savvy in other areas of financial support besides grant writing. As part of its communications training, UTHealth offers postdocs insight into fundraising and philanthropy, and lessons about communicating scientific results to a community of potential donors. "You will be interacting with these people in your careers," says Beckman, so it is important to know why people and private foundations donate money to science and how to partner with them to advance your own research mission.



Serina Diniega

"I sold myself as an applied mathematician who could solve any problem."
— Serina Diniega

Marketing Your Value

One of the best marketing tactics you can employ is adopting a niche and incorporating it into your career strategy. As Cournia contemplated returning to her home nation, she researched how her subfield of computer-aided drug design would fit in with the strategic initiatives of Greek institutions. And since there were very few Greek scientists with this expertise, she believed she could add value to the growing academic efforts in the pharmaceutical sector in the country. "A new field was starting in Greece—drug design—and there were not a lot of scientists who had been abroad and had been doing the specialized job that I was doing," she says. "You need to have a long-term plan and know where you want to be and what you want to be in the next 10 years, and create your niche accordingly."

Finding that niche in which to best market your value is absolutely essential. **Serina Diniega,** a mathematician who works for NASA's Jet Propulsion Laboratory (JPL), recognized this and put the concept into action. In the universe of planetary science, most researchers have geophysics or astronomy degrees. But with a strong desire to work in this field, Diniega realized that she could use her applied mathematics background as a competitive advantage. "I sold myself as an applied mathematician who could solve any problem," she says. Her postdoc centered around lava flow modeling, and even though she had "absolutely no experience with lava," she got the job because she pitched herself as an expert in modeling, which could be applied to multiple systems.

Getting Hired

Ultimately, when someone hires you, they need to know you will contribute value in all ways to the research group, department, and organization. "You have to demonstrate that you are a good playing card for the institution," stresses **Rodrigo Morales,** assistant professor of neurology at UTHealth, which includes having a positive attitude, and experience in leadership, fundraising, and communications. But, experts agree, having all of these abilities means absolutely nothing to potential employers if you don't have the solid scientific foundation on which to build upon them in the first place. "All of these other skills are important to get hired, but the most important thing is always to do good science," affirms Cournia.

Alaina G. Levine is a science writer and science careers consultant/speaker in Tucson, AZ.

DOI: 10.1126/science.opms.r1300135

CREDIT: PHOTO, SERINA DINIEGA

Call for Fellowship Applications

Postdocs Applying Climate Expertise (PACE)
Grow the pool of scientists qualified to work at the interface between climate science and its applications
Deadline 3 January 2014

Jack Eddy Postdoctoral Fellowship Program
Train the next generation of researchers needed for the emerging field of Heliophysics
Deadline 17 January 2014

NOAA Climate & Global Change Postdoctoral Fellowship Program
Create and train the next generation of researchers needed for climate studies
Deadline 10 January 2014

Experienced scientists at U.S. universities and research institutions host fellows and provide mentoring and a collaborative environment for the postdocs to carry out their research projects in an area of mutual interest.

Fellows are UCAR employees and receive a fixed annual salary plus UCAR's benefits (health and dental insurance, paid time off, paid holidays, TIAA/CREF retirement fund, and life insurance). Allowances are provided for relocation and scientific travel during the appointment.

Please visit the UCAR Visiting Scientist Programs website for detailed information on these programs, benefits details and application requirements at:

www.vsp.ucar.edu or call 303-497-8649.

VSP UCAR Visiting Scientist Programs

HSCRB
harvard department of stem cell & regenerative biology

Department of Stem Cell and Regenerative Biology (HSCRB) Harvard University

POSTDOCTORAL FELLOWSHIPS

The Department of Stem Cell and Regenerative Biology is actively seeking postdoctoral fellows in a wide variety of fields within stem cell and regenerative biology. Some appointments are funded through research grants awarded to Faculty members and are ordinarily for one year, sometimes renewable; other appointments are possible through individual postdoctoral fellowships.

For information on these research opportunities, application instructions, and the list of Faculty members with current openings, please visit the HSCRB website: **http://www.hscrb.harvard.edu**.

Harvard University is an Equal Opportunity/Affirmative Action Employer.

The Jackson Laboratory
Leading the search for tomorrow's cures

JAX Postdoctoral Scholars Program

Conduct research at a renowned genetics institution

Competitive base salary ($50k) and independent funds

Forge new paths in interdisciplinary biology

jax.org/scholars





Be Nominated

← *Start Here!*

(or at the address above if you prefer.)

Our Next Breakthrough **IS YOU.** Lawrence Postdoctoral Fellowship

The Lawrence Livermore National Laboratory (LLNL) has openings available under its Lawrence Fellowship Program. This is a highly desirable postdoctoral position that provides freedom to conduct independent, cutting-edge research, directed by the candidate, in an area of the candidate's choice. The duration of the Fellowship is up to three years. Typically two to four openings are available each year. Fellowships are awarded only to candidates with exceptional talent, credentials and a track record of research accomplishments.

Successful candidates will propose and subsequently conduct original research in one or more aspects of science relevant to the mission and goals of LLNL. Possible scientific areas include: Physics, Applied Mathematics, Computer Science, Chemistry, Material Science, Engineering, Environmental Science, Atmospheric Science, Geology, Energy, Lasers and Biology. Lawrence Fellows may participate in experimental or theoretical work at LLNL and will have access to LLNL's extensive computing facilities and specialized laboratory facilities. A senior scientist will be matched to the Fellow to serve as a collaborator and mentor. The candidates will receive full management and administrative support. The salary is $8,500/mo.

Please refer to the following web page **http://apptrkr.com/377790** and refer to job #11675 for eligibility requirements and instructions on how to apply. When applying and prompted, please mention where you saw this ad. The deadline for applications is November 1, 2013. LLNL is operated by the Lawrence Livermore National Security, LLC for the U.S. Department of Energy, National Nuclear Security Administration. We are an equal opportunity employer with a commitment to workforce diversity.

Lawrence Livermore National Laboratory

http://fellowship.llnl.gov

Post-doctoral opportunities in Systems Medicine and Bioinformatics at Stanford University

The laboratory of Dr. Atul Butte at Stanford Medical School is seeking highly motivated investigators to develop and study novel approaches in data-driven biomedical research to discover new biomarkers, therapeutics, and to revolutionize health and health-care. Post-doctoral fellowships are fully funded for at least 2 years.

Ideal candidates will have an M.D. and/or Ph.D. with a strong background in bioinformatics, computational biology, biostatistics, and genomics, excellent communication and programming skills, and a great publication record.

Strong problem-solving skills, creative thinking, and the ability to build new software tools as needed are required. A dual background in both computation and molecular biology or medicine or pharmacology will be a strong plus. Prior experience with genetic, microarray, drug, or clinical databases, text-mining, knowledge representation, or parallel computing platforms is a plus. Applicants must possess good communication skills and be fluent in both spoken and written English.

This exciting work will be guided by multidisciplinary collaborations with top scientists in stem-cell, immunology, diabetes, and cancer biology research at Stanford.

To apply, please send your CV, a brief statement of research interests, and contact information for three references. **Contact: Susan Aptekar**; **E-mail: butte-lab-jobs@lists.stanford.edu**

Weill Cornell Medical College

Faculty and Postdoctoral Positions in Molecular Imaging Innovations Institute

The Molecular Imaging Innovations Institute (MI^3) in the Department of Radiology at Weill Cornell Medical College is seeking highly motivated applicants to join newly established institute which will be located in the brand new state-of-the-art Belfer Research Building. MI^3 is committed to becoming an internationally recognized institute of excellence in discovery and development of new molecular imaging agents, and strategies for use in basic and translational research as well as in clinical care. Scientists will have access to on-site imaging systems for animal and human studies, including MRI, PET, SPECT, CT, optical and ultrasound.

Faculty positions: Experienced scientists with PhD and/or MD in developing multimodality imaging strategies are encouraged to apply. Junior candidates must have at least three years of postdoctoral experience, publications in high impact journals, and the demonstrated ability or potential to acquire external research funding. Senior positions will be considered commensurate with experience and track record of extramural funding and publications.

Postdoctoral Associate positions: MI^3 seeks both chemists and biologists who are creative, motivated, and enjoy working independently as well as in a collaborative environment. Research experience in peptide, liposome, nanotechnology, radiochemistry, organic chemistry, fluorescence chemistry, photodynamic therapy, drug delivery, immunology, stem cells or animal models are preferred, although other areas may also be considered. Applicants must have a doctoral degree, possess excellent oral and writing skills, and be fluent in English.

Qualified applicants should respond by sending or emailing a letter of interest, including: research interests, CV, and three references to: **Dr. Ching Tung, Director of Molecular Imaging Innovations Institute, Department of Radiology, Weill Cornell Medical College, 525 East 68th Street, Box 141, New York, NY 10065-4870**; Email at **MI3@med.cornell.edu**.

Weill Cornell Medical College is an Equal Opportunity Educator and Employer.

Argonne NATIONAL LABORATORY

The Argonne Named Postdoctoral Fellowship Program

Argonne National Laboratory is accepting applications for the 2014 Named Postdoctoral Fellowship. Argonne awards these special postdoctoral fellowships internationally on an annual basis to outstanding doctoral-level scientists and engineers who are at early points in promising careers. The fellowships are named after scientific and technical luminaries who have been associated with Argonne and its predecessors, and the University of Chicago, since the 1940's.

Candidates for these fellowships must display superb ability in scientific or engineering research, and must show definite promise of becoming outstanding leaders in the research they pursue. Fellowships are awarded annually and may be renewed up to three years. The 2014 fellowship carries a stipend of $80,000 per annum with an additional allocation of up to $20,000 per annum for research support and travel. The deadline for submission of application materials is **October 15, 2013**.

Applicants should identify an Argonne staff member to sponsor the nomination. The sponsor could be someone who is already familiar with your research work and accomplishments through previous collaborations or professional societies. If you have not yet identified an Argonne sponsor, visit the detailed websites of the various Research Programs and Research Divisions at **www.anl.gov**.

Applications must be submitted online through: **www.anl.gov/careers**. Correspondence and supporting letters of recommendation should be submitted to **Named-Postdoc@anl.gov**.

For more information visit the Argonne Postdoc Blog at **blogs.anl.gov/postdoc** or contact Postdoc Program Coordinator, **Kristene Henne**, at **khenne@anl.gov**.

Argonne is an Equal Opportunity Employer and we value diversity in our workforce. Argonne is a U.S. Department of Energy laboratory managed by UChicago Argonne, LLC.

WWW.NIH.GOV
Positions @ NIH
THE NATIONAL INSTITUTES OF HEALTH

The NIH Intramural Research Program is Recruiting Tenure-Track "Earl Stadtman Investigators"

The National Institutes of Health, the U.S. government's premier biomedical and behavioral research enterprise, is pleased to announce its fifth annual call for "NIH Earl Stadtman Investigators," a broad recruitment of tenure-track investigators for all NIH intramural programs. Scientific discoveries from our intramural laboratories, with their extensive infrastructure and critical mass of expertise, have a crucial role in both maintaining America's research excellence and advancing medical treatments and cures.

Come join the team whose hallmarks are stable funding, intellectual freedom, shared resources, and access to a wide range of scientific expertise. We seek creative, independent thinkers eager to take on high-risk, high-impact research. A fantastic array of early-career scientists already have been hired through the "Stadtman" recruitment in the last four years.

A variety of basic and translational/clinical positions are available, with areas of active recruitment including (but not limited to): Biochemistry, Biomedical Engineering, Biophysics, Biostatistics, Cancer Biology, Cell Biology, Cell Metabolism, Chemical Biology, Chromosome Biology, Circadian Biology, Computational Biology, Developmental Biology, Epidemiology, Genetics, Genomics, Health Disparities, Hearing & Balance, Immunology, Infectious Diseases, Microbiology, Molecular Pharmacology, Neurodevelopment, Neurosciences, Sensory Biology, Structural Biology, Systems Biology, Toxicology, Translational Research, and Virology.

Who we are: Among our approximately 1,100 principal investigators and 5,000 trainees are world-renowned experts in basic, translational, and clinical research. Our strength is our diversity in pursuit of a common goal, to alleviate human suffering from disease. Similar to academia, we offer our scientists the opportunity to mentor outstanding trainees at all levels (e.g., graduate students and postdoctoral fellows) in a research setting.

Whom we seek: For this broad, trans-NIH recruitment effort, we seek talented, early-career scientists with a clear and creative research vision who wish to contribute to the nation's health.

Qualifications/eligibility: Candidates must have an M.D., Ph.D., D.D.S./D.M.D., D.V.M, D.O., R.N./Ph.D., or equivalent doctoral degree and have an outstanding record of research accomplishments as evidenced by publications in major peer-reviewed journals. Applicants may be in early stages of their research careers or non-tenured early-to-mid career scientists. Appointees may be U.S. citizens, resident aliens, or non-resident aliens with, or eligible to obtain, a valid employment-authorization visa.

How to apply: Applicants must submit four items: (1) a CV; (2) a three-page proposal titled Research Goals, i.e., the research you hope to perform at the NIH; (3) a one-page statement titled Long-term Research Vision and Impact, i.e., what you hope to achieve for yourself, your field, and society; and (4) contact information for three professional references. Submit these through our online application system at http://tenuretrack.nih.gov/apply between August 1 and 11:59 p.m. EDT October 1, 2013. You will be asked to designate a primary and secondary scientific area of expertise to aid in assigning your application to the appropriate review committee. Requests for letters of recommendation will be sent to your references when you submit your application. Reference letters will be accepted via upload to the website until 11:59 p.m. EDT October 15, 2013. We cannot accept paper applications.

What to expect: Search committees of subject-matter experts will review and evaluate applicants based on publication record, scientific vision and potential scientific impact of current and proposed research, demonstrated independence, awards, and references. The committees will identify the most highly qualified candidates to invite to the NIH for a lecture in November or December 2013, open to the NIH scientific staff, and for subsequent interviews with the search committees. Search committee chairs and NIH Scientific Directors, who lead our intramural programs, will identify finalists for possible recruitment as Earl Stadtman Investigators. Candidates not selected as finalists can be considered for other open NIH research positions. The entire process from application review to job offer may take several months, depending on the volume of applications.

We call upon individuals who will open our eyes to possibilities we haven't yet envisioned, to complement our scientific mission and enhance our research efforts. More information about our program is at http://irp.nih.gov. The inspiring story of Earl and Thressa Stadtman's research at the NIH is at http://history.nih.gov/exhibits/stadtman. Specific questions regarding this recruitment effort may be directed to Dr. Roland Owens, Assistant Director, NIH Office of Intramural Research, at owensrol@mail.nih.gov. DHHS and NIH are Equal Opportunity Employers.

SFU SIMON FRASER UNIVERSITY
ENGAGING THE WORLD

Simon Fraser University is one of Canada's leading comprehensive universities with three campuses in Metro Vancouver. Through the strength and commitment of our staff and faculty, SFU is recognized as a top employer in both BC and Canada. We invite applications for the following position:

DEPARTMENT OF CHEMISTRY
FACULTY POSITION IN MATERIALS CHEMISTRY

The Department of Chemistry at Simon Fraser University (SFU) invites applications for a tenure track Assistant Professor position in Experimental Materials Chemistry to take effect in September 2014, subject to final budgetary approval. Candidates working in the area of Solar Energy who will make use 4D LABS' (www.4dlabs.ca) shared facilities in materials science, and who will help lead our expansion into the fabrication and testing of solar energy devices are especially encouraged to apply.

Applicants should have a Ph.D. degree and will normally have postdoctoral or industrial experience. Outstanding candidates with a commitment to excellence in research and teaching are being sought. The candidates will be expected to develop and maintain both an innovative, externally funded research program, and an excellent teaching record at both the undergraduate and graduate levels in Chemistry.

All qualified candidates are encouraged to apply; however, Canadians and Permanent Residents will be given priority. Simon Fraser University is committed to an equity employment program that includes special measures to achieve diversity among its faculty and staff. We therefore particularly encourage applications from qualified women, aboriginal Canadians, persons with disabilities, and members of visible minorities. Applicants should send a complete résumé, a concise research proposal, a description of teaching interest and experience, and a list of three individuals willing to act as referees with their addresses, telephone and/or fax numbers, and e-mail addresses. All correspondence should be sent to:

Dr. Zuo-Guang Ye, Professor and Chair, Department of Chemistry Simon Fraser University, 8888 University Drive, Burnaby BC V5A 1S6 Canada
E-mail: chemchr@sfu.ca

Please note: We thank all applicants for their interest, however, only those selected for interviews will be contacted.

Please note that under the University Act, personal information that is required by the University for academic appointment competitions will be collected. For further details see the Collection Notice. (www.chemistry.sfu.ca/about/employment)

www.sfu.ca/jobpostings

CUNY The City University of New York

DIRECTOR & PROFESSOR OF NANOSCIENCE

Advanced Science Research Center

The Advanced Science Research Center (ASRC) at the City University of New York (CUNY) seeks a dynamic and innovative scientist with demonstrated leadership and research accomplishments in a Nanoscience specialty area to serve as Professor and Director of Nanoscience. The position will be a tenured faculty member and program administrator. The successful candidate will be expected to engage in teaching and research; oversee the Nanoscience program; lead researchers in collaborative projects and activities; lead the continued acquisition of external funding; recruit new faculty; and ensure compliance with federal research guidelines and University policies.

Applicants must be accomplished and respected researchers in a Nanoscience area with a solid record of scholarly activities, and possess appropriate credentials for a senior faculty appointment at one of the CUNY colleges. Preference will be given to those whose experimental research focus areas include but are not limited to one or more of the following: nanomaterials, nanoelectronics, nanomedicine, nanophotonics, and bionanostructures.

Successful candidates will be scientists of outstanding merit and accomplishment with active, funded research programs in Nanoscience or a closely related area. Exceptional candidates may be appointed as a Distinguished Professor and/or Einstein Professor.

The ASRC is a 200,000 square feet science facility located at 85 St. Nicholas Terrace (close to 133rd Street) on the south campus of CUNY's City College and adjacent to the New York Structural Biology Center. Construction of the ASRC is well underway and due for completion in 2014. The innovatively designed center is a University-wide science enterprise that builds on the strengths CUNY has developed in five distinct but interconnected disciplines, Nanoscience, Photonics, Structural Biology, Neuroscience and Environmental Sciences. The center will be the nucleus of an integrated research network and will provide core facilities for CUNY scientists with the goal of fostering interdisciplinary research. To learn more about the ASRC visit www.asrc.cuny.edu.

Minimum Qualifications: Ph.D. in a life science, engineering, closely related science discipline or Nanoscience specialty area required.

To apply: Go to the CUNY website at http:www.cuny.edu/employment.html to view the complete job posting and qualification requirements. Click on 'Search Job Listings' under the Career Positions available section of the page, then click Faculty under the Employment Opportunities section; then look for the Job Posting title and Job ID #8638. Submit a letter of interest, curriculum vitae, summary of research interests/expertise area, a teaching statement, and the contact information for at least three (3) professional references. Compensation is commensurate with experience.

The City University of New York (CUNY) is an EO/AA Employer.

CUNY The City University of New York

DIRECTOR & PROFESSOR OF PHOTONICS

Advanced Science Research Center

The Advanced Science Research Center (ASRC) at the City University of New York (CUNY) seeks a dynamic and innovative scientist with demonstrated leadership and research accomplishments in Photonics to serve as Professor and Director of Photonics. The position will be a tenured faculty member and program administrator. The successful candidate will be expected to engage in teaching and research; oversee the Photonics program; lead researchers in collaborative projects and activities; lead the continued acquisition of external funding; recruit new faculty; and ensure compliance with federal research guidelines and University policies.

Applicants must be accomplished and respected researchers in a Photonics area with a solid record of scholarly activities, and possess appropriate credentials for a senior faculty appointment at one of the CUNY colleges. Preference will be given to those whose experimental research focus areas include but are not limited to one or more of the following: nanophotonics, terahertz technology, ultrafast spectroscopy, and plasmonics.

Successful candidates will be scientists of outstanding merit and accomplishment with active, funded research programs in Photonics or a closely related area. Exceptional candidates may be appointed as a Distinguished Professor and/or Einstein Professor.

The ASRC is a 200,000 square feet science facility located at 85 St. Nicholas Terrace (close to 133rd Street) on the south campus of CUNY's City College and adjacent to the New York Structural Biology Center. Construction of the ASRC is well underway and due for completion in 2014. The innovatively designed center is a University-wide science enterprise that builds on the strengths CUNY has developed in five distinct but interconnected disciplines - Nanoscience, Photonics, Structural Biology, Neuroscience, and Environmental Sciences. The center will be the nucleus of an integrated research network and will provide core facilities for CUNY scientists with the goal of fostering interdisciplinary research. To learn more about the ASRC visit www.asrc.cuny.edu.

Minimum Qualifications: Ph.D. in a life science, engineering, closely related science discipline, or Photonics specialty area required

To apply: Go to the CUNY website at http:www.cuny.edu/employment.html to view the complete job posting and qualification requirements. Click on 'Search Job Listings' under the Career Positions available section of the page, then click Faculty under the Employment Opportunities section; then look for the Job Posting title and Job ID #8640. Submit a letter of interest, curriculum vitae, summary of research interests/expertise area, a teaching statement, and the contact information for at least three (3) professional references. Compensation is commensurate with experience.

The City University of New York (CUNY) is an EO/AA Employer.

NANYANG TECHNOLOGICAL UNIVERSITY

DISTINCTIVE LEADERSHIP AND RESEARCH OPPORTUNITY

with the fastest-rising university in the world's top 50. **NTU, Singapore**







Nanyang Technological University, Singapore, invites applications for the position of

Chair, School of Biological Sciences in College of Science

About the Appointment

This is an exceptional opportunity for a visionary scientist to lead the School of Biological Sciences (SBS) in the next phase of its development at the hub of the rapidly growing Life Sciences cluster at the Nanyang Technological University.

The Chair reports to the Dean of Science and is expected to provide leadership and oversight for the academic, intellectual and administrative affairs of the School and its two major disciplines, Molecular Genetics & Cell Biology, and Structural Biology & Biochemistry. The Chair is expected to work closely with counterparts in the Schools of Chemical & Biomedical Engineering, and Physical & Mathematical Sciences, as well as the new Lee Kong Chian School of Medicine, to promote the ethos of cross cutting innovation in research and teaching embodied by NTU. Building on the existing disciplines in SBS, there will be significant scope for the new Chair to shape the School's future through recruiting world-class talent and cultivating a successful grant funding culture. The Chair is a member of the Dean Advisory Committee.

The appointee must have a record of academic achievements, research and teaching in a reputable university. The appointee must have strong interpersonal and communication skills to engage faculty, and commit to faculty shared governance.

The massive investment in Biomedical Science and engineering in Singapore over the past decade has generated a research landscape unparalleled in Asia, and on par with leading academic centres across the world. SBS is poised to assume a prominent position in this landscape through strategic partnerships with Research Centres of Excellence, such as the Singapore Centre on Environmental Life Sciences Engineering, in the life sciences cluster at NTU, and with the wider Singapore research community, notably the A*Star Research Institutes, and the new LKC Clinical Research Centre at Tan Tock Seng Hospital.

About Nanyang Technological University

NTU is an internationally reputed research-intensive university with globally acknowledged strengths in Engineering and Business. Science and Humanities have added to the strengths of the University, and a Medical School has been set up jointly with Imperial College London. Ranked 47th by the Quacquarelli Symonds (QS) World University Rankings, NTU is the fastest rising university in the QS global top 50 universities. It is 2nd in the world among the young elite universities, according to QS' Top 50 under 50 rankings, and also jumped seven places to break into Asia's Top 10 universities. NTU is also placed within the top 100 in the Times Higher Education rankings.

The University's academic and research programmes, with real-world relevance, have received strong support from major corporations and industry leaders, in terms of research funding, industry partnerships, and global internship opportunities for the students.

About the College and School

The College of Science is nascent amongst NTU's four colleges - College of Engineering; College of Science; College of Business (Nanyang Business School), and College of Humanities, Arts, and Social Sciences. More information on the College of Science and the School can be accessed at: **http://www.cos.ntu.edu.sg** and **http://www.sbs.ntu.edu.sg**

To apply, please send curriculum vitae, accompanied by a cover letter, to:

The Chairman of the Search Committee, Prof Staffan Kjelleberg,
Director, of the Singapore Centre on Environmental Life Sciences Engineering,
a NTU Research Centre of Excellence,

c/o Secretary to the Search Committee
Nanyang Technological University
Level 4, Administration Building
50, Nanyang Avenue
Singapore 639798

Fax: (65) 6795 9001
Email: CHAIRSEARCHSBS@NTU.EDU.SG

Closing Date: 31 October 2013

Korn/Ferry International Pte Ltd is the appointed Executive Search firm for the Chair Search.

All applications and materials submitted will be held in strict confidence.

www.ntu.edu.sg

Science Careers online @sciencecareers.org

MUSC
MEDICAL UNIVERSITY of SOUTH CAROLINA

Recruiting Faculty in Biochemistry and Molecular Biology

Faculty positions at the Assistant, Associate, and Full Professor ranks are available in the Department of Biochemistry and Molecular Biology at the Medical University of South Carolina (MUSC) in Charleston. Candidates with research interests in all areas of biochemistry, cell, molecular, and cancer biology are welcome to apply. State-of-the-art laboratories, outstanding resources and research support are available. In addition, endowed chair positions are available for exceptional candidates.

Candidates should have a national reputation and a solid record of collaborative and peer-reviewed funded research. We are seeking outstanding scientists who would complement and expand existing research foci and programs at MUSC.

Located on the Atlantic coast in South Carolina, Charleston boasts one of the nation's most historic downtown areas, beaches and year-round outdoor life, as well as international cultural events such as the Spoleto Festival USA.

Interested researchers should send their CV and a summary of future research plans to:
www.jobs.musc.edu/applicants/Central?quickFind=191045

Philip H. Howe, Ph.D.
Professor & Chair
Department of Biochemistry & Molecular Biology
Medical University of South Carolina
173 Ashley Avenue, MSC 509
Charleston, SC 29425
simmonva@musc.edu

MUSC is an Equal Opportunity Employer, promoting workplace diversity.

NORTHWESTERN UNIVERSITY

Department of Neurobiology Two Assistant Professor Positions

The Department of Neurobiology, in the Weinberg College of Arts and Sciences, seeks to recruit two new tenure-track faculty members at the level of Assistant Professor. Applicants holding a Ph.D. and/or M.D. degree and demonstrating an outstanding record of scientific achievement will be considered. We are interested in individuals whose research addresses fundamental issues in neuroscience and who show significant potential for innovation, scholarship, and commitment to excellence in research and teaching.

Successful candidates will be expected to establish and maintain a high-profile research program attracting substantial extramural funding. The appointees will have access to state-of-the-art life science research support facilities and opportunities to interact with colleagues in the Interdepartmental Neuroscience Program consisting of over 130 faculty, the Feinberg School of Medicine, the McCormick School of Engineering, the School of Communication, as well as the Center for Advanced Molecular Imaging, the Chemistry of Life Processes Institute, the Institute for Complex Systems, the Cognitive Neurology and Alzheimer's Disease Center, the Center for Reproductive Science, the Center for Sleep and Circadian Biology, and the Robert H. Lurie Comprehensive Cancer Center.

Applicants will submit (in PDF format) a cover letter, a CV, and a description of research plans. Applications must be submitted electronically. For details on preparing and submitting the application, please visit **neurobiology.northwestern.edu/openings**. Please plan to request at least three letters of recommendation. **Applications received by November 1, 2013 will be ensured full consideration. All other inquiries may be directed to neurobiofacsearch@northwestern.edu**.

AA/EOE. Women and minority applicants are encouraged to apply.

University of Minnesota Medical School

Department of Pharmacology TENURED/TENURE-TRACK POSITIONS (Assistant Professor, Associate Professor, Professor)

The Department of Pharmacology at the University of Minnesota invites applications to fill multiple tenured/tenure-track faculty positions. The successful applicant's research will contribute to one or more of the University of Minnesota's "Corridors of Discovery", which includes brain science, cancer, and cardiovascular disorders. Investigators with translational disease-oriented research programs are especially encouraged to apply. Qualifications include a Ph.D. in the biomedical sciences or an M.D. degree, and relevant postdoctoral research experience. Applicants must have a strong record of research accomplishments as documented by publications in leading peer-reviewed journals. The successful **Assistant Professor** applicant will be expected to develop an innovative, competitive research program supported by extramural funding and to participate in departmental teaching and service activities. Applicants for **Associate Professor** or **Full Professor** positions must demonstrate distinction in published research, evidence of consistent extramural funding, and a commitment to teaching and service. For additional information about the department, visit: **www.pharmacology.med.umn.edu**.

Interested applicants should apply online at:
employment.umn.edu/applicants/Central?quickFind=112948 (Assistant Professor)
employment.umn.edu/applicants/Central?quickFind=112953 (Associate or Full Professor)

Please attach a letter of interest, curriculum vitae, brief statement of research interests, and contact information for three references.

The University of Minnesota is committed to the policy that all persons shall have equal access to its programs, facilities, and employment without regard to race, color, creed, religion, national origin, sex, age, marital status, disability, public assistance status, veteran status or sexual orientation.

NATIONAL INSTITUTE OF IMMUNOLOGY, INDIA

Career Opportunities for Scientists

The National Institute of Immunology, New Delhi, is a leading research Institute in India with a long-standing reputation for scientific excellence. The institute is equipped with state-of-the-art infrastructure for pursuing research in immunology and allied sciences. The Institute also imparts vigorous long-term research training leading to a Ph.D degree.

The Institute invites applications from early as well as mid-career scientists to set up independent research programmes to address immunological problems at the expanding interface of modern biology. Applicants should possess a Ph.D degree or an M.D. with four years relevant experience post-Ph.D/M.D. Demonstrated record of scientific productivity in the form of outstanding publications in scientific journals of repute and/or internationally valid and productive patents is essential. Applicants should have a commitment to excellence and willingness to collaborate in interdisciplinary projects. Eligible & interested candidates are advised to visit the website, **http://www.nii.res.in** for detailed information.

FACULTY POSITIONS

Physiology & Pharmacology



The Department of Physiology & Pharmacology at Des Moines University invites applicants for open-rank, tenure-track faculty positions. Qualifications include preparation and expertise in one or more of the following areas:

Cardiovascular Physiology; Respiratory Physiology; Endocrine Physiology or Medical Pharmacology

We are committed to advancing our research enterprise and fostering an environment conducive to scholarly success through the cultivation of distinctive faculty and student researchers who discover and disseminate new knowledge. The expectation is for faculty to participate in scholarly activity including grant application, publications, research, as well as teaching to graduate and medical school students. Candidates should demonstrate the potential to develop an innovative and extramurally funded research program and have a Ph.D. or equivalent plus a minimum of two years postdoctoral experience. Compensation and lab start-up costs are funded by the University and are not dependent on grant funding.

Please submit a letter of application, a CV, a concise statement of teaching interests and educational philosophy, a well-defined research plan including specific aims and objectives and three references using the online applicant tracking system at ***www.dmu.edu/employment***. Candidates with questions specific to this position may contact Department Chair Dr. Matt Henry at 515-271-1434.

For more information on all that the Des Moines area has to offer regarding housing, schools, entertainment, lower cost of living and more, visit ***www.desmoinesmetro.com***.

DES MOINES UNIVERSITY

Job description, faculty benefit summary and information on Des Moines University are available at www.dmu.edu/employment.

Review of applications will begin immediately and continue until the positions are filled.

Des Moines University is an equal opportunity/affirmative action employer. The University seeks excellence through diversity among its administrators, faculty, employees and students. The University prohibits discrimination on the basis of race, color, national origin, creed, religion, age, disability, sex, gender identity, sexual orientation, veteran status, genetic information or any other legally protected status. Applications by members of all underrepresented groups are encouraged.

AAAS

ADVANCING SCIENCE, SERVING SOCIETY

The American Association for the Advancement of Science (AAAS) seeks a **Deputy Editor** to oversee the selection and editing process for the research section of Science magazine based on the overall vision, guidance, and advisement of the Editor-in-Chief and Executive Editor.

Major duties and responsibilities:

- Develop the content strategy for the journal in concert with the Editor-in-Chief, Senior Editorial Board, and other senior managers; Gather feedback and data to help shape the strategy and monitor progress; Identify target research areas, as well as, research groups for the editorial team to cultivate; Attend scientific meetings and visit research institutions to further these efforts
- Oversee the peer-review process for the journal by establishing and maintaining the Standard Operating Procedures, including handling problem papers, liaising with institutions as needed, and determining appropriate outcomes
- Monitor trends in the research community to ensure the journal's policies and practices are aligned with community expectations; Solicit feedback on performance and recommend corrective action as needed; Suggest innovations that will improve the competitive position of the journal
- Chair and represent the journal's research section at space meetings and weekly planning meetings; communicate information needed for effective coordination between the sections of the journal
- Develop the editorial calendar with counterparts in the News and Commentary section; Establish and monitor page budget and allocate pages to individual editors based on overall goals; Assign papers to editors upon submission
- Supervise team leaders, Senior Editors, and Editorial Assistants including assigning work, providing training, and recommending personnel actions; Act as a liaison and facilitate communication between the editorial team and the Editor-in-Chief and Executive Editor; Act as liaison with other AAAS departments as necessary; Prepare and monitor budgets and authorizes expenditures
- Evaluate manuscripts within specific research areas submitted for publication in Science

Minimum qualifications:

- Extensive university or college level training leading to a Doctoral degree in a scientific field with post-doctoral research experience
- Ten to fifteen years of experience evaluating research and scientific content; ability to identify high-quality research and new and emerging research groups and trends
- Comprehensive knowledge of scientific research methods and cutting edge research practices
- Experience managing staff, setting goals, and evaluating outcomes
- Excellent written, verbal, and interpersonal communication skills in order communicate with staff, editors, and members of the scientific community

Please visit our job information website **http://www.aaas.org/careercenter/employmentataaas/** to get more information, and to apply to AAAS online.

AAAS is an Equal Opportunity Employer.

Science Careers online @sciencecareers.org



AAAS is here – helping scientists achieve career success.

Every month, over 400,000 students and scientists visit ScienceCareers.org in search of the information, advice, and opportunities they need to take the next step in their careers.

A complete career resource, free to the public, *Science* Careers offers a suite of tools and services developed specifically for scientists. With hundreds of career development articles, webinars and downloadable booklets filled with practical advice, a community forum providing answers to career questions, and thousands of job listings in academia, government, and industry, *Science* Careers has helped countless individuals prepare themselves for successful careers.

As a AAAS member, your dues help AAAS make this service freely available to the scientific community. If you're not a member, join us. Together we can make a difference.

To learn more, visit
aaas.org/plusyou/sciencecareers

AAAS + U = Δ

THE UNIVERSITY OF MAINE

Neurobiology Tenure Track Position

The University of Maine, School of Biology and Ecology, invites applications for a full-time, tenure-track academic-year Assistant Professor of Neurobiology with a 50% research/50% teaching workload to begin September 1, 2014. Applicants with interdisciplinary interests that will complement the University's emerging research programs in zebrafish models of muscle and neurodegenerative diseases, and/or the neurobiology of stress are encouraged to apply. A Ph.D. in a relevant area of biology or neuroscience is required by date of hire. The candidate is expected to develop and maintain a research program in the general field of neuroscience and contribute to undergraduate and graduate courses in biology.

For complete job description and application instructions, please go to:
jobs.umaine.edu/blog/category/faculty/

Additional information can be obtained about the University of Maine and the School of Biology and Ecology at **www.umaine.edu** and **http://sbe.umaine.edu/**.

The University of Maine is an Equal Employment Opportunity/Affirmative Action Employer.

BRAINS

Diversifying Neuroscience

Are you a postdoctoral scholar or assistant professor in a neuroscience-related field?

Do you identify as someone from a group underrepresented in neuroscience?

Are you interested in receiving in-depth career support and direction over a two-year period?

Join the BRAINS professional development program
Applications for the next cohort open in 2014
Visit brains.washington.edu
E-mail brains@uw.edu

In order to be eligible to participate in BRAINS, you must be a citizen or permanent resident of the United States and from a group or background recognized as underrepresented in neuroscience. Please visit our website for detailed eligibility information. Program Funded by NINDS Grant 1R25NS076416-01

Science Careers is the forum that answers questions.



Science Careers is dedicated to opening new doors and providing timely answers to the career questions that matter to you.

***Science* Careers Forum:**

- Relevant Career Topics
- Timely Advice and Answers
- Community, Connections, and More!

Visit the forum and join the conversation today!

Your Future Awaits.

Science Careers
From the journal *Science* AAAS
ScienceCareers.org

UT SOUTHWESTERN MEDICAL CENTER

The Department of Molecular Biology at the University of Texas Southwestern Medical Center invites applications for tenure track Assistant Professor positions. We are seeking interactive individuals with strong research programs focused on mechanistic aspects of gene regulation, cell growth and differentiation, development, and stem cell biology, including the use of iPS cells to study reprogramming during development and disease. Attractive recruitment packages, state-of-the-art core facilities, and exceptional laboratory space are available. UT Southwestern has a vibrant graduate program and an atmosphere of collegiality and collaboration.

Applicants should submit a curriculum vitae containing a summary of past research accomplishments, a statement of future objectives, and names of three references via email to:

Search Committee
Department of Molecular Biology
University of Texas Southwestern Medical Center
MolBioSearch@UTSouthwestern.edu

UT Southwestern Medical Center is an Affirmative Action/Equal Opportunity Employer. Women, minorities, veterans and individuals with disabilities are encouraged to apply.

UK UNIVERSITY OF KENTUCKY

Chair
Department of Physiology
University of Kentucky College of Medicine

The University of Kentucky College of Medicine seeks to fill the position of Chair of the Department of Physiology (http://physiology.med.uky.edu/). The successful candidate should have a Ph.D., M.D., or equivalent degree, a record of sustained extramural grant support, an internationally recognized research program, and strong leadership skills. The new Chair will lead a top 20 research department with 26 primary faculty whose research strengths include muscle biology, cardiac and pulmonary physiology, neurophysiology, the biology of aging, and diseases related to these disciplines. The Chair will be charged with sustaining and building upon the Department's existing excellence in both research and teaching.

The University of Kentucky is a recipient of an NIH Clinical and Translational Science award and houses internationally recognized research centers in cardiovascular health, diabetes and obesity, muscle biology, Alzheimer's disease, aging, and neurotrauma. NIH funding to the College of Medicine of ~$62 million places it among the top 35 public medical schools nationwide. The UK Medical Center is contiguous with UK's undergraduate campus, located in the heart of the Bluegrass Region in Lexington, a mid-sized city known for its quality of life (http://www.locateinlexington.com).

Interested persons should send their curriculum vitae, statement of research interests and goals as Chair, as well as the names of three references, to:

Chair Search Committee
Department of Physiology
MS509 UK Medical Center
800 Rose St.
Lexington, KY 40536-0298

or send documents via email to: **PhysiologySearch@uky.edu**

The committee will begin to consider applicants on **September 19, 2013**, and will continue until an appropriate candidate is identified.

The University of Kentucky is an equal opportunity employer and encourages applications from minorities and women.

VE RI TAS

Tenure-Track Assistant Professorship in Chemistry (Organic)
Harvard University

Candidates are invited to apply for a tenure-track assistant professorship in organic chemistry, broadly defined to include chemical biology, organic synthesis, organic materials, physical-organic chemistry, organometallic chemistry, and catalysis. The appointment is expected to begin on July 1, 2014. The tenure-track professor will be responsible for teaching at the undergraduate and graduate levels. We are seeking candidates who have an outstanding research record and a strong commitment to undergraduate and graduate teaching. Doctorate required by expected start date.

Candidates should arrange to have three letters of recommendation sent independently and provide a curriculum vitae, statement of teaching philosophy, list of publications, and outline of their future research plans. All applications and supporting materials must be submitted via the ARIeS portal (**http://academicpositions.harvard.edu/postings/4914**) no later than **October 15, 2013**.

Harvard is an Equal Opportunity/Affirmative Action Employer. Applications from women and minorities are strongly encouraged.

VE RI TAS

Tenure-Track Assistant Professorship in Chemistry (Inorganic)
Harvard University

Candidates are invited to apply for a tenure-track assistant professorship in inorganic chemistry, broadly defined to include catalysis, synthesis, mechanism, materials, and energy-related research. The appointment is expected to begin on July 1, 2014. The tenure-track professor will be responsible for teaching at the undergraduate and graduate levels. We are seeking candidates who have an outstanding research record and a strong commitment to undergraduate and graduate teaching. Doctorate required by expected start date.

Candidates should arrange to have three letters of recommendation sent independently and provide a curriculum vitae, statement of teaching philosophy, list of publications, and outline of their future research plans. All applications and supporting materials must be submitted via the ARIeS portal (**http://academicpositions.harvard.edu/postings/4913**) no later than **October 15, 2013**.

Harvard is an Equal Opportunity/Affirmative Action Employer. Applications from women and minorities are strongly encouraged.

PRINCETON UNIVERSITY

ASSISTANT PROFESSORSHIP
ANIMAL BEHAVIOR

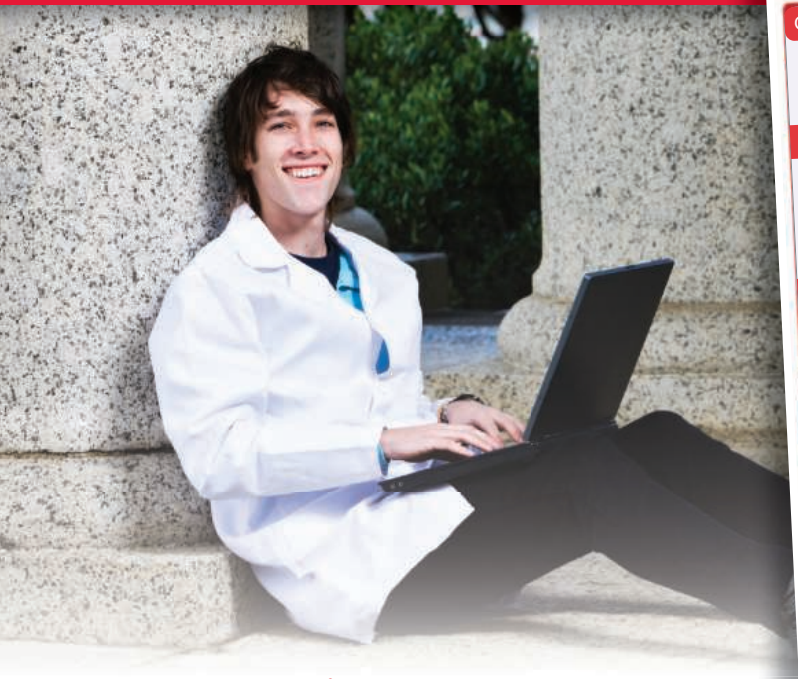
Princeton University's Department of Ecology and Evolutionary Biology plans to hire a tenure track assistant professor focusing on animal behavior. The Department has broad interests in behavioral ecology, behavioral dynamics, behavioral mechanisms, behavioral genetics, behavioral endocrinology and physiology, and behavioral links to other features of organismal biology. We seek applicants who pursue research that aims for significant conceptual and/or empirical integration of animal behavior in broader contexts of complex systems, neuroscience, genomics, ecology and evolution, and who have a strong commitment to teaching. A joint appointment with the Princeton Environmental Institute is possible, especially if the applicant's research focuses on problems of global or environmental change.

Applicants should write a vision statement, no longer than two pages, that outlines the conceptual dimensions of one or more major unsolved problems in their field and how their approach will contribute to solving them. The vision statement should be more than a summary of the applicant's prior and current research. Applications, including the vision statement, curriculum vitae, three reprints and contact information for three letters of recommendation, can be submitted online via **http://jobs.princeton.edu**, requisition **#1300555**. Screening of applications begins **September 23, 2013**.

Princeton University is an Equal Opportunity Employer and complies with applicable EEO and affirmative action regulations.

For your career in science, there's only one Science

A career plan customized *for* you, *by* you.



myIDP.sciencecareers.org



Recommended by leading professional societies and endorsed by the National Institutes of Health, an individual development plan will help you prepare for a successful and satisfying scientific career.

my IDP Science Careers

In collaboration with FASEB, UCSF, and the Medical College of Wisconsin and with support from the Burroughs Wellcome Fund, AAAS and *Science* Careers present the first and only online app that helps scientists prepare their very own individual development plan.

Visit the website and start planning today!
myIDP.sciencecareers.org

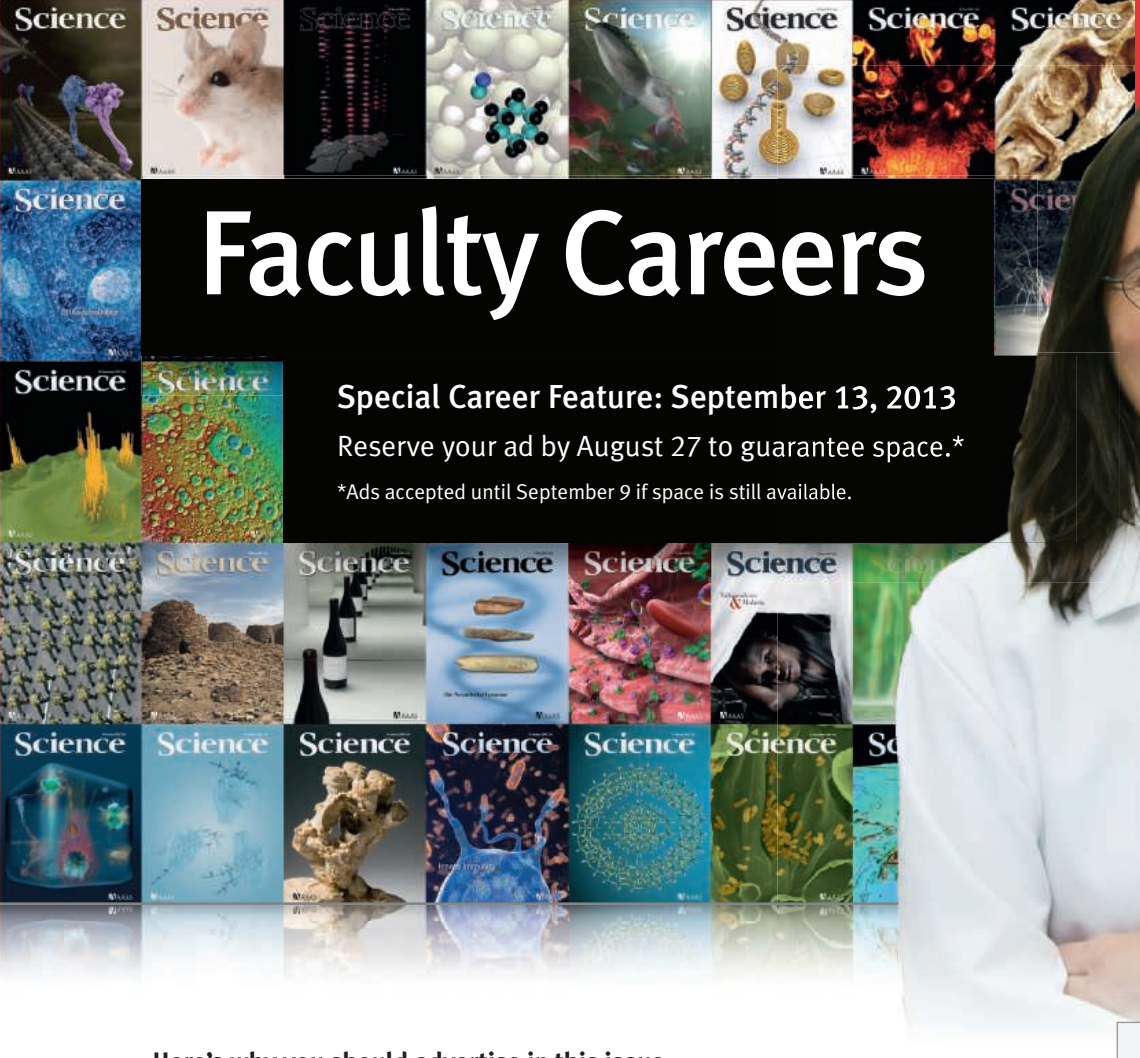
In partnership with:

advancing the life sciences 1912-2012 FASEB Federation of American Societies for Experimental Biology

UCSF University of California San Francisco

Medical College of Wisconsin

Burroughs Wellcome Fund



Faculty Careers

Special Career Feature: September 13, 2013

Reserve your ad by August 27 to guarantee space.*

*Ads accepted until September 9 if space is still available.

Here's why you should advertise in this issue:

Content: This feature examines how faculty and PIs are joining forces to maximize potential resources and grant money. Gear up to recruit for the faculty positions at your university with this much-anticipated issue that reaches thousands of Ph.D. scientists looking for positions in academia.

Reach: Your job ad is seen by 700,000 readers around the globe from varied backgrounds and it sits on special bannered pages promoting faculty careers. Over 57% of our weekly readers work in academia and 67% are Ph.D.s. *Science* connects you with more scientists in academia than any other publication.

Bonus Distribution to:

- ECCO-ESMO-ESTRO European Cancer Congress
 September 27–October 1, Amsterdam, Netherlands

Ask about customized packages for this feature

Results: If you are looking to hire qualified scientists, *Science* offers a simple formula: must-read content + your ad + a large and qualified audience = your hiring success.

Find your next faculty member by advertising in this special feature.

For recruitment in science, there's only one Science

To book your ad, contact:

East Coast/West Coast/ South America:
Tina Burks
Phone: 202-326-6577
E-mail: tburks@aaas.org

Midwest/Canada:
Marci Gallun
Phone: 202-326-6582
E-mail: mgallun@aaas.org

Corporate:
Candice Nulsen
Phone: 202-256-1528
E-mail: cnulsen@aaas.org

Science Careers
From the journal *Science* AAAS
ScienceCareers.org

Produced by the *Science*/AAAS Custom Publishing Office

POSITIONS OPEN

FACULTY POSITIONS in Neuroethics

Georgia State University is creating a new interdisciplinary Neuroethics Program, a cooperative venture of the Neuroscience Institute, the Department of Psychology, the Department of Philosophy, and the College of Law. The Neuroethics Program includes three new open-rank tenured/tenure-track hires, new Ph.D. fellowships, and new Ph.D. Concentrations in Neuroethics. It will be a part of a thriving interdisciplinary community, including the resources of the Center for Advanced Brain Imaging, the Brains & Behavior Program, the Language Research Center, the Blumenfeld Center for Ethics, and the Atlanta Neuroethics Consortium.

Candidates should have expertise in one or more of the following areas: (1) cognitive or affective neuroscience or psychology, specializing in moral cognition, emotion, or behavior; (2) ethical and/or legal theory as applied to neuroscience; (3) philosophy of neuroscience, cognitive science, moral psychology. Candidates must have a record of successful research and Ph.D. at time of application. Anticipated start date is fall 2014. Applicants apply online at **website: https://academicjobsonline.org/ajo/jobs/1576**, where they will find more information. Questions should be sent to chair of the search committee, **Eddy Nahmias, e-mail: enahmias@gsu.edu**.

In addition to these positions, the 2CI program is supporting hires in neuroimaging; primate social cognition, evolution, and behavior; and neurogenomics. For more information, see **website: http://secondcentury.gsu.edu/**.

Review of applications will continue until the positions are filled. *Georgia State University is an Affirmative Action/Equal Employment Opportunity Employer and encourages applications from women and minority candidates.*

ASSISTANT PROFESSOR
Physical Chemistry
California State University East Bay

The California State University, East Bay (CSUEB) Department of Chemistry & Biochemistry invites applications for a tenure-track Assistant Professor position in Physical Chemistry (**#14-15 CHEM-PHYSICAL-TT**) for the 2014–2015 academic year. The successful candidate must have extensive training in physical chemistry and a strong commitment to teaching. Applicants are expected to establish an externally funded research program appropriate for undergraduate and M.S. students pursuing a chemistry curriculum. Teaching responsibilities may include general chemistry, physical chemistry lecture and laboratory, environmental chemistry lecture and laboratory, and advanced topics in physical chemistry. A Ph.D. is required; postdoctoral research and teaching experience in chemistry are preferred. Applicants must submit, via regular mail, hard copies of a cover letter specifying the position number, curriculum vitae, a one-page statement of teaching philosophy, a three-page statement of research plans, and arrange to have undergraduate and graduate transcripts and three letters of recommendation sent to: **Dr. Ann McPartland, Chair, Department of Chemistry and Biochemistry, California State University, East Bay, Hayward, CA 94542.** Applicants must also submit the cover letter and the curriculum vita electronically at the following **website: https://my.csueastbay.edu/psp/pspdb1/EMPLOYEE/HRMS/c/HRS_HRAM.HRS_CE.GBL.** Review of applications will begin September 30, 2013 and continue until the position is filled. *CSUEB, an Equal Opportunity Employer, is committed to the principles of diversity in employment.*

Get your questions answered.
Careers Forum
www.ScienceCareers.org

POSITIONS OPEN

ASSISTANT PROFESSOR

Prokaryotic Microbiology

The Department of Biological Sciences at California State University, Long Beach invites applications for a tenure-track Assistant Professor position starting August 18, 2014. We seek broadly trained applicants who use genomic or metagenomic tools to study prokaryotes. The successful candidate will be expected to develop an externally funded research program involving undergraduate and M.S. students and teach at the undergraduate and graduate levels. Applicants must have a Ph.D. and postdoctoral experience. For further information, please see the position description at **website: http://www.csulb.edu/divisions/aa/personnel/jobs/posting/2050/index.html**. Screening of applications will begin September 15, 2013. *CSULB is an Equal Opportunity Employer.*

ASSISTANT PROFESSOR
Department of Chemistry Massachusetts Institute of Technology

The Massachusetts Institute of Technology (MIT) Department of Chemistry invites applications for tenure-track appointments beginning July 2014. Outstanding applicants with research interests in all areas of chemistry are encouraged to apply. MIT Chemistry has particular interest in appointments of faculty whose preference is to teach in the area of physical chemistry, broadly defined. Appointments are at the rank of assistant professor, but outstanding senior applicants may be considered. A complete application must include a curriculum vitae, a one-page summary of research plans, two or more research proposals, a brief statement of teaching interests, and three or more letters of recommendation.

Applications are being accepted at Academic Jobs Online (**website: https://academicjobsonline.org/ajo/MIT/Department of Chemistry**). To receive full consideration, completed applications must be received by October 7, 2013.

Search Contact: **Ms. Karen Fosher, Personnel Administrator, Department of Chemistry, Massachusetts Institute of Technology, Room 18-392, 77 Massachusetts Avenue, Cambridge MA 02139-4307** (**e-mail: kfosher@mit.edu**).

MIT is an Equal Opportunity/Affirmative Action Employer. Applications from women, minorities, veterans, older workers, and individuals with disabilities are strongly encouraged.

DEAN
College of Science, National Taiwan University

National Taiwan University (NTU) invites applications for the position of the Dean of the College of Science. The candidate should be a **FULL PROFESSOR**, while serving as Dean at National Taiwan University. Nomination would come from a minimum of 15 full-time faculty members, who hold at least lecturer status at the College of Science. Required Application Materials: Candidate nomination statement for deanship, academic and professional background of the candidate, publication list, written agreement to accept nomination. Deadline of submission: September 12, 2013. Inquiries via **e-mail: isalee@ntu.edu.tw** (Secretary, COS, NTU) or **telephone: 886-2-23637562. Website: http://www.science.ntu.edu.tw/index_en.php**.

Find your future here.
www.ScienceCareers.org

POSITIONS OPEN

RESEARCH ASSOCIATE
Indiana University, Bloomington
Biological Mass Spectrometry

The Department of Chemistry at Indiana University, Bloomington (IU) seeks a full-time Research Associate in Laboratory for Biological Mass Spectrometry (**website: http://www.chem.indiana.edu/bms/**). The Laboratory specializes in the development of novel mass spectrometry methodology and provides service for researchers both within and external to IU. We seek a creative, highly motivated scientist with a Ph.D. chemistry, biochemistry, or cell biology with 0–3 years postdoctoral experience. The ideal candidate will possess a creative, analytical approach to problem solving, the ability to work independently and the ability to lead interdisciplinary collaborations among multiple laboratories. Prior experience with mass spectrometry/proteomics is desirable, however candidates with a strong background in biochemistry or cell biology will also be considered. The salary range is $35,000 and $45,000 commensurate with qualifications and experience. Applications should provide a cover letter indicating research interests, career goals, and experience and curriculum vitae as a single PDF file, and arrange to have three letters of reference sent to: **Dr. Jonathan Trinidad, Director of Biological Mass Spectrometry, Department of Chemistry, Indiana University, Bloomington, IN 47405-7102** (**e-mail: trinidad@indiana.edu**). Review of applications will begin immediately and will continue until the position is filled. *Indiana University is an Equal Employment Affirmative Action Employer and especially encourages applications from women and members of minority groups.*

ASSISTANT PROFESSOR in Social Psychology

Harvard University Department of Psychology anticipates making two tenure-track appointments at the assistant professor level to begin July 1, 2014.

We seek candidates with exceptional promise in the area of social psychology. We are less concerned with specific research interests than with excellence, and applicants in all areas of social behavior and social cognition will be considered (e.g., altruism & cooperation, emotion, group processes, health & well-being, ideology, interpersonal relationships, judgment & decision-making, person perception, prejudice & stereotyping, social-cognitive development, social neuroscience, etc.).

It is required that candidates will have completed all requirements for the Ph.D. by the start date of the appointment. Teaching duties will include offerings at both undergraduate and graduate levels.

Candidates should submit curriculum vitae, research and teaching statements, representative reprints, the contact information for at least three references, and three letters of recommendation to **website: https://academicpositions.harvard.edu/postings/4884.** The application is complete only when all three letters have been submitted.

Questions regarding this position can be addressed to **e-mail: socialsearch@wjh.harvard.edu.** The closing date for applying is September 16.

Harvard University is an Affirmative Action/Equal Opportunity Employer, and we actively encourage applications from women and minority groups.

☑ More scientists agree—we are the most useful website.
Science Careers
From the journal Science AAAS
www.ScienceCareers.org